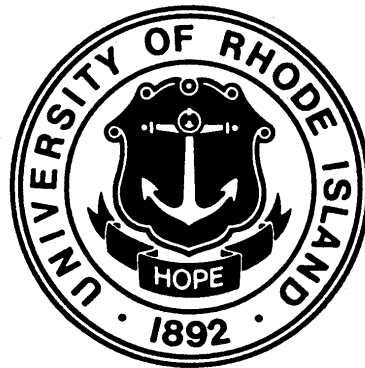


Aerospace and Materials Science Directorate
Structural Mechanics program
DEPARTMENT OF THE AIR FORCE
Grant # FA 95500610162

Final Report

**Dynamic Failure of Integrated Durable Hot
Structure for Space Access Vehicles**



ARUN SHUKLA
Simon Ostrach Professor
Dynamic Photomechanics Laboratory (DPML)
Department of Mechanical Engineering and Applied Mechanics
University of Rhode Island
Kingston, RI 02881
USA

REPORT DOCUMENTATION PAGE				Form Approved OMB No. 0704-0188	
<small>The public reporting burden for this collection of information is estimated to average 1 hour per response, including the time for reviewing instructions, searching existing data sources, gathering and maintaining the data needed, and completing and reviewing the collection of information. Send comments regarding this burden estimate or any other aspect of this collection of information, including suggestions for reducing the burden, to Department of Defense, Washington Headquarters Services, Directorate for Information Operations and Reports (0704-0188), 1215 Jefferson Davis Highway, Suite 1204, Arlington, VA 22202-4302. Respondents should be aware that notwithstanding any other provision of law, no person shall be subject to any penalty for failing to comply with a collection of information if it does not display a currently valid OMB control number.</small> PLEASE DO NOT RETURN YOUR FORM TO THE ABOVE ADDRESS.					
1. REPORT DATE (DD-MM-YYYY) August 2009		2. REPORT TYPE Final Report		3. DATES COVERED (From - To) 01/01/2006 - 12/30/2008	
4. TITLE AND SUBTITLE Dynamic Failure of Integrated Durable Hot Structure for Space Access Vehicles				5a. CONTRACT NUMBER	
				5b. GRANT NUMBER FA 95500610162	
				5c. PROGRAM ELEMENT NUMBER	
6. AUTHOR(S) Arun Shukla				5d. PROJECT NUMBER	
				5e. TASK NUMBER	
				5f. WORK UNIT NUMBER	
7. PERFORMING ORGANIZATION NAME(S) AND ADDRESS(ES) University of Rhode Island 92 Upper College Road, Kingston, RI 02881				8. PERFORMING ORGANIZATION REPORT NUMBER	
9. SPONSORING/MONITORING AGENCY NAME(S) AND ADDRESS(ES) Aerospace and Materials Science Directorate Structural Mechanics program DEPARTMENT OF THE AIR FORCE				10. SPONSOR/MONITOR'S ACRONYM(S) AFOSR	
				11. SPONSOR/MONITOR'S REPORT NUMBER(S) AFRL-SR-AR-TR-10-0045	
12. DISTRIBUTION/AVAILABILITY STATEMENT Distribution A- Approved for Public Release					
13. SUPPLEMENTARY NOTES					
14. ABSTRACT A fundamental study was conducted to evaluate dynamic fracture and failure in functionally graded materials (FGM) at room and high temperatures. Asymptotic analysis in conjunction with displacement potentials was used to develop thermo-mechanical stress fields for a mixed mode propagating crack in homogenous and FGMs. First, asymptotic temperature fields were derived for an exponential variation of thermal conductivity and later these temperature fields were used in deriving stress fields. Using asymptotic thermo-mechanical stress fields the variation of maximum shear stress, circumferential stress and strain energy density as a function of temperature around the crack-tip were generated. Finally, utilizing the minimum strain energy density criterion and the maximum circumferential stress criterion, the crack growth direction for various crack-tip speeds, non-homogeneity coefficients and temperature fields were determined.					
15. SUBJECT TERMS Functionally Graded Materials, Thermo -mechanical, Dynamic Fracture, Constitutive Behavior, Ti/TiB					
16. SECURITY CLASSIFICATION OF:			17. LIMITATION OF ABSTRACT	18. NUMBER OF PAGES	19a. NAME OF RESPONSIBLE PERSON
a. REPORT	b. ABSTRACT	c. THIS PAGE			19b. TELEPHONE NUMBER (Include area code)

Objectives

- Experimental visualization of the stress and deformation fields near dynamically propagating crack tips subjected to thermal, mechanical and thermo-mechanical loading in graded materials.
- Development of rate-dependent constitutive models for graded multifunctional materials under thermo-mechanical loading.
- Identification of damage mechanics in graded multifunctional materials subjected to high strain rate loading.
- Development of asymptotic stress fields for stationary and propagating cracks subjected to combined thermo-mechanical loading in graded materials.
- A critical evaluation of the influence of material gradation, thermal loading and loading rates on the damage mechanisms of graded materials.

ACCOMPLISHMENTS

A project entitled “*Dynamic Failure of Integrated Durable Hot Structure for Space Access Vehicles*” was funded by the AFOSR for a period of 3 years (Jan 2006 to Nov 2008). During this project a fundamental study was conducted to evaluate dynamic fracture and failure in functionally graded materials at room and at high temperatures. Room temperature studies included experimental and analytical evaluation of dynamic fracture in model materials. Analytical studies were also conducted to develop thermo-mechanical stress, strain and displacement fields around stationary cracks and around cracks propagating under steady state conditions. We also initiated preliminary studies on dynamic constitutive behavior as well as fracture-initiation toughness of a realistic FGM (Ti/TiB) at various temperatures and high strain rates of loading.

This research work produced (8) journal and (6) proceedings papers. One of the papers received the “Best Paper Award” from the Journal of Strain and also received the Flyde Prize from the British Society of Strain Measurement. Some of the details of the work conducted on this project are given below.

1. Asymptotic Stress Fields for Thermo-mechanically Loaded Cracks in FGMs

The problem of a stationary crack in functionally graded materials (FGM) subjected to a combination of thermal and mechanical loading was considered. An asymptotic analysis coupled with Westergaard’s stress function approach was used to characterize the stress field around the crack-tip. Thermal and mechanical properties (e.g. elastic modulus, coefficient of thermal expansion and thermal conductivity) were assumed to vary exponentially. The crack was assumed to be inclined to the direction of the property gradation. The thermal loading was taken to be a uniform heat flow in a direction inclined to the crack. The principal of superposition from linear elasticity was used to solve the problem, whereby the problem was divided into a number of sub-problems. The first four terms in the expansion of the stress field were derived to explicitly bring out the influence of nonhomogeneity on the structure of the stress field. It was observed that the presence of heat flow produced no additional singularity and hence the classical inverse square root singularity still prevails around the crack tip. Using these stress fields, contours of constant maximum shear stress were generated and the effect of thermal loading on the crack-tip stress field was discussed.

2. Asymptotic Analysis and Reflection Photoelasticity to Study Transient Crack Propagation in FGMs

The behavior of a rapidly moving transient crack in functionally graded materials (FGMs) was investigated theoretically and experimentally. First, a systematic theoretical analysis was presented for the development of the transient elastodynamic local stress, strain and displacement field expansions near a growing mixed mode crack tip in FGMs. The crack propagation direction was assumed to be inclined to the direction of the property variation. The displacement potential approach in conjunction with asymptotic analysis was utilized to derive explicit expressions for stress, strain and in-plane displacement fields. To further understand the transient crack growth behavior a series of dynamic fracture experiments were performed with in-house fabricated functionally graded material. The full-field stress data around the crack was recorded using dynamic photoelasticity and high-speed digital photography. Due to opaqueness of FGMs, birefringent coatings were employed to obtain the full-field isochromatics around the crack-tip. The stress field expansions developed in the first part of the study were used to interpret the experimental observations. The results of the experiments showed that the higher order transient expansion provides an accurate representation of crack-tip fields under severe transient conditions.

3. Dynamic Crack Tip Stress and Displacement Fields under Thermo-Mechanical Loading

Thermomechanical stress and displacement fields for a propagating crack in functionally graded materials (FGMs) were developed using displacement potentials and asymptotic analysis. The shear modulus, mass density, and coefficient of thermal expansion of the FGMs were assumed to vary exponentially along the gradation direction. Temperature and heat flux distribution fields were also derived for an exponential variation of thermal conductivity. The mode mixity due to mixed-mode loading conditions around the crack tip was accommodated in the analysis through the superposition of opening and shear modes. Using the asymptotic stress fields, contours of constant maximum shear stress were developed and the results were discussed for various crack-tip thermo-mechanical loading conditions.

4. Dynamic Constitutive Behavior of Ti/TiB layer FGM under Thermo-mechanical Loading

An experimental investigation was conducted to evaluate the thermo-mechanical constitutive behavior of a functionally graded material (FGM) under dynamic loading. Cylindrical specimens were machined from titanium / titanium mono-boride (Ti/TiB) layered FGM plate using electrical discharge machining (EDM). A Split Hopkinson Pressure Bar (SHPB) apparatus with infrared spot heaters was used to investigate the effect of temperature on mechanical response of the FGM material. A series of experiments were conducted at different temperatures and the stress strain relation for different temperatures was obtained. The material showed high thermal softening at elevated temperature resulting in a reduction in compressive strength and an increase in failure strain.

5. Effect of Dynamic Thermo-Mechanical Stress Field on Crack Propagation Direction in Functionally Graded Materials

Asymptotic analysis in conjunction with displacement potentials was used to develop thermo-mechanical stress fields for a mixed mode propagating crack in a functionally graded material (FGM). First, asymptotic temperature fields were derived for an exponential variation of thermal conductivity and later these temperature fields were used in deriving stress fields. Using asymptotic thermo-mechanical stress fields the variation of maximum shear stress, circumferential stress and strain energy density as a function of temperature around the crack-tip were generated. Finally, utilizing the minimum strain energy density criterion and the maximum

circumferential stress criterion, the crack growth direction for various crack-tip speeds, non-homogeneity coefficients and temperature fields were determined.

6. Dynamic Fracture Initiation Toughness of Ti/TiB Layered FGM under Thermo-mechanical Loading

Initial experiments were conducted to study dynamic fracture initiation toughness of Ti/TiB layered FGM was investigated using the modified SHPB apparatus. A three-point bending test specimen was machined from Ti/TiB plate using EDM technique. The crack was made using EDM wire of 0.002" which results in a very small notch radius. For the elevated temperature experiment, the specimen was first heated up using an induction heating system and the incident bar was made in contact manually just before propelling the projectile. A series of experiment were conducted at a fixed high loading rate and different temperatures to study the effect of temperature and loading rate on the fracture initiation toughness.

7. Experimental Facilities Developed

During the grant, facilities for high temperature testing of FGMs were established. These included set-ups with infrared heating system and induction coil heating system that were coupled to our existing SHPB apparatus. Also, two and three dimensional full field digital image correlation (DIC) techniques including three high speed cameras (Photron SA1) have been procured.

8. Student Supported: Addis Kidane (Ph.D. 2009) joined Caltech as post doc.

9. Refereed Journal Publications

1. N. Jain, R. Chona and A. Shukla "Asymptotic Stress Fields for Thermo-mechanically Loaded Cracks in FGM's," *Journal of ASTM International*, 3(7), 88-90, 2006.
2. N. Jain and A. Shukla "Asymptotic Analysis and Reflection Photoelasticity to Study Transient Crack Growth in Graded Materials," *Journal of Mechanics of Materials and Structures*, Vol. 2, No. 4, pp. 595-612, 2007.
3. A. Shukla, N. Jain and R. Chona "A Review of Dynamic Fracture Studies in Functionally Graded Materials", *Strain*, Vol. 43, No. 2, pp. 76-95, 2007.
4. K. H. Lee, V. Chalivendra and A. Shukla "Dynamic Crack Tip Stress and Displacement Fields Under Thermo-Mechanical Loading", *Journal of Applied Mechanics*, Vol. 75, pp. 1-7, 2008.
5. A. Kidane and A. Shukla, "Dynamic Constitutive Behavior Of Ti/Tib FGM Under Thermo Mechanical Loading", *Journal of Materials Science*, Vol. 43 Issue 8, 2008, p2771-2777.
6. A. Kidane, V. Chalivendra, A. Shukla, and R. Chona "Effect of Dynamic Thermo-Mechanical Stress Field on Crack Propagation Direction in Functionally Graded Materials", *Mechanics of material* (submitted).
7. A. Kidane, V. Chalivendra, and A. Shukla, "Thermo-Mechanical Stress Fields and Strain Energy associated with a Mixed-Mode Propagating Crack", *Acta Mechanica* (submitted).
8. A. Kidane and A. Shukla, "Quasi-Static and Dynamic Fracture Initiation Toughness of Ti/TiB Layered Functionally Graded Material under Thermo-Mechanical Loading", *Engineering Fracture mechanics* (accepted for publications)

10. Conference, Proceedings Publications

1. Kwang-Ho Lee, Addis Kidane, Venkit Parameswaran, and Arun Shukla, Dynamic crack propagation in transparent functionally graded material, SEM Annual Conference and Exposition on Experimental and Applied Mechanics, June 4-6, 2007, Springfield, MA.

2. A. Shukla and A. Kidane, "Dynamic constitutive behavior and fracture toughness of Ti/TiB FGM under thermomechanical loading," Proceedings of the International Symposium on Advances in Mechanics, Materials and Structures, China 2008.
3. A. Kidane and A. Shukla "Effect of temperature on the dynamic constitutive behavior of functionally graded materials" SEM Annual Conference and Exposition on Experimental and Applied Mechanics, June 2-5, 2008, Orlando, Florida
4. A. Kidnae, V. Chalivendra and A. Shukla "Effect of temperature on the dynamic crack tip stress field on FGM SEM XI Annual Conference and Exposition on Experimental and Applied Mechanics, June 2-5, 2008, Orlando, Florida.
5. A. Kidne and A. Shukla "Static and dynamic constitutive behavior and fracture of titanium based FGM under thermo-mechanical loading", Accepted, SEM Annual Conference and Exposition on Experimental and Applied Mechanics, June 1-4, 2009, Albuquerque, New Mexico.
6. A. Kidane, "Dynamic fracture initiation toughness and failure Of Ti/TiB FGM under thermo- mechanical loading" Student Paper Competition, Accepted, SEM Annual Conference and Exposition on Experimental and Applied Mechanics, June 1-4, 2009, Albuquerque, New Mexico.

11. Invited Lectures

1. "Functionally Graded Materials for Space Access Vehicles," Mid-Western Structural Mechanics Center, University of Illinois, February 2007.
2. Keynote Lecture, Photomechanics , Loughborough, UK, July 2008.
3. Keynote Lecture, UK Institute of Physics, 7 th International Conference on Stress and Vibration Analysis, Cambridge University, 2009.
4. Plenary Lecture, XI International Congress on Experimental Mechanics, Orlando, June'08.
5. Keynote Lecture, Interquadrennial Conference of International Congress on Fracture, Bangalore India, August 2008.
6. Seminar at IIT Kanpur, December 2008.
7. Invited Lecture, Nanjing Institute of Aeronautics and Astronautics, China 2008.
8. Invited Lecture, Heijang University, China 2008.

Appendix

AN EXPERIMENTAL AND ANALYTICAL STUDY OF GRADED
MATERIALS UNDER THERMO-MECHANICAL DYNAMIC LOADING

BY

ADDIS ASMELASH KIDANE

A DISSERTATION SUBMITTED IN PARTIAL FULFILLMENT OF THE

REQUIREMENTS FOR THE DEGREE OF

DOCTOR OF PHILOSOPHY

IN

DEPARTMENT OF MECHANICAL ENGINEERING AND APPLIED

MECHANICS

UNIVERSITY OF RHODE ISLAND

2009

DOCTOR OF PHILOSOPHY DISSERTATION
OF
ADDIS ASMELASH KIDANE

APPROVED:

Dissertation Committee:

Major Professor

DEAN OF THE GRADUATE SCHOOL

UNIVERSITY OF RHODE ISLAND

2009

ABSTRACT

A fundamental study is conducted to evaluate dynamic fracture and failure in functionally graded materials (FGM) at room and high temperatures. The study includes both analytical and experimental evaluation of dynamic fracture in model and commercially available materials.

Asymptotic analysis in conjunction with displacement potentials is used to develop thermo-mechanical stress fields for a mixed mode propagating crack in homogenous and FGMs. First, asymptotic temperature fields are derived for an exponential variation of thermal conductivity and later these temperature fields are used in deriving stress fields. Using asymptotic thermo-mechanical stress fields the variation of maximum shear stress, circumferential stress and strain energy density as a function of temperature around the crack-tip are generated. Finally, utilizing the minimum strain energy density criterion and the maximum circumferential stress criterion, the crack growth direction for various crack-tip speeds, non-homogeneity coefficients and temperature fields are determined.

An experimental investigation is conducted to evaluate the thermo-mechanical constitutive behavior of a FGM under dynamic loading. Cylindrical specimens are machined from titanium / titanium mono-boride (Ti/TiB) layered FGM plate using electrical discharge machining (EDM). A split Hopkinson pressure bar (SHPB) apparatus with infrared spot heaters is used to investigate the effect of temperature on mechanical response of the FGM. A series of experiments are conducted at different temperatures and the stress strain relation for different temperatures is obtained. The material showed high thermal softening at elevated temperature resulting in a reduction in compressive strength and an increase in failure strain.

Quasi-static and dynamic fracture initiation toughness of Ti/TiB layered FGM is investigated using a three point bend specimen. The modified SHPB apparatus

in conjunction with induction coil heating system is used during elevated temperature dynamic loading experiments. A simple and accurate technique has been developed to identify the time corresponding to the load at which the fracture initiates. A series of experiments are conducted at different temperatures ranging from room temperature to 800 °C, and the effect of temperature and loading rate on the fracture initiation toughness is investigated. The material fracture toughness is found to be sensitive to temperature and the fracture initiation toughness increases as the temperature increases. Furthermore, the fracture initiation toughness is strain rate sensitive and is higher for dynamic loading as compared to quasi-static loading.

A model transparent graded materials is used to investigate the steady state and transient crack propagation in a functionally graded material. High-speed digital photography combined with photoelasticity technique is used to record the full-field stress data around the propagating crack. By analyzing the photoelastic fringe patterns, the propagation crack tip velocity and displacement are obtained.

ACKNOWLEDGMENTS

I thanks the almighty for giving me the strength and determination to weather the demands of life. (SLECHERNETU EGZIABHER YIMSEGEN)

I would like to express my sincere gratitude to Dr. Arun Shukla for his continues guidance and support through this research. His patience and inspiring nature has been great source of motivation through out my doctoral studies.

A special thanks to Dr. Vijay Chalvendra who helped me to understand the physics in different angles and Dr. Martin Sadd for his time and discussion during the development of analytical work. I am also grateful to my PhD committee for their valuable comments during my comprehensive exam.

A spacial thanks to my colleagues in dynamic photomechanics laboratory Mathew Jackson, Erheng Wang, Nathaniel Gardner, Vijayalakshimi Manneth and Puneet Kumar for their support and encouragement. The help from the mechanical engineering department faculty and staffs Kevin, Jim , Rob, Joseph, Donna, Jennifer, Chati and Nanci is greatly acknowledged.

The financial support of the Air Force Office of Scientific Research under grant No. FA9550-06-1-0162 is acknowledged.

Last but not list, I would like to thank my beloved family my father (Abaye), my mother (Talem), my sisters and brothers, for their understanding nature, love and moral and material support. Many thanks to my friends (family) in Boston and Providence whom I am very close with for their help, affection and encouragement in making my dreams come true.

PREFACE

The present study addresses the dynamic fracture and failure of functionally graded materials (FGMs) under thermo - mechanical loading. Analytical and experimental investigation on the model and commercially available FGMs are presented.

The first chapter provides a detailed summary of a relevant review of literatures followed by a brief introduction and scope of the present study.

Chapter 2 presents analytical solution for homogenous material subjected to thermo-mechanical loading. Thermo-mechanical stress field equations are developed for a mixed-mode crack propagating at constant velocity in homogeneous and isotropic materials using asymptotic approach along with displacement potentials. Using these thermo-mechanical stress fields, various components of the stresses are developed and the effects of temperature on these stress components are discussed.

Asymptotic analysis in conjunction with displacement potentials has been used to develop thermo-mechanical stress fields for a mixed mode propagating crack in a FGMs and discussed in detail in chapter 3. Using asymptotic thermo-mechanical stress fields the variation of maximum shear stress, circumferential stress and strain energy density as a function of temperature around the crack-tip are generated. Utilizing the minimum strain energy density criterion and the maximum circumferential stress criterion, the crack growth direction for various crack-tip speeds, non-homogeneity coefficients and temperature fields are determined.

Chapter 4 discusses an experimental investigation conducted to evaluate the thermo-mechanical constitutive behavior of a FGMs under dynamic loading. A split Hopkinson pressure bar (SHPB) apparatus with infrared spot heaters is used to investigate the effect of temperature on mechanical response of the FGM. The

material showed high thermal softening at elevated temperature resulting in a reduction in compressive strength and an increase in failure strain.

Chapter 5 presents the quasi-static and dynamic fracture initiation toughness of Ti/TiB layered FGM. The modified SHPB apparatus in conjunction with induction coil heating system is used during elevated temperature dynamic loading experiments. A simple and accurate technique has been developed to identify the time corresponding to the load at which the fracture initiates. The material fracture toughness is found to be sensitive to temperature and the fracture initiation toughness increases as the temperature increases. Furthermore, the fracture initiation toughness is strain rate sensitive and is higher for dynamic loading as compared to quasi-static loading.

Chapter 6 discusses an experimental investigation of the steady state and transient crack propagation in a transparent functionally graded material. High-speed digital photography combined with photoelasticity technique is used to record the full-field stress data around the propagating crack. By analyzing the photoelastic fringe patterns the dynamic stress intensity factor and propagation velocity of the crack tip are obtained.

Finally, the summary of the present work and recommendation for the future work are presented in chapter 7.

TABLE OF CONTENTS

ABSTRACT	ii
ACKNOWLEDGMENTS	iv
PREFACE	v
TABLE OF CONTENTS	vii
LIST OF TABLES	xi
LIST OF FIGURES	xii
CHAPTER	
1 Introduction	1
1.1 Introduction	1
1.2 Related Literatures	2
1.3 Present Study	8
List of References	8
2 Dynamic Thermo-Mechanical Stress Fields for a Mixed-Mode Propagating Cracks	12
2.1 Abstract	12
2.2 Introduction	12
2.3 Theoretical Formulation	14
2.3.1 Temperature Fields around the Crack Tip	15
2.3.2 Asymptotic Expansion of Crack Tip Fields	17
2.3.3 Thermo-mechanical Stress Fields	19
2.4 Results and Discussion	21

	Page
2.4.1 Variation of Stress Components Near the Crack Tip . . .	21
2.4.2 Direction of Crack Growth	25
2.5 Summary	30
List of References	32
3 Effect of Dynamic Thermo-Mechanical Stress Field on Crack Propagation Direction in Functionally Graded Materials . . .	34
3.1 Abstract	34
3.2 Introduction	34
3.3 Theoretical Formulation	36
3.3.1 Temperature Fields around the Crack Tip	39
3.3.2 Asymptotic Expansion of Crack Tip Stress Fields	42
3.4 Results and Discussions	49
3.4.1 Variation of Stress Components Near the Crack Tip . . .	50
3.4.2 Crack Extension Angle	50
3.5 Summary	66
List of References	66
4 Dynamic Constitutive Behavior of Ti/TiB FGM under Thermo- Mechanical Loading	69
4.1 Abstract	69
4.2 Introduction	69
4.3 Material and Specimen Geometry	71
4.4 Experimental Procedure	73
4.5 Results and Discussion	76
4.5.1 Stress-strain Relation	76

	Page
4.5.2 Post Failure Analysis	81
4.6 Summary	82
List of References	85
5 Quasi-Static and Dynamic Fracture Initiation Toughness of Ti/TiB Layered Functionally Graded Material under Thermo-Mechanical Loading	88
5.1 Abstract	88
5.2 Introduction	88
5.3 Material and Specimen Geometry	90
5.4 Experimental Procedure	92
5.4.1 Quasi-static Fracture Initiation Toughness	92
5.4.2 Dynamic Fracture Initiation Toughness	93
5.5 Results and Discussions	96
5.5.1 Quasi-static Fracture Initiation Toughness of FGM Graded in the Thickness Direction	96
5.5.2 Quasi-static Fracture Initiation Toughness of FGM Graded in the Crack Direction	98
5.5.3 Dynamic Fracture Initiation Toughness of FGM Graded in the Thickness Direction	101
5.5.4 Dynamic Fracture Initiation Toughness of FGM Graded in the Crack Direction	104
5.5.5 Effect of Loading Rate on the Fracture Initiation Tough- ness of FGM	109
5.6 Summary	109
List of References	111

	Page
6 Dynamic Crack Propagation in Transparent Functionally Graded Material	113
6.1 Abstract	113
6.2 Introduction	113
6.3 Material and Specimen Preparation	115
6.4 Experimental Procedure	116
6.4.1 Dynamic Fracture at Constant Velocity	116
6.4.2 Transient Crack Propagation	118
6.5 Results and Discussion	118
6.5.1 Crack tip velocity	118
6.5.2 Dynamic Stress Intensity Factor	122
6.6 Summary	123
List of References	124
7 Conclusions and Recommendations	125
7.1 Conclusions	125
7.2 Recommendations	126
APPENDIX	
A Validation Plots	128
B Matlab Code	134
C Theoretical Formulation	141
D Split Hopkinson Bar Theory	163
BIBLIOGRAPHY	171

LIST OF TABLES

Table	Page
4.1	Composition and elastic properties of Ti/TiB FGM 73
5.1	Composition and elastic properties of Ti/TiB FGM 90
6.1	Material properties of polymer resins 116
D.1	Material properties of marring steel and tungsten carbide . . 167

LIST OF FIGURES

Figure		Page
2.1	Propagating crack tip orientation with respect to reference co- ordinate system	15
2.2	Contour of σ_{yy} in MPa for thermo-mechanical stress field around the crack-tip ($q_0=250$, $c/c_s = 0.5$ and $K_{ID} = 1\text{MPa}\cdot\text{m}^{1/2}$)(a) Before the opposite traction field is applied (b) After the oppo- site traction field is applied.	22
2.3	Normalized mixed mode in-plane stress fields as a function of θ around the crack-tip for different temperature fields ($c/c_s = 0.5$, $r = 0.002\text{m}$, $K_{ID} = 1\text{MPa } m^{1/2}$, $K_{IID} = 0.2 K_{ID}$)	23
2.4	Normalized mixed mode principal stress fields as a function of θ around the crack-tip for different temperature fields ($c/c_s =$ 0.5 , $r = 0.002\text{m}$, $K_{ID} = 1\text{MPa } m^{1/2}$, $K_{IID} = 0.2 K_{ID}$)	24
2.5	Crack extension angle as a function of crack tip velocity for mixed mode thermo-mechanical loading ($r=0.002\text{m}$).	28
2.6	Effect of temperature on the crack extension angle for mixed mode loading ($K_{IID}/K_{ID} = 0.2$, $c/c_s = 0.5$, $r = 0.002\text{m}$).	29
2.7	Crack extension angle as a function of crack tip velocity for mixed mode thermo-mechanical loading ($K_{IID}/K_{ID} = 0.2$, $r =$ 0.002m).	31
3.1	Propagating crack tip orientation with respect to reference co- ordinate configuration.	38
3.2	Variation of normalized maximum shear stress with angle around the crack-tip for mixed mode thermo-mechanical load- ing in a FGM for several values of temperature coefficients ($K_{IID}/K_{ID} = 0.2$, $c/c_s = 0.5$, $r = 0.002\text{m}$).	51
3.3	Variation of normalized the largest principal stress with an- gle around the crack-tip for mixed mode thermo-mechanical loading in a FGM for several values of temperature coefficients ($K_{IID}/K_{ID} = 0.2$, $c/c_s = 0.5$, $r = 0.002\text{m}$).	52

Figure		Page
3.4	Variation of normalized circumferential stress with angle around the crack-tip for mixed mode thermo-mechanical loading in a FGM for several values of temperature coefficients ($K_{IID}/K_{ID} = 0.2$, $c/c_s = 0.5$, $r = 0.002\text{m}$).	53
3.5	Variation of strain energy density with angle around the crack-tip for mixed mode thermo-mechanical loading in FGM subjected to different temperature fields ($K_{IID}/K_{ID} = 0.2$, $c/c_s = 0.5$, $r = 0.002\text{m}$).	55
3.6	Variation of normalized circumferential stress with angle around the crack-tip for mixed mode thermo-mechanical loading in FGM subjected to different temperature fields ($K_{IID}/K_{ID} = 0.2$, $c/c_s = 0.5$, $r = 0.002\text{m}$).	57
3.7	Crack extension angle as a function of crack tip velocity for mixed mode thermo-mechanical loading in homogeneous material ($\zeta = 0$, $r = 0.002\text{m}$).	58
3.8	Crack extension angle as a function of non-homogeneity parameter for mixed mode crack without heat ($c/c_s = 0.5$, $r = 0.002\text{m}$).	59
3.9	Effect of temperature on the crack extension angle for mixed mode loading in FGM ($K_{IID}/K_{ID} = 0.2$, $c/c_s = 0.5$, $r = 0.002\text{m}$).	61
3.10	Crack extension angle as a function of crack tip velocity for mixed mode thermo-mechanical loading for homogenous material ($K_{IID}/K_{ID} = 0.2$, $\zeta = 0$, $r = 0.002\text{m}$).	63
3.11	Crack extension angle as a function of crack tip velocity for mixed mode thermo-mechanical loading at different temperature ($K_{IID}/K_{ID} = 0.2$, $\zeta = 0.4$, $r = 0.002\text{m}$).	64
3.12	Crack extension angle as a function of crack tip velocity for mixed mode thermo-mechanical loading at different temperature ($K_{IID}/K_{ID} = 0.2$, $\zeta = -0.4$, $r = 0.002\text{m}$).	65
4.1	Scanning electron microscope image of layer 1 (TiB 0%), layer 2 (TiB 15%) and layer 3 (TiB 30%).	72
4.2	Wire EDM machined specimens (a) cooled by flooding, (b) cooled by fully immersing in coolant.	73
4.3	Schematic of split Hopkinson pressure bar.	75

Figure		Page
4.4	Split Hopkinson pressure bar with heater assembly.	75
4.5	Specimen-carbide inserts, thermocouple and sleeves assembly. .	76
4.6	Typical strain pulse profiles obtained during an experiment. . .	77
4.7	True stress-True strain curve as a function of temperature (specimen cooled by flooding during EDM).	78
4.8	A typical failed specimen at room temperature under dynamic loading.	79
4.9	A flash of light produced during room temperature dynamic experiment of specimen machined by EDM and cooled by flooding.	79
4.10	True stress - True stain curve as a function of temperature (specimen fully immersed in coolant during EDM).	80
4.11	Failure stress as a function of temperature.	81
4.12	Typical failed specimen during dynamic loading at elevated temperature.	82
4.13	Typical fracture surface of Ti/TiB specimen.	83
4.14	SEM images, at a magnification of 1000, of fracture surface of four different specimens tested at four different temperatures. .	84
4.15	SEM images, at a magnification of 5000, of fracture surface of specimens tested as two different temperatures.	85
5.1	Three point bend specimen (a) FGM graded in the thickness direction (b) FGM graded in the crack direction (all dimensions are in mm)	91
5.2	Quasi-static three point bed experimental setup.	92
5.3	Schematic representation of modified SHPB apparatus with induction heater.	93
5.4	A schematic of strain signals from the semiconductor strain gages and the foil type strain gage connected with silver paint. .	96
5.5	Typical load-time plot for FGM graded in the thickness direction under quasi-static loading (25 °C).	97

Figure	Page
5.6	Typical failed specimen of FGM graded in thickness direction under quasi-static loading (25 °C). 98
5.7	Effect of temperature on the fracture initiation toughness of FGM graded in the thickness direction under quasi-static loading. 99
5.8	A schematic representation of crack on FGM specimen graded in the crack direction. 100
5.9	Typical load-time plot for FGM graded in the crack direction under quasi-static and room temperature loading (25 °C). . . . 100
5.10	Typical failed specimen of FGM graded in the crack direction under quasi-static loading (25 °C). 101
5.11	Typical load - time plot for FGM graded in the crack direction under quasi-static elevated temperature loading. 102
5.12	Effect of temperature on the fracture initiation toughness of FGM graded in the crack direction under quasi-static loading. . 102
5.13	Typical incident and reflected strain plot of FGM graded in the thickness direction subject to room temperature dynamic loading. 103
5.14	Effect of temperature on the fracture initiation toughness of FGM graded in the thickness direction under dynamic loading. . 104
5.15	SEM images of typical fracture surface of FGM graded in the thickness direction subjected to dynamic loading at different temperatures. 105
5.16	Typical strain signal obtained from the dynamic fracture experiments of FGM graded in the crack direction subjected to dynamic loading. 106
5.17	Typical high speed digital images of FGM graded in the crack direction subjected to dynamic loading at 800 °C. 107
5.18	Effect of temperature on the fracture initiation toughness of FGM graded in the crack direction under dynamic loading. . . . 107
5.19	SEM images of typical fracture surface of FGM graded in the crack direction subjected to dynamic loading at different temperatures. 108

Figure	Page
5.20	Effect of temperature on the fracture initiation toughness of FGM graded in the thickness direction under quasi-static and dynamic loading. 109
5.21	Effect of temperature on the fracture initiation toughness of FGM graded in the crack direction under quasi-static and dynamic loading. 110
6.1	In-house fabricated typical SENT specimen: a) FGM with increasing Young's modulus in the direction of crack propagation, b) FGM decreasing in young's modulus in the direction of crack propagation (Dimensions W=127mm, H/W=2, h/W=1.45) . . 115
6.2	Schematic configuration for dynamic photoelastic experiment of transparent FGM 117
6.3	Modified SENT specimen for transient crack propagation in FGM (Dimensions W=127mm, H/W=2, h/W=1.45, $a_1=12\text{mm}$, $a_2=5\text{ mm}$, D=5 mm l =20mm). 119
6.4	The dynamic isochromatic fringes at the crack tip for FGM with decreasing Young's modulus along the crack propagating direction. Time interval between each frame is 20 s 120
6.5	The dynamic isochromatic fringes at the crack tip for FGM with increasing Young's modulus along the crack propagating direction. Time interval between each frame is 20 s 121
6.6	Crack length and velocity as a function of time for linearly varying FGM under dynamic loading 121
6.7	The dynamic isochromatic fringes for transient crack propagation on FGM with increasing Young's modulus along the crack propagating direction. Time interval between each frame is 7 s . 122
6.8	Crack length and velocity as a function of time for linearly varying FGM under transient dynamic loading 123
A.1	Variation of the circumferential tensile stress with angle θ around the crack edge for several value of normalized crack speed. Crack growth is in mode I. ($r = 0.002\text{m}$, $K_{ID} = 1\text{MPa } m^{1/2}$) 128

Figure	Page
A.2	Variation of maximum principal stress with angle θ around the crack edge for several value of normalized crack speed. Crack growth is in mode I. ($r = 0.002\text{m}$, $K_{ID} = 1\text{MPa } m^{1/2}$) 129
A.3	Variation of the maximum shear stress with angle θ around the crack edge for several value of normalized crack speed. Crack growth is in mode II. ($r = 0.002\text{m}$, $K_{IID} = 1\text{MPa } m^{1/2}$) 130
A.4	Variation of the circumferential tensile stress with angle θ around the crack edge for several value of normalized crack speed. Crack growth is in mode II. ($r = 0.002\text{m}$, $K_{IID} = 1\text{MPa } m^{1/2}$) 131
A.5	Variation of maximum principal stress with angle θ around the crack edge for several value of normalized crack speed. Crack growth is in mode II. ($r = 0.002\text{m}$, $K_{IID} = 1\text{MPa } m^{1/2}$) 132
A.6	Variation of the maximum shear stress with angle θ around the crack edge for several value of normalized crack speed. Crack growth is in mode I. ($r = 0.002\text{m}$, $K_{ID} = 1\text{MPa } m^{1/2}$) 133
C.1	Propagating crack tip orientation with respect to reference coordinate configuration. 142
D.1	Schematic representation of SHPB 164
D.2	Schematic description of SHPB with heaters 167
D.3	Schematic description of calibration experimental setup 168
D.4	Typical incident and transmitted signal from calibration experiment 169
D.5	Incident and transmitted signals plotted at the same position . 169

CHAPTER 1

Introduction

1.1 Introduction

The way to outer space requires a high level of technology to design safe, reliable, economical and novel transportation systems. When developing a new design, the engineers consider the conceivable failures of the new system. Today the main challenging technical problem in designing space access vehicles is the development of the reentry heat shield that can be reused with minimal refurbishment and testing. On reentry, a shock wave forms ahead of the spacecraft, which heats the compressed air in the region near the spacecraft to as much as 20,000 °C, creating thermal loads in excess of one megawatt per square meter. This enormous thermal load heats the aircraft structure up to approximately 1,700 °C. This requires an external thermal protection systems (TPS) which usually in the form of rigid surfaces in areas of high or moderate working temperature. In addition to high temperature and high convective fluxes, TPS must be able to withstand mechanical stresses associated with vibrations at launch, acoustic-frequency vibrations and structural movement of the vehicle, as well as landing impact. Usually TPS are composite layers of two different materials with ceramic on the top due to its high thermal properties and metals in the other end for structural integrity. However, the property mismatch and high thermal gradient across these two materials results in delamination and interface failure. A very recent unfortunate example of this type of failure was the Space Shuttle Columbia. All of the materials involved in the Columbia accident were classified as belonging to the TPS.

In recent years a new system called functionally graded material (FGM) has been developed to circumvent for the interface problems that occurs in bi-material systems. FGMs are materials, which have continuously or discreetly varying me-

chanical and thermal properties in a specific direction. This type of material was first proposed in Japan in 1987 for space access vehicles as an alternative to thermal barrier coatings [1]. FGMs are potential candidates to be used as integrated hot structure in space access vehicles as the material combination and the composition of gradation in these materials can be tailored to optimize their performance to meet multiple functions like thermal resistance and structural integrity. Typically, FGMs are made of a metal and a ceramic as opposite faces with the intermediate zones consisting of varying volume fractions of constituents. Titanium / titanium mono-boride (Ti/TiB), FGM which is currently in use, consists of the desirable properties of ceramic, such as hardness, corrosion resistance, and high melting temperature, without losing the required properties of metallic titanium, such as good fracture toughness, machinability and weldability. For efficient design of structures using FGM a fundamental understanding of the properties of the material at different loading conditions is required. For designing a failure criteria the fracture parameters and constitutive behavior of this material is important.

1.2 Related Literatures

The elasticity of non-homogeneous solids had been an interesting subject well before FGMS are developed. Solutions to different types of mixed boundary value problems in non-homogeneous solids have been obtained by Plevako, [2], Kassir [3, 4], Popov [5] and Singh [6, 7]. The earliest study into the crack problems in non-homogeneous solids can be traced down to early 1970s. Kassir [3] investigated the problem of an axisymmetric penny shaped crack in a cylinder subjected to pure torsion by varying the shear modulus in axial direction. Later, Dhaliwal and Singh [8] obtained an expression for the stress intensity factor for a crack in a semi-infinite non-homogeneous solid subjected to crack face anti plane shear loading. Clements et al. [9] also solved antiplane crack problems for inhomogeneous

materials and obtained the energy release rates for various crack orientations and property variations. These initial investigations were focussed on the tearing mode of fracture, because of its simplicity among the three modes of fracture. Gerasoulis and Srivastav [10] are the first to analysis the opening mode fracture in nonhomogeneous solids, which is of the more practical importance, by assuming plane strain conditions. Later on Delale and Erdogan [11], Eischen [12] and Erdogan et al. [13] solved crack problems for non-homogeneous materials under quasi-static loading.

With the introduction of FGMs, research on fracture mechanics of nonhomogeneous solids gained additional impetus. Jin and Noda [14], Konda and Erdogan [15] and Erdogan [16] obtained the stress intensity factors for cracks in FGMs for different crack orientation, types of loading and levels of nonhomogeneity. Jin and Batra [17, 18], studied the fracture toughness and resistance curve (R-curve) of metal-ceramic FGMs using the crack bridging concept and rule of mixtures and showed that the fracture toughness is significantly increased when a crack grows from the ceramic-rich region to the metal-rich region in the FGM. All these investigations concluded that the inverse-square root singularity at the crack is not affected by nonhomogeneity.

All the above investigations are limited to quasi-static loading conditions. For propagating cracks in FGMs, Nakagaki et al. [19] developed a finite element simulation of fracture occurring in a ceramic-metal FGM under a dynamic load. They observed that the crack opening displacement (COD) was higher in the FGM when crack propagated from the ceramic rich side to the metal rich side as compared to the reverse direction of propagation. Later on Parameswaran and Shukla [20] and Chalivendra et al. [21] developed the structure of the first stress invariant and the out of plane displacement. In their study they brought out the effects

of nonhomogeneity through an asymptotic analysis. Rousseau and Tippur [22] have investigated the dynamic fracture of continuously graded particulate (glass - epoxy) FGMs for cracks aligned along the gradient using interferometry. Lee [23] developed nonhomogeneity specific terms for individual stress and displacement components using displacement potentials. Recently, Shukla and Jain [24] and Chalivendra and Shukla [25] developed transient field equations for cracks propagating at arbitrary velocities. Chalivendra [26] developed an asymptotic analysis of the transient out of plane displacement fields for a curved crack propagating at arbitrary velocity in FGMs. Kim and Paulino [27] evaluated the mixed-mode stress intensity in the form of an equivalent domain integral, in combination with the finite element method. In another numerical study, Jin and Dodds [28] simulated the crack growth resistance in a ceramic/metal FGM using a cohesive zone ahead of the crack front. A review paper by Shukla et al. [29] presents a comprehensive summary of dynamic fracture studies in FGM.

There are very few studies on the crack problems of FGM under thermal or thermo-mechanical loading. Kawasaki and Watanabe [30], evaluated the thermo-mechanical properties of metal/ceramic which simulated the real environment of the heated inner wall of a rocket combustor. They used Disk-shaped graded samples of a material combination of partially stabilized zirconia and stainless steel, in which the ceramic surface of the sample was heated with a burner flame and the back surface was cooled with flowing water. They determined the critical temperature of the first crack formation, which was always observed on the ceramic surface during cooling, and they found that it is almost constant regardless of specimen size and compositional profile. Based on the experiment, they concluded that the critical temperature is material-dependent. They also discussed the mechanism of crack formation and deflection, including spallation, on the basis of the stress

distributions in the specimen during testing and the fracture mechanics approach. According to their study, FGM structure is advantageous for TBC application with the particular emphasis on the capability of vertical-crack arrest and the possibility of its propagation control by tailoring the graded structure on the basis of fracture mechanics. Noda [31] studied the thermal stresses and thermal stress intensity factor (SIF) in the FGM subjected to steady temperature fields or thermal shock. He also presented analytical and numerical studies on the optimal composition profile problems of the FGM in decreasing thermal stresses. Based on his study he forwarded the following remarks: 1. When the continuously changing composition between ceramics and metals selected properly, thermal stresses and the thermal SIF in FGM can be drastically decreased. 2. The crack propagation path can be predicted by fracture mechanics analysis. Kawasaki and Watanabe [32], conducted a well controlled burner-heating-test in order to study the thermal fracture behavior, the cyclic thermal fracture behavior and spallation life of different metal/ceramic functionally graded thermal barrier coatings (TBC). In PSZ/IN100 FGM, the fracture toughness improved with an increase in the metal phase content. In PSZ/Inco718 FGM the fracture toughness was lower than that of PSZ/In100 FGM, owing to roughly dispersed metal particles. They observed that functionally graded TBC possess the desirable effect for improvement of spallation life under cyclic thermal loads. In addition, they observed that the spallation life in functionally graded coatings depends on the composition profile.

All the analytical studies presented in the previous section provide a closed form solution for determining SIF, however for extracting fracture parameters from experimental studies under thermo-mechanical loading an asymptotic stress field around the crack tip is required. In this aspect recently, Jain et al. [33] developed a field equation for a stationary crack in FGMs, subjected to thermo-mechanical

loading. They used an asymptotic analysis coupled with Westergaard's stress function approach to characterize the stress field around the crack tip. Using the stress fields they generated the contour of constant maximum shear stress and discussed the effect of thermal loading on the-crack tip stress fields. They observed that the presence of a thermal load produces no additional singularity and hence the classical inverse square root singularity still prevails around the crack tip. The development of an asymptotic expansion field equation for FGMs under thermo-mechanical dynamic loading is a problem yet to be investigated.

In other directions, there are several studies related to the stress and displacement response of FGMs under different loading conditions. For instance Wang et al. [34] present a solution for the displacement and stress in an FGM subjected to a vertical point load in a continuously nonhomogeneous transversely isotropic half-space with Young's and shear moduli varying exponentially with depth. Horgan and Chan [35] investigate the effects of material nonhomogeneity on the response of linearly elastic isotropic hollow circular cylinders under uniform internal or external pressure. Li et al. [36] examined the mechanical behavior of layered plates made of metal-ceramic composites with the volume fraction of ceramic reinforcement varying through thickness direction under impulse loading. Chi and Chung [37] studies the mechanical behavior of a functionally graded material plate under transverse loading.

There are also a few theoretical studies on displacement and stress response of FGMs under thermo-mechanical loading. Praveen and Reddy [38] investigated the response of functionally graded ceramic-metal plates under mechanical and thermal loading using a plate finite element method. They investigated the static and dynamic response of FGM plates by varying the volume fraction of the ceramic and metallic constituents using a simple power law distribution. They found that

the deflection and stresses response of the plates with material properties between those of the ceramic and metal is not intermediate to the responses of the ceramic and metal plates in the case of both thermal and mechanical loading. However, in the absence of thermal loading, they found that the dynamic response of the graded plates is intermediate to that of the metal and ceramic plates.

Dai et al., [39] presented a meshfree model for the active shape control as well as the dynamic response repression of FGM plate containing distributed piezoelectric sensors and actuators subjected to thermo-mechanical loading. They assumed that the FGM plate was made of ceramics and metals whose volume fractions vary continuously in the thickness direction according to the power law. They used the element-free Galerkin method to derive the shape functions using the moving least squares (MLS) method. They studied the mechanical loading as well as thermal gradient. They found that the relations between the deflection and the volume fraction exponent are quite different under the two loadings. The theoretical studies presented above attempts to find the displacement and stress response of FGMs at different loading conditions, however, the studies are not supported by experimental evidence and experimental investigation on the constitutive behavior of metal/ceramic FGM are not reported.

To date there is not a detailed study on the dynamic thermo-mechanical behavior of FGM, particularly on the metal-ceramic based materials. Fundamental investigation into the thermomechanical response and dynamic failure of the graded materials is necessary before they can be incorporated into the design of future space access vehicles that can operate reliably in combined and extreme environments. The proposed research is intended to fill this gap by a detailed experimental and analytical investigation of dynamic thermo-mechanical failure of graded materials.

1.3 Present Study

The present research is aimed at the critical investigation of the dynamic fracture and failure properties of functionally graded material under thermo-mechanical loading. The study involves both analytical and experimental techniques and can be categorized in the following list.

- Analytical study to develop a thermo-mechanical dynamic stress field around the crack tip in functionally graded material using high order stress field equations.
- To experimentally investigate the dynamic constitutive behavior of Ti/TiB functionally graded material under thermo-mechanical loading.
- To experimentally investigate the dynamic fracture initiation toughness in FGM under thermo-mechanical loading.

List of References

- [1] T. Niino, M. Hirai and R. Watanabe, "The functionally gradient materials," *Journal of the Japan Society of Composite Materials*, vol. 13 (1), p. 257, 1987.
- [2] V. Plevako, "On the theory of elasticity of inhomogeneous media," *PMM*, vol. 35:, pp. 5,853, 1971.
- [3] M. Kassir, "Boussinesq problems for a nonhomogeneous solid," *Proc. ASCE, J. Engng. Mech. Div.*, vol. 98, pp. 457–570, 1972.
- [4] M. Kassir, "A note on the twisting deformation of a nonhomogeneous shaft containing a circular crack," *Int. J. Frac. Mech.*, vol. 8:3, pp. 325–334, 1972.
- [5] G. I. Popov, "Axisymmetric contact problem for an elastic inhomogeneous half-space in the presence of cohesion," *J. Appl. Math. Mech.*, vol. 37, pp. 1052–1059, 1973.
- [6] B. Singh, "The reissner-sagoci problem for a nonhomogeneous solid," *Def. Sci. J.*, vol. 22, pp. 81–86, 1972.
- [7] B. Singh, "A note on the reissner-sagoci problem for a nonhomogeneous solid," *ZAAM*, vol. 53, pp. 419–420, 1973.

- [8] R. Dhaliwal and B. Singh, "On the theory of elasticity of a nonhomogeneous medium," *J. Elasticity*, vol. 8:2, pp. 211–219, 1978.
- [9] C. Clements, D.L. Atkinson and C. Rogers, "Antiplane crack problems for an inhomogeneous elastic material," *Acta Mechanica*, vol. 29, pp. 199–211, 1978.
- [10] A. Gerasoulis and R. Srivastav, "A griffith crack problem for a nonhomogeneous medium," *Int. J. Engng. Sci.*, vol. 18, pp. 239–247, 1980.
- [11] F. Delale and F. Erdogan, "The crack problem for a nonhomogeneous plane," *J. Appl. Mech.*, vol. 50, p. 6780, 1983.
- [12] J. Eischen, "Fracture of nonhomogeneous materials," *International Journal of Fracture*, vol. 34 (3), p. 322, 1987.
- [13] C. Erdogan, F. Kaya and P. Joseph, "The crack problem in bonded nonhomogeneous materials," *J. Appl. Mech.*, vol. 58, pp. 410–418, 1991.
- [14] Z. Jin and N. Noda, "Crack-tip singular fields in nonhomogeneous materials," *J. Appl. Mech.*, vol. 61, pp. 738–739, 1994.
- [15] N. Konda and F. Erdogan, "The mixed mode crack problem in a nonhomogeneous elastic medium," *Engng. Frac. Mech.*, vol. 47, pp. 533–545, 1994.
- [16] F. Erdogan, "Fracture mechanics of functionally graded materials," *Comp. Engng.*, vol. 5:7, pp. 753–770, 1995.
- [17] Z. Jin and R. Batra, "Some fracture mechanics concepts in functionally graded materials," *J. Mech. Phys. Solids.*, vol. 44:8, pp. 1221–235, 1996.
- [18] Z. Jin and R. Batra, "R-curve and strength behavior of functionally graded material," *Mat. Sci. Engng., A*, vol. 242, pp. 70–76, 1998.
- [19] H. Nakagaki, M. Sasaki and S. Hagihara, "A study of crack in functionally graded material under dynamic loading," *PVP, Dynamic Fracture, Failure and Deformation, ASME*, vol. 300, pp. 1–6, 1995.
- [20] V. Parameswaran and A. Shukla, "Crack-tip stress fields for dynamic fracture in functionally gradient materials," *Mechanics of Materials*, vol. 31, pp. 579–596, 1999.
- [21] A. Chalivendra, V. B. Shukla and V. Parameswaran, "Dynamic out of plane displacement fields for an inclined crack in graded materials," *Journal of Elasticity*, vol. 69, pp. 99–119, 2002.
- [22] C. E. Rousseau and H. V. Tippur, "Dynamic fracture of compositionally graded materials with cracks along the elastic gradient: Experiments and analysis," *Mechanics of Materials*, vol. 33, pp. 403–421, 2001.

- [23] K. H. Lee, "Characteristics of a crack propagating along the gradient in functionally gradient materials," *Int. J. of Solids and Structures*, vol. 41, pp. 2879–2898, 2004.
- [24] A. Shukla and N. Jain, "Dynamic damage growth in particle reinforced graded materials," *International Journal of Impact Engineering*, vol. 30, p. 777803, 2004.
- [25] V. B. Chalivendra and A. Shukla, "Transient elastodynamic crack growth in functionally graded materials," *Journal of Applied Mechanics*, vol. 72, p. 23727, 2005.
- [26] V. B. Chalivendra, "Asymptotic analysis of transient curved crack in functionally graded materials," *International Journal of Solids and Structures*, vol. 44, p. 465479, 2007.
- [27] J. H. Kim and G. H. Paulino, "T-stress, mixed-mode stress intensity factors, and crack initiation angles in functionally graded materials: A unified approach using the interaction integral method," *Comput. Methods Appl. Mech. Engr.*, vol. 192, p. 14631494, 2003.
- [28] Z. Jin and R. Dodds, "Crack growth resistance behavior of a functionally graded material: Computational studies," *Engineering Fracture Mechanics*, vol. 71, p. 16511672, 2004.
- [29] N. Shukla, A. Jain and R. Chona, "A review of dynamic fracture studies in functionally graded materials," *Strain*, vol. 43, pp. 76–95, 2007.
- [30] A. Kawasaki and R. Watanabe, "Evaluation of thermomechanical performance for thermal barrier type of sintered functionally graded materials," *Composites Part B*, vol. 28B, pp. 29–35., 1997.
- [31] N. Noda, "Thermal stresses in functionally graded materials, general lecture third international congress on thermal stresses," in *Thermal Stresses 99*, Cracow, Poland, June 13-17 1999.
- [32] A. Kawasaki and R. Watanabe, "Thermal fracture behavior of metal/ceramic functionally graded materials," *Engineering Fracture Mechanics*, vol. 69, p. 17131728, 2000.
- [33] R. Jain, N. Chona and A. Shukla, "Asymptotic stress fields for thermomechanically loaded cracks in fgmsn," *Journal of ASTM International*, vol. 3(7), 2006.
- [34] C. S. P. E. Wang, C. D. Tzeng and J. J. Lio, "Displacements and stresses due to a vertical point load in an inhomogeneous transversely isotropic half-space," *International Journal of Rock Mechanics and Mining Science*, vol. 40(5), pp. 667–685, 2003.

- [35] C. O. Horgan and A. M. Chan, “The pressurized hollow cylinder or disk problem for functionally graded isotropic linearly elastic materials,” *J. Elasticity*, vol. 55, pp. 43–59, 1999.
- [36] K. T. Li, Y. Ramesh and E. Chin, “Dynamic characterization of layered and graded structures under impulsive loading,” *International Journal of Solids and Structures*, vol. 38(34-35), pp. 6045–6061, 2001.
- [37] S. H. Chi and Y. L. Chung, “Mechanical behavior of functionally graded material plates under transverse load part i: Analysis,” *Int. J. Solids. Struct.*, vol. 43, pp. 3657–3674, 2006.
- [38] G. N. Praveen and J. N. Reddy, “Nonlinear transient thermoelastic analysis of functionally graded ceramic-metal plates,” *Int. J. Solids Structure.*, vol. 35, pp. 4457–4476, 1998.
- [39] G. H. X. Dai, K.Y. Liu and K. Lim, “Thermomechanical analysis of functionally graded material (fgm) plates using element-free galerkin method,” *Computers and Structures*, vol. 83, p. 14871502, 2005.

CHAPTER 2

Dynamic Thermo-Mechanical Stress Fields for a Mixed-Mode Propagating Cracks

2.1 Abstract

Thermo-mechanical stress field equations are developed for a mixed-mode crack propagating at constant velocity in homogeneous and isotropic materials using asymptotic approach along with displacement potentials. Asymptotic temperature field equations are first developed for steady state temperature conditions using insulating crack-face boundary conditions. These temperature field equations are later used to derive the first three terms of thermo-mechanical stress field equations for a steady state propagating mixed-mode crack. Using these thermo-mechanical stress fields, various components of the stresses are developed and the effects of temperature on these stress components are discussed.

2.2 Introduction

In many practical engineering problems, the structures are subjected to thermo-mechanical loads. Under these thermo-mechanical loads the cracks in these structures can initiate and cause catastrophic failure. The crack-tip initiation, rapid crack growth, crack branching and arrest are of significant importance to understand material's failure under combined thermo-mechanical loads. In the classical studies of thermoelastic crack problems, Sih [1] and Kassir and Bergman [2] investigated quasi-static stress fields for a crack in infinite medium when it is subjected to special thermal loadings. Later Wilson and Yu [3] employed finite element analysis and J-integral approach to determine crack-tip stress intensity factors for finite specimen geometries under thermal loads.

In continuation of the above studies, Lee and Sim [4] determined mode-I ther-

mal shock stress intensity factor using Bueckner' weight function method for a surface cracked infinite strip under sudden conductive cooling. Using a general finite element model, Chen and Weng [5], investigated a coupled transient thermoelastic problem for an edge- cracked plate without an inertia term. Katsareas et al. [6] determined shock stress intensity factors using boundary-only element method for surface cracked infinite strip and finite edge cracked plate. Recently, Hosseini-Tehrani et al. [7] investigated dynamic mode-I stress intensity factors for an edge crack in a finite specimen geometry using boundary element method in conjunction with Laplace transforms.

The above studies are focused on the determination of stress intensity factor values from numerical models using integral transforms. The closed-form solutions obtained using numerical and integral transform methods cannot be used in extracting fracture parameters from experimental stress or deformation fields. To meet this requirement, asymptotic expansion of stress field equations are essential [8]. Hence in this paper, thermo-mechanical stress fields are developed for a mixed-mode propagating crack of constant velocity in homogeneous isotropic materials using asymptotic approach along with displacement potentials. Asymptotic temperature field equations are first developed for a steady state temperature conditions using insulated crack-tip boundary conditions. These temperature fields are later used to derive first three terms of thermo-mechanical stress fields for steady state propagating crack. Using these thermo-mechanical stress fields, various stress components are developed and the effect of temperature on these stresses is discussed.

2.3 Theoretical Formulation

Hooke's law for a plane strain thermo-mechanical problem can be written as

$$\sigma_{XX} = ((\lambda + 2\mu)\epsilon_{XX} + \lambda\epsilon_{YY} - (3\lambda + 2\mu)\alpha T) \quad (2.1)$$

$$\sigma_{YY} = ((\lambda + 2\mu)\epsilon_{YY} + \lambda\epsilon_{XX} - (3\lambda + 2\mu)\alpha T) \quad (2.2)$$

$$\tau_{XY} = \mu\epsilon_{XY} \quad (2.3)$$

where X and Y are reference coordinates, σ_{ij} and ϵ_{ij} where $i = X, Y$ and $j = X, Y$ are in-plane stress and strain components, λ and μ denote Lamé's constant and shear modulus respectively. α is coefficient of thermal expansion and T represents the change in temperature in the infinite medium. The equations of motion for a plane problem in homogeneous isotropic material are given in Eq. 2.4

$$\frac{\partial \sigma_{XX}}{\partial X} + \frac{\partial \tau_{XY}}{\partial Y} = \rho \frac{\partial^2 u}{\partial t^2}, \quad \frac{\partial \sigma_{YY}}{\partial Y} + \frac{\partial \tau_{XY}}{\partial X} = \rho \frac{\partial^2 v}{\partial t^2} \quad (2.4)$$

where u and v are functions of X , Y and t and represent the displacements in the X and Y directions respectively with t representing the time. For plane strain deformation, the displacements u and v are derived from dilatational and shear wave potentials ϕ and ψ . These potentials can be expressed as

$$u = \frac{\partial \phi}{\partial X} + \frac{\partial \psi}{\partial Y}, \quad v = \frac{\partial \phi}{\partial Y} - \frac{\partial \psi}{\partial X} \quad (2.5)$$

Substituting Eqs. 2.1 - 2.3 in to Eq.2.4 and utilizing Eq.2.5 and after simplification the equations of motion in terms of displacement potentials can be expressed as

$$(2\mu + \lambda) \nabla^2 \phi - \alpha(3\lambda + 2\mu)T = \rho \frac{\partial^2 \phi}{\partial t^2} \quad (2.6)$$

$$\mu \nabla^2 \psi = \rho \frac{\partial^2 \psi}{\partial t^2} \quad (2.7)$$

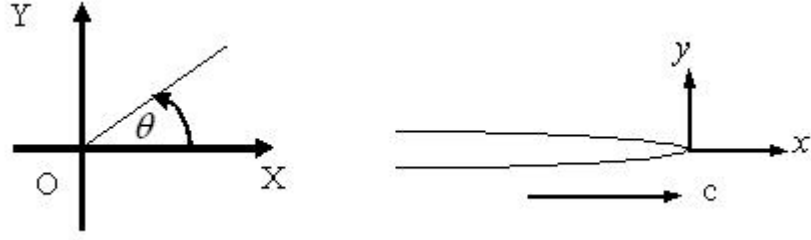


Figure 2.1. Propagating crack tip orientation with respect to reference coordinate system

where $\nabla^2 = \frac{\partial^2}{\partial X^2} + \frac{\partial^2}{\partial Y^2}$

For a propagating crack as shown in Fig. 2.1, the reference coordinates (X and Y) can be transformed to crack tip coordinates using the relations $x = Xc - t$, $y = Y$, where c is constant crack tip speed. By transforming to crack-tip coordinates and rearranging terms, the above equations of motion can be written as

$$\alpha_l^2 \frac{\partial^2 \phi}{\partial x^2} + \frac{\partial^2 \phi}{\partial y^2} - \alpha \frac{3\delta + 2}{\delta + 2} T = 0 \quad (2.8)$$

$$\alpha_s^2 \frac{\partial^2 \psi}{\partial x^2} + \frac{\partial^2 \psi}{\partial y^2} = 0 \quad (2.9)$$

where $\alpha_l = \sqrt{1 - \frac{\rho}{\mu} \frac{c^2}{(k+2)}}$, $\alpha_s = \sqrt{1 - \frac{\rho}{\mu} c^2}$ and $\delta = \frac{\lambda}{\mu}$

It is assumed that in the above transformation, the fields ϕ and ψ do not depend explicitly on time in the moving coordinate system and their time dependence is only through the transformation $x = X - ct$.

2.3.1 Temperature Fields around the Crack Tip

In this analysis the thermo-elastic cooling and the transient effects are neglected. The steady state heat conduction equation can be written as

$$\frac{\partial}{\partial X} \left(k \frac{\partial T}{\partial X} \right) + \frac{\partial}{\partial Y} \left(k \frac{\partial T}{\partial Y} \right) = 0 \quad (2.10)$$

Where k is the coefficient of thermal conductivity

Assuming that k is constant in the small region around the crack tip, and again

transforming the above equation to the crack-tip moving coordinate system ($x = Xc - t, y = Y$), it can be written as

$$\nabla^2 T = 0 \quad (2.11)$$

where $\nabla^2 = \frac{\partial^2}{\partial x^2} + \frac{\partial^2}{\partial y^2}$

As this stages asymptotic analysis is performed to solve the above Eq. 2.11 . In the asymptotic analysis, first a new set of coordinates is introduce as

$$\eta_1 = \frac{x}{\epsilon} \quad \eta_2 = \frac{y}{\epsilon} \quad (2.12)$$

where ϵ is an arbitrary parameter and is assumed to be $0 < \epsilon < 1$

Equation 2.11 can be written in a new scaled coordinates (η_1, η_2) as

$$\nabla^2 T = 0 \quad (2.13)$$

where $\nabla^2 = \frac{\partial^2}{\partial \eta_1^2} + \frac{\partial^2}{\partial \eta_2^2}$

For the asymptotic analysis T is represented as a power series expansion in ϵ as

$$T(x, y) = T(\eta_1 \epsilon, \eta_2 \epsilon) = \sum_{m=0}^{\infty} \epsilon^{\frac{(m+1)}{2}} T_m(\eta_1, \eta_2) \quad (2.14)$$

Substituting the infinite series expansion into Eq. 2.13 results in

$$\sum_{m=0}^{\infty} \epsilon^{\frac{(m+1)}{2}} \left(\frac{\partial^2 T_m}{\partial \eta_1^2} + \frac{\partial^2 T_m}{\partial \eta_2^2} \right) = 0 \quad (2.15)$$

For Eq. 2.15 to be valid, the partial differential equations corresponding to each power of ϵ ($\epsilon^{1/2}, \epsilon, \epsilon^{3/2} \dots$) should vanish independently. This leads to a set of partial differential equations. Assuming the crack surfaces are insulated (i.e $\partial T / \partial \theta = 0$ at $\theta = \pi$), the solutions for the first three temperature terms can be written as

$$T = q_0 \rho^{1/2} \sin \left(\frac{1}{2} \theta \right) + q_1 \rho \cos (\theta) + q_2 \rho^{3/2} \sin \left(\frac{3}{2} \theta \right) \quad (2.16)$$

where $\rho = (\eta_1^2 + \eta_2^2)^{1/2}$ and q_0, q_1 and q_2 are real constants

By transforming T into crack-tip coordinates x and y , the temperature fields near

the crack-tip can be given as

$$T = q_0 r^{1/2} \sin\left(\frac{1}{2}\theta\right) + q_1 r \cos(\theta) + q_2 r^{3/2} \sin\left(\frac{3}{2}\theta\right) \quad (2.17)$$

where $r = (x^2 + y^2)^{1/2}$ and $\tan(\theta) = \frac{y}{x}$

2.3.2 Asymptotic Expansion of Crack Tip Fields

The Eqs. 2.8 and 2.9 are now written in these scaled coordinates as below

$$\alpha_l^2 \frac{\partial^2 \phi}{\partial \eta_1^2} + \frac{\partial^2 \phi}{\partial \eta_2^2} - \alpha \frac{(3\delta + 2)}{(\delta + 2)} \epsilon^2 T = 0 \quad (2.18)$$

$$\alpha_s^2 \frac{\partial^2 \psi}{\partial \eta_1^2} + \frac{\partial^2 \psi}{\partial \eta_2^2} = 0 \quad (2.19)$$

At this stage it is assumed that ϕ , ψ and T are represented as a power series expansion in

$$\phi(x, y) = \phi(\epsilon \eta_1, \epsilon \eta_2) = \sum_{m=0}^{\infty} \epsilon^{\frac{(m+3)}{2}} \phi_m(\eta_1, \eta_2) \quad (2.20)$$

$$\psi(x, y) = \psi(\epsilon \eta_1, \epsilon \eta_2) = \sum_{m=0}^{\infty} \epsilon^{\frac{(m+3)}{2}} \psi_m(\eta_1, \eta_2) \quad (2.21)$$

$$T(x, y) = T(\epsilon \eta_1, \epsilon \eta_2) = \sum_{m=0}^{\infty} \epsilon^{\frac{(m+1)}{2}} T_m(\eta_1, \eta_2) \quad (2.22)$$

As given by Jin and Noda [9] the solution for the temperature field is obtained by considering the singularity of heat flux near the crack tip. This requires in that the derivative of temperature field is singular resulting in the potential for temperature to be one power less than the displacement potentials.

Now substituting Eqs. 2.20 - 2.22 into Eqs. 2.18 and 2.19 gives the following equations

$$\sum_{m=0}^{\infty} \epsilon^{(m+3)/2} \left(\alpha_l^2 \frac{\partial^2 \phi_m}{\partial \eta_1^2} + \frac{\partial^2 \phi_m}{\partial \eta_2^2} \right) - \alpha \frac{(3\delta + 2)}{(\delta + 2)} \sum_{m=0}^{\infty} \epsilon^{(m+5)/2} T_m = 0 \quad (2.23)$$

$$\sum_{m=0}^{\infty} \epsilon^{(m+3)/2} \left(\alpha_s^2 \frac{\partial^2 \psi_m}{\partial \eta_1^2} + \frac{\partial^2 \psi_m}{\partial \eta_2^2} \right) = 0 \quad (2.24)$$

For Eqs. 2.23 and 2.24 to be valid, the partial differential equations corresponding to each power of ϵ ($\epsilon^{1/2}$, ϵ , $\epsilon^{3/2}$...) should vanish independently. This leads to a set of partial differential equations. The solutions for $m = 0$ and $m = 1$ are well known and available in literature [10] and can be written as

$$\phi_m(\rho_l, \theta_l, t) = A_m \rho_l^{(m+3)/2} \cos \left(\frac{(m+3)}{2} \theta_l \right) + C_m \rho_l^{(m+3)/2} \sin \left(\frac{(m+3)}{2} \theta_l \right) \quad (2.25)$$

$$\psi_m(\rho_s, \theta_s, t) = B_m \rho_s^{(m+3)/2} \sin \left(\frac{(m+3)}{2} \theta_s \right) + D_m \rho_s^{(m+3)/2} \cos \left(\frac{(m+3)}{2} \theta_s \right) \quad (2.26)$$

where $\rho_l = (\eta_1^2 + \alpha_l^2 \eta_2^2)^{1/2}$, $\tan(\theta_l) = \frac{\alpha_l \eta_2}{\eta_1}$, $\rho_s = (\eta_1^2 + \alpha_s^2 \eta_2^2)^{1/2}$, $\tan(\theta_s) = \frac{\alpha_s \eta_2}{\eta_1}$ and A_m , B_m , C_m , and D_m are real constants

The solution for equation corresponding to higher power of ($m = 2$) consists of two parts: classical solution and particular solution. The classical solution is similar to the general solution given in Eqs. 2.25 and 2.26. The particular solution can be obtained using recursive approach [10]. The solutions for $m = 2$ (ϕ_2 and ψ_2) are given below.

$$\phi_2 = A_2 r_l^{5/2} \cos \left(\frac{5}{2} \theta_l \right) + C_2 r_l^{5/2} \sin \left(\frac{5}{2} \theta_l \right) + \frac{4}{15} \frac{(3\delta + 2)}{(\delta + 2)} \frac{\alpha}{(\alpha_l^2 - 1)} q_0 r^{5/2} \sin \frac{5}{2} \theta \quad (2.27)$$

$$\psi_2 = B_2 r_s^{5/2} \sin \left(\frac{5}{2} \theta_s \right) + D_2 r_s^{5/2} \cos \left(\frac{5}{2} \theta_s \right) \quad (2.28)$$

By substituting the expressions for ϕ_0 , ϕ_1 , ϕ_2 , ψ_0 , ψ_1 , and ψ_2 into the Eqs. 2.20-2.22 and representing the Eqs. 2.20 and 2.21 in terms of crack-tip coordinates, the

displacement potentials can be represented as

$$\begin{aligned}\phi = & A_0 r_l^{3/2} \cos\left(\frac{3}{2}\theta_l\right) + C_0 r_l^{3/2} \sin\left(\frac{3}{2}\theta_l\right) + A_1 r_l^2 \cos(2\theta_l) + C_1 r_l^2 \sin(2\theta_l) \\ & + A_2 r_l^{5/2} \cos\left(\frac{5}{2}\theta_l\right) + C_2 r_l^{5/2} \sin\left(\frac{5}{2}\theta_l\right) + \frac{4}{15} \frac{(3\delta+2)}{(\delta+2)} \frac{\alpha}{(\alpha_l^2-1)} q_0 r^{5/2} \sin \frac{5}{2}\theta\end{aligned}\quad (2.29)$$

$$\begin{aligned}\psi = & B_0 r_s^{3/2} \sin\left(\frac{3}{2}\theta_s\right) + D_0 r_s^{3/2} \cos\left(\frac{3}{2}\theta_s\right) + B_1 r_s^2 \sin(2\theta_s) + D_1 r_s^2 \cos(2\theta_s) \\ & + B_2 r_s^{5/2} \sin\left(\frac{5}{2}\theta_s\right) + D_2 r_s^{5/2} \cos\left(\frac{5}{2}\theta_s\right)\end{aligned}\quad (2.30)$$

where $r_l = (x^2 + \alpha_l^2 y^2)^{1/2}$, $\tan(\theta_l) = \frac{\alpha_l y}{x}$, $r_s = (x^2 + \alpha_s^2 y^2)^{1/2}$, $\tan(\theta_s) = \frac{\alpha_s y}{x}$

2.3.3 Thermo-mechanical Stress Fields

By substituting Eq. 2.29 and Eq. 2.30 into the Eq. 2.5, the displacement field can be obtained. Further differentiating the displacement field, the in-plane strain field can be obtained. The strain expressions along with Eq. 2.17 can be substituted into Eqs. 2.1- 2.3 to obtain in-plane thermo-mechanical stress fields

$$\begin{aligned}\frac{\sigma_{xx}}{\mu} = & \left(\frac{3}{4} r_l^{-1/2} \cos\left(\frac{\theta_l}{2}\right) (\delta(1-\alpha_l^2)+2)\right) A_0 - \left(\frac{3}{4} r_l^{-1/2} \sin\left(\frac{\theta_l}{2}\right) (\delta(1-\alpha_l^2)+2)\right) C_0 \\ & + \left(\frac{3}{2} r_s^{-1/2} \cos\left(\frac{\theta_s}{2}\right) \alpha_s\right) B_0 + \left(\frac{3}{2} r_s^{-1/2} \sin\left(\frac{\theta_s}{2}\right) \alpha_s\right) D_0 + 2A_1 (\delta(1-\alpha_l^2)+2) \\ & + 4B_1 \alpha_s + \left(\frac{15}{4} r_l^{1/2} \cos\left(\frac{\theta_l}{2}\right) (\delta(1-\alpha_l^2)+2)\right) A_2 \\ & + \left(\frac{15}{4} r_l^{1/2} \sin\left(\frac{\theta_l}{2}\right) (\delta(1-\alpha_l^2)+2)\right) C_2 + \left(\frac{15}{2} r_s^{1/2} \cos\left(\frac{\theta_s}{2}\right) \alpha_s\right) B_2 \\ & - \left(\frac{15}{2} r_s^{-1/2} \sin\left(\frac{\theta_s}{2}\right) \alpha_s\right) D_2 + 2 \left(\frac{3\delta+2}{\delta+2} \frac{\alpha}{\alpha_l^2-1} r^{1/2} \sin\left(\frac{\theta}{2}\right)\right) q_0 \\ & + \alpha(3\delta+2) \left(q_0 r^{1/2} \sin \frac{\theta}{2} + q_1 r \cos(\theta) + q_2 r^{2/2} \sin \frac{3\theta}{2}\right)\end{aligned}\quad (2.31)$$

$$\begin{aligned}
\frac{\sigma_{yy}}{\mu} = & \left(\frac{3}{4} r_l^{-1/2} \cos \left(\frac{\theta_l}{2} \right) (\delta - \alpha_l^2 (\delta + 2)) \right) A_0 - \left(\frac{3}{4} r_l^{-1/2} \sin \left(\frac{\theta_l}{2} \right) (\delta - \alpha_l^2 (\delta + 2)) \right) C_0 \\
& - \left(\frac{3}{2} r_s^{-1/2} \cos \left(\frac{\theta_s}{2} \right) \alpha_s \right) B_0 - \left(\frac{3}{2} r_s^{-1/2} \sin \left(\frac{\theta_s}{2} \right) \alpha_s \right) D_0 - 4A_1 (\delta - \alpha_l^2 (\delta + 2)) \\
& - 4B_1 \alpha_s + \left(\frac{15}{4} r_l^{1/2} \cos \left(\frac{\theta_l}{2} \right) (\delta - \alpha_l^2 (\delta + 2)) \right) A_2 \\
& + \left(\frac{15}{4} r_l^{1/2} \sin \left(\frac{\theta_l}{2} \right) (\delta - \alpha_l^2 (\delta + 2)) \right) C_2 - \left(\frac{15}{2} r_s^{1/2} \cos \left(\frac{\theta_s}{2} \right) \alpha_s \right) B_2 \\
& + \left(\frac{15}{2} r_s^{1/2} \sin \left(\frac{\theta_s}{2} \right) \alpha_s \right) D_2 - 2 \left(\frac{3\delta + 2}{\delta + 2} \frac{\alpha}{\alpha_l^2 - 1} r^{1/2} \sin \left(\frac{\theta}{2} \right) \right) q_0 \\
& - \alpha(3\delta + 2) \left(q_0 r^{1/2} \sin \frac{\theta}{2} + q_1 r \cos(\theta) + q_2 r^{2/2} \sin \frac{3\theta}{2} \right) \quad (2.32)
\end{aligned}$$

$$\begin{aligned}
\frac{\tau_{xy}}{\mu} = & \left(\frac{3}{2} \alpha_l r_l^{-1/2} \sin \left(\frac{\theta_l}{2} \right) \right) A_0 + \left(\frac{3}{2} \alpha_l r_l^{-1/2} \cos \left(\frac{\theta_l}{2} \right) \right) C_0 \\
& + \left(\frac{3}{4} r_s^{-1/2} \sin \left(\frac{\theta_s}{2} \right) (1 + \alpha_s^2) \right) B_0 - \left(\frac{3}{4} r_s^{-1/2} \cos \left(\frac{\theta_s}{2} \right) (1 + \alpha_s^2) \right) D_0 \\
& + 4C_1 \alpha_l - 2D_1 (1 - \alpha_s^2) - \left(\frac{15}{2} \alpha_l r_l^{1/2} \sin \left(\frac{\theta_l}{2} \right) \right) A_2 \\
& + \left(\frac{15}{2} \alpha_l r_l^{1/2} \cos \left(\frac{\theta_l}{2} \right) \right) C_2 - \left(\frac{15}{4} r_s^{1/2} \sin \left(\frac{\theta_s}{2} \right) (1 + \alpha_s^2) \right) B_2 \\
& - \left(\frac{15}{4} r_s^{1/2} \cos \left(\frac{\theta_s}{2} \right) (1 + \alpha_s^2) \right) D_2 + 2 \left(\frac{3\delta + 2}{\delta + 2} \frac{\alpha}{\alpha_l^2 - 1} r^{1/2} \sin \left(\frac{\theta}{2} \right) \right) q_0 \quad (2.33)
\end{aligned}$$

By considering the singular term in the above equation and using the definition of the dynamic stress intensity factor K_{ID} and K_{IID} for opening and shear modes and considering the crack face boundary conditions [11] we get

$$A_0 = \frac{4(1 + \alpha_s^2)}{4\alpha_l \alpha_s - (1 + \alpha_s^2)^2} \frac{K_{ID}}{\mu \sqrt{2\pi}}, \quad B_0 = \frac{-2\alpha_l}{1 + \alpha_s^2} A_0 \quad (2.34)$$

$$C_0 = \frac{4\alpha_s^2}{3(4\alpha_l \alpha_s - (1 + \alpha_s^2)^2)} \frac{K_{IID}}{\mu \sqrt{2\pi}}, \quad D_0 = \frac{1 + \alpha_s^2}{2\alpha_s} C_0 \quad (2.35)$$

where μ is the shear modulus of the material at the propagating crack-tip, K_{ID} is mode-I dynamic stress intensity factor and K_{IID} is mode-II dynamic stress intensity factor.

2.4 Results and Discussion

2.4.1 Variation of Stress Components Near the Crack Tip

Using the developed stress fields, various components of the stress tensor are evaluated and the effect of temperature on these stress components is discussed. The coefficient of thermal expansion (α) of titanium (which is of primary interest in our experimental research), $8.9 \times 10^{-6}/^{\circ}C$ is used. In all the plots only the first terms are considered.

The superposition of the temperature stress field with the mechanical stress field results in imposing normal stress on traction free crack faces as shown in Fig. 2.2a. These stresses on the crack face are generated due to the thermal stresses produced by the temperature field. The presence of these normal stresses on the crack face violates one of the boundary conditions and these stresses need to be removed. The removal of these stresses from the crack face is accomplished by superimposing an equal and opposite stress field on the crack face. In particular each point on the crack face is subjected to a line load of specific magnitude such that normal stresses from the crack face are removed. The solution given by Jiang et al. [12] for a single line load is extended to derive the stress field around the crack tip for multiple line loads applied on the crack face line. Fig. 2.2b represents normal stress (σ_{yy}) near the crack tip after the superposition has been added. It must be mentioned that the crack face loads are relatively small in this example even for large T and have little influence on the crack tip stress fields.

The thermo-mechanical stress fields these obtained by superposition of the thermal and mechanical stress fields and suitably modified to ensure proper boundary conditions were used to generate contours of in plane stresses, maximum principal stress, maximum shear stress and maximum tangential stress around the crack tip.

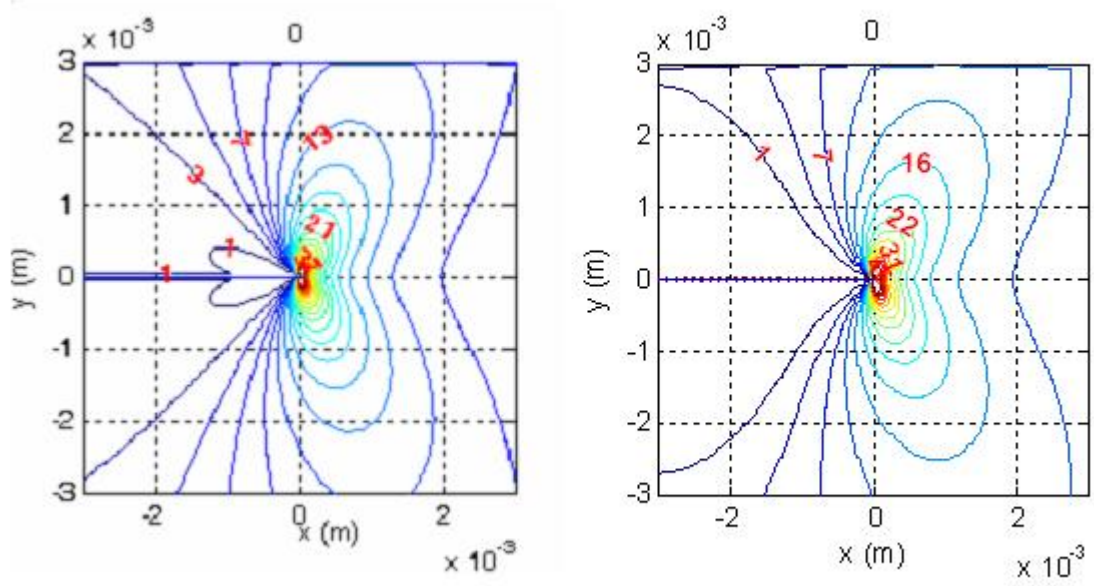


Figure 2.2. Contour of σ_{yy} in MPa for thermo-mechanical stress field around the crack-tip ($q_0=250$, $c/c_s = 0.5$ and $K_{ID} = 1\text{MPa}\cdot\text{m}^{1/2}$) (a) Before the opposite traction field is applied (b) After the opposite traction field is applied.

Fig. 2.3 shows the various normalized in-plane stress components (a) in-plane σ_{xx} , (b) in-plane σ_{yy} , (c) in-plane τ_{xy} , and Fig. 2.4 shows the various normalized principal stress (a) hoop stress $\sigma_{\theta\theta}$, (b) maximum principal stress σ_1 and (c) maximum shear stress τ_{max} as a function of angular position θ around the crack tip for a fixed value of c/c_s and different temperature fields. The stresses are normalized with far-field stress determined for $K_{ID} = 1\text{ MPa}\cdot\text{m}^{1/2}$, $K_{IID} = 0.2K_{ID}$, $K_{eff} = \sqrt{K_{ID}^2 + K_{IID}^2}$ and $r = 0.002\text{m}$. The stress field is assumed to be elastic for the temperature field associated with $q_0 = 100$ and $q_0 = 250$.

In Fig. 2.3 and Fig. 2.4, $q_0 = 0$ means no temperature field around the crack-tip and for this value Fig. 2.4 collapse to the isothermal solution given by Freund [8] if mode-I and mode-II fields are separated and plotted as shown in Figs. A.1 - A.6 in Appendix A.

The in-plane stress σ_{xx} shown in Fig. 2.3(a) has a maximum value ahead of the crack tip, i.e. at $\theta = 0^\circ$ and a local maximum about $\pm 135^\circ$ for $q_0 = 0$. These local

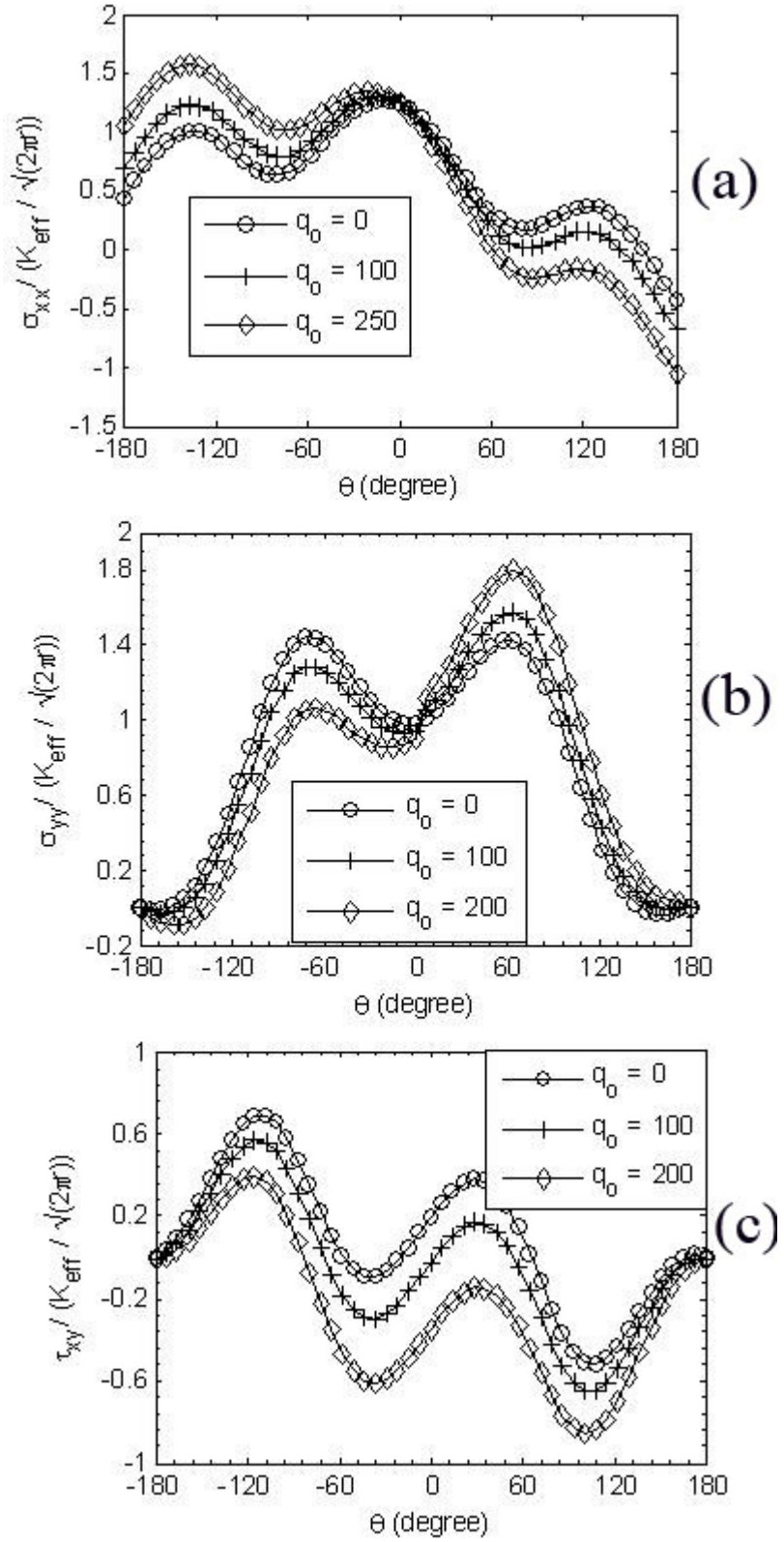


Figure 2.3. Normalized mixed mode in-plane stress fields as a function of θ around the crack-tip for different temperature fields ($c/c_s = 0.5$, $r = 0.002\text{m}$, $K_{ID} = 1\text{MPa } m^{1/2}$, $K_{IID} = 0.2 K_{ID}$)

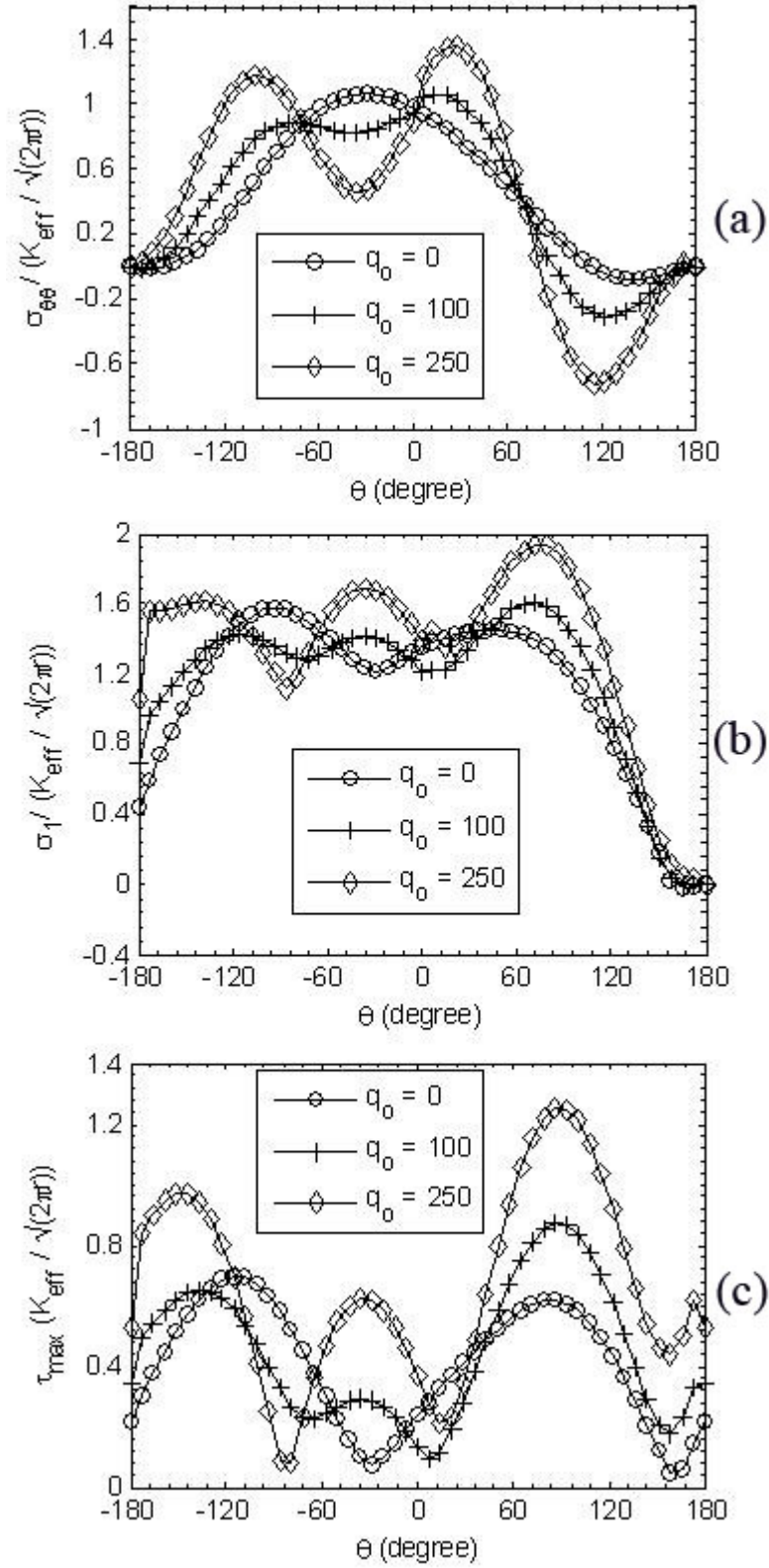


Figure 2.4. Normalized mixed mode principal stress fields as a function of θ around the crack-tip for different temperature fields ($c/c_s = 0.5$, $r = 0.002\text{m}$, $K_{ID} = 1\text{MPa } m^{1/2}$, $K_{IID} = 0.2 K_{ID}$)

maximums increase in magnitude with an increase in q_0 . It is also observed that the effect of temperature on σ_{xx} is predominantly in the region near to the crack face. The in-plane stress σ_{yy} shown in Fig. 2.3(b) has a maximum value around -70° for $q_0 = 0$ and this value decreases with an increase in applied temperature. It also has a local maximum at about 60° and this value increases with an increase in applied temperature. The in-plane shear stress τ_{xy} shown in Fig. 2.3(c) has a maximum value around -110° and a local maximum around 20° . These maximum values decreases as q_0 increases. There is no shift in the position of the maximum value of in-plane stresses as the temperature field around the crack-tip changes.

For $q_0 = 0$, the hoop stress as shown in Fig. 2.4(a) has a single maximum value along $\theta = -30^\circ$. As the temperature field increases, this stress develops a maximum and local maximum values. For example for $q_0 = 250$, the hoop stress develops a maximum value at an angle of 30° and a local maximum value at angle of -120° to the direction of crack growth. The angular variation of the principal stresses around the crack tip is shown in Fig. 2.4(b). For no temperature field, this stress has a maximum value at about -90° and local maximum value at about 45° from the direction of crack growth. As the temperature field increases, however, the maximum value shifts towards the direction away from the crack growth. In Fig. 2.4(c), the maximum shear stress as a function of temperature field around the crack tip is shown. In the case of no temperature field (i.e., $q_0 = 0$), the maximum shear stress has a maximum value at about -115° and a local maximum value at about 85° from the direction of crack growth. It can be seen from the figure that as the temperature increases, maximum values occur at four different locations.

2.4.2 Direction of Crack Growth

The theoretical prediction of crack extension angle is investigated by using the two well-known fracture criterias: minimum strain energy density (S-criterion)

and maximum circumferential stress ($\sigma_{\theta\theta}$ -criterion).

Minimum Strain-energy Density (MSED) Criterion

According to this criterion [13], the crack initiates when the strain energy density achieves a critical value and propagates in the direction of minimum strain-energy density value. The strain energy density dW/dV near the crack tip for an FGM is given as

$$\frac{dW}{dV} = S = \frac{1}{4\mu} ((1 - \nu) (\sigma_{xx}^2 + \sigma_{yy}^2) - 2\nu\sigma_{xx}\sigma_{yy} + \sigma_{xy}^2) \quad (2.36)$$

Fracture takes place in the direction of minimum S, and the condition can be obtained by using Eq. 2.37.

$$\frac{\partial S}{\partial \theta} = 0, \quad \frac{\partial^2 S}{\partial \theta^2} > 0 \quad \text{at} \quad S = S_c \quad (2.37)$$

where S_c is the critical strain energy density

Maximum Circumferential-stress (MCS) Criterion

The maximum circumferential stress criterion [14] states that, crack growth will occur in the direction of the maximum circumferential stress and will take place when the maximum circumferential stress reaches a critical value, and it can be given as Eq. 2.38.

$$\frac{\partial \sigma_{\theta\theta}}{\partial \theta} = 0, \quad \frac{\partial^2 \sigma_{\theta\theta}}{\partial \theta^2} < 0 \quad \text{at} \quad \sigma_{\theta\theta} = (\sigma_{\theta\theta})_c \quad (2.38)$$

where $(\sigma_{\theta\theta})_c$ is the critical circumferential stress

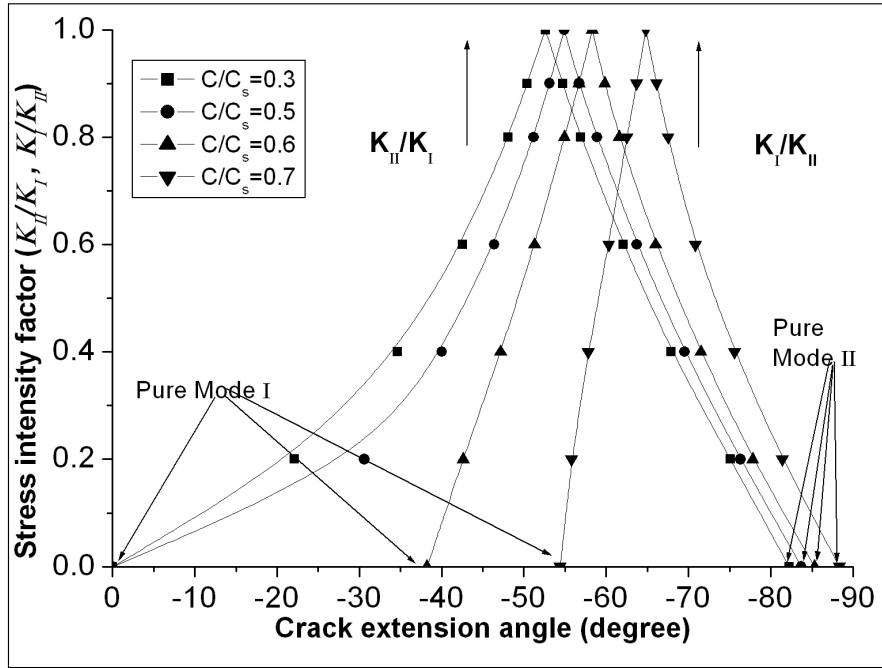
Based on the above two criteria's, the effects of velocity and temperature on the crack extension angle (θ) are investigated.

The crack extension angles as a function of crack tip velocities as predicted by the above two criterias are shown in Fig. 2.5. For pure mode-I loading

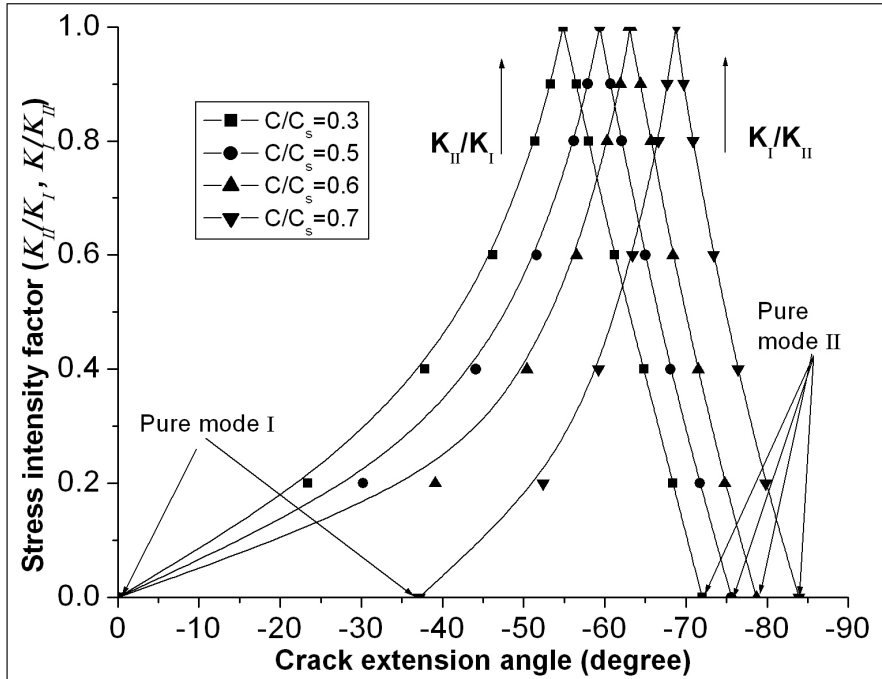
($K_{IID}/K_{ID} = 0$), the crack extends along (θ)=0 until the crack tip velocity reaches a critical value at which instability occurs [15]. When the crack tip velocity reaches the critical value, the crack deviates and extends to a different angle. For example at a crack tip velocity of $c/c_s = 0.7$, the MSED criterion predicts a crack extension angle of about -55° and the MCS criterion predicts about -38° . As the value of K_{IID}/K_{ID} increases from 0 to 1 and later from 1 to ∞ the crack extension angle increases monotonically. Broek [16], in his book gives the crack extension angles for mixed mode quasi static loading and these results match well with the predictions from the current study.

The effect of temperature field on the crack extension angle for a crack tip velocity of $0.5c_s$ is shown in Fig. 2.6. The figure shows the predicted of crack extension angle by both the minimum strain energy density and the maximum circumferential stress criterions. These two criterions predict same crack extension angles at lower temperatures. Both the criterion show that, the crack extension direction at room temperature is along $\theta = -30^\circ$ and the value decreases slowly with increase in applied temperature field. For FGM with $\alpha > 0$, the crack extension angle is along $\theta = -15^\circ$ at room temperature and again the value decreases with increase in applied temperature field.

The effects of temperature on the crack extension angle as a function of crack tip velocity are plotted in Fig. 2.7. Fig. 2.7(a) represents crack extension angle as a function of crack tip velocity for mixed-mode mechanical loading at room and elevated temperatures predicted by minimum strain energy density criterion. For a crack tip velocity of $c/c_s = 0.3$, the minimum strain energy density criterion predict decrease in crack extension angle for increasing temperature fields. Fig. 2.7(b) represents crack extension angle as a function of crack tip velocity for mixed-mode mechanical loading at room and elevated temperatures predicted by maximum



(a) Minimum strain energy density criterion



(b) Maximum circumferential stress criterion

Figure 2.5. Crack extension angle as a function of crack tip velocity for mixed mode thermo-mechanical loading ($r=0.002m$).

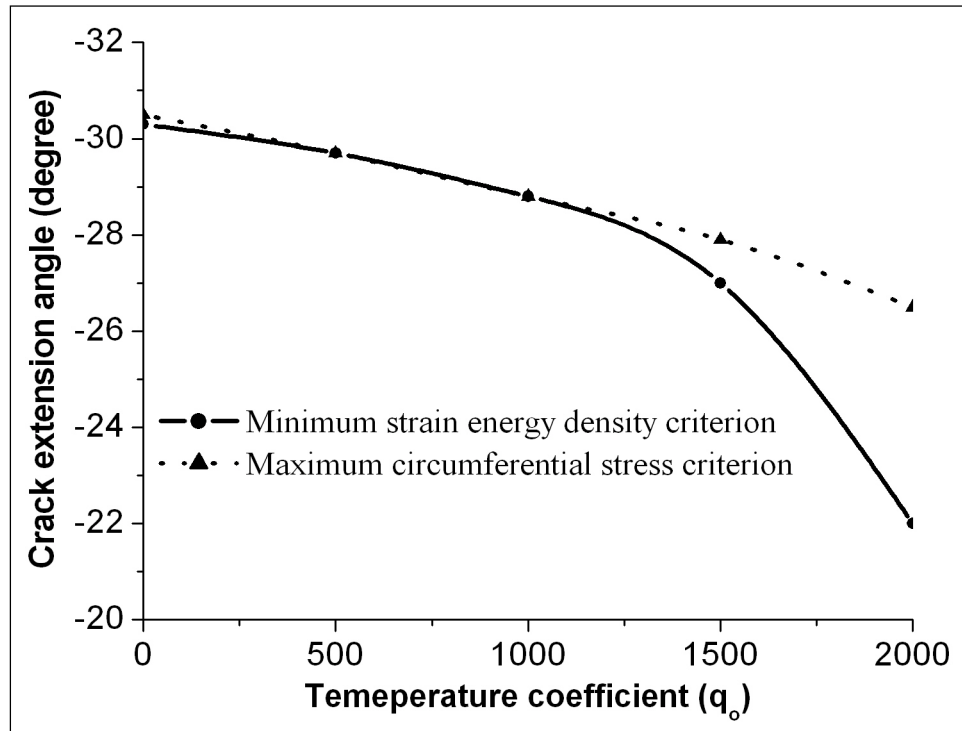


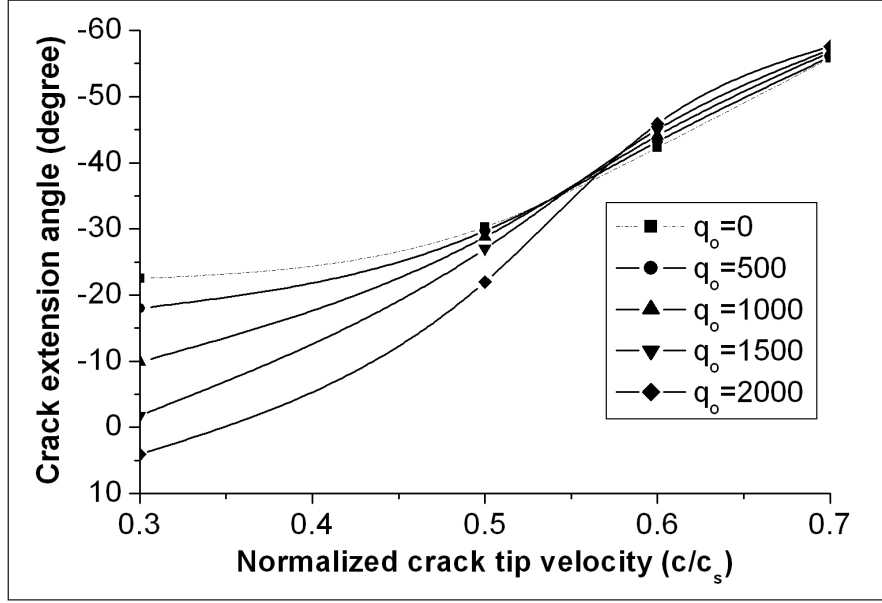
Figure 2.6. Effect of temperature on the crack extension angle for mixed mode loading ($K_{IID}/K_{ID} = 0.2$, $c/c_s = 0.5$, $r = 0.002\text{m}$).

circumferential stress criterion. Furthermore, for $c/c_s > 0.3$, both criteria predict decrease in crack extension angle for increasing temperature field. The difference in the predicted crack extension angles decreases as the velocity increases and becomes insignificant at velocities $c/c_s > 0.55$.

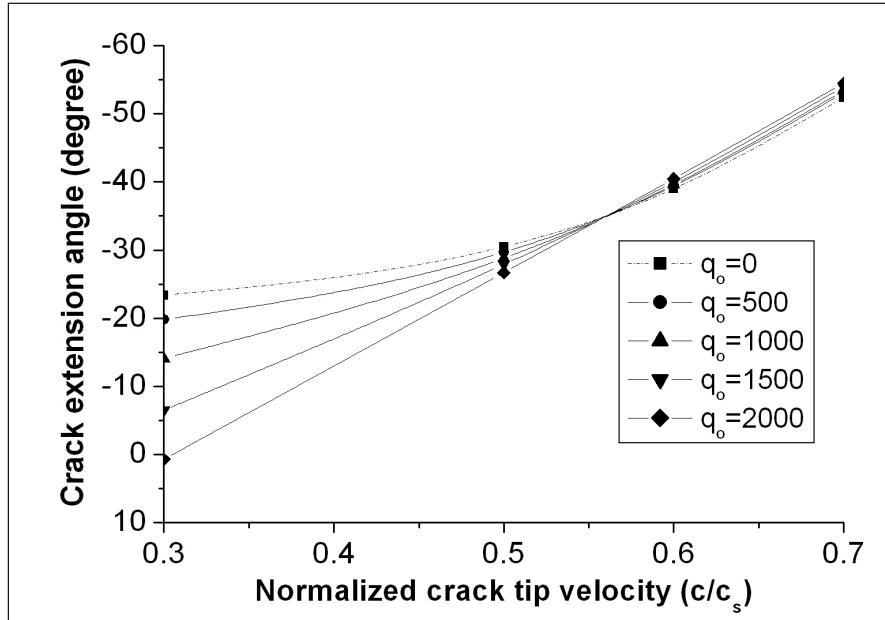
2.5 Summary

The stress-fields near the crack tip for mixed-mode thermo-mechanical loading are developed using displacement potentials in conjunction with an asymptotic approach. These crack-tip field equations can be successfully used in extracting fracture parameters from experimental stress and deformation fields when materials are subjected to thermo-mechanical loading. The following are the key observations of the analytical stress field contours developed using the stress field equations.

- The temperature field changes the magnitude of the in-plane stress components (σ_{xx} , σ_{yy} and τ_{xy}) but the qualitative profile around the crack tip is not influenced.
- The temperature field influences both the magnitude and the profile of maximum shear stress τ_{max} , hoop stress $\sigma_{\theta\theta}$ and the principal stress σ_1 around the crack-tip.
- The crack growth angle decreases with increase in temperature for a given crack-tip velocity.
- The crack growth angle increases with increase in crack-tip velocity for a given temperature conditions around the crack-tip.
- The effect of temperature on the crack growth angle is insignificant at higher crack-tip velocities $c/c_s > 0.55$.



(a) Minimum strain energy density criterion



(b) Maximum circumferential stress criterion

Figure 2.7. Crack extension angle as a function of crack tip velocity for mixed mode thermo-mechanical loading ($K_{IID}/K_{ID} = 0.2$, $r = 0.002\text{m}$).

List of References

- [1] G. C. Sih, "On the singular character of thermal stress near a crack tip," *ASME J. Appl. Mech.*, vol. 29, pp. 587–589, 1962.
- [2] A. M. Kassir, M. K. Bergman, "Thermal stress in a solid containing parallel circular crack," *Appl. Res. Sci.*, vol. 25, pp. 262–280, 1971.
- [3] W. K. Wilson and I. W. Yu, "The use of the j-integral in the thermal stress crack problems," *Int. J. Fract.*, vol. 15, pp. 377–387, 1979.
- [4] K. Y. Lee and K. Sim, "Thermal shock stress intensity factor by bueckners weight function method," *Eng. Fract. Mech.*, vol. 37, pp. 799–804, 1990.
- [5] T. C. Chen and C. I. Weng, "Coupled transient thermoelastic response in an edge-cracked plate," *Eng. Fract. Mech.*, vol. 39, pp. 915–925, 1991.
- [6] D. E. Katsareas and N. K. Anifantis, "On the computation of mode-i and ii thermal shock stress intensity factors using a boundary-only element method," *Int. J. Numer. Methods. Eng.*, vol. 38, pp. 4157–4169, 1995.
- [7] M. R. D. H. R. Hosseini-Tehrani, P. Eslami, "Dynamic crack analysis under coupled thermoelastic assumption," *Trans. ASME.*, vol. 68, pp. 584–588, 2001.
- [8] L. B. Freund, *Dynamic Fracture Mechanics, first ed.* Cambridge Press, 1990.
- [9] Z. Jin and N. Noda, "Crack-tip singular fields in nonhomogeneous materials," *J. Appl. Mech.*, vol. 61, pp. 738–739, 1994.
- [10] V. B. Chalivendra and A. Shukla, "Transient elastodynamic crack growth in functionally graded materials," *Journal of Applied Mechanics*, vol. 72, p. 23727, 2005.
- [11] A. Shukla and N. Jain, "Dynamic damage growth in particle reinforced graded materials," *International Journal of Impact Engineering*, vol. 30, p. 777803, 2004.
- [12] Z. Z. W. D. Jiang, C.P. Zou and Y. W. Liu, "A discussion about a class of stress intensity factors and its verification," *International Journal of Fracture*, vol. 49, pp. 141–157, 1991.
- [13] G. C. Sih, "Strain-energy-density factor applied to mixed mode crack problems," *International of Journal of fracture*, vol. 10 (3), pp. 305–321, 1974.
- [14] F. Erdogan and G. C. Sih, "On the crack extension in plates under plane loading and transverse shear," *Journal of Basic Engineering*, vol. 85, pp. 519–527, 1963.

- [15] E. H. Yoffe, “The moving griffith crack,,” *Philosophical Magazine*, vol. 42, pp. 739–750, 1952.
- [16] D. Broek, *Elementary engineering fracture mechanics*. Martinus Nishoff Publishers, 1978.

CHAPTER 3

Effect of Dynamic Thermo-Mechanical Stress Field on Crack Propagation Direction in Functionally Graded Materials

3.1 Abstract

Asymptotic analysis in conjunction with displacement potentials has been used to develop thermo-mechanical stress fields for a mixed mode propagating crack in a functionally graded material (FGM). The shear modulus, mass density, thermal conductivity and coefficient of thermal expansion of the FGM are assumed to vary exponentially along the gradation direction. First, asymptotic temperature fields are derived for an exponential variation of thermal conductivity and later these temperature fields are used in deriving stress fields. Using asymptotic thermo-mechanical stress fields the variation of maximum shear stress, circumferential stress and strain energy density as a function of temperature around the crack-tip are generated. Finally, utilizing the minimum strain energy density criterion and the maximum circumferential stress criterion, the crack growth direction for various crack-tip speeds, non-homogeneity coefficients and temperature fields are determined.

3.2 Introduction

Functionally graded materials (FGMs) are essentially non-homogeneous composites which have characteristics of spatially varying microstructure and mechanical/thermal properties to meet a predetermined functional performance [1, 2]. Although their performance in real-life engineering applications are still under investigation, FGMs have shown promising results when they are subjected to thermo-mechanical loading [2]. Hasselman and Youngblood [3] were among the first to study thermal stresses in nonhomogeneous structures associated with thermo-

mechanical loading. By introducing thermal conductivity gradient, they realized significant reductions in the magnitude of the tensile thermal stress in ceramic cylinders. In other studies, thermal residual stresses are relaxed in metal-ceramic layered materials by inserting a functionally graded interface layer between the metal and ceramic [4–6]. In their studies, Kudora et al., and Takashashi et al., reported that when subjected to thermal shocks, FGM coatings suffer significantly less damage than conventional ceramic coatings [7, 8].

In continuation of above studies, several studies on the quasi-static fracture of FGMs under thermo-mechanical loading have been reported. Assuming exponential variation of material properties, Jin and Noda [9] investigated the steady thermal stress intensity factors in functionally gradient semi-infinite space with an edge crack subjected to thermal load. Later, Erdogan and Wu [10] also determined the steady thermal stress intensity factor of a FGM layer with a surface crack perpendicular to the boundaries. By further assuming the exponential variation of thermal and mechanical properties of the materials, Jin and Batra [11] investigated stress intensity relaxation problem at the tip of an edge crack in a FGM subjected to a thermal shock. Using both experimental and numerical techniques, Kokini and Choules [12] and Kokini and Case [13] studied surface and interface cracking in FGM coatings subjected to thermal shocks. By employing a finite element method (FEM), Noda [14] analyzed an edge crack problem in a zirconia/titanium FGM plate subjected to cyclic thermal loads. Using finite element method and boundary element method, Jin and Paulino [15] studied transient thermal stresses in an FGM with an edge crack and having constant Young’s modulus and Poisson’s ratio but varying thermal properties along the thickness direction. Walters et al. [16] developed general domain integral methods to obtain stress intensity factors for surface cracks in FGMs under mode-I thermo-mechanical loading conditions.

The above studies provide closed form solutions for stress intensity factors under thermo-mechanical loading, however for extracting fracture parameters from experimental studies, asymptotic expansion of thermo-mechanical stress fields around the crack tip are essential. In this direction, recently, Jain et al. [17] developed quasi-static stress and displacement fields for a crack in an infinite FGM medium under thermo-mechanical loading.

In this paper, the stress fields for a propagating crack at uniform speed along the direction of mechanical and thermal property variation in a FGM under thermo-mechanical loading conditions are developed. The elasto-dynamic problem for FGM is formulated in terms of displacement potentials and the solutions are obtained through an asymptotic analysis. In analyzing this problem, we transform the general partial differential equation in the dynamic equilibrium into Laplace's equation whose solution involves harmonic functions. Using the developed equations, angular variation of the maximum shear stress, circumferential stress and minimum strain energy density are plotted as a function of temperature around the crack-tip. Using both minimum strain energy density criterion and maximum circumferential stress criterion, the crack growth directions for various crack-tip speeds, non-homogeneous coefficients and different temperatures fields are also determined.

3.3 Theoretical Formulation

At a continuum level, the properties at any given point in an FGM can be assumed to be same in all directions; hence FGMs can be treated as isotropic non-homogeneous solids. Spatial variation of elastic properties, mass density and thermal properties make analytical solutions to the elastodynamic equations extremely difficult. Hence, an asymptotic analysis similar to that employed by Freund [18] is used to expand the stress field around a propagating crack under thermo-

mechanical loading conditions. The complete derivation is provided in Appendix C.

Shear modulus (μ), Lamé's constant (λ), density (ρ), thermal expansion (α) and heat conductivity (k) of the FGM are assumed to vary in an exponential manner as given by Eq. 3.1, whereas, Poisson's ratio (ν) is assumed to be a constant.

$$\mu = \mu_0 e^{(\zeta X)}, \lambda = \lambda_0 e^{(\zeta X)}, \rho = \rho_0 e^{(\zeta X)}, \alpha = \alpha_0 e^{(\beta X)}, k = k_0 e^{(\beta X)} \quad (3.1)$$

The equations of motion for a plane problem are given by Eq. 3.2

$$\frac{\partial \sigma_{XX}}{\partial X} + \frac{\partial \tau_{XY}}{\partial Y} = \rho \frac{\partial^2 u}{\partial t^2}, \quad \frac{\partial \sigma_{YY}}{\partial Y} + \frac{\partial \tau_{XY}}{\partial X} = \rho \frac{\partial^2 v}{\partial t^2} \quad (3.2)$$

The relationship between stresses and strains for a plane strain thermo-mechanical problem can be written as

$$\sigma_{XX} = e^{(\zeta X)} ((\lambda_0 + 2\mu_0)\epsilon_{XX} + \lambda\epsilon_{YY} - (3\lambda_0 + 2\mu_0)\alpha_0 e^{(\beta X)} T) \quad (3.3)$$

$$\sigma_{YY} = e^{(\zeta X)} ((\lambda_0 + 2\mu_0)\epsilon_{YY} + \lambda\epsilon_{XX} - (3\lambda_0 + 2\mu_0)\alpha_0 e^{(\beta X)} T) \quad (3.4)$$

$$\tau_{XY} = e^{(\zeta X)} \mu_0 \epsilon_{XY} \quad (3.5)$$

where X and Y are reference coordinates, σ_{ij} and ϵ_{ij} where $i = X, Y$ and $j = X, Y$ are in-plane stress and strain components, λ and μ denote Lamé's constant and shear modulus respectively and subscript "o" means at $X = 0$ as shown in Fig. C.1. α is coefficient of thermal expansion and T represents the change in temperature in the infinite medium and ζ and β are nonhomogeneity constants that have the dimension $(length)^{-1}$. For plane strain deformation, the displacements u and v are derived from dilatational and shear wave potentials ϕ and ψ . These potentials can be expressed as

$$u = \frac{\partial \phi}{\partial X} + \frac{\partial \psi}{\partial Y}, \quad v = \frac{\partial \phi}{\partial Y} - \frac{\partial \psi}{\partial X} \quad (3.6)$$

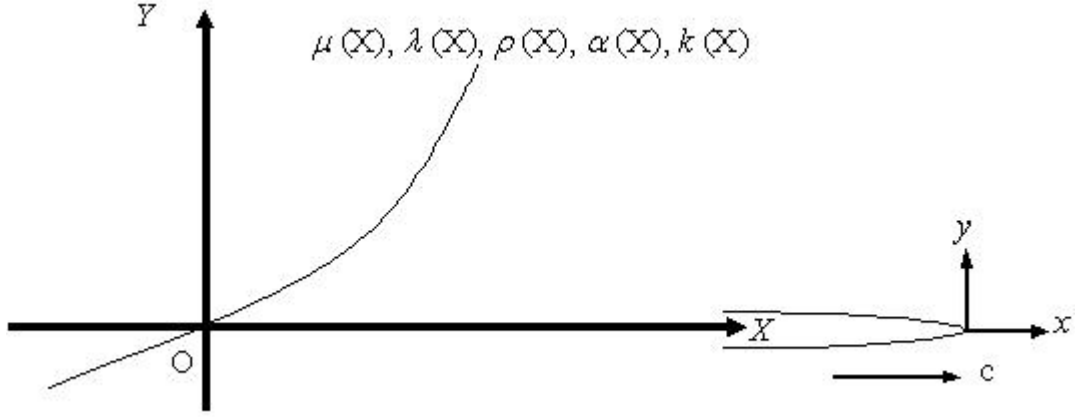


Figure 3.1. Propagating crack tip orientation with respect to reference coordinate configuration.

Substituting for the stresses and density from Eqs. 3.3 - 3.5 and Eq. 3.1 respectively into Eq. 3.2 and after simplification, the equations of motion become

$$(2\mu_0 + \lambda_0) \nabla^2 \nabla^2 \phi - \zeta \left((2\mu_0 + \lambda_0) \frac{\partial}{\partial X} \nabla^2 \phi + \rho_0 \frac{\partial}{\partial Y} \nabla^2 \psi \right) - \alpha_c (3\lambda_0 + 2\mu_0) \left(\left((\beta + \zeta) \beta T + (2\beta + \zeta) \frac{\partial T}{\partial X} \right) + \nabla^2 T \right) = \rho_0 \frac{\partial^2}{\partial t^2} \nabla^2 \phi \quad (3.7)$$

$$\rho_0 \nabla^2 \nabla^2 \psi - \zeta \left(\left(\mu_0 \frac{\partial}{\partial X} \nabla^2 \psi + \lambda_0 \frac{\partial}{\partial Y} \nabla^2 \phi \right) - \alpha_c (3\lambda_0 + 2\mu_0) \zeta \frac{\partial T}{\partial Y} \right) = \rho_0 \frac{\partial^2}{\partial t^2} \nabla^2 \psi \quad (3.8)$$

α_c is the coefficient of thermal expansion in the vicinity of the instantaneous crack tip and is assumed to be constant.

Equations 3.7 and 3.8 can be written as

$$(\delta + 2) \nabla^2 \phi - \zeta \left((\delta + 2) \frac{\partial}{\partial X} + \frac{\partial}{\partial Y} \right) - \alpha_c (3\lambda_0 + 2\mu_0) \left(\left((\beta + \zeta) \beta \Delta^{-1} T + (2\beta + \zeta) \Delta^{-1} \frac{\partial T}{\partial X} \right) + T \right) = \frac{\rho_0}{\mu_0} \frac{\partial^2 \phi}{\partial t^2} \quad (3.9)$$

$$\nabla^2 \psi - \zeta \frac{\partial \psi}{\partial X} + \zeta \delta \frac{\partial \phi}{\partial Y} - \alpha_c (3\lambda_0 + 2\mu_0) \zeta \Delta^{-1} \frac{\partial T}{\partial Y} = \frac{\rho_0}{\mu_0} \frac{\partial^2 \psi}{\partial t^2} \quad (3.10)$$

where

$$\Delta^{-1} = \frac{1}{\nabla^2}, \quad \delta = \frac{\lambda_0}{\mu_0}$$

For a propagating crack shown in C.1, the transformed crack tip coordinates can be written as $x = X - ct$ where c is constant crack tip speed. In the moving coordinate systems the above Eqs. 3.9 and 3.10 can be written as

$$\begin{aligned} & \alpha_l^2 \frac{\partial^2 \phi}{\partial x^2} + \frac{\partial^2 \phi}{\partial y^2} \zeta \frac{\partial \phi}{\partial x} + \frac{\zeta}{\delta + 2} \frac{\partial \psi}{\partial y} \\ & - \alpha_c \frac{(3\delta + 2)}{(\delta + 2)} \left(\left((\beta + \zeta) \beta \Delta^{-1} T + (2\beta + \zeta) \Delta^{-1} \frac{\partial T}{\partial X} \right) + T \right) = 0 \end{aligned} \quad (3.11)$$

$$\alpha_s^2 \frac{\partial^2 \psi}{\partial x^2} + \frac{\partial^2 \psi}{\partial y^2} + \zeta \frac{\partial \psi}{\partial x} + \zeta \delta \frac{\partial \phi}{\partial y} - \alpha_c (3\delta + 2) \zeta \Delta^{-1} \frac{\partial T}{\partial y} = 0 \quad (3.12)$$

where

$$\alpha_l = \sqrt{1 - \left(\frac{c}{c_l} \right)^2}, \quad \alpha_s = \sqrt{1 - \left(\frac{c}{c_s} \right)^2}, \quad c_s = \sqrt{\frac{\mu_c}{\rho_c}}, \quad \nabla^2 = \frac{\partial^2}{\partial x^2} + \frac{\partial^2}{\partial y^2}$$

$c_l = c_s \sqrt{2(1 - \nu)/(1 - 2\nu)}$ for plane strain and $c_l = c_s \sqrt{2/(1 - \nu)}$ for plane stress. c_l and c_s are the elastic dilatational wave speed and the elastic shear wave speed of the material at the crack tip.

It is assumed that in the above transformation, the fields ϕ and ψ do not depend explicitly on time in the moving coordinate reference and their time dependence is only through the transformation $x = X - ct$. To solve the above equations of motion for displacement potentials ϕ and ψ using asymptotic approach, first the derivation of temperature field around the crack-tip is essential. Hence its derivation is discussed in the following section.

3.3.1 Temperature Fields around the Crack Tip

In this analysis it is assumed that the temperature field around the crack tip changes asymptotically. Also, the transient effects are neglected. The heat

conductivity is assumed to vary exponentially as given by Eq. 3.1. The steady state heat conduction equation can be written as

$$\frac{\partial}{\partial X} \left(k \frac{\partial T}{\partial X} \right) + \frac{\partial}{\partial Y} \left(k \frac{\partial T}{\partial Y} \right) = 0 \quad (3.13)$$

Where k is the coefficient of thermal conductivity

Assuming that k is constant in the region considered, the above equation can be written as

$$\nabla^2 T + \beta \frac{\partial T}{\partial X} = 0 \quad (3.14)$$

where $\nabla^2 = \frac{\partial^2}{\partial X^2} + \frac{\partial^2}{\partial Y^2}$

Transforming the above equation to the crack-tip moving coordinate system ($x = Xc - t, y = Y$), Eq. 3.14 can be written as

$$\nabla^2 T + \beta \frac{\partial T}{\partial x} = 0 \quad (3.15)$$

where $\nabla^2 = \frac{\partial^2}{\partial x^2} + \frac{\partial^2}{\partial y^2}$

As this stages asymptotic analysis is performed to solve the above Eq. 3.15. In this process, first a new set of coordinates is introduce as

$$\eta_1 = \frac{x}{\epsilon} \quad \eta_2 = \frac{y}{\epsilon} \quad (3.16)$$

where ϵ is an arbitrary parameter and is assumed to be $0 < \epsilon < 1$

Equation 3.15 can be written in a new scaled coordinates (η_1, η_2) as

$$\nabla^2 T + \epsilon \beta \frac{\partial T}{\partial \eta_1} = 0 \quad (3.17)$$

where $\nabla^2 = \frac{\partial^2}{\partial \eta_1^2} + \frac{\partial^2}{\partial \eta_2^2}$

For the asymptotic analysis T is represented as a power series expansion in ϵ as

$$T(x, y) = T(\eta_1 \epsilon, \eta_2 \epsilon) = \sum_{m=0}^{\infty} \epsilon^{\frac{(m+1)}{2}} T_m(\eta_1, \eta_2) \quad (3.18)$$

Substituting Eq.3.18 into Eq.3.17 gives the following equation.

$$\sum_{m=0}^{\infty} \epsilon^{\frac{(m+1)}{2}} \left(\left(\frac{\partial^2 T_m}{\partial \eta_1^2} + \frac{\partial^2 T_m}{\partial \eta_2^2} \right) + \epsilon^{\frac{(m+3)}{2}} \beta \frac{\partial T_m}{\partial \eta_1} \right) = 0 \quad (3.19)$$

For Eq.3.19 to be valid, the partial differential equations corresponding to each power of ϵ ($\epsilon^{1/2}$, ϵ , $\epsilon^{3/2}$...) should vanish independently. This leads to the set of partial differential equations.

For $m = 0$ and $m = 1$

$$\frac{\partial^2 T_m}{\partial \eta_1^2} + \frac{\partial^2 T_m}{\partial \eta_2^2} = 0 \quad (3.20)$$

For $m = 2$

$$\frac{\partial^2 T_2}{\partial \eta_1^2} + \frac{\partial^2 T_2}{\partial \eta_2^2} + \beta \frac{\partial T_0}{\partial \eta_1} = 0 \quad (3.21)$$

Equation 3.20 (i.e. for $m = 0$ and $m = 1$) is ordinary Laplace's equation in the domain $\rho = \eta_1 + i\eta_2$ and the solution is same as for homogenous material [19, 20]. By assuming insulated crack surface boundary condition, (i.e. $\frac{\partial T}{\partial \theta} = 0$ at $\theta = \pm\pi$), the solution for Eq.3.20 can now be written as

For $m = 0$

$$T_0 = q_0 \rho^{1/2} \sin \left(\frac{1}{2} \theta \right) \quad (3.22)$$

For $m = 1$

$$T_1 = q_1 \rho^{1/2} \cos (\theta) \quad (3.23)$$

where $\rho = (\eta_1^2 + \eta_2^2)^{1/2}$

The solution T_2 , for Eq.3.21 corresponding to higher powers of ϵ ($m = 2$) has two parts: homogeneous and particular solution. The particular solution can be obtained using recursive approach [19, 20], and the complete solution for Eq.3.21 is given below.

$$T_2 = q_2 \rho^{3/2} \sin \left(\frac{3}{2} \theta \right) + \left(\frac{1}{4} \right) q_0 \beta \rho^{3/2} \sin \left(\frac{1}{2} \theta \right) \quad (3.24)$$

Transforming back to crack tip coordinates x and y , the temperature field near the crack tip is given as

$$T = q_0 r^{1/2} \sin\left(\frac{1}{2}\theta\right) + q_1 r \cos(\theta) + q_2 r^{3/2} \sin\left(\frac{3}{2}\theta\right) + \left(\frac{1}{4}\right) q_0 \beta r^{3/2} \sin\left(\frac{1}{2}\theta\right) \quad (3.25)$$

where $r = (x^2 + y^2)^{1/2}$ and $\theta = \tan^{-1}\left(\frac{y}{x}\right)$

3.3.2 Asymptotic Expansion of Crack Tip Stress Fields

Similar to derivation of temperature field, asymptotic approach is again used in deriving solutions for displacement potentials of equations of motion Eqs. 3.11 and 3.12. Scaled coordinates as discussed in Eq.3.16 are now applied to Eqs. 3.11 and 3.12 as given below

$$\alpha_l^2 \frac{\partial^2 \phi}{\partial \eta_1^2} + \frac{\partial^2 \phi}{\partial \eta_2^2} - \epsilon \left(\zeta \frac{\partial \phi}{\partial \eta_1} + \frac{\zeta}{\delta + 2} \frac{\partial \psi}{\partial \eta_2} \right) - \alpha_c \frac{(3\delta + 2)}{(\delta + 2)} \left(\epsilon^2 T + \epsilon^3 (2\beta + \zeta) \Delta^{-1} \frac{\partial T}{\partial \eta_1} + \epsilon^4 (\beta + \zeta) \beta \Delta^{-1} T \right) = 0 \quad (3.26)$$

$$\alpha_s^2 \frac{\partial^2 \psi}{\partial \eta_1^2} + \frac{\partial^2 \psi}{\partial \eta_2^2} - \epsilon \left(\zeta \frac{\partial \psi}{\partial \eta_1} + \zeta \delta \frac{\partial \phi}{\partial \eta_2} \right) - \alpha_c (3\delta + 2) \epsilon^3 \zeta \Delta^{-1} \frac{\partial T}{\partial \eta_2} = 0 \quad (3.27)$$

At this stage it is assumed that ϕ , ψ , and T can be represented as a power series expansion in ϵ .

$$\phi(x, y) = \phi(\epsilon \eta_1, \epsilon \eta_2) = \sum_{m=0}^{\infty} \epsilon^{\frac{(m+3)}{2}} \phi_m(\eta_1, \eta_2) \quad (3.28)$$

$$\psi(x, y) = \psi(\epsilon \eta_1, \epsilon \eta_2) = \sum_{m=0}^{\infty} \epsilon^{\frac{(m+3)}{2}} \psi_m(\eta_1, \eta_2) \quad (3.29)$$

$$T(x, y) = T(\epsilon \eta_1, \epsilon \eta_2) = \sum_{m=0}^{\infty} \epsilon^{\frac{(m+1)}{2}} T_m(\eta_1, \eta_2) \quad (3.30)$$

As given by Jin and Noda [9] the solution for the temperature field is obtained by ensuring the heat flux or the derivative of the temperature field near the crack tip is singular. This means that the potentials for temperature are one power less than the displacement potentials. Substituting Eqs. 3.28-3.30 into Eqs.3.26 and 3.27 gives the following equations.

$$\sum_{m=0}^{\infty} (\epsilon^{\frac{m+3}{2}} \left(\alpha_l^2 \frac{\partial^2 \phi_m}{\partial \eta_1^2} + \frac{\partial^2 \phi_m}{\partial \eta_2^2} \right) - \epsilon^{\frac{m+5}{2}} \left(\zeta \frac{\partial \phi_m}{\partial \eta_1} + \frac{\zeta}{\delta+2} \frac{\partial \psi_m}{\partial \eta_2} \right) - \alpha_c \frac{(3\delta+2)}{(\delta+2)} \left(\epsilon^{\frac{m+5}{2}} T_m + \epsilon^{\frac{m+7}{2}} (2\beta+\zeta) \Delta^{-1} \frac{\partial T_m}{\partial \eta_1} + \epsilon^{\frac{m+9}{2}} (\beta+\zeta) \beta \Delta^{-1} T_m \right)) = 0 \quad (3.31)$$

$$\sum_{m=0}^{\infty} (\epsilon^{\frac{m+3}{2}} \left(\alpha_s^2 \frac{\partial^2 \psi_m}{\partial \eta_1^2} + \frac{\partial^2 \psi_m}{\partial \eta_2^2} \right) - \epsilon^{\frac{m+5}{2}} \left(\zeta \frac{\partial \psi_m}{\partial \eta_1} + \zeta \delta \frac{\partial \phi_m}{\partial \eta_2} \right) - \alpha_c (3\delta+2) \epsilon^{\frac{m+7}{2}} \zeta \Delta^{-1} \frac{\partial T_m}{\partial \eta_2}) = 0 \quad (3.32)$$

For Eqs.3.31 and 3.32 to be valid, the partial differential equations corresponding to each power of ϵ ($\epsilon^{3/2}, \epsilon^2, \epsilon^{5/2}, \dots$) should vanish independently. This leads to the following set of partial differential equations.

For $m = 0$ and $m = 1$

$$\alpha_l^2 \frac{\partial^2 \phi_m}{\partial \eta_1^2} + \frac{\partial^2 \phi_m}{\partial \eta_2^2} = 0 \quad (3.33)$$

$$\alpha_s^2 \frac{\partial^2 \psi_m}{\partial \eta_1^2} + \frac{\partial^2 \psi_m}{\partial \eta_2^2} = 0 \quad (3.34)$$

For $m = 2$

$$\alpha_l^2 \frac{\partial^2 \phi_2}{\partial \eta_1^2} + \frac{\partial^2 \phi_2}{\partial \eta_2^2} = -\zeta \left(\frac{\partial \phi_0}{\partial \eta_1} + \frac{1}{\delta+2} \frac{\partial \psi_0}{\partial \eta_2} \right) + \frac{3\delta+2}{\delta+2} \alpha_c T_0 \quad (3.35)$$

$$\alpha_l^2 \frac{\partial^2 \psi_2}{\partial \eta_1^2} + \frac{\partial^2 \psi_2}{\partial \eta_2^2} = -\zeta \left(\frac{\partial \psi_0}{\partial \eta_1} + \frac{1}{\delta + 2} \frac{\partial \phi_0}{\partial \eta_2} \right) \quad (3.36)$$

Eqs. 3.33 and 3.34 are similar to that for homogeneous material where as the partial differential equations Eqs.3.35 and 3.36, associated with higher powers of are coupled to the differentials of the lower order functions through the nonhomogeneity parameters and temperature term. Eqs. 3.33 and 3.34 (i.e. for $m = 0$ and $m = 1$) can be easily reduced to Laplace's equation in the respective complex domains $\zeta_l = \eta_1 + i\alpha_l\eta_2$, $\zeta_s = \eta_1 + i\alpha_s\eta_2$, $i = \sqrt{-1}$ and the solutions are same as that for homogenous material [18-21] and can be written as

$$\phi_m(\rho_l, \theta_l, t) = A_m \rho_l^{(m+3)/2} \cos \left(\frac{(m+3)}{2} \theta_l \right) + C_m \rho_l^{(m+3)/2} \sin \left(\frac{(m+3)}{2} \theta_l \right) \quad (3.37)$$

$$\psi_m(\rho_s, \theta_s, t) = B_m \rho_s^{(m+3)/2} \sin \left(\frac{(m+3)}{2} \theta_s \right) + D_m \rho_s^{(m+3)/2} \cos \left(\frac{(m+3)}{2} \theta_s \right) \quad (3.38)$$

where

$$\rho_l = (\eta_1^2 + \alpha_l^2 \eta_2^2)^{1/2}, \quad \tan(\theta_l) = \frac{\alpha_l \eta_2}{\eta_1}, \quad \rho_s = (\eta_1^2 + \alpha_s^2 \eta_2^2)^{1/2}, \quad \tan(\theta_s) = \frac{\alpha_s \eta_2}{\eta_1}$$

and A_m , B_m , C_m , and D_m are real constants.

Using the definition of dynamic stress intensity factor K_{ID} and K_{IID} for opening mode and shear mode [21], the relation between A_o and K_{ID} and C_o and K_{IID} are obtained.

$$A_0 = \frac{4(1 + \alpha_s^2)}{4\alpha_l\alpha_s - (1 + \alpha_s^2)^2} \frac{K_{ID}}{\mu\sqrt{2\pi}}, \quad (3.39)$$

$$C_0 = \frac{4\alpha_s^2}{3(4\alpha_l\alpha_s - (1 + \alpha_s^2)^2)} \frac{K_{IID}}{\mu\sqrt{2\pi}}, \quad (3.40)$$

where μ is the shear modulus of the material at the propagating crack-tip, K_{ID} is mode-I dynamic stress intensity factor and K_{IID} mode-II dynamic stress intensity factor. Now considering the crack face boundary conditions $\sigma_{22} = 0$ and $\sigma_{12} = 0$ we can also obtain the following relationship between A_o and B_o and C_o and D_o

$$B_0 = \frac{-2\alpha_l}{1 + \alpha_s^2} A_0 \quad (3.41)$$

$$D_0 = \frac{1 + \alpha_s^2}{2\alpha_s} C_0 \quad (3.42)$$

The solution for the Eqs. 3.35 and 3.36 corresponding to higher powers of ϵ ($m = 2$) consists of two parts: solution for homogeneous equation and a particular solution due to nonhomogeneity and temperature and these can be obtained recursively [18, 21]. The solutions ϕ_2 and ψ_2 obtained are given below. The solutions ϕ_0 , ψ_0 , ϕ_1 and ψ_1 automatically satisfy the compatibility equations because these the solutions are same as those for homogeneous materials. Since the non-homogeneous specific parts of ϕ_2 and ψ_2 are obtained from ϕ_0 and ψ_0 , they also automatically satisfy the compatibility equations.

$$\begin{aligned} \phi_2 = & A_2 \rho_l^{5/2} \cos\left(\frac{5}{2}\theta_l\right) + C_2 \rho_l^{5/2} \sin\left(\frac{5}{2}\theta_l\right) \\ & - \frac{1}{4} \frac{\zeta}{\alpha_l^2} \rho_l^{5/2} \left(A_0 \cos\left(\frac{1}{2}\theta_l\right) + (C_0 \sin\left(\frac{1}{2}\theta_l\right)) \right) \\ & - \frac{2}{5} \frac{\zeta}{(\delta + 2)} \frac{\alpha_s}{(\alpha_l^2 - \alpha_s^2)} \rho_s^{5/2} \left(B_0 \cos\left(\frac{5}{2}\theta_s\right) + (D_0 \sin\left(\frac{5}{2}\theta_s\right)) \right) \\ & + \frac{4}{15} \frac{(3\delta + 2)}{(\delta + 2)} \frac{\alpha_c}{(\alpha_l^2 - 1)} q_0 \rho^{5/2} \sin \frac{5}{2}\theta \end{aligned} \quad (3.43)$$

$$\begin{aligned} \psi_2 = & B_2 \rho_s^{5/2} \cos\left(\frac{5}{2}\theta_s\right) + D_2 \rho_s^{5/2} \sin\left(\frac{5}{2}\theta_s\right) \\ & - \frac{1}{4} \frac{\zeta}{\alpha_s^2} \rho_s^{5/2} \left(B_0 \sin\left(\frac{1}{2}\theta_s\right) + (D_0 \cos\left(\frac{1}{2}\theta_s\right)) \right) \\ & - \frac{2}{5} \delta \frac{\zeta \alpha_l}{(\alpha_l^2 - \alpha_s^2)} \rho_l^{5/2} \left(A_0 \sin\left(\frac{5}{2}\theta_l\right) + (C_0 \sin\left(\frac{5}{2}\theta_l\right)) \right) \end{aligned} \quad (3.44)$$

By assembling together the above result for the first few terms and by transforming back to the $x - y$ plane, the combined solution can be written for ϕ and ψ as Eq. 3.45 and 3.46

$$\begin{aligned}
\phi = & A_0 r_l^{3/2} \cos\left(\frac{3}{2}\theta_l\right) + C_0 r_l^{3/2} \sin\left(\frac{3}{2}\theta_l\right) + A_1 r_l^2 \cos(2\theta_l) + C_1 r_l^2 \sin(2\theta_l) \\
& + A_2 r_l^{5/2} \cos\left(\frac{5}{2}\theta_l\right) + C_2 r_l^{5/2} \sin\left(\frac{5}{2}\theta_l\right) \\
& - \frac{1}{4} \frac{\zeta}{\alpha_l^2} r_l^{5/2} \left(A_0 \cos\left(\frac{1}{2}\theta_l\right) + (C_0 \sin\left(\frac{1}{2}\theta_l\right)) \right) \\
& - \frac{2}{5} \frac{\zeta}{(\delta+2)} \frac{\alpha_s}{(\alpha_l^2 - \alpha_s^2)} r_s^{5/2} \left(B_0 \cos\left(\frac{5}{2}\theta_s\right) + (D_0 \sin\left(\frac{5}{2}\theta_s\right)) \right) \\
& + \frac{4}{15} \frac{(3\delta+2)}{(\delta+2)} \frac{\alpha_c}{(\alpha_l^2 - 1)} q_0 r^{5/2} \sin \frac{5}{2}\theta
\end{aligned} \tag{3.45}$$

$$\begin{aligned}
\psi = & B_0 r_s^{3/2} \sin\left(\frac{3}{2}\theta_s\right) + D_0 r_s^{3/2} \cos\left(\frac{3}{2}\theta_s\right) + B_1 r_s^2 \sin(2\theta_s) + D_1 r_s^2 \cos(2\theta_s) \\
& + B_2 r_s^{5/2} \cos\left(\frac{5}{2}\theta_s\right) + D_2 r_s^{5/2} \sin\left(\frac{5}{2}\theta_s\right) \\
& - \frac{1}{4} \frac{\zeta}{\alpha_s^2} r_s^{5/2} \left(B_0 \sin\left(\frac{1}{2}\theta_s\right) + (D_0 \cos\left(\frac{1}{2}\theta_s\right)) \right) \\
& - \frac{2}{5} \delta \frac{\zeta \alpha_l}{(\alpha_l^2 - \alpha_s^2)} r_l^{5/2} \left(A_0 \sin\left(\frac{5}{2}\theta_l\right) + (C_0 \sin\left(\frac{5}{2}\theta_l\right)) \right)
\end{aligned} \tag{3.46}$$

where

$$r_l = (x^2 + \alpha_l^2 y^2)^{1/2}, \quad \tan(\theta_l) = \frac{\alpha_l y}{x}, \quad r_s = (x^2 + \alpha_s^2 y^2)^{1/2}, \quad \tan(\theta_s) = \frac{\alpha_s y}{x}$$

The above definitions of the displacement potentials are now used with Eq. 3.6 to get the displacements fields. These displacement fields are then used to get strain fields. These strain fields and Eq. 3.25 are substituted into Eqs. 3.3 - 3.5 to obtain

in-plane stress fields around the crack tip. They are shown in Eq. 3.47 - 3.50.

$$\begin{aligned}
\frac{\sigma_{xx}}{exp(\zeta x)\mu_0} = & \left(\frac{3}{4} r_l^{-1/2} \cos\left(\frac{\theta_l}{2}\right) (\delta (1 - \alpha_l^2) + 2) \right) A_0 \\
& - \left(\frac{3}{16} \frac{\zeta}{\alpha_l^2} r_l^{1/2} \cos\left(\frac{3\theta_l}{2}\right) (\delta (1 - \alpha_l^2) + 2) \right) A_0 \\
& - \left(\frac{3}{4} \frac{\zeta}{\alpha_l^2} r_l^{1/2} \cos\left(\frac{\theta_l}{2}\right) (\delta (1 + \alpha_l^2) + 2) \right) A_0 \\
& - \left(\frac{3}{4} r_l^{-1/2} \sin\left(\frac{\theta_l}{2}\right) (\delta (1 - \alpha_l^2) + 2) \right) C_0 \\
& + \left(\frac{3}{16} \frac{\zeta}{\alpha_l^2} r_l^{1/2} \sin\left(\frac{3\theta_l}{2}\right) (\delta (1 - \alpha_l^2) - 2) \right) C_0 \\
& + \left(\frac{3}{4} \frac{\zeta}{\alpha_l^2} r_l^{1/2} \sin\left(\frac{\theta_l}{2}\right) (\delta (1 + \alpha_l^2) + 2) \right) C_0 \\
& + \left(\frac{3}{2} r_s^{-1/2} \alpha_s \cos\left(\frac{\theta_s}{2}\right) - \frac{3}{8} \frac{\zeta}{\alpha_s} r_s^{1/2} \cos\left(\frac{3\theta_s}{2}\right) \right) B_0 \\
& + \left(\frac{3}{2} r_s^{-1/2} \alpha_s \sin\left(\frac{\theta_s}{2}\right) - \frac{3}{8} \frac{\zeta}{\alpha_s} r_s^{1/2} \sin\left(\frac{3\theta_s}{2}\right) \right) D_0 \\
& + 2A_1 (\delta (1 - \alpha_l^2) + 2) + 4B_1 \alpha_s \\
& + \left(\left(\frac{15}{4} r_l^{1/2} \cos\left(\frac{\theta_l}{2}\right) (\delta (1 - \alpha_l^2) + 2) \right) A_2 + \left(\frac{15}{2} r_s^{1/2} \alpha_s \cos\left(\frac{\theta_s}{2}\right) \right) B_2 \right) \\
& + \left(\left(\frac{15}{4} r_l^{1/2} \sin\left(\frac{\theta_l}{2}\right) (\delta (1 - \alpha_l^2) + 2) \right) C_2 - \left(\frac{15}{2} r_s^{1/2} \alpha_s \sin\left(\frac{\theta_s}{2}\right) \right) D_2 \right) \\
& - \left(\left(3 \frac{\zeta \delta \alpha_l^2}{\alpha_l^2 - \alpha_s^2} r_l^{1/2} \cos\left(\frac{\theta_l}{2}\right) \right) A_0 - \left(3 \frac{\zeta \delta \alpha_l^2}{\alpha_l^2 - \alpha_s^2} r_l^{1/2} \sin\left(\frac{\theta_l}{2}\right) \right) C_0 \right) \\
& - \left(\frac{3}{2} \frac{\zeta}{\delta + 2} \frac{\alpha_s}{\alpha_l^2 - \alpha_s^2} r_s^{1/2} \cos\left(\frac{\theta_l}{2}\right) (\delta (1 - \alpha_s^2) + 2) \right) B_0 \\
& + \left(\frac{3}{2} \frac{\zeta}{\delta + 2} \frac{\alpha_s}{\alpha_l^2 - \alpha_s^2} r_s^{1/2} \sin\left(\frac{\theta_s}{2}\right) (\delta (1 - \alpha_s^2) + 2) \right) D_0 \\
& + 2 \left(\frac{3\delta + 2}{\delta + 2} \frac{\alpha_c}{\alpha_l^2 - 1} r^{1/2} \sin\left(\frac{\theta}{2}\right) \right) q_0 \\
& - \alpha_c (3\delta + 2) (q_0 r^{1/2} \sin\left(\frac{\theta}{2}\right) + q_1 r \cos(\theta) + q_2 r^{3/2} \sin\left(\frac{3\theta}{2}\right) \\
& + \frac{1}{4} q_0 \beta r^{3/2} \sin\left(\frac{\theta}{2}\right))
\end{aligned} \tag{3.47}$$

$$\begin{aligned}
\frac{\sigma_{YY}}{\exp(\zeta x)\mu_0} = & \left(\frac{3}{4} r_l^{-1/2} \cos\left(\frac{\theta_l}{2}\right) (\delta - \alpha_l^2 (\delta + 2)) \right) A_0 \\
& - \left(\frac{3}{16} \frac{\zeta}{\alpha_l^2} r_l^{1/2} \cos\left(\frac{3\theta_l}{2}\right) (\delta - \alpha_l^2 (\delta + 2)) \right) \\
& - \left(\frac{3}{4} \frac{\zeta}{\alpha_l^2} r_l^{1/2} \cos\left(\frac{\theta_l}{2}\right) (\delta + \alpha_l^2 (\delta + 2)) \right) A_0 \\
& - \left(\frac{3}{4} r_l^{-1/2} \sin\left(\frac{\theta_l}{2}\right) (\delta - \alpha_l^2 (\delta + 2)) \right) C_0 \\
& - \left(\frac{3}{16} \frac{\zeta}{\alpha_l^2} r_l^{1/2} \sin\left(\frac{3\theta_l}{2}\right) (\delta - \alpha_l^2 (\delta + 2)) \right) C_0 \\
& + \left(\frac{3}{4} \frac{\zeta}{\alpha_l^2} r_l^{1/2} \sin\left(\frac{\theta_l}{2}\right) (\delta + \alpha_l^2 (\delta + 2)) \right) C_0 \\
& - \left(\frac{3}{2} r_s^{-1/2} \alpha_s \cos\left(\frac{\theta_s}{2}\right) - \frac{3}{8} \frac{\zeta}{\alpha_s} r_s^{1/2} \cos\left(\frac{3\theta_s}{2}\right) \right) B_0 \\
& - \left(\frac{3}{2} r_s^{-1/2} \alpha_s \sin\left(\frac{\theta_s}{2}\right) - \frac{3}{8} \frac{\zeta}{\alpha_s} r_s^{1/2} \sin\left(\frac{3\theta_s}{2}\right) \right) D_0 \\
& - 4A_1 (\delta - \alpha_l^2 (\delta + 2)) - 4B_1 \alpha_s \\
& + \left(\left(\frac{15}{4} r_l^{1/2} \cos\left(\frac{\theta_l}{2}\right) (\delta - \alpha_l^2 (\delta + 2)) \right) A_2 - \left(\frac{15}{2} r_s^{1/2} \alpha_s \cos\left(\frac{\theta_s}{2}\right) \right) B_2 \right) \\
& + \left(\left(\frac{15}{4} r_l^{1/2} \sin\left(\frac{\theta_l}{2}\right) (\delta - \alpha_l^2 (\delta + 2)) \right) C_2 + \left(\frac{15}{2} r_s^{1/2} \alpha_s \sin\left(\frac{\theta_s}{2}\right) \right) D_2 \right) \\
& + \left(\left(3 \frac{\zeta \delta \alpha_l^2}{\alpha_l^2 - \alpha_s^2} r_l^{1/2} \cos\left(\frac{\theta_l}{2}\right) \right) A_0 - \left(3 \frac{\zeta \delta \alpha_l^2}{\alpha_l^2 - \alpha_s^2} r_l^{1/2} \sin\left(\frac{\theta_l}{2}\right) \right) C_0 \right) \\
& - \left(\frac{3}{2} \frac{\zeta}{\delta + 2} \frac{\alpha_s}{\alpha_l^2 - \alpha_s^2} r_s^{1/2} \cos\left(\frac{\theta_l}{2}\right) (\delta - \alpha_s^2 (\delta + 2)) \right) B_0 \\
& - \left(\frac{3}{2} \frac{\zeta}{\delta + 2} \frac{\alpha_s}{\alpha_l^2 - \alpha_s^2} r_s^{1/2} \sin\left(\frac{\theta_s}{2}\right) (\delta - \alpha_s^2 (\delta + 2)) \right) D_0 \\
& - 2 \left(\frac{3\delta + 2}{\delta + 2} \frac{\alpha_c}{\alpha_l^2 - 1} r^{1/2} \sin\left(\frac{\theta}{2}\right) \right) q_0 \\
& + \alpha_c (3\delta + 2) (q_0 r^{1/2} \sin\left(\frac{\theta}{2}\right) + q_1 r \cos(\theta) + q_2 r^{3/2} \sin\left(\frac{3\theta}{2}\right) \\
& + \frac{1}{4} q_0 \beta r^{3/2} \sin\left(\frac{\theta}{2}\right))
\end{aligned} \tag{3.48}$$

$$\begin{aligned}
\frac{\sigma_{xy}}{\exp(\zeta x)\mu_0} = & \left(\frac{3}{2}\alpha_l r_l^{-1/2} \sin\left(\frac{\theta_l}{2}\right) - \frac{3}{8}\frac{\zeta}{\alpha_l} r_l^{1/2} \sin\left(\frac{3\theta_l}{2}\right) \right) A_0 \\
& + \left(\frac{3}{2}\alpha_l r_l^{-1/2} \cos\left(\frac{\theta_l}{2}\right) - \frac{3}{8}\frac{\zeta}{\alpha_l} r_l^{1/2} \cos\left(\frac{3\theta_l}{2}\right) \right) C_0 \\
& + \left(\frac{3}{4}r_s^{-1/2} (1 + \alpha_s^2) \sin\left(\frac{\theta_s}{2}\right) \right) B_0 \\
& - \left(\frac{3}{16}\frac{\zeta}{\alpha_s^2} r_s^{1/2} \left(\sin\left(\frac{3\theta_s}{2}\right) (1 + \alpha_s^2) + 4 \sin\left(\frac{\theta_s}{2}\right) (\alpha_s^2 - 1) \right) \right) B_0 \\
& - \left(\frac{3}{4}r_s^{-1/2} (1 + \alpha_s^2) \cos\left(\frac{\theta_s}{2}\right) \right) D_0 \\
& + \left(\frac{3}{16}\frac{\zeta}{\alpha_s^2} r_s^{1/2} \left(\cos\left(\frac{3\theta_s}{2}\right) (1 + \alpha_s^2) - 4 \cos\left(\frac{\theta_s}{2}\right) (\alpha_s^2 - 1) \right) \right) D_0 \\
& - \left(\left(\frac{15}{2}\alpha_l r_l^{1/2} \sin\left(\frac{\theta_l}{2}\right) \right) A_2 - \left(\frac{15}{2}\alpha_l r_l^{1/2} \alpha_l \cos\left(\frac{\theta_l}{2}\right) \right) C_2 \right) \\
& - \left(\left(\frac{15}{4}r_s^{1/2} (1 + \alpha_s^2) \sin\left(\frac{\theta_s}{2}\right) \right) B_2 + \left(\frac{15}{4}r_s^{1/2} (1 + \alpha_s^2) \cos\left(\frac{\theta_s}{2}\right) \right) D_2 \right) \\
& + \left(\frac{3}{2}\frac{\zeta\delta\alpha_l}{\alpha_l^2 - \alpha_s^2} r_l^{1/2} (1 + \alpha_l^2) \sin\left(\frac{\theta_l}{2}\right) \right) A_0 \\
& + \left(\frac{3}{2}\frac{\zeta\delta\alpha_l}{\alpha_l^2 - \alpha_s^2} r_l^{1/2} (1 + \alpha_s^2) \cos\left(\frac{\theta_l}{2}\right) \right) C_0 \\
& + \left(3\frac{\zeta}{\delta + 2}\frac{\alpha_s^2}{\alpha_l^2 - \alpha_s^2} r_s^{1/2} \sin\left(\frac{\theta_s}{2}\right) \right) B_0 \\
& - \left(3\frac{\zeta}{\delta + 2}\frac{\alpha_s^2}{\alpha_l^2 - \alpha_s^2} r_s^{1/2} \cos\left(\frac{\theta_s}{2}\right) \right) D_0 \\
& + 2 \left(\frac{3\delta + 2}{\delta + 2} \frac{\alpha_c}{\alpha_l^2 - 1} r^{1/2} \cos\left(\frac{\theta}{2}\right) \right) q_0
\end{aligned} \tag{3.49}$$

3.4 Results and Discussions

The thermo-elasticity relations developed above are next used to study the effect of temperature field, crack velocity and the non-homogeneity on the variation of maximum shear stress, the circumferential stress and the strain energy density around the crack-tip. The coefficient of thermal expansion (α_c) of titanium (which is of primary interest in our experimental research), $8.9 \times 10^{-6}/^\circ C$ is used in the analysis. The temperature coefficient q_o is varied from 0 to $2000 \text{ }^\circ C/m^{1/2}$. This variation results in nominal temperature change of about $100 \text{ }^\circ C$. It is assumed

that the resulting temperature range generates elastic deformation around the crack-tip.

To plot the stresses described in the next section, the following fracture parameters are used: crack tip velocity $c/c_s=0.5$, $K_{ID}=100$ MPa, $K_{IID}=0.2K_{ID}$ MPa and $k_{eff}=\sqrt{K_{ID} + K_{IID}}$

3.4.1 Variation of Stress Components Near the Crack Tip

The variation of stress field near the crack tip for the given thermo-mechanical conditions can be represented in many different ways. In this paper, three major stress components; circumferential tensile stress, maximum principal stress and maximum shear stress are plotted as a function of angle around the crack-tip. The variation of maximum shear stress (τ_{max}) for a typical fixed value of $K_{eff}/\sqrt{2\pi r}$ and constant crack tip velocity ($c/c_s = 0.5$) is plotted as shown in Fig. 3.2. is plotted for different temperature fields around the crack-tip. The angle at which maximum shear stress occurs changes with temperature and non homogeneity parameter. Angular variation of the maximum principal stress and circumferential tensile stress with fixed value of and constant crack tip velocity ($c/c_s = 0.5$) are plotted in Fig. 3.3 and Fig. 3.4. Similar trend as seen for maximum shear stress is observed in both the figures and the values and the angle at which the maximums occur change with temperature and non-homogeneity parameters. The results obtained in the present study collapse to the ones given by Freund [18] for homogeneous materials without temperature fields ($q_0 = 0$) if mode-I and mode-II fields are separated and plotted.

3.4.2 Crack Extension Angle

A dynamically moving crack tends to deviate from its path due to crack tip instability conditions. In the present study, using the derived thermo-mechanical

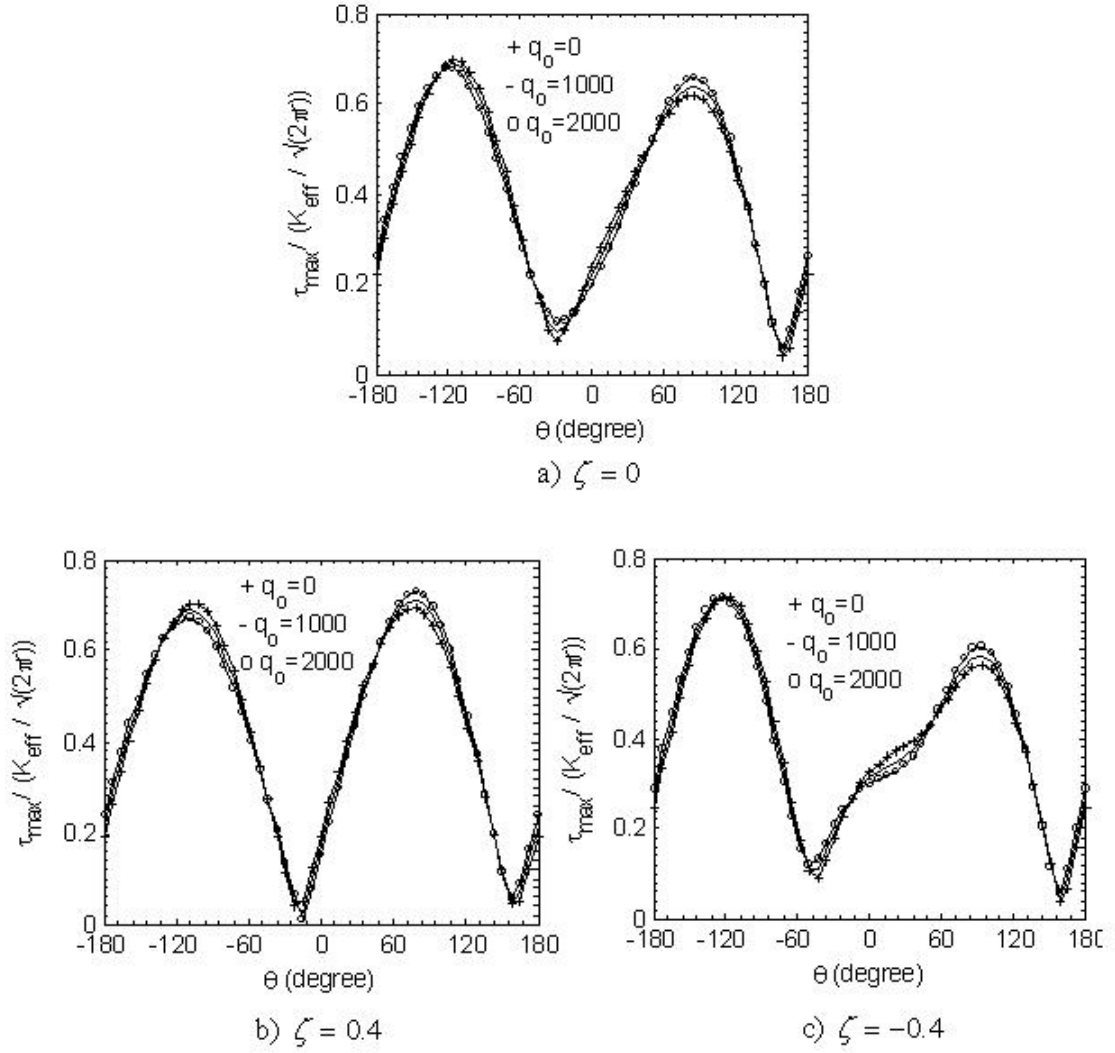


Figure 3.2. Variation of normalized maximum shear stress with angle around the crack-tip for mixed mode thermo-mechanical loading in a FGM for several values of temperature coefficients ($K_{IID}/K_{ID} = 0.2$, $c/c_s = 0.5$, $r = 0.002\text{m}$).

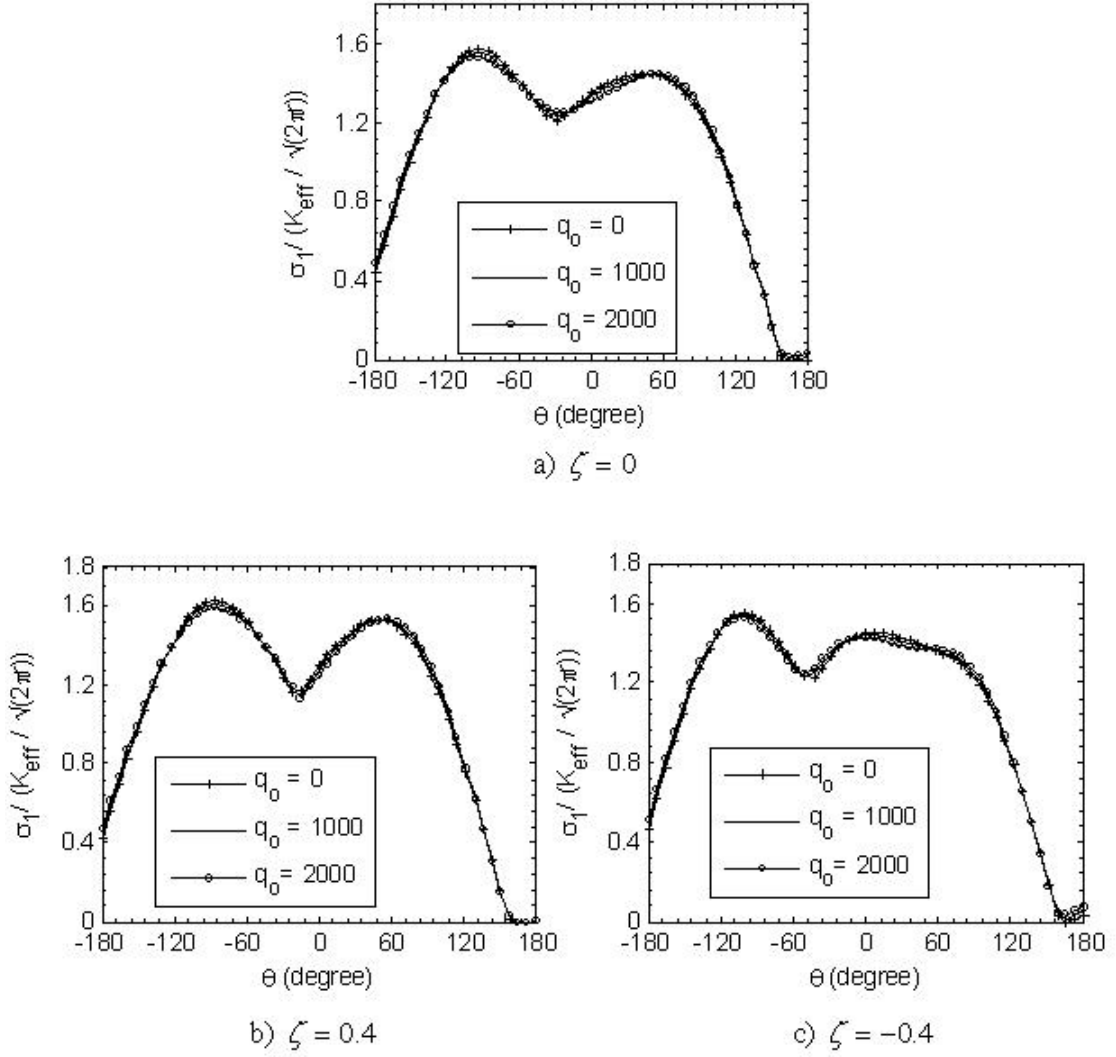


Figure 3.3. Variation of normalized the largest principal stress with angle around the crack-tip for mixed mode thermo-mechanical loading in a FGM for several values of temperature coefficients ($K_{IID}/K_{ID} = 0.2$, $c/c_s = 0.5$, $r = 0.002\text{m}$).

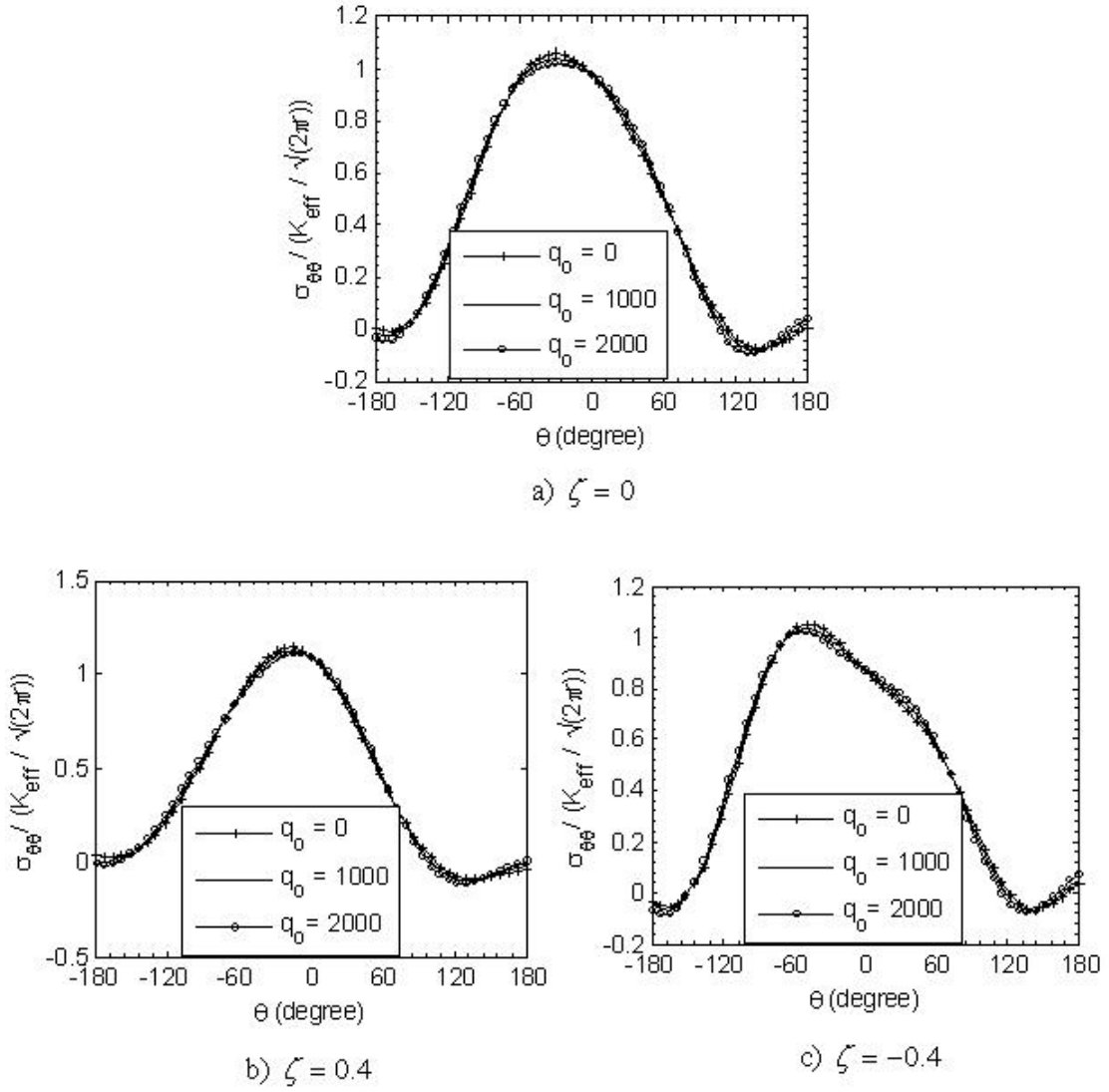


Figure 3.4. Variation of normalized circumferential stress with angle around the crack-tip for mixed mode thermo-mechanical loading in a FGM for several values of temperature coefficients ($K_{IID}/K_{ID} = 0.2$, $c/c_s = 0.5$, $r = 0.002\text{m}$).

stress field equations, the effect of temperature, crack-tip velocity and material non-homogeneity on the crack instability is presented. The theoretical prediction of crack extension angle is investigated by using the two well-known fracture criterias: minimum strain energy density (S-criterion) and maximum circumferential stress ($\sigma_{\theta\theta}$ -criterion).

Minimum strain-energy density (MSED) criterion

According to this criterion [21], the crack initiates when the strain energy density achieves a critical value and propagates in the direction of minimum strain-energy density value. The strain energy density dW/dV near the crack tip for an FGM is given as

$$\frac{dW}{dV} = S = \frac{1}{4\mu e^{\zeta x}} ((1 - \nu) (\sigma_{xx}^2 + \sigma_{yy}^2) - 2\nu\sigma_{xx}\sigma_{yy} + \sigma_{xy}^2) \quad (3.50)$$

Fracture takes place in the direction of minimum S, and the condition can be obtained by using Eq.(37)

$$\frac{\partial S}{\partial \theta} = 0, \quad \frac{\partial^2 S}{\partial \theta^2} > 0 \quad \text{at} \quad S = S_c \quad (3.51)$$

where S_c is the critical strain energy density

Variations of strain energy density with angle θ from $-\pi$ to π around the crack-tip for mixed mode thermo-mechanical loading in an FGM for several values of the temperature coefficient are plotted in Fig. 3.5. The angle at which the strain energy density reaches a minimum value changes with temperature and the non-homogeneity parameter.

Maximum circumferential-stress (MCS) criterion

The maximum circumferential stress criterion [22] states that, crack growth will occur in the direction of the maximum circumferential stress and will take place when the maximum circumferential stress reaches a critical value, and it can be

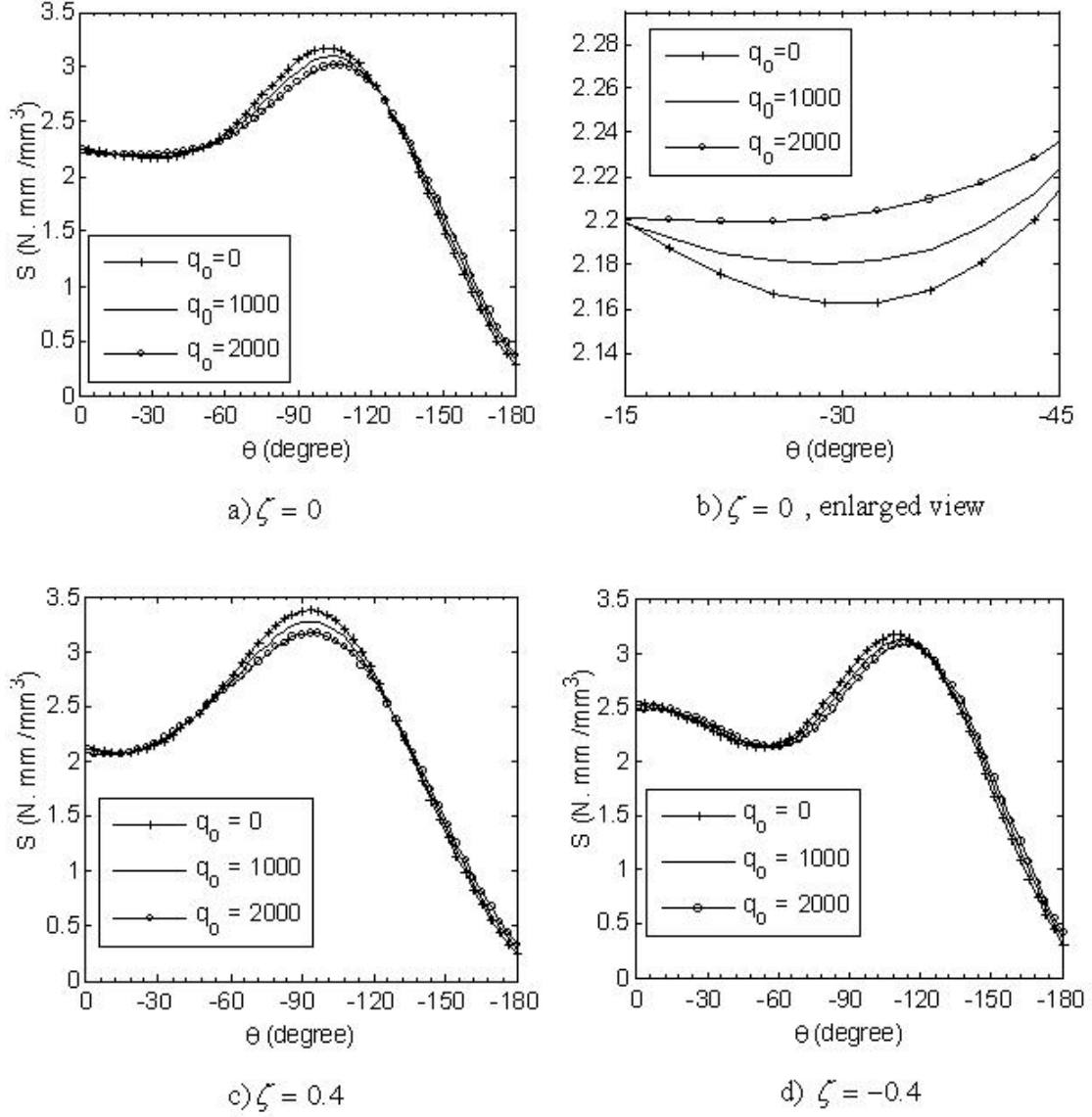


Figure 3.5. Variation of strain energy density with angle around the crack-tip for mixed mode thermo-mechanical loading in FGM subjected to different temperature fields ($K_{IID}/K_{ID} = 0.2$, $c/c_s = 0.5$, $r = 0.002\text{m}$).

given as Eq.3.52

$$\frac{\partial \sigma_{\theta\theta}}{\partial \theta} = 0, \quad \frac{\partial^2 \sigma_{\theta\theta}}{\partial \theta^2} < 0 \quad \text{at} \quad \sigma_{\theta\theta} = (\sigma_{\theta\theta})_c \quad (3.52)$$

where $(\sigma_{\theta\theta})_c$ is the critical circumferential stress

Variations of circumferential stress with angle θ around the crack-tip for mixed mode thermo-mechanical loading in an FGM for several values of temperature coefficients are plotted in Fig. 3.6. The angle at which the circumferential stress reaches a maximum value changes with temperature and non-homogeneity parameter.

Based on the above two criteria's, the effects of velocity, non-homogeneity and temperature on the crack extension angle (θ) are further investigated.

Effect of Crack Tip Velocity

The crack extension angles as a function of crack tip velocities as predicted by the above two criterias are shown in Fig. 3.7. For pure mode-I loading ($K_{IID}/K_{ID} = 0$), the crack extends along until the crack tip velocity reaches a critical value at which instability occurs [23]. When the crack tip velocity reaches the critical value, the crack deviates and extends to a different angle. For example at a crack tip velocity of $c/c_s = 0.7$, the MSED criterion predicts a crack extension angle of about -55° and the MCS criterion predicts about -38° . On the other hand, as the value of K_{IID}/K_{ID} increases from 0 to 1 and later from 1 to ∞ the crack extension angle increases monotonically. Broek [24], in his book gives the crack extension angles for mixed mode quasi static loading and these results match well with the predictions from the current study.

Effect of Non-homogeneity

The effect of non-homogeneity parameter on crack extension angle for a crack tip velocity of $0.5c_s$ at room temperature ($q_0 = 0$) is shown in Fig. 3.8. For both

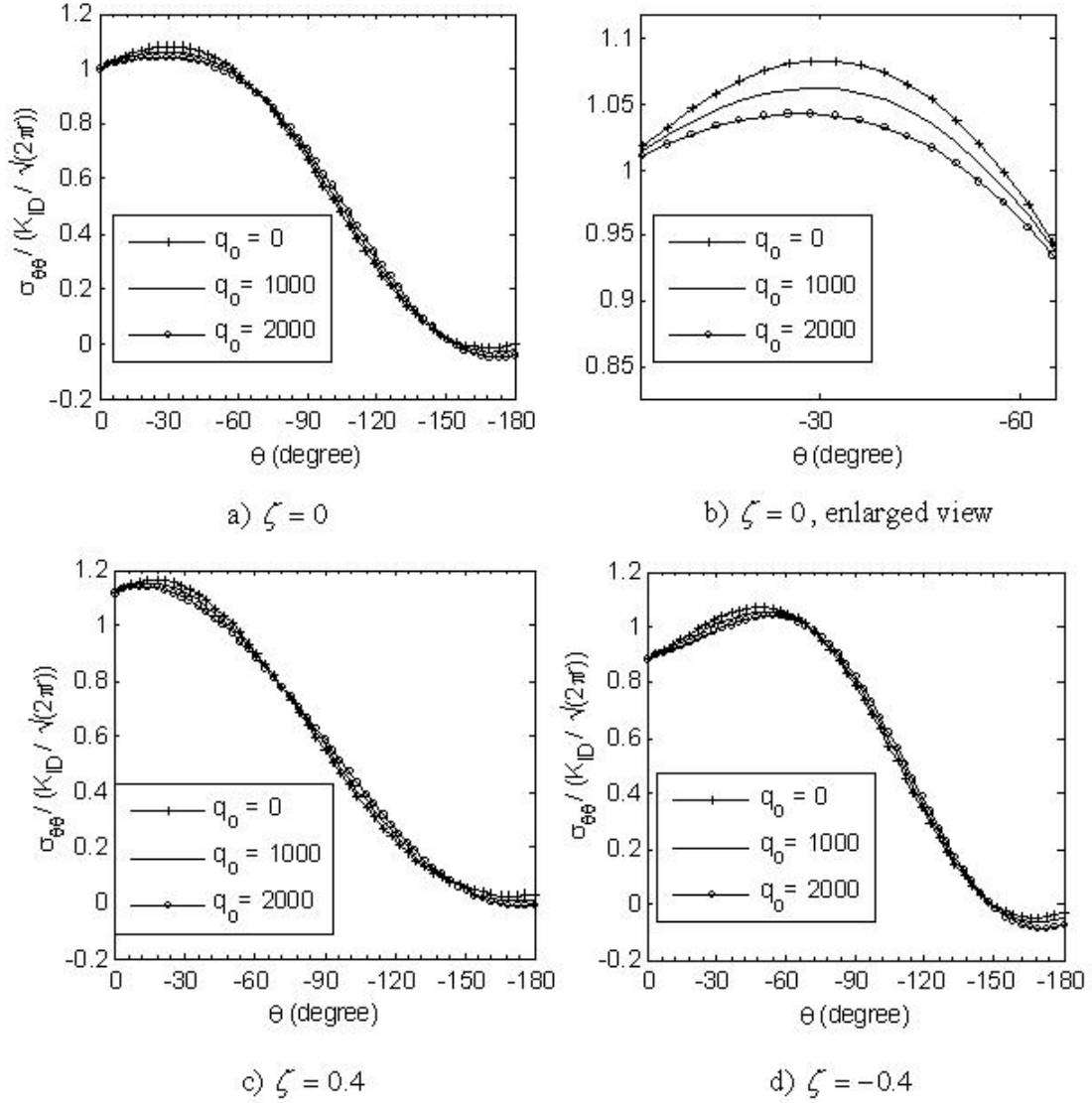
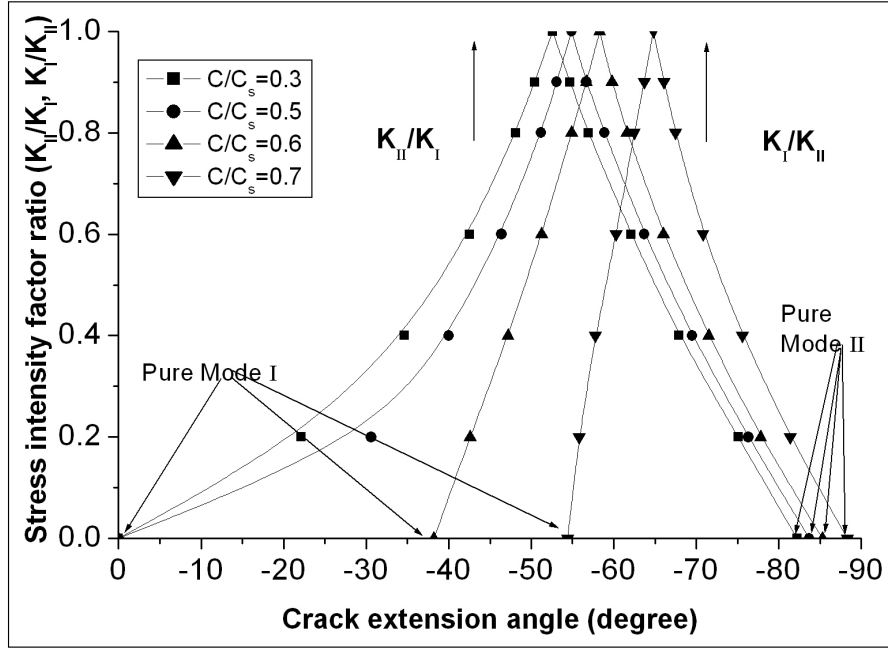
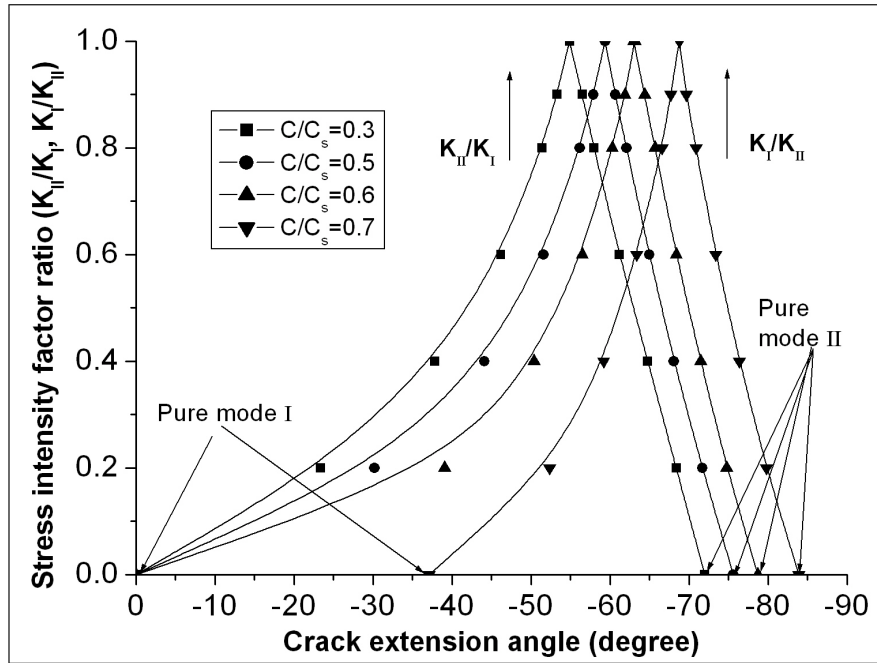


Figure 3.6. Variation of normalized circumferential stress with angle around the crack-tip for mixed mode thermo-mechanical loading in FGM subjected to different temperature fields ($K_{IID}/K_{ID} = 0.2$, $c/c_s = 0.5$, $r = 0.002m$).

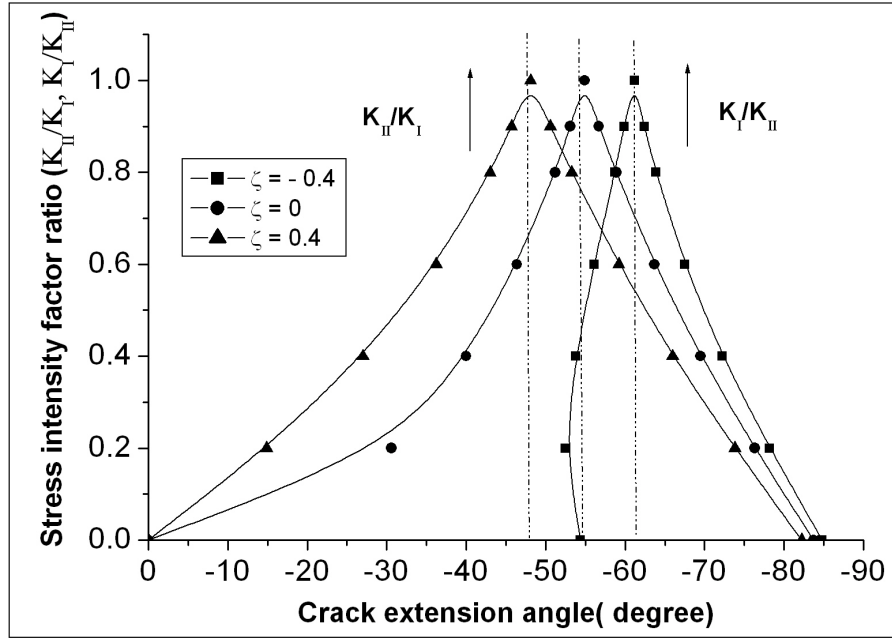


(a) Minimum strain energy density criterion

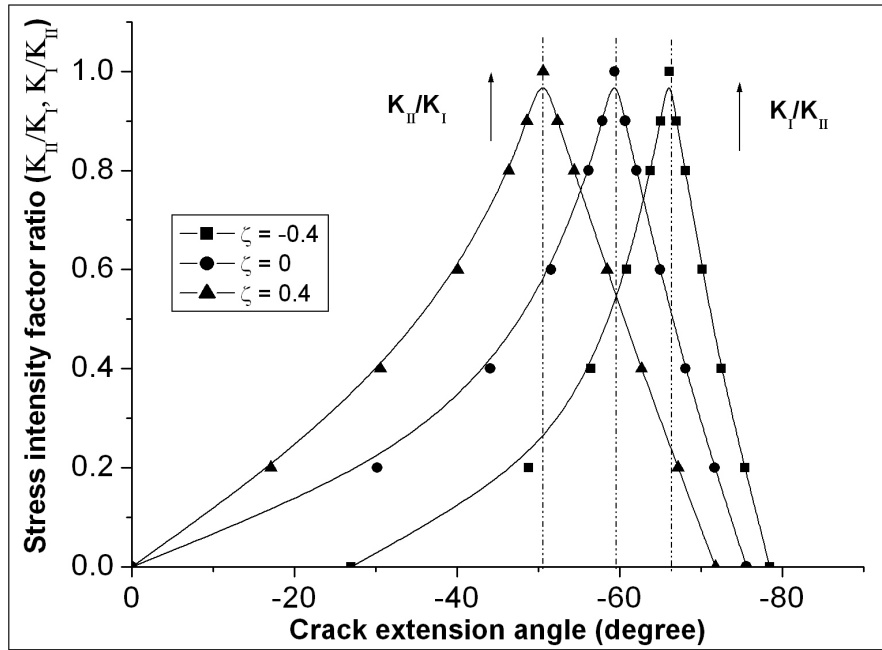


(b) Maximum circumferential stress criterion

Figure 3.7. Crack extension angle as a function of crack tip velocity for mixed mode thermo-mechanical loading in homogeneous material ($\zeta = 0$, $r = 0.002m$).



(a) Minimum strain energy density criterion



(b) Maximum circumferential stress criterion

Figure 3.8. Crack extension angle as a function of non-homogeneity parameter for mixed mode crack without heat ($c/c_s=0.5$, $r=0.002m$).

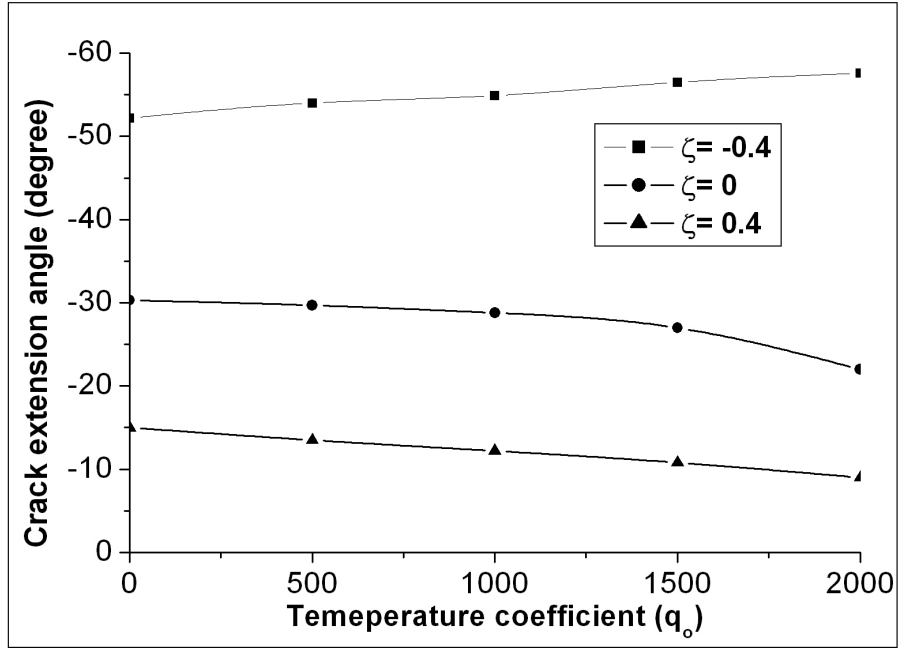
homogenous material (i.e. $\zeta = 0$) and a FGM with increasing stiffness in the direction of crack growth (i.e. $\zeta > 0$), the MCS criterion provides a maximum value and the MSED criterion provides a minimum value along $\theta = 0$ under pure mode-I loading ($K_{IID}/K_{ID} = 0$). However, for a FGM with decreasing stiffness in the direction of crack growth (i.e. $\zeta < 0$), the MCS criterion provides a maximum value at angle of about -55° and the MSED criterion provides minimum value at angle of about -28° . It can be also observed that, for complete range of K_{IID}/K_{ID} values, a FGM with $\alpha < 0$ has larger crack extension angle compared to both homogenous and a FGM with $\alpha > 0$. This might be attributed to presence of compliant material ahead of the crack tip and the propagating crack needs less energy to be unstable.

Effect of Temperature

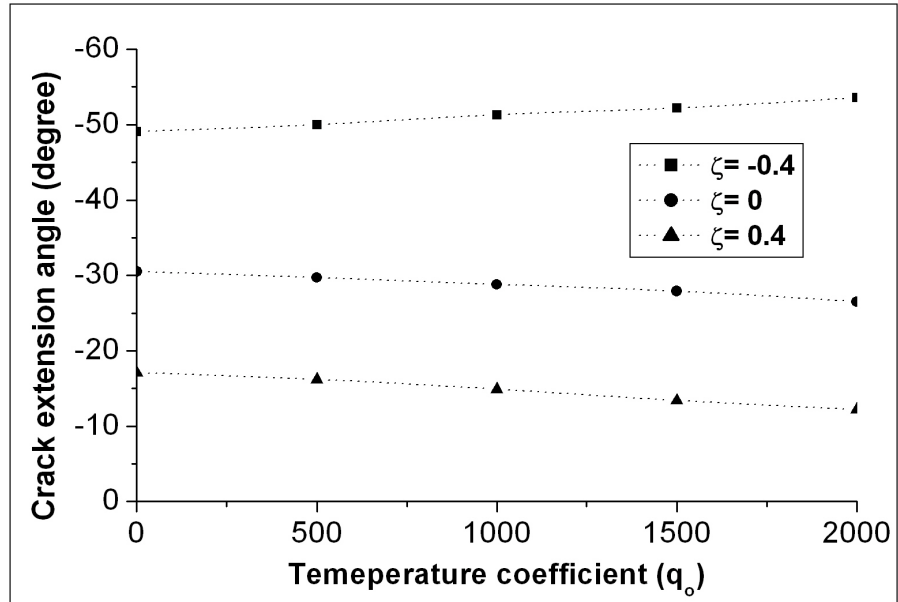
The effect of temperature field on the crack extension angle for a crack tip velocity of $0.5c_s$ is shown in Fig. 3.9. Both the criterion show that, for homogeneous material, the crack extension direction at room temperature is along $\theta = -30^\circ$ and the value decreases slowly with increase in applied temperature field. For FGM with $\alpha > 0$, the crack extension angle is along $\theta = -15^\circ$ at room temperature and again the value decreases with increase in applied temperature field. In the case of FGM with $\alpha < 0$, the crack extension angle is about -50° at room temperature and increases in magnitude as the temperature increases. The increased temperature field increases the compliance of the already compliant material (in case of $\alpha < 0$) and hence the propagating crack needs less energy to cause instability.

Effect of Crack Tip Velocity, Temperature and Non-homogeneity

The effects of temperature on the crack extension angle as a function of crack tip velocity in homogeneous material, a FGM with $\alpha > 0$ and a FGM with $\alpha < 0$



(a) Minimum strain energy density criterion



(b) Maximum circumferential stress criterion

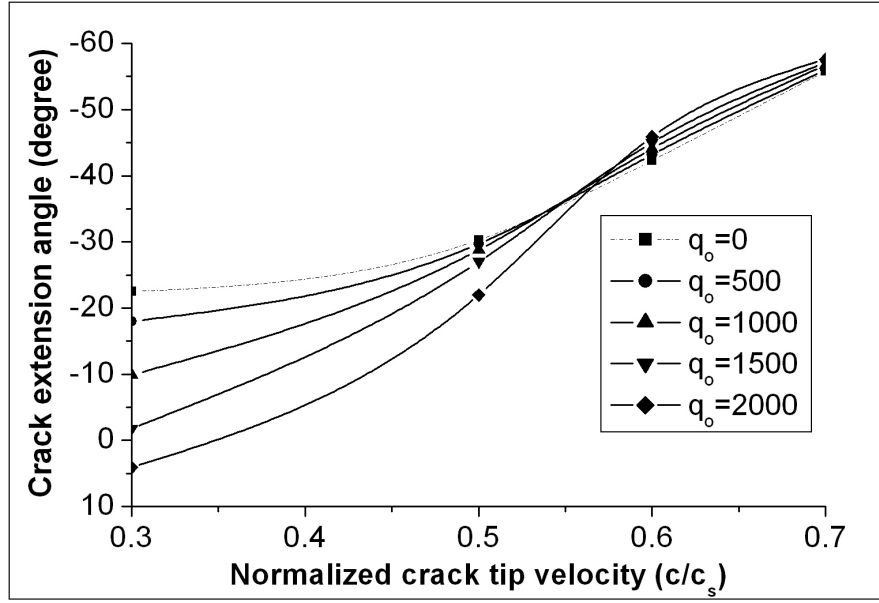
Figure 3.9. Effect of temperature on the crack extension angle for mixed mode loading in FGM ($K_{IID}/K_{ID} = 0.2$, $c/c_s = 0.5$, $r = 0.002\text{m}$).

are plotted in Figs. 3.10, 3.11 and 3.12. Figure 3.10 represents crack extension angle as a function of crack tip velocity for mixed-mode mechanical loading in homogeneous material at room and elevated temperatures. For a crack tip velocity of $c/c_s = 0.3$, both the criterions predict decrease in crack extension angle for increasing temperature fields. Furthermore, for $c/c_s > 0.3$, both criterions initially predict decrease in crack extension angle for increasing temperature field and show insignificant change at higher velocities.

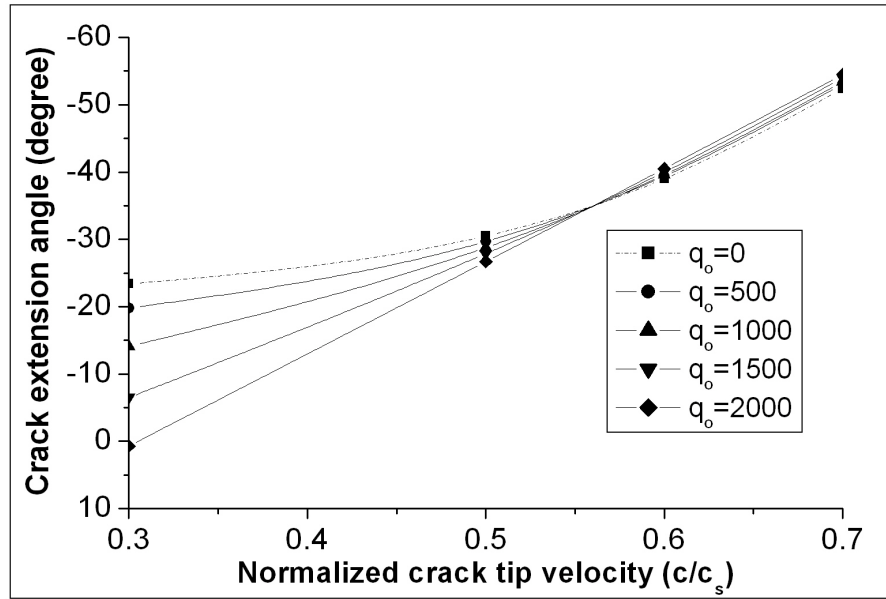
Figure 3.11 represents crack extension angle as a function of crack-tip velocity at room and at elevated temperatures for mixed mode mechanical loading in FGM with $\alpha > 0$. For a crack tip velocity of $c/c_s = 0.3$, the MSED criterion predicts a single value of $\theta = 0^\circ$. However for the same crack tip velocity, the MCS criterion predicts different crack extension angles for different temperature fields. Again similar to Fig. 3.10, for $c/c_s > 0.3$, FGM with $\alpha > 0$ the crack extension angle decreases as the temperature increases. However, as the crack velocity increases the difference in crack extension angles becomes less and less.

Figure 3.12 represents crack extension angle as a function of crack-tip velocity in the direction of crack growth at room and at elevated temperatures for mixed mode mechanical loading in FGM with $\alpha < 0$. The variation of crack extension angle in Fig. 3.12 shows significantly different trend compared to the above two cases. Both criterions predict different crack extension angles at $c/c_s = 0.3$ for different temperature fields. As the velocity increases, the crack extension angle initially decreases and then increases. It is quite contrasting to above two cases that for any crack tip velocity, higher the temperature higher the crack extension angle. The different trend predicted for FGM with $\alpha < 0$ might be again attributed to compliant material ahead of the propagating crack tip.

Previous work in literature states that the critical velocity at which the crack

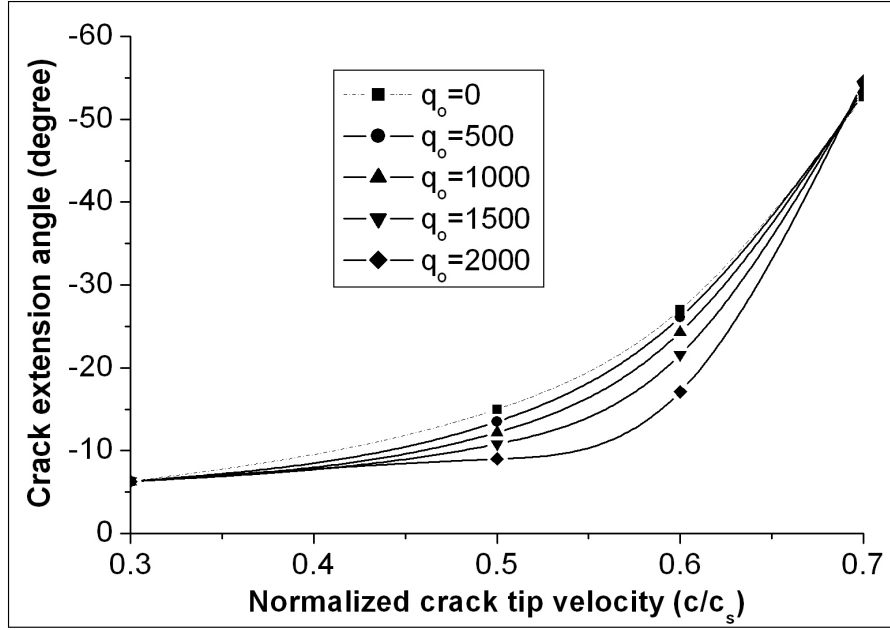


(a) Minimum strain energy density criterion

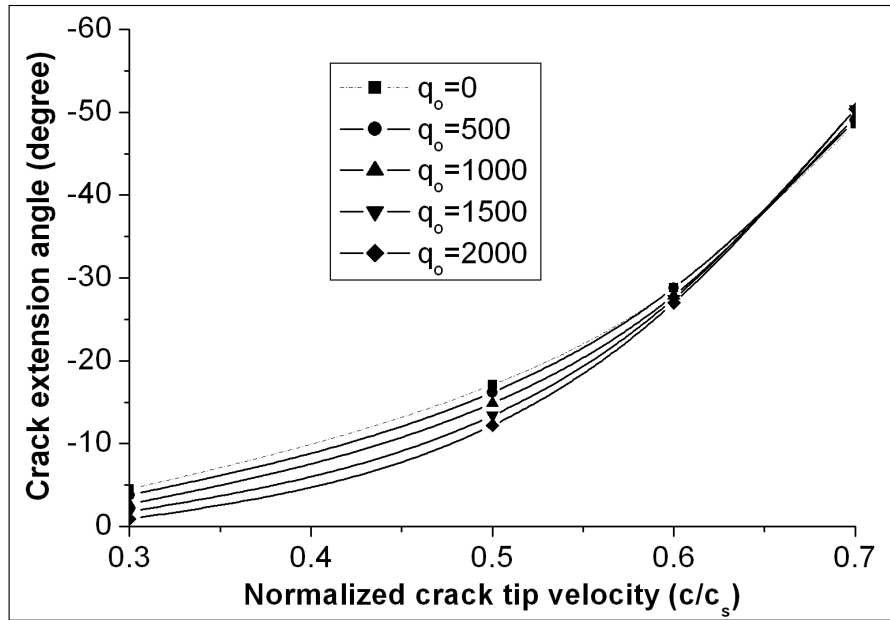


(b) Maximum circumferential stress criterion

Figure 3.10. Crack extension angle as a function of crack tip velocity for mixed mode thermo-mechanical loading for homogenous material ($K_{IID}/K_{ID} = 0.2$, $\zeta = 0$, $r = 0.002\text{m}$).

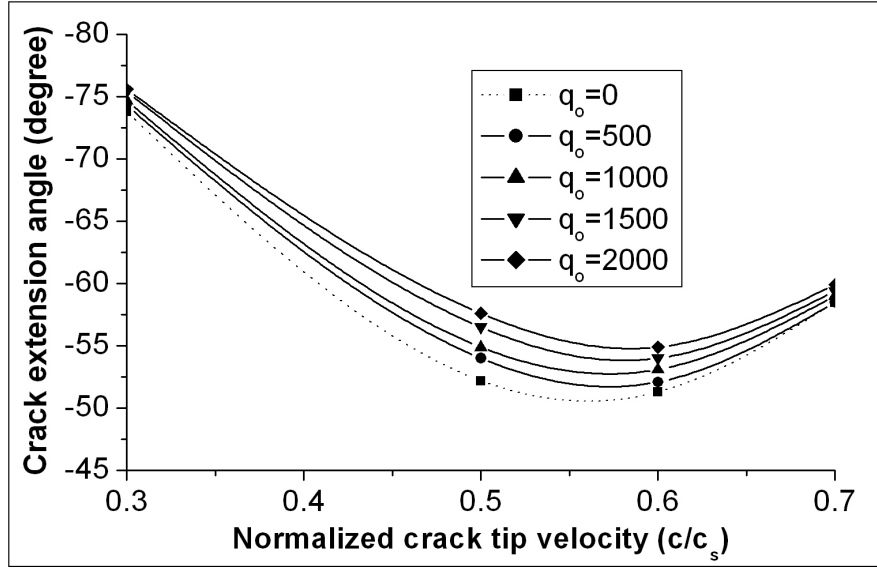


(a) Minimum strain energy density criterion

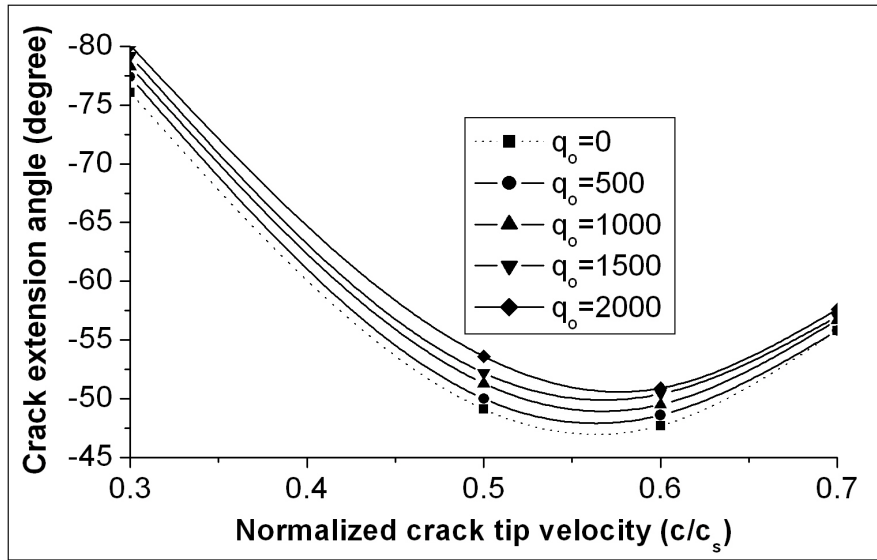


(b) Maximum circumferential stress criterion

Figure 3.11. Crack extension angle as a function of crack tip velocity for mixed mode thermo-mechanical loading at different temperature ($K_{IID}/K_{ID} = 0.2$, $\zeta = 0.4$, $r = 0.002\text{m}$).



(a) Minimum strain energy density criterion



(b) Maximum circumferential stress criterion

Figure 3.12. Crack extension angle as a function of crack tip velocity for mixed mode thermo-mechanical loading at different temperature ($K_{IID}/K_{ID} = 0.2$, $\zeta = -0.4$, $r = 0.002\text{m}$).

instability starts in running cracks depends on the extent of non-singular stress fields at the crack-tip [18]. It is noted from the derived equations that stress-field terms associated with non-homogeneity and temperature field are non-singular and this could be the reason why the crack extension angle is different for different non-homogeneity parameters and temperatures. However, the non-homogeneity parameter has more significant role in the crack extension angle compared to the effect of temperature field.

3.5 Summary

The stress-fields near the crack tip for mixed mode thermo-mechanical loading in graded material are developed using displacement potentials in conjugation with an asymptotic approach. Using insulated crack face boundary condition and steady state heat conduction assumption, first the temperature field near to the crack tip is developed. By incorporating the developed temperature field into the mechanical field, the thermo-mechanical stress fields near to the crack tip are developed. Using the developed equations, angular variation of maximum shear stress, circumferential stress and the largest principal stress are plotted as a function of temperature around the crack-tip. Using both minimum strain energy density criterion and maximum circumferential stress criterion, the crack instability direction for various crack-tip speeds and non-homogeneous coefficients is also determined.

List of References

- [1] T. Niino, M. Hirai and R. Watanabe, "The functionally gradient materials," *Journal of the Japan Society of Composite Materials*, vol. 13 (1), p. 257, 1987.
- [2] S. Suresh and A. Mortensen, *Fundamentals of functionally graded materials, processing and thermo-mechanical behavior of graded metals and metal-ceramic composites*. IOM Communications Ltd., London, 1998.
- [3] D. P. H. Hasselman and G. E. Youngblood, "Enhanced thermal stress resistance of structural ceramics with thermal conductivity gradient," *Journal of the American Ceramic Society*, vol. 61, pp. 49–52, 1978.

- [4] A. Kawasaki and W. R., "Finite element analysis of thermal stress of the metal/ceramics multi-layer composites with controlled compositional gradients," *Journal of the Japan institute of metal*, vol. 51, pp. 525–529, 1987.
- [5] R. L. Drake, J. T. Williamson and B. H. Rabin, "Finite element analysis of thermal residual stresses at graded ceramic-metal interfaces, part ii: interface optimization for residual stress reduction," *Journal of Applied Physics*, vol. 74, pp. 1321–1326, 1993.
- [6] S. F. M. Giannakopoulos, A. E. Suresh and M. Olsson, "Elastoplastic analysis of thermal cycling: layered materials with compositional gradient," *Acta metallurgica et materialia*, vol. 43, pp. 1335–1354, 1995.
- [7] K. M. A. Kuroda, Y. Kusaka and M. Togawa, "Evaluation tests of zro2/ni functionally gradient materials for regeneratively cooled thrust engine applications," in *Ceramic Transactions, Functionally Gradient Materials*, T. H. J.B. Holt, M. Koisumi and Z. Munir, Eds., vol. 34, no. 289-296. American Ceramic Society, Westerville, Ohio, vol., 1993.
- [8] T. O. D. Takahashi, H. T. Ishikawa and T. Hashida, "Laser and plasma-arc thermal shock/fatigue fracture evaluation procedure for functionally gradient materials." in *Thermal Shock and Thermal Fatigue Behavior of Advanced Ceramics*, G. Scheneider and G. Petzow, Eds. Dordrecht.: Kluwer Academic Publishers, 1993, pp. 543–554.
- [9] Z. Jin and N. Noda, "Crack-tip singular fields in nonhomogeneous materials," *J. Appl. Mech.*, vol. 61, pp. 738–739, 1994.
- [10] E. F and B. H. Wu, "Crack problems in fgm layers under thermal stresses," *Journal of Thermal Stresses*, vol. 12, pp. 237–265, 1996.
- [11] Z. H. Jin and R. C. Batra, "Stress intensity relaxation at the tip of an edge crack in a functionally graded materials subjected to a thermal shock,," *Journal of Thermal Stresses*, vol. 19, pp. 317–339, vol. 19, pp. 317–339, 1996.
- [12] K. Kokini and B. D. Choules, "Surface thermal fracture of functionally graded ceramic coatings: effect of architecture and materials,," *Composite Engineering*, vol. 5, pp. 865–877, 1995.
- [13] K. Kokini and M. Case, "Initiation of surface and interface edge cracks in functionally graded ceramic thermal barrier coatings," *ASME Journal of Engineering Materials and Technology*, vol. 119, pp. 148–152, 1997.
- [14] N. Noda, "Thermal stress intensity for functionally graded plate with an edge crack," *Journal of Thermal Stresses*, vol. 20, pp. 373–387, 1997.

- [15] Z. H. Jin and G. H. Paulino, “Transient thermal stress analysis of an edge crack in a functionally graded materials,,” *International Journal of Fracture*, vol. 107, pp. 73–98, 2001.
- [16] G. H. Walters, M. C. Paulino and J. R. H. Dodds, “Stress-intensity factors for surface cracks in functionally graded materials under mode-i thermomechanical loading,” *International Journal of Solids and Structures*, vol. 41, pp. 1081–1118, 2004.
- [17] R. Jain, N. Chona and A. Shukla, “Asymptotic stress fields for thermomechanically loaded cracks in fgmsn,” *Journal of ASTM International*, vol. 3(7), 2006.
- [18] L. B. Freund, *Dynamic Fracture Mechanics, first ed.* Cambridge Press, 1990.
- [19] G. R. Irwin, “Series representation of the stress field around constant speed cracks,” university of Maryland Lecture Notes.
- [20] A. Shukla and N. Jain, “Dynamic damage growth in particle reinforced graded materials,” *International Journal of Impact Engineering*, vol. 30, p. 777803, 2004.
- [21] G. C. Sih, “Strain-energy-density factor applied to mixed mode crack problems,” *International of Journal of fracture*, vol. 10 (3), pp. 305–321, 1974.
- [22] F. Erdogan and G. C. Sih, “On the crack extension in plates under plane loading and transverse shear,” *Journal of Basic Engineering*, vol. 85, pp. 519–527, 1963.
- [23] E. H. Yoffe, “The moving griffith crack,,” *Philosophical Magazine*, vol. 42, pp. 739–750, 1952.
- [24] D. Broek, *Elementary engineering fracture mechanics.* Martinus Nishoff Publishers, 1978.

CHAPTER 4

Dynamic Constitutive Behavior of Ti/TiB FGM under Thermo-Mechanical Loading

4.1 Abstract

An experimental investigation is conducted to evaluate the thermo-mechanical constitutive behavior of a functionally graded material (FGM) under dynamic loading. Cylindrical specimens are machined from titanium / titanium monoboride (Ti/TiB) layered FGM plate using electrical discharge machining (EDM). A Split Hopkinson Pressure Bar (SHPB) apparatus with infrared spot heaters is used to investigate the effect of temperature on mechanical response of the FGM material. A series of experiments are conducted at different temperatures and the stress strain relation for different temperatures is obtained. The material showed high thermal softening at elevated temperature resulting in a reduction in compressive strength and an increase in failure strain.

4.2 Introduction

FGMs are materials, which have continuously or discretely varying mechanical and thermal properties in a specific direction. Ideally, by grading the composition from one surface to another, it is possible to create a material suitable for a particular application. This type of material was first proposed in Japan in 1987 for space access vehicles that can operate reliably in combined thermal and mechanical loadings. Typically, FGMs are made of a metal and a ceramic as opposite faces with the intermediate zones consisting of varying volume fractions of constituents. Titanium / titanium monoboride (Ti/TiB) is one of the FGM which is currently in use. This material consists of the desirable properties of ceramic, such as hardness, corrosion resistance, and high melting temperature, without los-

ing the required properties of metallic titanium, such as good fracture toughness, machinability and weldability.

For efficient design of structures using FGM materials a fundamental understanding of the properties of FGM materials at different loading conditions is required. To date research on FGM materials has focused mostly on quasi-static problems with very few studies in the dynamic regime. Also, most of the mechanics studies relate to crack problems. Delale and Erdogan [1], Eischen [2] and Jin and Noda [3] solved crack problems for non-homogeneous materials under quasi-static mechanical loading. All these investigations concluded that the inverse-square root singularity at the crack is not affected by nonhomogeneity. For propagating cracks in FGMs, Parameswaran and Shukla [4] and Chalivendra et al. [5] developed the structure of the first stress invariant and the out of plane displacement. In their study they brought out the effects of nonhomogeneity through an asymptotic analysis. Lee [6] developed nonhomogeneity specific terms for individual stress and displacement components using displacement potentials. Recently, Shukla and Jain [7] and Chalivendra and Shukla [8] developed transient field equations for cracks propagating at arbitrary velocities. Chalivendra [9] developed an asymptotic analysis of the transient out of plane displacement fields for a curved crack propagating at arbitrary velocity in FGMs. A review paper by Shukla et al. [10] presents a comprehensive summary of dynamic fracture studies in FGM's.

There are few studies related to the stress and displacement fields due to applied loads in graded materials, For instance Wang et al. [11] present the solution for displacements and stresses in an FGM subjected to a vertical point load in a continuously inhomogeneous transversely isotropic half-space with Young's and shear moduli varying exponentially with depth. Horgan and Chan [12] investigate the effects of material inhomogeneity on the response of linearly elastic isotropic

hollow circular cylinders under uniform internal or external pressure. Li et al. [13] examined the mechanical behavior of layered plates made of metal-ceramic composites with the volume fraction of ceramic reinforcement varying through thickness direction under impulse loading. Chi and Chung [14] studies the mechanical behavior of functionally graded material plate under transverse loading.

There are very few studies on the properties of FGM under thermal or thermo-mechanical loading. Jain et al. [15] developed the stress field equations for quasi static cracks under thermo-mechanical loading in FGM's. Praveen and Reddy [16] carried out the nonlinear transient analysis of stress and deflection for a functionally graded ceramic-metal plate under thermal loading by using the finite element method (FEM). They found that the response of the plates with material properties between those of the ceramic and metal is not intermediate to the response of the ceramic and metal plates. Dai et al. [17] also presented thermo-mechanical analysis of deflections under different loadings in FGM plates containing distributed piezoelectric sensors and actuators using element-free Galerkin method.

In this paper an experimental investigation on the dynamic constitutive behavior of Ti/TiB FGM under thermo-mechanical loading is presented. SHPB apparatus with infrared spot heating system is used to investigate the constitutive properties of the FGM at different temperatures. The material exhibited thermal softening at higher temperatures, which results in a decrease in flow stress and an increase in failure strain. The effect of machining conditions on the constitutive behavior is also demonstrated in these experiments.

4.3 Material and Specimen Geometry

The layered (Ti/TiB) functionally graded material used in this study is supplied by BAE Systems in the form 3.175 mm thick plates. Hill et al. [18] have explained the fabrication technique for this material and their procedure is pre-

sented below. Tape cast layer composed of varying mixtures of titanium and titanium diboride powders are placed on top of commercially pure titanium metal plate. The assembled laminate is hot pressed at 1578 K at a pressure of 12.8 MPa. In order to facilitate densification at this temperature, a proprietary sintering aid-containing nickel is added to the starting powders. This material creates a liquid phase at 1215 K that also catalyzes the reaction of titanium and TiB_2 to form TiB with virtually no residual TiB_2 . The resulting FGM is composed of seven layers ranging from pure Ti on one side to 85% TiB on the other [18]. The material used in our studies shows no clear or distinct interface between the layers as shown in Fig. 4.1. Table 4.1 shows the composition and the physical properties of each layer of the FGM as provided by the vendor and [18].

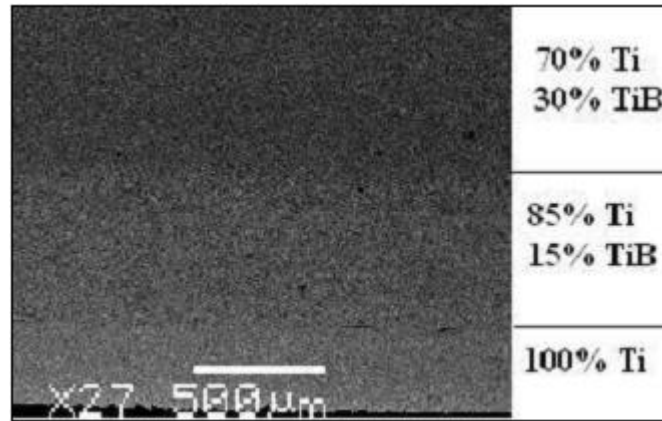


Figure 4.1. Scanning electron microscope image of layer 1 (TiB 0%), layer 2 (TiB 15%) and layer 3 (TiB 30%).

Cylindrical specimens with diameter of 7.62 mm and thickness of 3.175 mm are machined from the FGM plate discussed above. An electrical discharge machining (EDM) technique is used to machine the specimens. The thickness of the specimen is selected from the available FGM plate thickness, where as the diameter of the specimen is selected based on the SHPB theory to assure uniform loading and constant strain rate. The first batch of specimens is machined using wire EDM and

Table 4.1. Composition and elastic properties of Ti/TiB FGM

Layer no.	Vol. %Ti	Vol. %TiB	Thickness (mm)	E (GPa)	ν
1	100	0	0.2032	106	0.340
2	85	15	0.3810	170	0.278
3	70	30	0.3810	227	0.238
4	55	45	0.3810	262	-
5	40	60	0.3810	289	-
6	25	75	0.3810	303	0.152
7	15	85	1.0668	316	0.140

cooled by flooding (Fig. 4.2a). The second batch of specimens is machined with wire EDM with the material fully immersed in coolant (Fig. 4.2b).



Figure 4.2. Wire EDM machined specimens (a) cooled by flooding, (b) cooled by fully immersing in coolant.

4.4 Experimental Procedure

SHPB apparatus with infrared spot heaters is used to investigate the dynamic behavior of Ti/TiB FGM at room and at elevated temperatures. In the present study, the technique used by Lennon and Ramesh, [19] and Shazly et al. [20] is adapted. The schematic description of the SHPB in our lab is shown in Fig. 4.3 and the set-up with infrared (IR) spot heaters is shown in Fig. 4.4. The IR spot heaters have a circular cut shields that can concentrate a heat flux as high as 650

watts per 6.45 square centimeters at the focal point with a 6.35 mm diameter. The bars are made up of 12.7 mm diameter maraging steel having nominal yield strength of 2500 MPa. The striker bar is 101.6 mm long, while the incident and transmitter bars are 1.27 m long. The striker bar is propelled using an air-operated gun. Two strain gages are placed on both the incident and the transmitter bar at equal distance from the bar-specimen assembly. These gages are placed at 1800 to each other to avoid the bending effect on the strain data. The strain signals are recorded using a Vishay 2301A signal-conditioning amplifier that connects with an oscilloscope. The specimen is sandwiched between the two bars. However, during the elevated temperature testing two-carbide inserts are placed between the two bars and the specimen is sandwiched between the inserts. The inserts are used to eliminate the temperature gradient in the bars. The inserts are impedance matched to the bars and hence do not disturb the incident, transmitted and reflected wave profiles. The insert and the bar are placed in a sleeve to assist in alignment. The assembly of the carbide inserts with the specimen and the position of the thermocouple is shown in Fig. 4.5.

For elevated temperature experiment, the specimen is heated up to the desired temperature (usually about 30 °C - 40 °C higher than the test temperature) and the bars are brought manually in contact with the inserts-specimen-inserts assembly. The temperature of the specimen is monitored by 0.127 mm chromel-alumel thermocouple, which is attached into the specimen using high temperature epoxy. Digital camera is used to record the temperature reading and to monitor the sequence of loading on the specimen. The exact temperature on the specimen at which the load applied is found from the record. Boron nitride is used as the lubrication between specimen-inserts and inserts-bar assembly for all elevated tem-

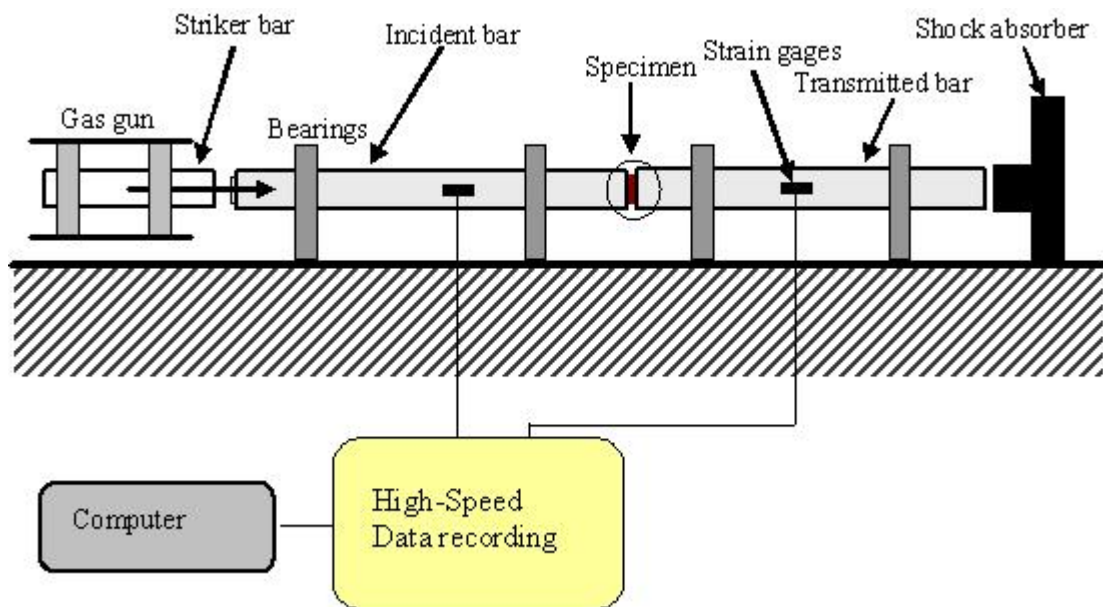


Figure 4.3. Schematic of split Hopkinson pressure bar.

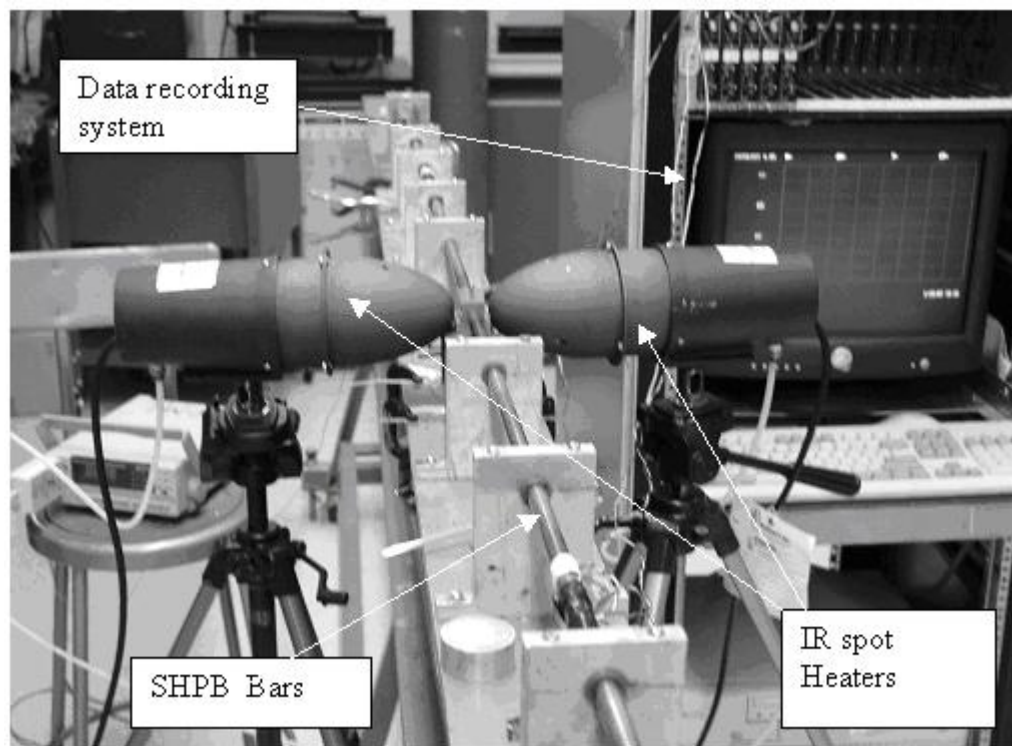


Figure 4.4. Split Hopkinson pressure bar with heater assembly.

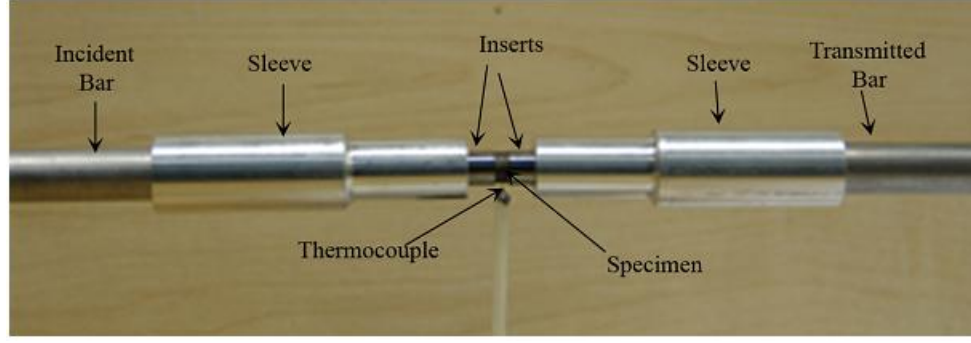


Figure 4.5. Specimen-carbide inserts, thermocouple and sleeves assembly.

perature experiments. In most of the experiments it takes less than two minutes to heat the specimen to the required temperature. It takes less than 10 seconds to bring the bars in contact with the specimen and fire the gun.

Using the above configuration a series of experiments was conducted. For all experiments a clay pulse shaper is placed on the impact face of the incident bar. The pulse shaper smoothes the relative sharp front of the incident stress wave, thus allowing high strain-rate experiments to be conducted at near constant strain rates [20]. This also helps the premature failure of the relatively brittle Ti/TiB FGM, especially during the early part of stress wave loading [20]. A typical strain record from one of the experiment is shown in Fig. 4.6.

4.5 Results and Discussion

4.5.1 Stress-strain Relation

A series of eight experiments is conducted at four different temperatures on specimens machined by wire EDM and cooled by flooding. The stress strain curves obtained from the dynamic experiments with strain rate of about 3 ± 10^3 per sec are shown in Fig. 4.7. The stress-strain curves show a monotonic increase till failure is reached. In all these experiments failure was achieved. The unloading part of the curves after failure is not meaningful. At room temperature a failure stress of 2150 MPa and a failure strain of 1.4 % is observed. As the temperature

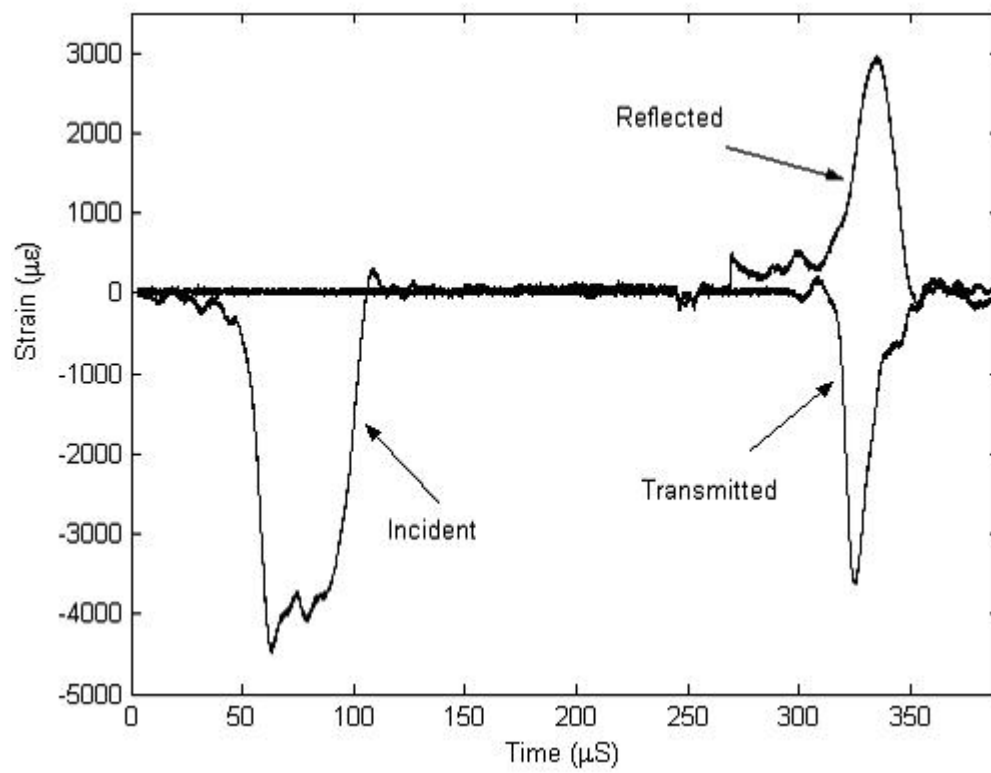


Figure 4.6. Typical strain pulse profiles obtained during an experiment.

increases a reduction in the failure stress and an increase in the failure strain is observed. For example at 600 °C a failure stress of 910 MPa and a failure strain of 2.6 % is observed. In all the room temperature experiments the specimens fail completely leaving small fragments as shown in Fig. 4.8. It was also observed that the fragmentation process even at room temperature was associated with a flash of light. A typical flash of light during failure was recorded using a digital camera and is shown in Fig. 4.9. The occurrence of flash led us to believe that high residual stresses were present in the material and these could have been created during the machining process. The material fabrication technique is believed to create a relatively stress free material. The coloration on the edge of the specimen shown in Fig. 4.2a indicates a heat-affected zone generated during machining by wire EDM.

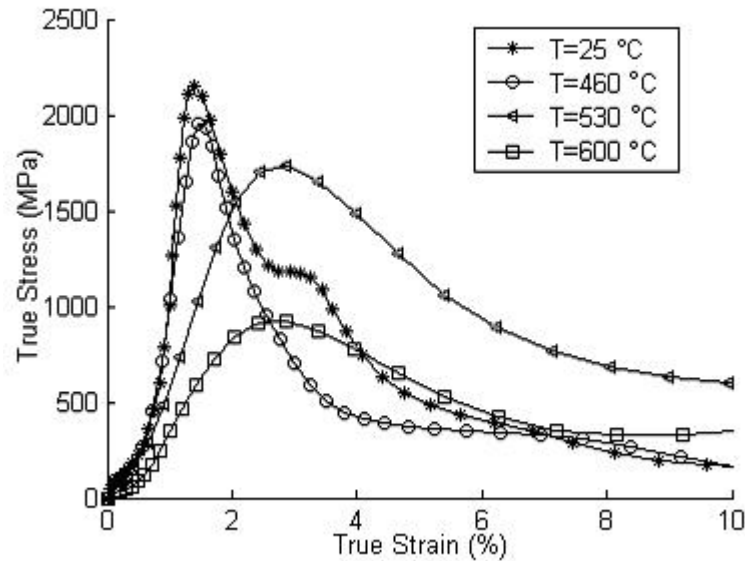


Figure 4.7. True stress-True strain curve as a function of temperature (specimen cooled by flooding during EDM).

To investigate the effect of machining technique on the behavior of the material another batch of sample was machined using EDM with the material fully

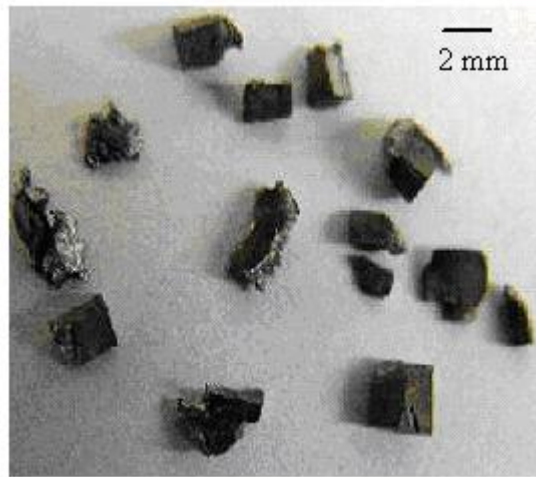


Figure 4.8. A typical failed specimen at room temperature under dynamic loading.

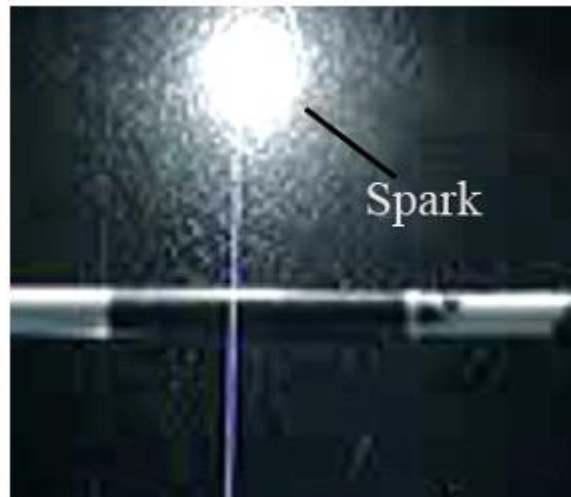


Figure 4.9. A flash of light produced during room temperature dynamic experiment of specimen machined by EDM and cooled by flooding.

immersed in the coolant. A series of eight experiments was again conducted using these specimens at four different temperatures. Figure 4.10 shows the dynamic compressive stress strain curve of the materials at different temperatures. At room temperature a failure stress of 3050 MPa and a failure strain of 1.2 % is obtained. As the temperature increases, the ductility of the material increases and results in an increase in the failure strain and a decrease in failure stress. For example, at the testing temperature of 730 °C a failure stress of 2300 MPa and a failure strain of 2.6 % are observed and at 800 °C a failure stress of 2100 MPa and a failure strain of 3.4 % are obtained. There was no flash of light observed during testing of these specimens. Figure 4.11 shows the effect of temperature on the failure stress

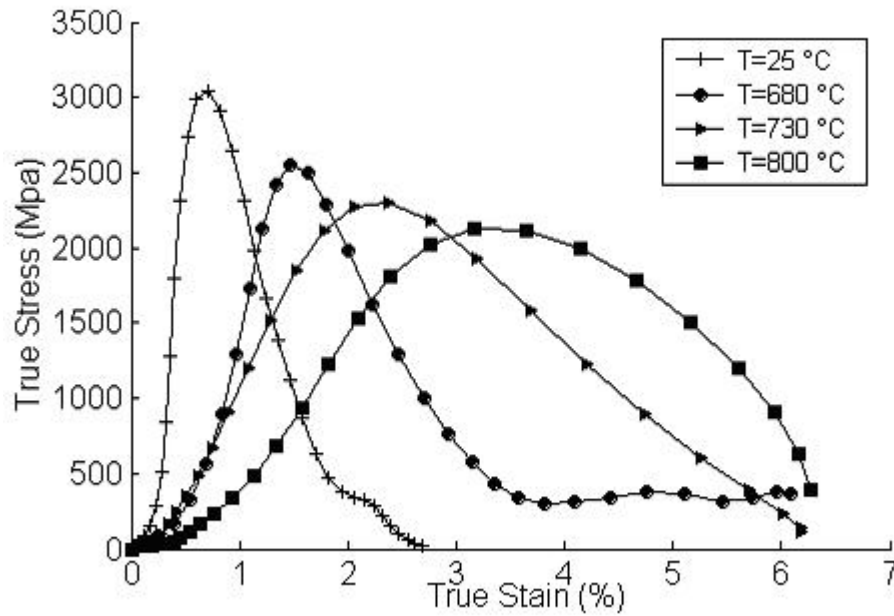


Figure 4.10. True stress - True strain curve as a function of temperature (specimen fully immersed in coolant during EDM).

of Ti/TiB for both the machining cases considered. Both the curves show similar trend that the failure stress decreases as the temperature increase. In the case of specimen machined by EDM and cooled by flooding the failure stress at 600 °C is reduced by 54 % compared with the room temperature failure stress. For fully

immersed cooling EDM specimen the failure stress at 800 °C is reduced by 30 % compared with the room temperature failure stress.

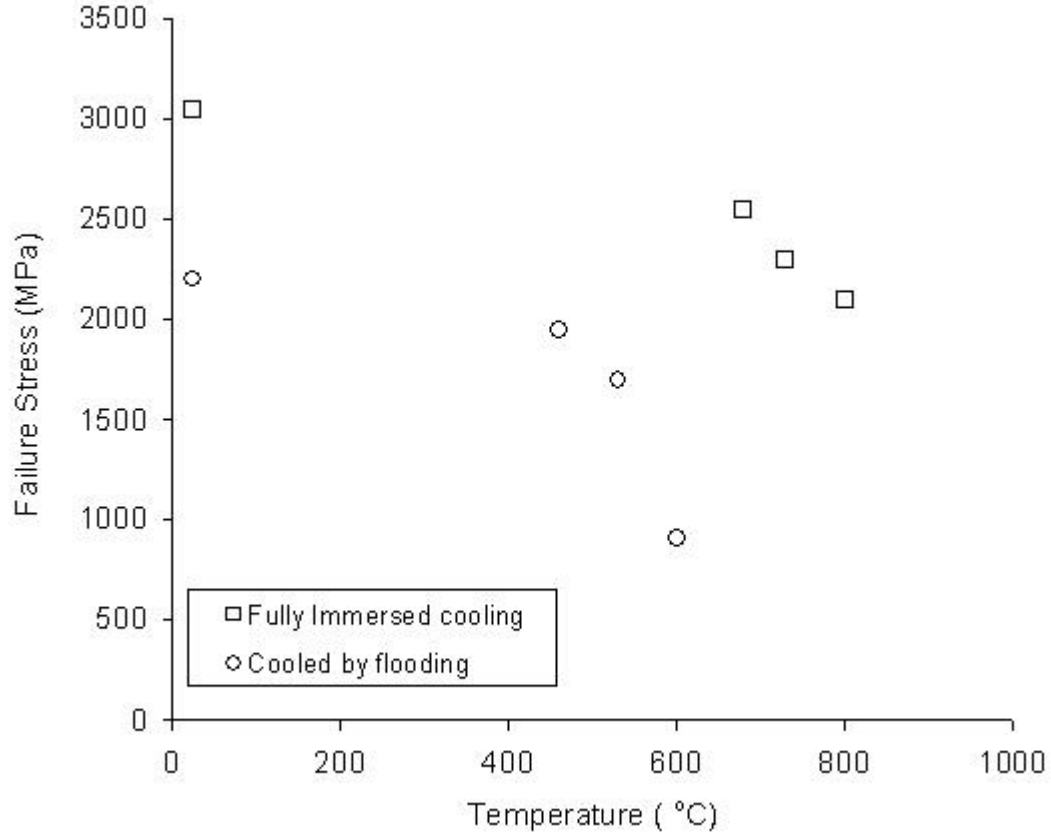


Figure 4.11. Failure stress as a function of temperature.

4.5.2 Post Failure Analysis

Photographs of the fracture specimen were taken for post failure analysis. In all the room temperature experiments the specimens fractured completely, leaving small fragments as shown in Fig. 4.8. However in the case of high temperature experiments the specimens fracture leaving the fragments loosely bonded as shown in Fig. 4.12. This indicates at higher temperature the material is thermally softened and shows a ductile failure. Figure 4.13 shows a micrograph image of fragment from a room temperature experiment. From the figure it is observed that the

cracks run predominantly in the loading direction, which is perpendicular to the interface of layers, indicating the bonding of the interface is strong. Scanning



Figure 4.12. Typical failed specimen during dynamic loading at elevated temperature.

Electron Microscopic (SEM) images were taken of the fractured specimens tested at four different temperatures. Figure 14 shows SEM images of four high temperature specimens taken at a magnification of 1000. The post mortem examination of the failed specimens showed that at room temperature and at $460\text{ }^{\circ}\text{C}$ the specimens fracture by cleavage (Fig. 4.14a and Fig. 4.14b). The fracture surfaces from specimens tested at temperatures of $730\text{ }^{\circ}\text{C}$ and $800\text{ }^{\circ}\text{C}$ are shown in Fig. 4.14c and Fig. 4.14d respectively, and both of them indicate a ductile failure mode. A number of large smooth surfaces observed in Fig. 4.14c and Fig. 4.14d are believed to have been caused by plastic shear [21]. These smooth surfaces are shown at higher magnification (5000 times) in Fig. 4.15a and Fig. 4.15b.

4.6 Summary

The dynamic constitutive behavior of Ti/TiB FGM under thermo-mechanical loading is investigated. SHPB apparatus along with spot heaters is utilized to

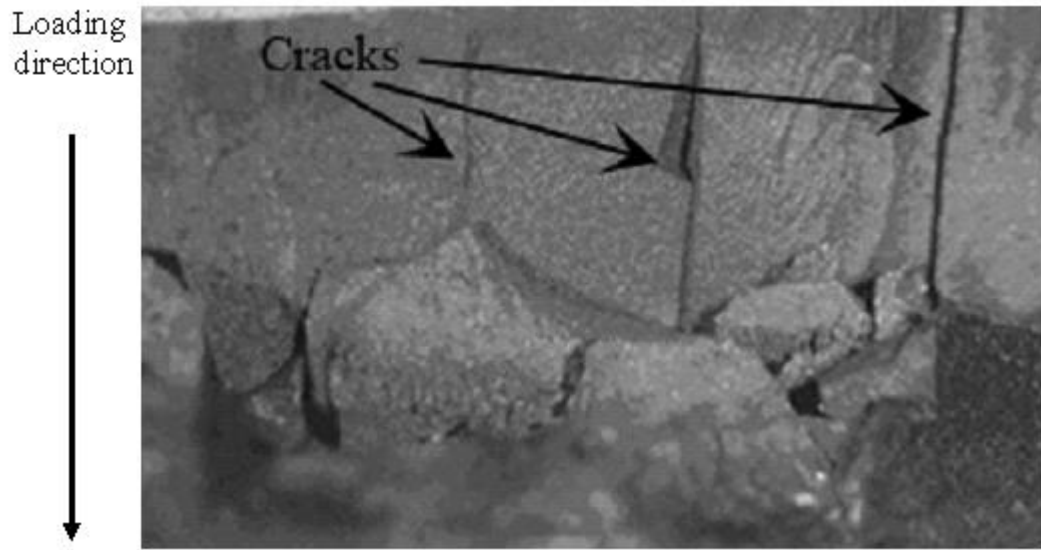
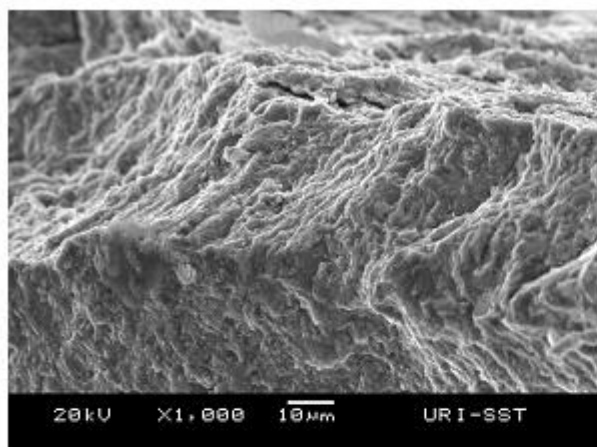


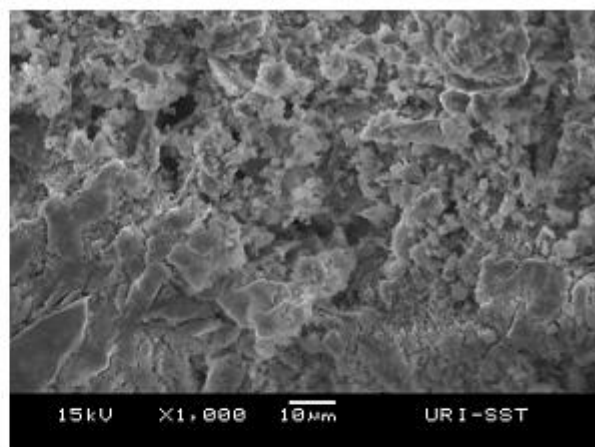
Figure 4.13. Typical fracture surface of Ti/TiB specimen.

study the dynamic constitutive behavior of the material in the temperature range from 25 °C to 800 °C. The findings are summarized and presented as follows:

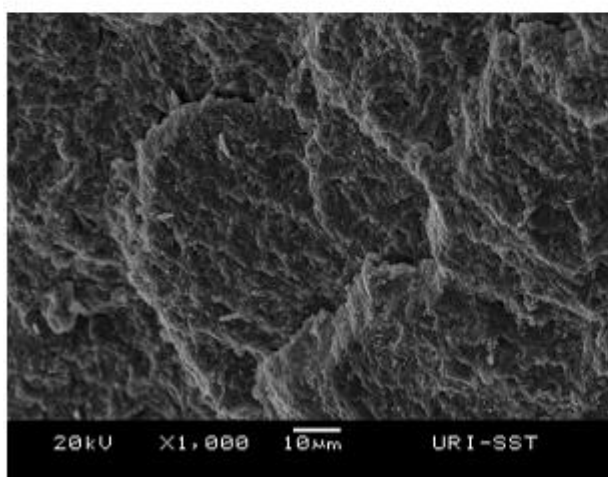
- There are no distinct interfaces between the layers of the FGM material investigated. The bonds between the layers are strong and the cracks run predominantly perpendicular to the layers during fracture.
- Samples cut by wire EDM and cooled by flooding and tested at 25 °C show a failure stress of 2150 MPa and a failure strain of 1.4 %. At 600 °C the same sample type shows a failure stress of 910 MPa and a failure strain of 2.6 %. This represents a 54 % reduction in failure stress and an 85 % increase in failure strain.
- Fully immersed cooled EDM specimens tested at 25 °C show a failure stress of 3050 MPa and a failure strain of 1.25 %. At 800 °C a failure stress of 2100 MPa and a failure strain of 3.4 % is observed. This represents a 30 % reduction in failure stress and a 125 % increase in failure strain.



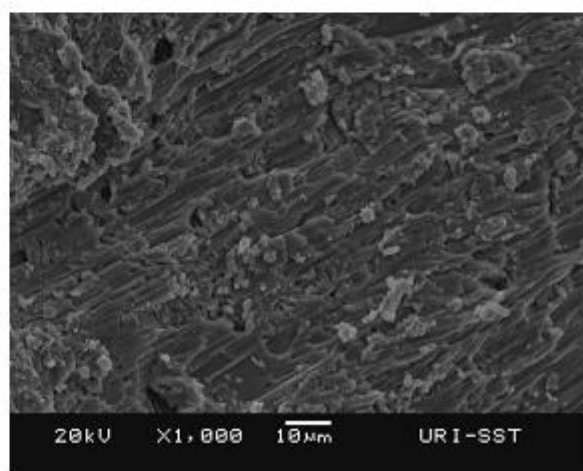
(a) $T=25\text{ }^{\circ}\text{C}$



(b) $T=460\text{ }^{\circ}\text{C}$



(c) $T=730\text{ }^{\circ}\text{C}$



(d) $T=800\text{ }^{\circ}\text{C}$

Figure 4.14. SEM images, at a magnification of 1000, of fracture surface of four different specimens tested at four different temperatures.

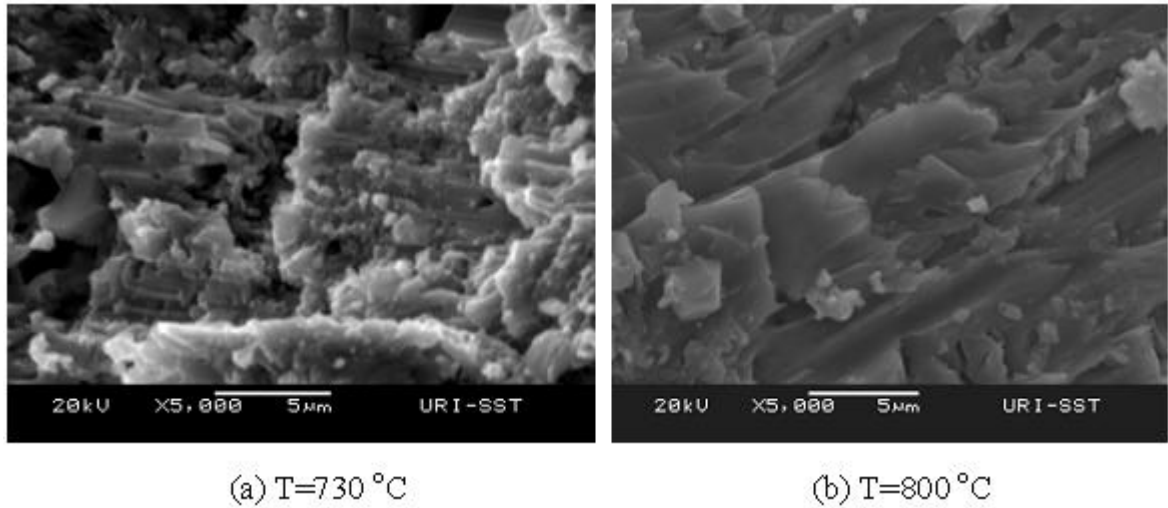


Figure 4.15. SEM images, at a magnification of 5000, of fracture surface of specimens tested at two different temperatures.

- The FGM material showed thermal softening at higher temperature with a decrease in failure stress and an increase in failure strain for both the machining cases considered.
- The specimens machined from fully immersed cooling EDM show superior compressive strength at room and at elevated temperature when compared to sample machined by EDM with flooding. This is due to the presence of residual stresses in the specimens that were not fully immersed for cooling during machining.
- The post mortem SEM images indicate cleavage type failure in specimens tested at $460\text{ }^{\circ}\text{C}$ and below. The failure mechanism changes to ductile at higher temperatures.

List of References

- [1] F. Delale and F. Erdogan, "The crack problem for a nonhomogeneous plane," *J. Appl. Mech.*, vol. 50, p. 6780, 1983.

- [2] J. Eischen, "Fracture of nonhomogeneous materials," *International Journal of Fracture*, vol. 34 (3), p. 322, 1987.
- [3] Z. Jin and N. Noda, "Crack-tip singular fields in nonhomogeneous materials," *J. Appl. Mech.*, vol. 61, pp. 738–739, 1994.
- [4] V. Parameswaran and A. Shukla, "Crack-tip stress fields for dynamic fracture in functionally gradient materials," *Mechanics of Materials*, vol. 31, pp. 579–596, 1999.
- [5] A. Chalivendra, V. B. Shukla and V. Parameswaran, "Dynamic out of plane displacement fields for an inclined crack in graded materials," *Journal of Elasticity*, vol. 69, pp. 99–119, 2002.
- [6] K. H. Lee, "Characteristics of a crack propagating along the gradient in functionally gradient materials," *Int. J. of Solids and Structures*, vol. 41, pp. 2879–2898, 2004.
- [7] A. Shukla and N. Jain, "Dynamic damage growth in particle reinforced graded materials," *International Journal of Impact Engineering*, vol. 30, p. 777803, 2004.
- [8] V. B. Chalivendra and A. Shukla, "Transient elastodynamic crack growth in functionally graded materials," *Journal of Applied Mechanics*, vol. 72, p. 23727, 2005.
- [9] V. B. Chalivendra, "Asymptotic analysis of transient curved crack in functionally graded materials," *International Journal of Solids and Structures*, vol. 44, p. 465479, 2007.
- [10] N. Shukla, A. Jain and R. Chona, "A review of dynamic fracture studies in functionally graded materials," *Strain*, vol. 43, pp. 76–95, 2007.
- [11] C. S. P. E. Wang, C. D. Tzeng and J. J. Lio, "Displacements and stresses due to a vertical point load in an inhomogeneous transversely isotropic half-space," *International Journal of Rock Mechanics and Mining Science*, vol. 40(5), pp. 667–685, 2003.
- [12] C. O. Horgan and A. M. Chan, "The pressurized hollow cylinder or disk problem for functionally graded isotropic linearly elastic materials," *J. Elasticity*, vol. 55, pp. 43–59, 1999.
- [13] K. T. Li, Y. Ramesh and E. Chin, "Dynamic characterization of layered and graded structures under impulsive loading," *International Journal of Solids and Structures*, vol. 38(34-35), pp. 6045–6061, 2001.

- [14] S. H. Chi and Y. L. Chung, “Mechanical behavior of functionally graded material plates under transverse load part i: Analysis,” *Int. J. Solids. Struct.*, vol. 43, pp. 3657–3674, 2006.
- [15] R. Jain, N. Chona and A. Shukla, “Asymptotic stress fields for thermomechanically loaded cracks in fgmsn,” *Journal of ASTM International*, vol. 3(7), 2006.
- [16] G. N. Praveen and J. N. Reddy, “Nonlinear transient thermoelastic analysis of functionally graded ceramic-metal plates,” *Int. J. Solids Structure.*, vol. 35, pp. 4457–4476, 1998.
- [17] G. H. X. Dai, K.Y. Liu and K. Lim, “Thermomechanical analysis of functionally graded material (fgm) plates using element-free galerkin method,” *Computers and Structures*, vol. 83, p. 14871502, 2005.
- [18] R. P. G. M. Z. Hill, M. Carprnter and J. Gibeling, “Fracture resistance testing of monolithic and composite brittle materials,” in *ASTM STP 1409*, 2002.
- [19] A. M. Lennon and K. T. Ramesh, “A technique for measuring the dynamic behavior of materials at high temperatures,” *International Journal of Plasticity*, vol. 14, p. 12791292., 1998.
- [20] V. Shazly, M. Prakash and S. Draper, “Mechanical behavior of gamma-met px under uniaxial loading at elevated temperatures and high strain rates,” *International Journal of Solids and Structures*, vol. 41, pp. 6485–6503, 2004.
- [21] “Metals handbook, fractography and atlas of fractographs, asm vol. 9, eighth edition, 1974.”

CHAPTER 5

Quasi-Static and Dynamic Fracture Initiation Toughness of Ti/TiB Layered Functionally Graded Material under Thermo-Mechanical Loading

5.1 Abstract

Quasi-static and dynamic fracture initiation toughness of Ti/TiB layered Functionally Graded Material (FGM) is investigated using a three point bend specimen. The modified split Hopkinson pressure bar (SHPB) apparatus in conjunction with induction coil heating system is used during elevated temperature dynamic loading experiments. A simple and accurate technique has been developed to identify the time corresponding to the load at which the fracture initiates. A series of experiments are conducted at different temperatures ranging from room temperature to 800 °C, and the effect of temperature and loading rate on the fracture initiation toughness is investigated. The material fracture toughness is found to be sensitive to temperature and the fracture initiation toughness increases as the temperature increases. Furthermore, the fracture initiation toughness is strain rate sensitive and is higher for dynamic loading as compared to quasi-static loading.

5.2 Introduction

An experimental investigation is conducted to research quasi-static and dynamic fracture initiation toughness of Ti/TiB FGM under thermo-mechanical loading. Ti/TiB is a commercially available metal/ceramic FGM that has been proposed for many different applications. The basic idea behind the design of metal/ceramic FGMs is to reduce the problem associated with the low toughness of ceramics. Hence the fracture toughness is the primary and limiting parameter to design structures using metal/ceramic FGMs. Due to this fact, number of researchers have studied theoretically the fracture behavior of FGMs. For example,

Delale and Erdogan [1], Eischen [2] and Jin and Noda [3] solved crack problems for non-homogeneous materials under quasi-static mechanical loading. All these investigations concluded that the inverse-square root singularity at the crack is not affected by non-homogeneity. Similarly, for propagating cracks in FGMs, the theoretical studies concluded that the crack tip fields are similar to that of homogeneous material provided that the FGMs are continuous and piece-wise continuously differentiable [4–6]. Jin and Batra [7] further studied the effects of quasistatic loading conditions, specimen size and metal particle size on the crack growth resistance curve (R-curve) and the residual strength of a ceramic-metal FGM using crack-bridging concept.

On the other hand, there are very limited experimental studies on the fracture behavior of metal/ceramic FGMs. Hill et al. [8] have studied the fracture behavior of Ti/TiB FGM using single-edged-notched bend specimens and reported that the pre-cracking method and residual stress have a significant effect on the measured fracture toughness. The study is limited to room temperature and quasi-static loading. The study by Kidane and Shukla [9] on the constitutive behavior of Ti/TiB FGM confirmed that the material showed thermal softening at higher temperatures and this resulted in a decrease in failure stress and an increase in failure strain. But the fracture behavior of Ti/TiB under dynamic loading and at elevated temperatures has not been investigated yet.

The purpose of this experimental study is to fill that gap and investigate the effect of temperature and loading rate on the fracture initiation toughness of this material. An experimental investigation on the fracture initiation toughness of Ti/TiB under quasi-static and dynamic loading is conducted at different temperatures ranging from room temperature to 800 °C. The fracture initiation toughness is found to be temperature dependant, increases with raise in temperature, and

Table 5.1. Composition and elastic properties of Ti/TiB FGM

Layer no.	Vol. %Ti	Vol. %TiB	Thickness (mm)	E (GPa)	ν
1	100	0	0.4064	106	0.340
2	85	15	0.7620	170	0.278
3	70	30	0.7620	227	0.238
4	55	45	0.7620	262	-
5	40	60	0.7620	289	-
6	25	75	0.7620	303	0.152
7	15	85	2.1336	316	0.140

also loading rate dependant, higher at dynamic loading compared with quasi-static loading.

5.3 Material and Specimen Geometry

The material used in this experimental study is a Ti/TiB FGM layered plate supplied by BAE systems. It is a 7.36 mm thick pate with seven layers, no clear or distinct interface between them, ranging from pure Ti on one side to 85 % TiB on the other. The details of the fabrication technique and material properties can be found in the literature [8, 9]. The thickness and the properties of each layer are listed in Table 5.1.

Two different batches of three point bend specimens are machined, from the FGM plate discussed above, using an electrical discharge machining (EDM) technique. The first batch of specimens is machined in such a way that the gradation is in the thickness direction, i.e. the crack is perpendicular to the gradation (Fig. 5.1a). The second batch of specimens is machined in such a way that the crack is along the gradation direction (Fig. 5.1b). The thickness of the specimen is selected from the available FGM plate thicknesses, where as the other dimensions are determined based on ASTM Test Methods for Measurement of Fracture Toughness (E1820-96). Due to the brittle nature of this material no fatigue pre-crack was made. However, the crack was made using EDM wire of 0.0508 mm,

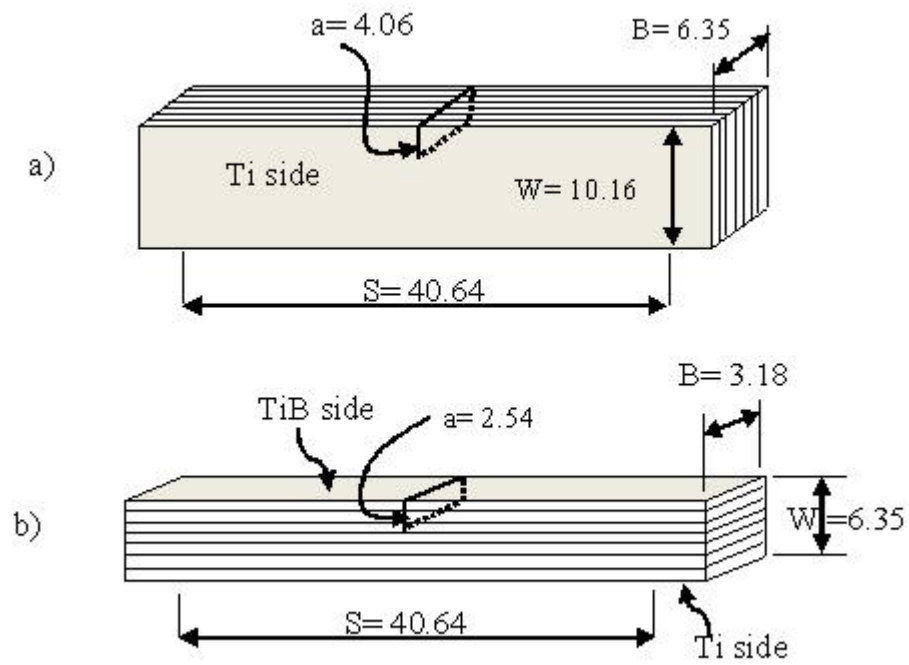


Figure 5.1. Three point bend specimen (a) FGM graded in the thickness direction (b) FGM graded in the crack direction (all dimensions are in mm)

resulting in a very small notch root radius.

5.4 Experimental Procedure

5.4.1 Quasi-static Fracture Initiation Toughness

The quasi-static fracture initiation toughness is investigated using a three-point bending experiment. The three point bend specimen is placed between the loading bar and supporting block as shown in Fig. 5.2. The experiment is conducted at different temperatures ranging from 25 °C to 800 °C. A tungsten carbide loading tip is used to eliminate the deformation of the loading bar at higher temperature. The specimen is heated to the desired temperature using an induction heating system. The induction heater has a precise controller that enables us to control the temperature to the desired value. The experiment is conducted under a fixed loading rate of 1mm/min at room temperature. To avoid the creep effect during elevated temperature, a loading rate of 5 mm/min is used.

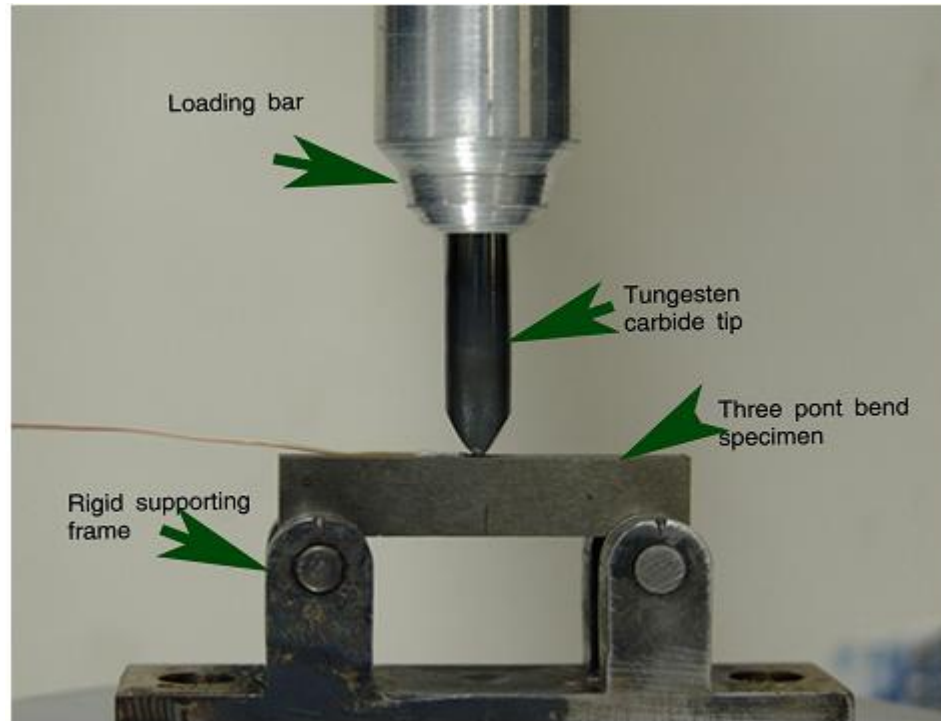


Figure 5.2. Quasi-static three point bend experimental setup.

5.4.2 Dynamic Fracture Initiation Toughness

A modified split Hopkinson pressure bar (SHPB) apparatus with induction heating system is used to investigate the dynamic fracture initiation toughness of Ti/TiB FGM. The modified SHPB is a well-developed method to study the dynamic fracture initiation toughness of engineering materials. The principle of modified SHPB is presented in brief and the detailed theory can be found in the literature [10, 11]. The schematic of the modified SHPB apparatus is shown in Fig. 5.3. As displayed in the figure, the apparatus mainly consists of an incident bar, striker bar and pressure gun. To reduce the impedance mismatch between the specimen and the incident bar, a T6061 aluminum material is used for the incident bar. To generate a well-defined loading pulse, the same material that is used for the incident bar is used for the striker bar. Two semiconductor strain gages are attached in the middle of the incident bar diametrically opposite to one another. The semiconductor strain gages are about 75 times more sensitive than the foil type strain gages and are preferred to capture very small strain signals.

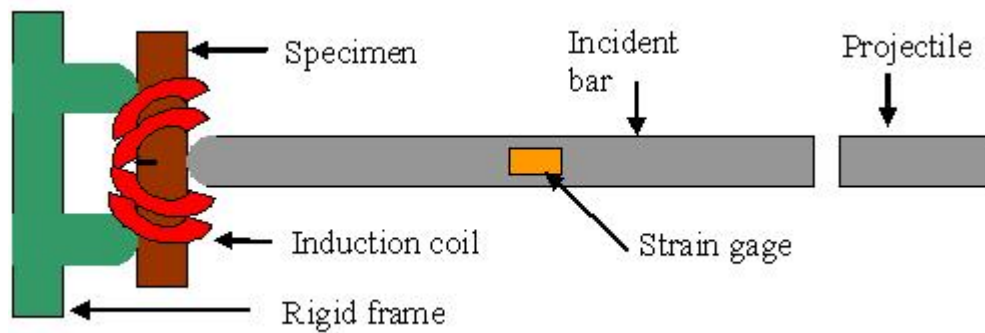


Figure 5.3. Schematic representation of modified SHPB apparatus with induction heater.

During loading, the specimen is sandwiched between the incident bar and the rigid frame. For an elevated temperature experiment, the bar is first kept apart and the specimen is heated to the desired temperature (usually about 20 °C to 50

$^{\circ}C$ higher than the test temperature) and later the bar is brought manually into contact with the specimen. The temperature of the specimen is monitored by 0.127 mm chromel-alumel thermocouple, which is spot welded onto the specimen. Once the specimen is in contact with the incident bar, the striker bar is propelled towards the incident bar using an air-operated gun. The impact generates a compressive stress wave in the bar which propagates toward the bar/specimen interface. When the wave reaches the specimen, some of the wave is reflected back and part of the wave is transmitted into the specimen. The incident and reflected strain signals are recorded using a Vishay 2301A signal-conditioning amplifier that is connected with an oscilloscope. The load history at the specimen/bar interface is obtained from the recorded strain data using a one dimensional elastic wave theory [10] given by Eq. 5.1.

$$F(t) = (\epsilon_i(t) + \epsilon_r(t)) EA \quad (5.1)$$

where F is the force, ϵ_i and ϵ_r are the incident and reflected strain pulses, E is the Young's modulus, and A is the cross sectional area of the bar.

In order to avoid the transient effects all dynamic experiments are conducted at a striker speed of 1.0 m/sec. When the time of fracture is sufficiently long, the dynamic stress intensity factor can be calculated from the input load as

$$K_I(t) = \frac{F(t)}{B\sqrt{W}} f\left(\frac{a}{W}\right) \quad (5.2)$$

where K_I is the stress intensity factor, B the specimen thickness, W the specimen width, a the initial crack length and $f(a/W)$ is a geometric factor.

The dynamic fracture initiation toughness (K_{ID}) corresponds to the stress intensity factor at the time of crack initiation. i.e. $K_{ID} = K_I(t_{initiation})$.

One of the challenges in the dynamic fracture initiation toughness experiment is to find a method to accurately determine the crack initiation time. Researchers [12–14] used a strain gage to detect the fracture-initiation time at high loading

rate. Usually the gage is placed on the specimen near the crack tip, and when the fracture initiates, the sudden decrease of strain as a function of time corresponds to the crack initiation point. However, the time that the stress wave travels from the crack tip to the strain gage has to be deducted to obtain the correct crack initiation time. This is difficult in the case of materials with unknown stress wave speed. In the present study, a simple and accurate technique is developed to identify the time corresponding to the load required to initiate the crack. A conductive silver paint is placed ahead of the crack tip on a non-conductive substrate, in the direction of expected crack path. The paint is connected to a strain gage which is attached to the loading bar at the same position where the two semiconductor strain gages are located. When the fracture initiates, the sudden jump in the strain signal indicates the crack initiation time, and this is used later to determine the load associated with the fracture initiation time.

A schematic of strain signals from the semiconductor strain gages and the foil type strain gage connected with the silver paint are shown in Fig. 5.4. In the figure, t_1 is the duration of the incident wave, t_2 is the duration of the reflected wave, t_3 is the time required by the wave to travel from the location of the strain gages to the bar-specimen interface and to return back to the location of the strain gages and t is the total time duration starting from the wave passing the location of the strain gages until the fracture occurs (silver paint broken). Hence, $t_3/2$ is the time required by the wave to travel from the location of the strain gages to the bar-specimen interface. Therefore, $t_i = t - t_3/2$ is the time required to initiate the fracture. Also the location of this time (t_i) in the incident and reflected signal is shown by the dotted.

Using the above configuration a series of experiments are conducted at different temperatures. For all experiments a pulse shaper is placed on the impact

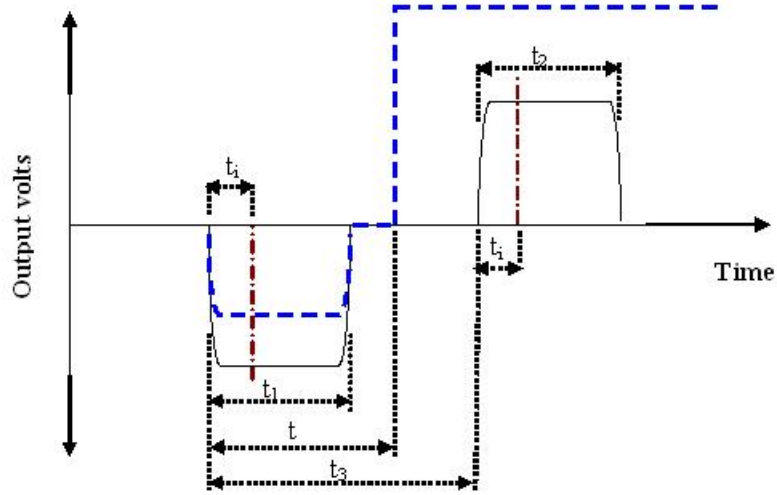


Figure 5.4. A schematic of strain signals from the semiconductor strain gages and the foil type strain gage connected with silver paint.

face of the incident bar. The pulse shaper smoothes the relative sharp front of the incident stress wave, thus allowing high strain-rate experiments to be conducted at near constant strain rates [9]. This also helps the premature failure of the relatively brittle Ti/TiB FGM, especially during the early part of stress wave loading [9].

5.5 Results and Discussions

5.5.1 Quasi-static Fracture Initiation Toughness of FGM Graded in the Thickness Direction

Fig. 5.5 shows, a typical load history curve for a quasi-static three point bend experiment of FGM graded in the thickness direction. From the plot, it can be seen that there is a clear and well defined peak load at which the crack initiates. The load history shown above represents the integrated structure resistance, not the load in each separate layer. The fracture resistance across the thickness in each layer may vary, as observed by Wadgaonkar and Parameswaran [15]. This phenomenon is also observed from the failed specimen subjected to quasi-static loading shown in Fig. 5.6. As shown in the figure, the fracture topography of the surface is different from one end to the other. The fracture surface near the TiB

rich layer is smooth and the surface near the Ti rich layer is rough. This indicates that, the energy required to fracture the surface is different for the two extreme ends, and the fracture may first start from the TiB rich end and later propagate towards Ti rich side.

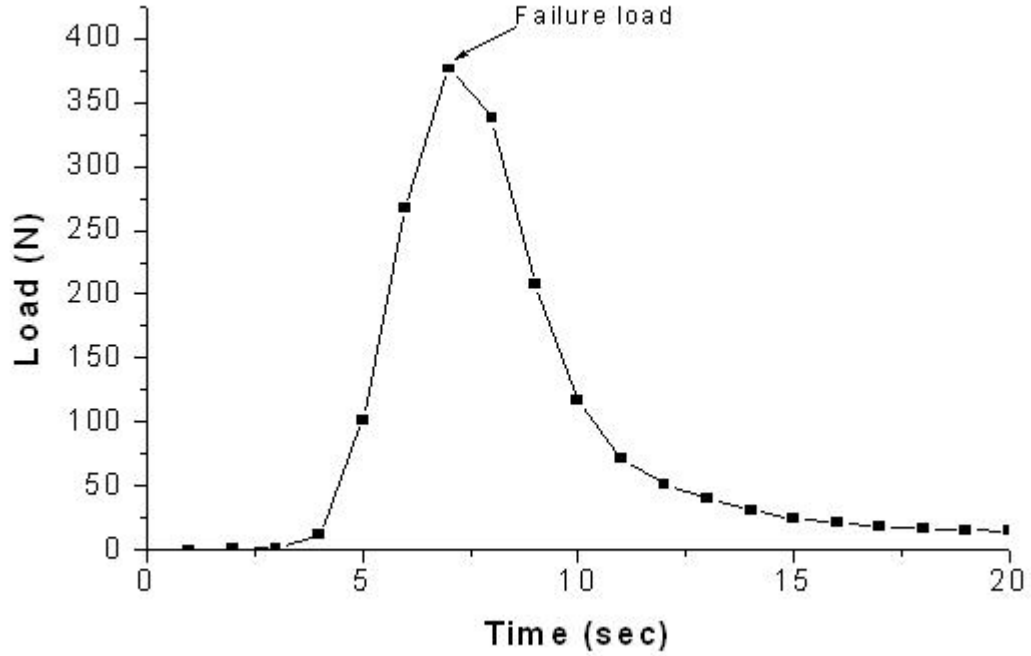


Figure 5.5. Typical load-time plot for FGM graded in the thickness direction under quasi-static loading (25 °C).

However, the intention of the present study is to determine the fracture initiation toughness of the integrated structure, and not the fracture resistance of each layer. Hence, the single load history obtained from the integrated structure is used to calculate the fracture initiation toughness. By following a similar procedure, a series of experiments are conducted, and the fracture initiation toughness at different temperatures is obtained.

Fig. 5.7 shows the quasi-static fracture initiation toughness of FGM graded in the thickness direction as a function of temperature. A total of three experiments are conducted at each temperature and the bars indicate the range of values ob-

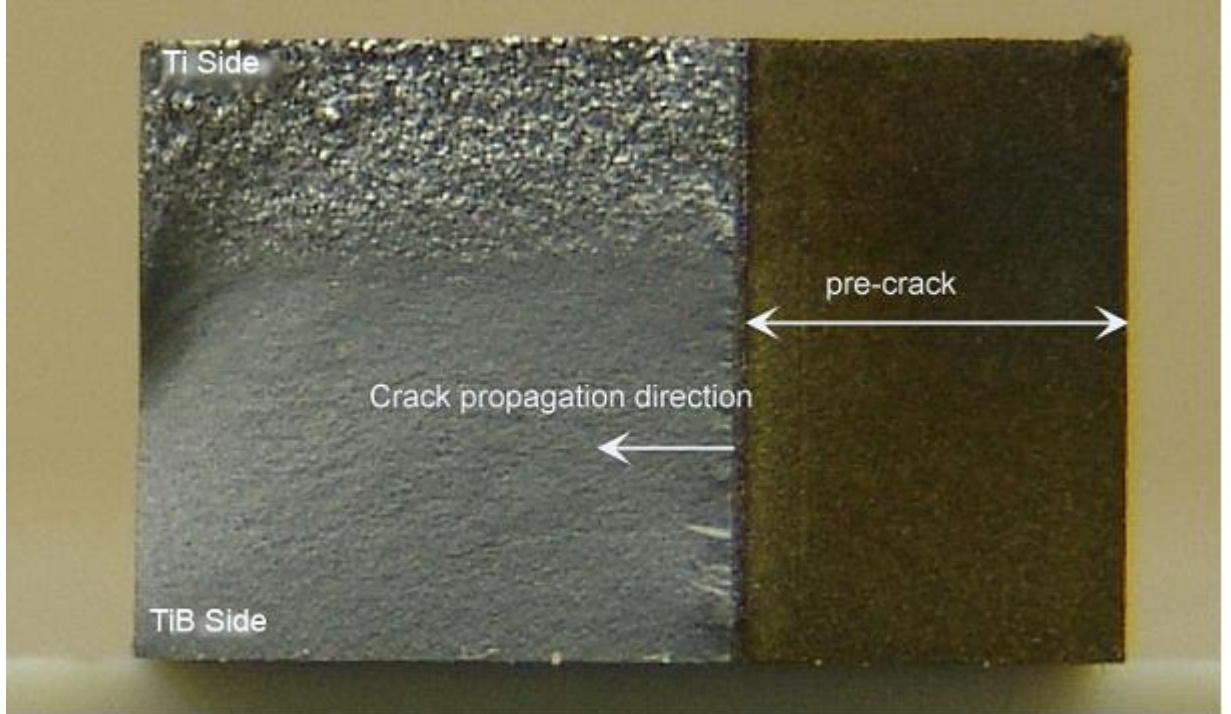


Figure 5.6. Typical failed specimen of FGM graded in thickness direction under quasi-static loading (25 °C).

tained. The room temperature quasi-static fracture initiation toughness is about $4.75 \pm 0.07 \text{ MPa } m^{1/2}$ and the value increase to $10.43 \pm 0.52 \text{ MPa } m^{1/2}$ at 800 °C. The quasi-static fracture initiation toughness increases linearly as the test temperature raises. It can be argued that at elevated temperature the material is thermally softened and this results in an increase in fracture toughness.

5.5.2 Quasi-static Fracture Initiation Toughness of FGM Graded in the Crack Direction

In this experiment the specimen is first pre-cracked to 2.54 mm from TiB rich side, which means up to the middle of 75 % TiB and 25 % Ti layer, and the crack is allowed to run towards Ti rich end as shown in Fig. 5.8. The crack is chosen to start from the TiB side, as the fracture resistance of TiB is much lower than that of Ti. Fig. 5.9 shows a typical load history curve for a quasi-static fracture experiment at 25 °C. The figure displays a definite and clear peak load followed

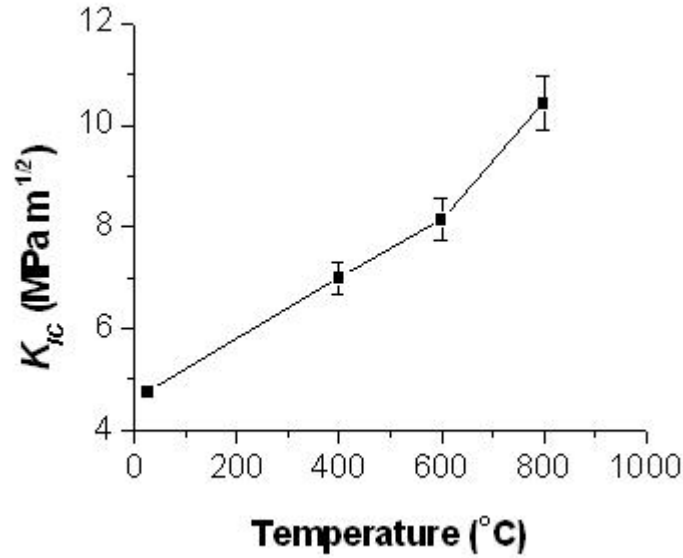


Figure 5.7. Effect of temperature on the fracture initiation toughness of FGM graded in the thickness direction under quasi-static loading.

by yet another peak load that occurred after the decline of the first. The first peak load corresponds to the load required to initiate the crack, in 75 % TiB and 25 % Ti layer, and the second peak load corresponds to the load required to crack the next layer, i.e. 60 % TiB and 40 % Ti, which is 0.35 mm away from the initial position of crack tip. Fig. 5.10 shows a typical fracture surface, investigated at room temperature. From the figure it is clear where the second peak load occurred. Furthermore, it is observed the fracture surface near to the TiB rich layer is smooth and is rough towards the Ti rich side. Even though the crack has already started at the first peak load, still more energy is required for the crack to propagate to the next layer.

Fig. 5.11 shows a typical load time curve for a quasi-static fracture experiment at elevated temperatures. Unlike the room temperature experiment, there is no repeated peak load, the load decreased slowly after it reached the critical value. From the load history it can be clearly seen that the temperature reduces the

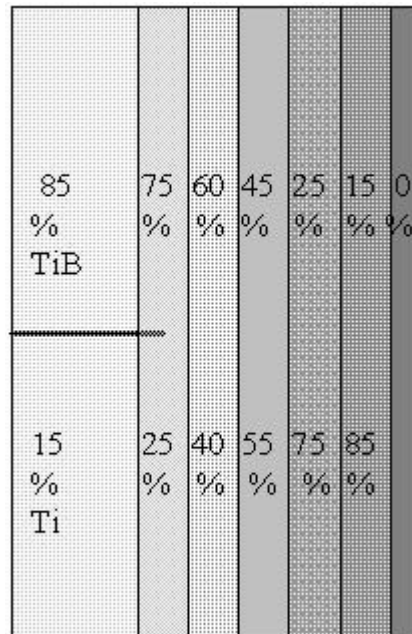


Figure 5.8. A schematic representation of crack on FGM specimen graded in the crack direction.

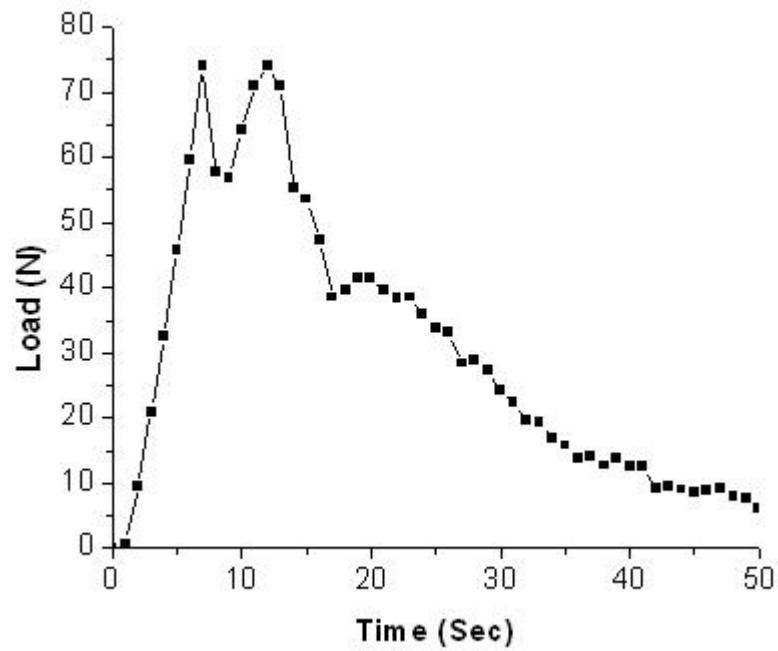


Figure 5.9. Typical load-time plot for FGM graded in the crack direction under quasi-static and room temperature loading (25 °C).

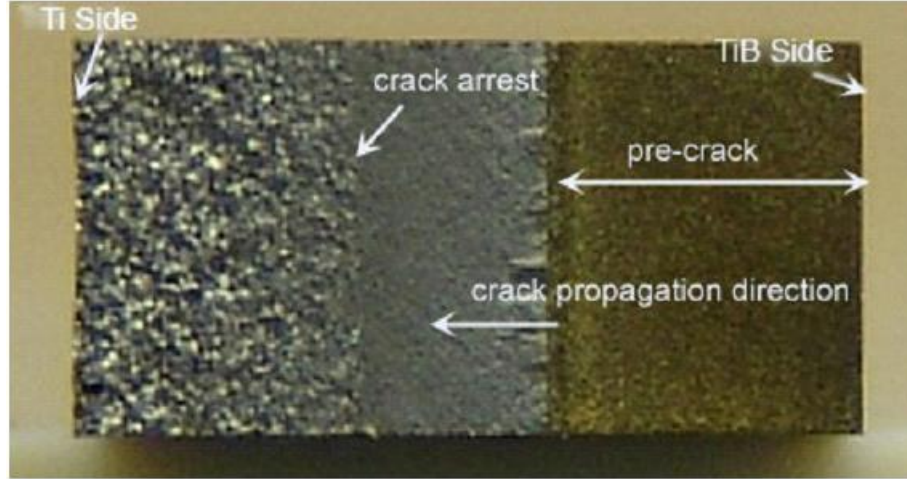


Figure 5.10. Typical failed specimen of FGM graded in the crack direction under quasi-static loading (25 °C).

brittleness of the material. For all the cases considered, the first peak load is used to calculate the fracture initiation toughness.

Fig. 5.12 shows the fracture initiation toughness as a function of temperature for FGM graded in the crack direction. A total of three experiments are conducted at each temperature and the bars indicate the range of values obtained. The quasi-static fracture initiation toughness at room temperature (25 °C) is about $3.75 \pm 0.05 \text{ MPa } m^{1/2}$ and increases to about $9.55 \pm 0.44 \text{ MPa } m^{1/2}$ at 800 °C. The trend on the quasi-static fracture initiation toughness of FGM graded in the crack direction is same as that of FGM graded in the thickness direction. With both, the fracture initiation toughness increases consistently with an increase in temperature.

5.5.3 Dynamic Fracture Initiation Toughness of FGM Graded in the Thickness Direction

A typical strain record from one of the dynamic experiments of FGM graded in the thickness direction is shown in Fig. 5.13. The sudden jump in strain signal from the strain gage, which was attached to the conductive silver paint, indicates

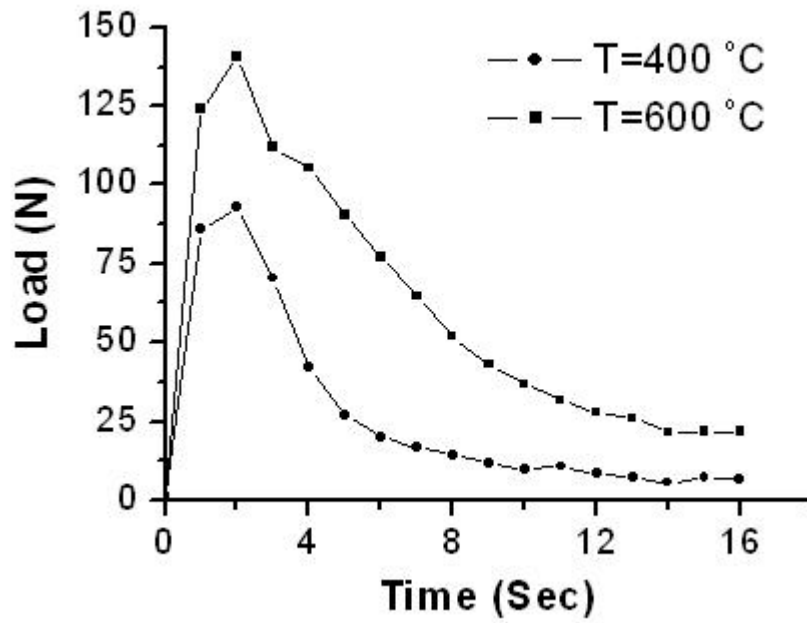


Figure 5.11. Typical load - time plot for FGM graded in the crack direction under quasi-static elevated temperature loading.

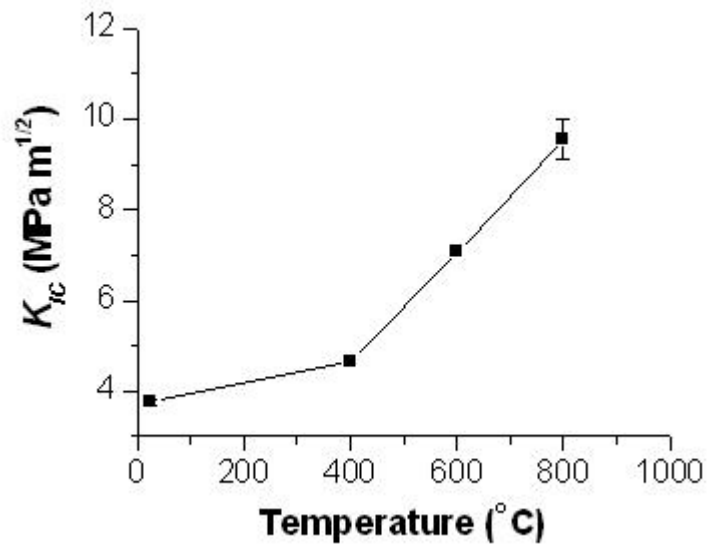


Figure 5.12. Effect of temperature on the fracture initiation toughness of FGM graded in the crack direction under quasi-static loading.

the crack initiation time. As shown in the figure, the crack initiates 140 μs after the stress wave enters the specimen and this allows the wave to reverberate sufficiently to create an equilibrium loading condition before the crack initiates. Fig. 5.14

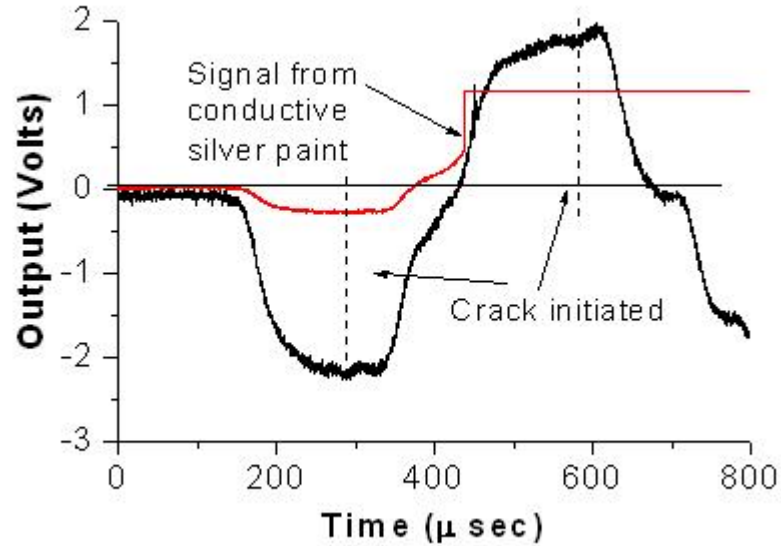


Figure 5.13. Typical incident and reflected strain plot of FGM graded in the thickness direction subject to room temperature dynamic loading.

shows the dynamic fracture initiation toughness of FGM graded in the thickness direction as a function of temperature. A total of three experiments are conducted at each temperature and the bars indicate the range of values obtained. At room temperature the dynamic fracture initiation toughness is about $5.2 \pm 0.20 \text{ MPa } m^{1/2}$ and about $11.96 \pm 0.77 \text{ MPa } m^{1/2}$ at $800^\circ C$. It is also observed that the fracture initiation toughness increases linearly with increase in temperature. This can be attributed to the fact that, at higher temperature the material is softened and results in increased fracture toughness. This phenomenon agrees with the one observed by the authors in their previous study during the investigation of the dynamic constitutive behavior of this material [9]. Fig. 5.15 shows the SEM images of typical fracture surface of FGM graded in the thickness direction subjected to

dynamic loading at different temperatures. The images are taken near the crack tip at the Ti rich end. It can be seen that the fracture surface becomes more ductile as the temperature increases.

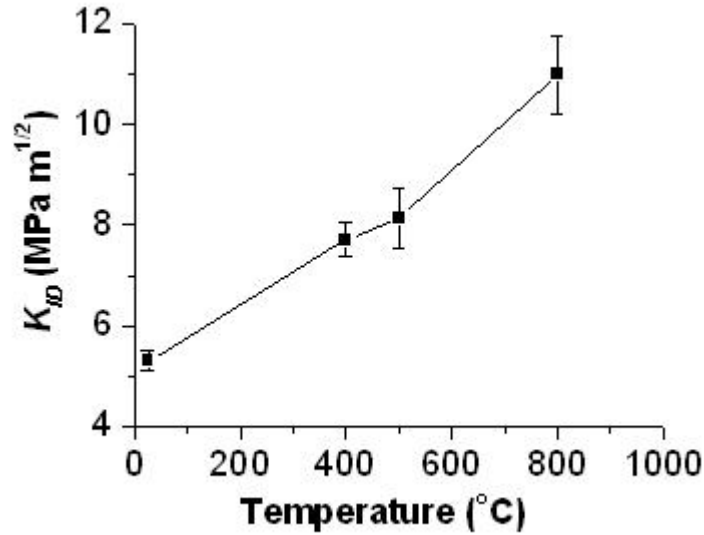
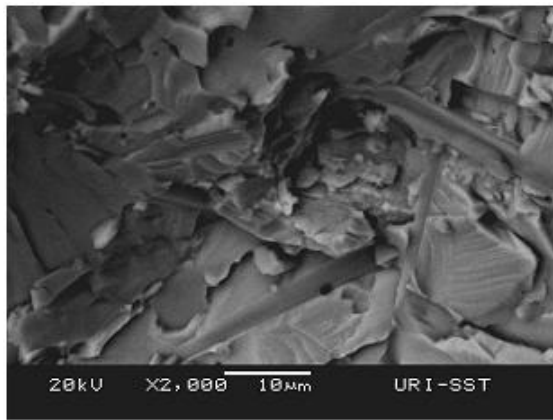


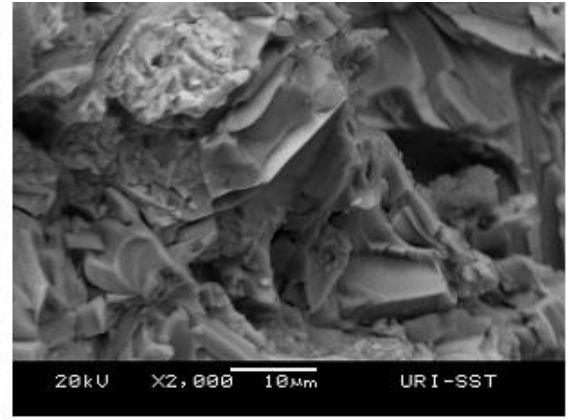
Figure 5.14. Effect of temperature on the fracture initiation toughness of FGM graded in the thickness direction under dynamic loading.

5.5.4 Dynamic Fracture Initiation Toughness of FGM Graded in the Crack Direction

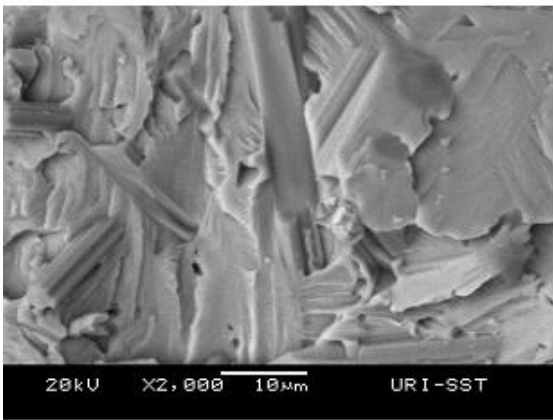
A typical strain signal obtained from the dynamic fracture experiment for FGM graded in the crack direction is shown in Fig. 5.16. As discussed in the previous section, the conductive silver paint is used to identify the load which corresponds to the fracture initiation time. The fracture initiates after 60 μs and this allowed the wave to reverberate about 20 times in the specimen before crack initiates. This is sufficient to create an equilibrium loading condition before the crack initiates. High speed digital imaging is also used to study the contact history of the bar and specimen and the fracture process. Fig. 5.17 shows typical high speed images taken during a dynamic fracture experiment of FGM graded in



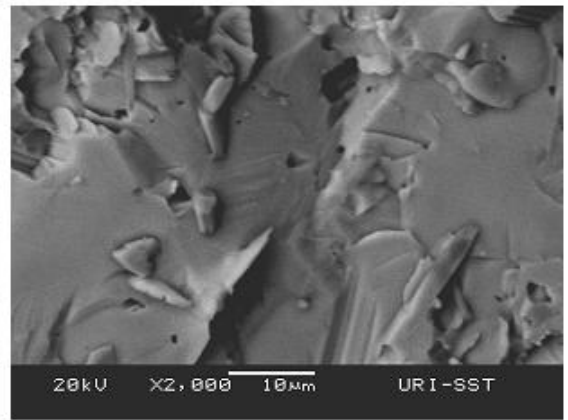
a) $T = 25\text{ }^{\circ}\text{C}$



b) $T = 400\text{ }^{\circ}\text{C}$



c) $T = 600\text{ }^{\circ}\text{C}$



d) $T = 800\text{ }^{\circ}\text{C}$

Figure 5.15. SEM images of typical fracture surface of FGM graded in the thickness direction subjected to dynamic loading at different temperatures.

the crack direction at a temperature of 800 °C. It can be clearly seen that the bar is always in contact with the specimen during the failure process. Hence, the use of load corresponding to the crack initiation time is justified in the calculation of calculate the dynamic fracture initiation toughness.

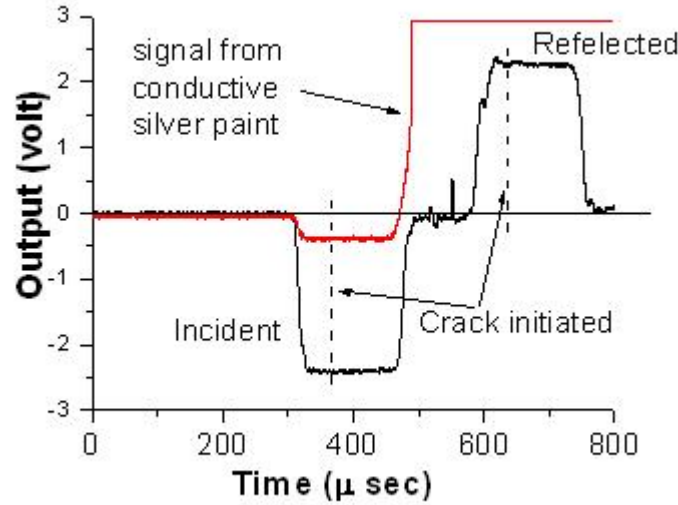


Figure 5.16. Typical strain signal obtained from the dynamic fracture experiments of FGM graded in the crack direction subjected to dynamic loading.

Fig. 5.18 shows the dynamic fracture initiation toughness as a function of temperature for FGM along the crack direction. A total of three experiments are conducted at each temperature and the bars indicate the range of values obtained. A similar trend as observed in the previous batch of specimen is seen here, the dynamic fracture initiation toughness increases with increase in temperature. At room temperature the dynamic fracture initiation toughness is about 5.0 ± 0.07 MPa $m^{1/2}$ and increases to 10.55 ± 0.85 MPa $m^{1/2}$ at 800 °C. SEM images of the micro structure at different temperatures at the crack tip (75 % TiB, 25 % Ti) are shown in Fig. 5.19. Some evidence of stretching associated with material softening appears at high temperatures.

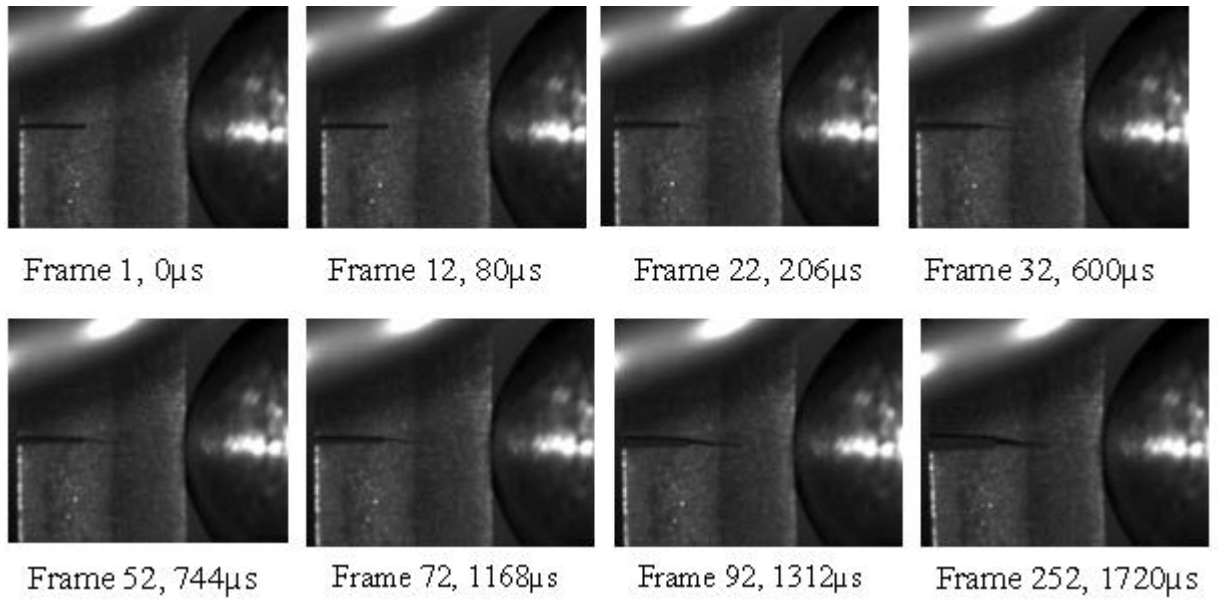


Figure 5.17. Typical high speed digital images of FGM graded in the crack direction subjected to dynamic loading at 800 °C.

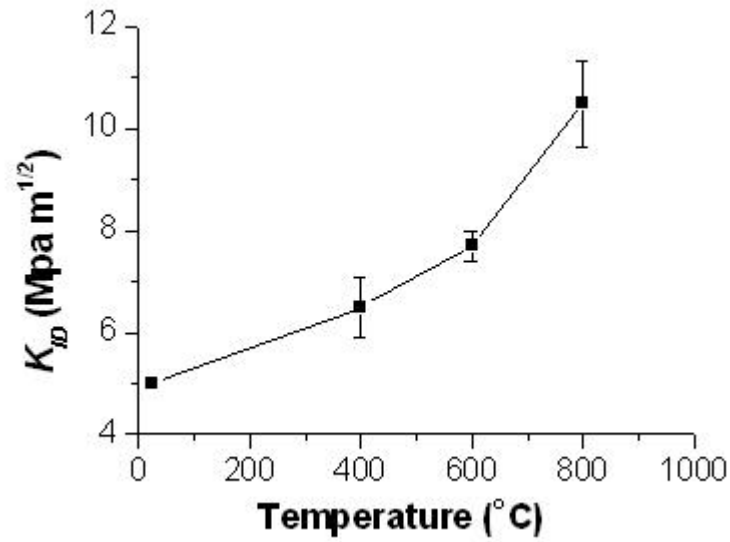


Figure 5.18. Effect of temperature on the fracture initiation toughness of FGM graded in the crack direction under dynamic loading.

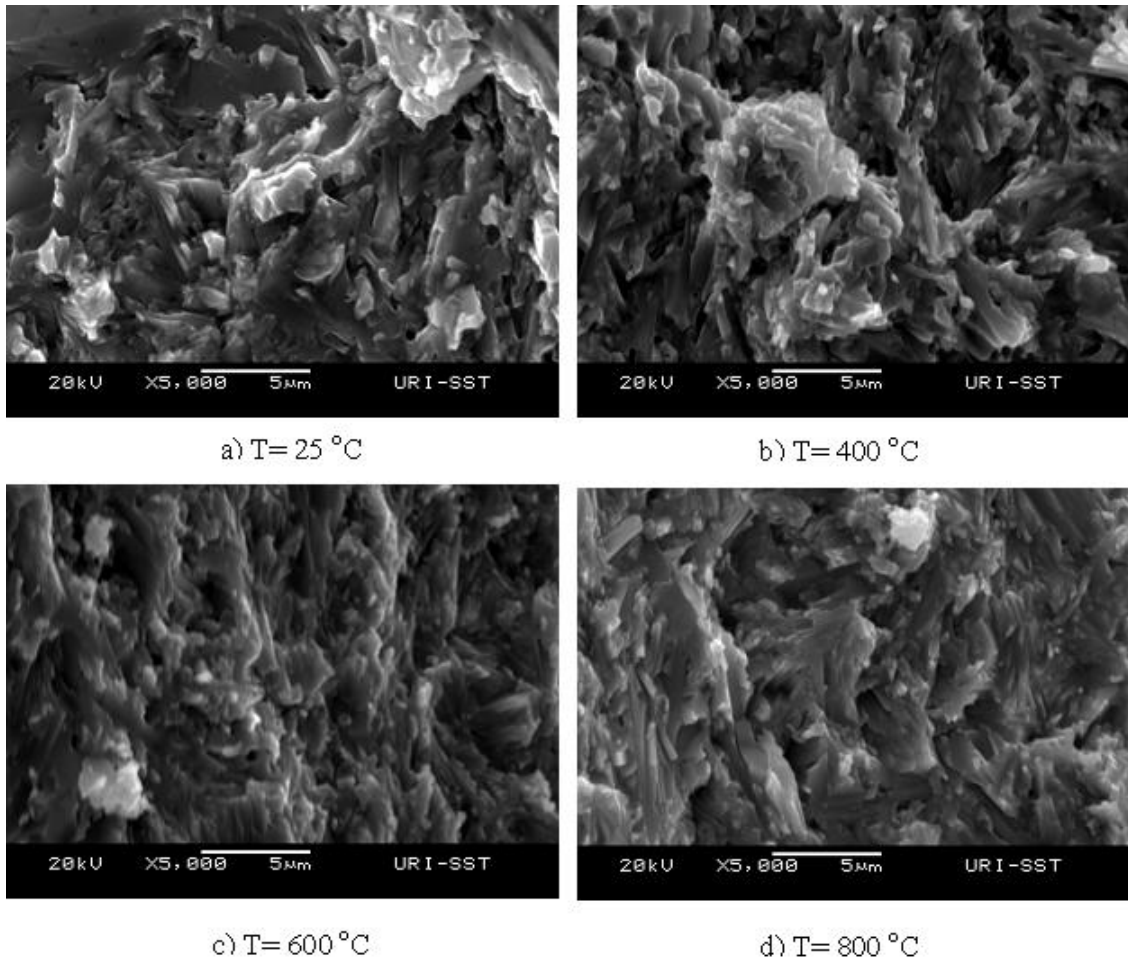


Figure 5.19. SEM images of typical fracture surface of FGM graded in the crack direction subjected to dynamic loading at different temperatures.

5.5.5 Effect of Loading Rate on the Fracture Initiation Toughness of FGM

The quasi-static and dynamic fracture initiation toughness of FGM, through the thickness direction and along the crack direction, as a function of temperature are shown in Fig. 5.20 and Fig. 5.21. In the figure, it is clear the fracture initiation toughness is load rate dependant. The fracture initiation toughness at all temperatures is higher in dynamic loading (2.5 MN/sec) as compared with the corresponding quasi-static loading (100 N/Sec).

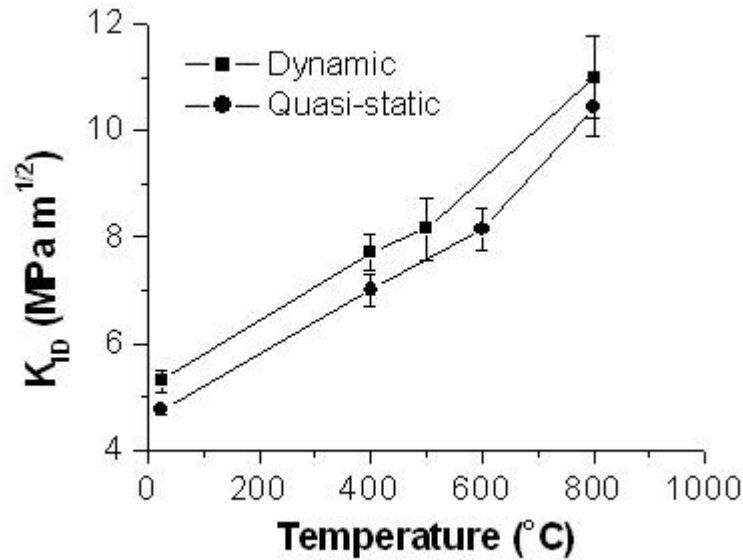


Figure 5.20. Effect of temperature on the fracture initiation toughness of FGM graded in the thickness direction under quasi-static and dynamic loading.

5.6 Summary

The quasi-static and dynamic fracture initiation toughness of Ti/TiB FGM is investigated under thermo-mechanical loading. A simple and accurate technique has been developed to identify the time corresponding to the load at which the crack initiates. The findings are summarized below:

- The fracture initiation toughness is temperature dependent, and it increases

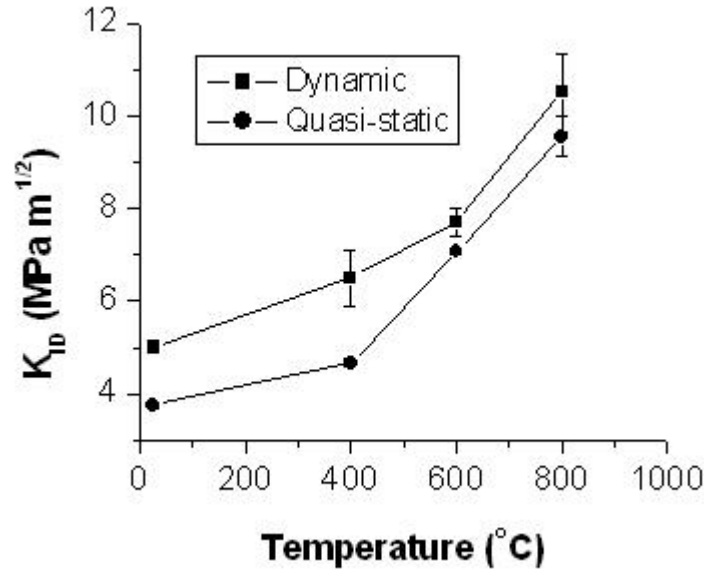


Figure 5.21. Effect of temperature on the fracture initiation toughness of FGM graded in the crack direction under quasi-static and dynamic loading.

as the temperature increases. For FGM graded in the thickness direction, as the temperature increase from room temperature to 800 °C, the quasi-static fracture initiation toughness increased by 160 % and the dynamic fracture initiation toughness increased by 130 %. For FGM graded in the crack direction, as the temperature increased from room temperature to 800 °C, the quasi-static fracture initiation toughness increased by 154 % and the dynamic fracture initiation toughness increased by 110 %.

- The fracture initiation toughness is rate dependent; it is higher at dynamic loading as compared with quasi-static loading. For FGM graded in the thickness direction, the room temperature fracture initiation toughness increased by 30 % and the fracture initiation toughness at 800 °C increased by 15 % as the loading rate increased from 100 N/sec to 2.5 MN/sec. For FGM graded in the crack direction, the room temperature fracture initiation toughness increased by 33 % and the fracture initiation toughness at 800 °C increased

by 10 % for the same increasing in the loading rate.

List of References

- [1] F. Delale and F. Erdogan, "The crack problem for a nonhomogeneous plane," *J. Appl. Mech.*, vol. 50, p. 6780, 1983.
- [2] J. Eischen, "Fracture of nonhomogeneous materials," *International Journal of Fracture*, vol. 34 (3), p. 322, 1987.
- [3] Z. Jin and N. Noda, "Crack-tip singular fields in nonhomogeneous materials," *J. Appl. Mech.*, vol. 61, pp. 738–739, 1994.
- [4] V. Parameswaran and A. Shukla, "Crack-tip stress fields for dynamic fracture in functionally gradient materials," *Mechanics of Materials*, vol. 31, pp. 579–596, 1999.
- [5] A. Shukla and N. Jain, "Dynamic damage growth in particle reinforced graded materials," *International Journal of Impact Engineering*, vol. 30, p. 777803, 2004.
- [6] V. B. Chalivendra, "Mode-i crack-tip stress fields for inhomogeneous orthotropic medium," *Mechanics of Materials*, vol. 40, pp. 293–301, 2008.
- [7] Z. Jin and R. Batra, "R-curve and strength behavior of functionally graded material," *Mat. Sci. Engng., A*, vol. 242, pp. 70–76, 1998.
- [8] R. P. G. M. Z. Hill, M. Carprnter and J. Gibeling, "Fracture resistance testing of monolithic and composite brittle materials," in *ASTM STP 1409*, 2002.
- [9] A. Kidane and A. Shukla, "Dynamic constitutive behavior of ti/tib fgm under thermo-mechanical loading," *Journal of Material Science*, vol. 43, p. 27712777, 2008.
- [10] J. Rubio, L. Fernandez-Saez and C. Navarro, "Determination of dynamic fracture-initiation toughness using three-point bending tests in a modified hopkinson pressure bar," *Experimental Mechanics*, vol. 43 (4), pp. 379–386, 2003.
- [11] V. Shazly, M. Prakash and S. Draper, "Mechanical behavior of gamma-metpx under uniaxial loading at elevated temperatures and high strain rates," *International Journal of Solids and Structures*, vol. 41, pp. 6485–6503, 2004.
- [12] R. Z. X. K. S. V. A. R. Jiang, F. Liu, "Evaluation of dynamic fracture toughness kid by hopkinson pressure bar loaded instrumented charpy impact test," *Engineering Fracture Mechanics*, vol. 71, pp. 279–287, 2004.

- [13] J. Dally and D. Barker, “Dynamic measurements of initiation toughness at high loading rates,” *Experimental Mechanics*, vol. 28, pp. 298–303, 1988.
- [14] T. Yokoyama, “Determination of dynamic fracture-initiation toughness using a novel impact bend test procedure,” *ASME J Pressure Vessel Technology*, vol. 115, pp. 389–396., 1993.
- [15] S. C. Wadgaonkar and V. Parameswaran, “Structure of near-tip stress fields and variation of stress intensity factor for a crack in a transversely graded material,” *Journal of Applied Mechanics, Transactions of the ASME*, vol. 76, 2009.

CHAPTER 6

Dynamic Crack Propagation in Transparent Functionally Graded Material

6.1 Abstract

A model transparent graded materials is used to investigate the steady state and transient crack propagation in a functionally graded material. A transparent graded material was fabricated using two different materials systems of polymer resin, which were cast using a special mold; to give continuously graded properties along the crack propagation direction. High-speed digital photography combined with photoelasticity technique is used to record the full-field stress data around the propagating crack. By analyzing the photoelastic fringe patterns the propagation velocity of the crack tip are obtained.

6.2 Introduction

In this study, dynamic fracture in transparent FGM has been investigated for different crack configuration and specimen geometries to completely characterize the behavior of a moving crack in FGMs. The specimen geometry used in this study was Single Edge Notch Tension (SENT). Dynamic photoelastic studies along with high-speed photography were applied to obtain full-field stress data for a propagating crack in above-mentioned FGMs. The real time images were analyzed to calculate the crack length, crack velocity and dynamic stress intensity factor. FGMs are materials, which have continuously varying mechanical properties in a specific direction. Even though FGM is a preferable material for different specific applications, few studies are available on the dynamic fracture behavior of these materials. This calls for further investigation of fracture behavior of FGM under different loading conditions. Photoelasticity technique with high speed digital

imaging system is one of the most widely used technique to study the fracture behavior of materials and was used in this study.

Analytical work on functionally graded materials goes back as early as the late 1960s when soil was modeled as a nonhomogeneous material by Gibson [1]. More recently, for propagating cracks in FGMs, Parameswaran and Shukla [2] and Chalivendra et al. [3], developed the structure of the first stress invariant and the out of plane displacement. In their study they brought out the effects of non-homogeneity through an asymptotic analysis. Lee [4] developed nonhomogeneity specific terms for individual stress and displacement components using displacement potentials. A review paper by Shukla et al. [5] presents a comprehensive summary of dynamic fracture studies in FGM.

In contrast there are only few experimental studies on the dynamic fracture of FGM. Parameswaran and Shukla [6] used photoelasticity to investigate dynamic fracture in FGMs with discrete property variation. Li et al. [7] have investigated the quasi static fracture properties of FGM created by selective ultraviolet (UV) irradiation of a polymer. Rousseau and Tippur [8] studied the crack-tip deformation in FGMs subjected to low velocity impact. Recently, Jain and Shukla [9] investigated the transient crack growth behavior in FGM fabricated as a particulate composite with continuously varying particle volume fraction along a single dimension.

Apart from a few studies reported above there is no sufficient experimental work, explaining the stress fields near the crack tip. In this experimental study, dynamic photoelasticity and high-speed digital imaging were used to study the dynamic fracture behavior of FGM. The crack tip stress fields were recorded at different time intervals. The crack velocity, acceleration and the dynamic stress intensity factor have been calculated.

6.3 Material and Specimen Preparation

A transparent graded material was fabricated and the mechanical properties was determined, at Sangju National University, South Korea, using two different materials systems of polymer resin. This was accomplished by pouring the two resins in a specially prepared mold. Resin 1 was poured first in an inclined mold and was let to cure till gelation occurred. Resin 2 was then poured at top of Resin 1 and let to cure. These two polymers had different Young's modulus, different fringe constants but the same density. The resulting composite created an inclined interface as shown in Fig. 6.1 and produced graded properties. The Young's modulus and Poisson's ratio of these two resins were obtained using a cross strain gage in tensile load. The stress fringe constant was determined using a compressive diamond test. The materials and photoelasticity properties of these resins are shown in Table. 6.1.

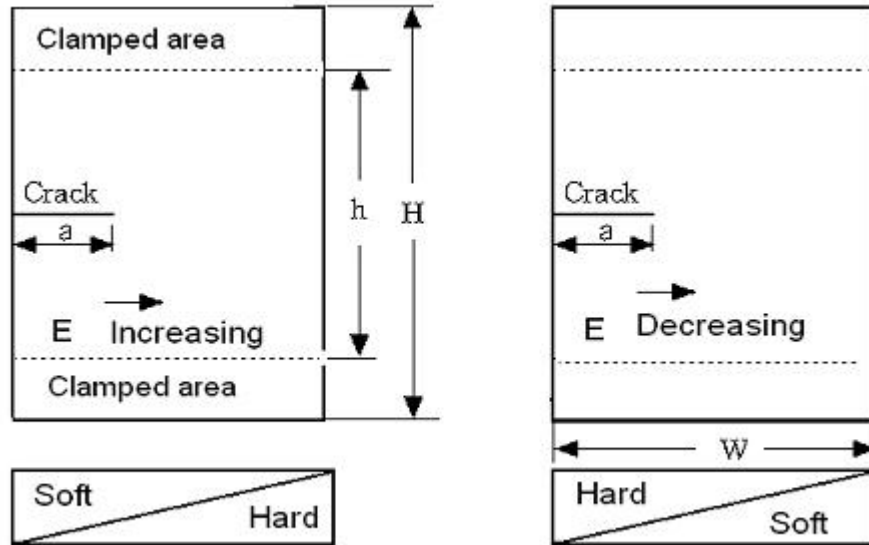


Figure 6.1. In-house fabricated typical SENT specimen: a) FGM with increasing Young's modulus in the direction of crack propagation, b) FGM decreasing in young's modulus in the direction of crack propagation (Dimensions $W=127\text{mm}$, $H/W=2$, $h/W=1.45$)

Table 6.1. Material properties of polymer resins

Polymer type	Young's modulus (GPa)	Poisson's ratio	Stress fringe constant (kN/m)	Density (ρ)
Resin 1 (hard)	2.45	0.38	17.30	1200
Resin 2 (soft)	0.46	0.50	5.10	1200

6.4 Experimental Procedure

6.4.1 Dynamic Fracture at Constant Velocity

A schematic of the photoelastic configuration used for studying dynamic crack propagation is shown in Fig. 6.2. High-speed digital imaging was employed along with dynamic photoelasticity to obtain real time, full-field quantification of the dynamic failure process. Two circular polarizers were placed on either side of the specimen to form a light-field circular polariscope. Power Light 2500DR xenon flash lamps (Photogenic Inc.) were used as light sources to illuminate the specimen and a monochromatic filter was placed just before the camera to ensure that the imaged isochromatic fringe patterns correspond to a single wavelength of light. The isochromatic images were captured at preset time interval using an Imacon 200 ultra-high-speed digital camera. This CCD based camera provides 16 independently programmable digital images of dynamic events up to a maximum framing rate of 200×10^6 frames/s. The camera has a facility to choose different range of interframe times. Interframe times were chosen so as to ensure that the dynamic fracture event was captured within the 16 frames.

Single Edge Notched Tension (SENT) specimens were machined from FGM material prepared in the procedure explained above. A series of experiments was conducted with two different SENT specimen geometries. The configurations considered in this study were (a) crack propagating towards increasing fracture toughness direction, Fig. 6.1a and (b) crack propagating towards decreasing fracture

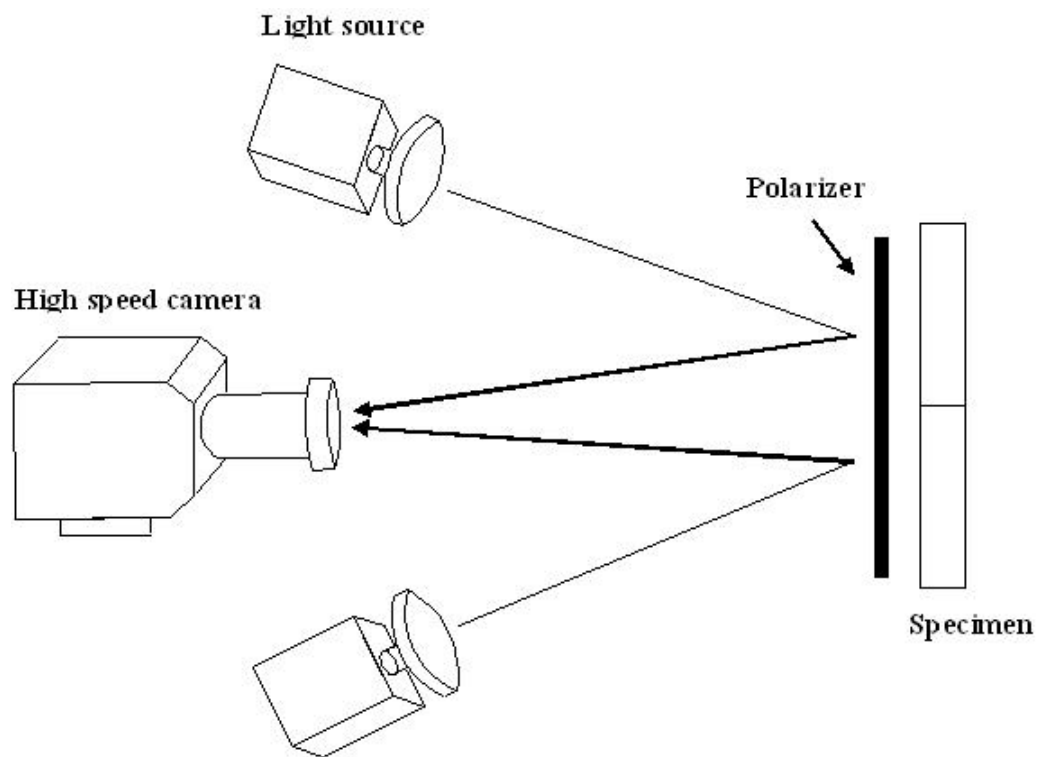


Figure 6.2. Schematic configuration for dynamic photoelastic experiment of transparent FGM

toughness directions, Fig. 6.1b. During the experiment the specimens were statically loaded to a predetermined value of initiation stress intensity factor using INSTRON 5585 apparatus. The crack was initiated by tapping a sharp razor blade on the specimen notch. Upon initiation of crack, a conductive silver paint lined near the crack tip in the direction of crack growth and connected with an electronic circuit triggered a high-speed camera IMACON 200. The camera was set to take photographs at a rate of 50,000 frames per second and an exposure time of 200 ns. The camera recorded 16 frames of the crack propagation event (0-400 μ s).

6.4.2 Transient Crack Propagation

Dynamic fracture in the FGM material explained above for transient crack tip loading was also investigated. The modified SENT specimen shown in Fig. 6.3 was used. The same experimental procedure as explained above was followed. However, in this case the camera was set at a rate of 140,000 frames per sec. During loading, first the crack propagates towards the circular hole and arrests until the load reach its critical value to propagates into the second crack. Once again the load reach the critical value it suddenly accelerates resulting in a transient crack propagation.

6.5 Results and Discussion

6.5.1 Crack tip velocity

Typical isochromatic fringes obtained from the dynamic fracture experiments with constantly moving crack tip loading are shown in Fig. 6.4 and 6.5. From isochromatic fringes shown above, it was observed that, there is a closure force acting behind the crack tip. This can be clearly seen in the case of crack propagating towards decreasing fracture toughness (increasing Young's modulus) direction as shown in Fig. 6.5. This is expected because at the left end of the specimen, the

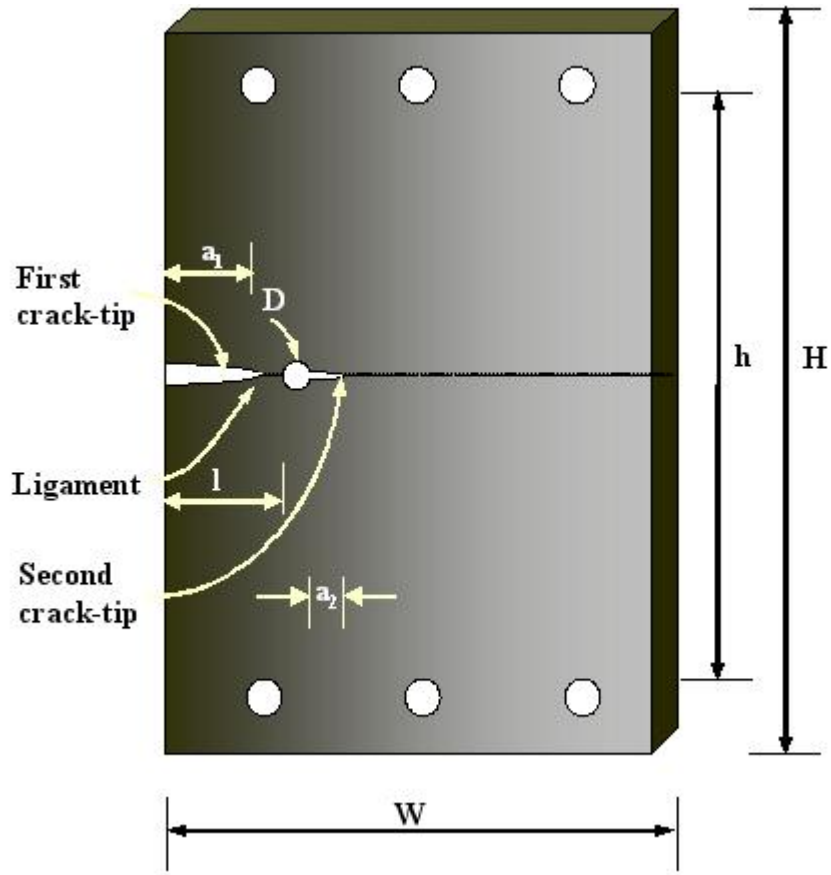


Figure 6.3. Modified SENT specimen for transient crack propagation in FGM (Dimensions $W=127\text{mm}$, $H/W=2$, $h/W=1.45$, $a_1=12\text{mm}$, $a_2=5\text{ mm}$, $D=5\text{ mm}$ $l=20\text{mm}$).

beginning of the crack, the softer part of the material is thick and has a tendency to stay together as the crack propagates through the harder layer. The crack tip distance with the corresponding time is determined from the images. Using these images the crack length as a function of time is plotted in Fig. 6.6. The data is later used to determine the crack tip velocity as a function of time as shown in Fig. From these figures it can be seen that for both the cases, for increasing and decreasing stiffness in the crack propagation direction, the crack velocity is constant and about 350 m/s.

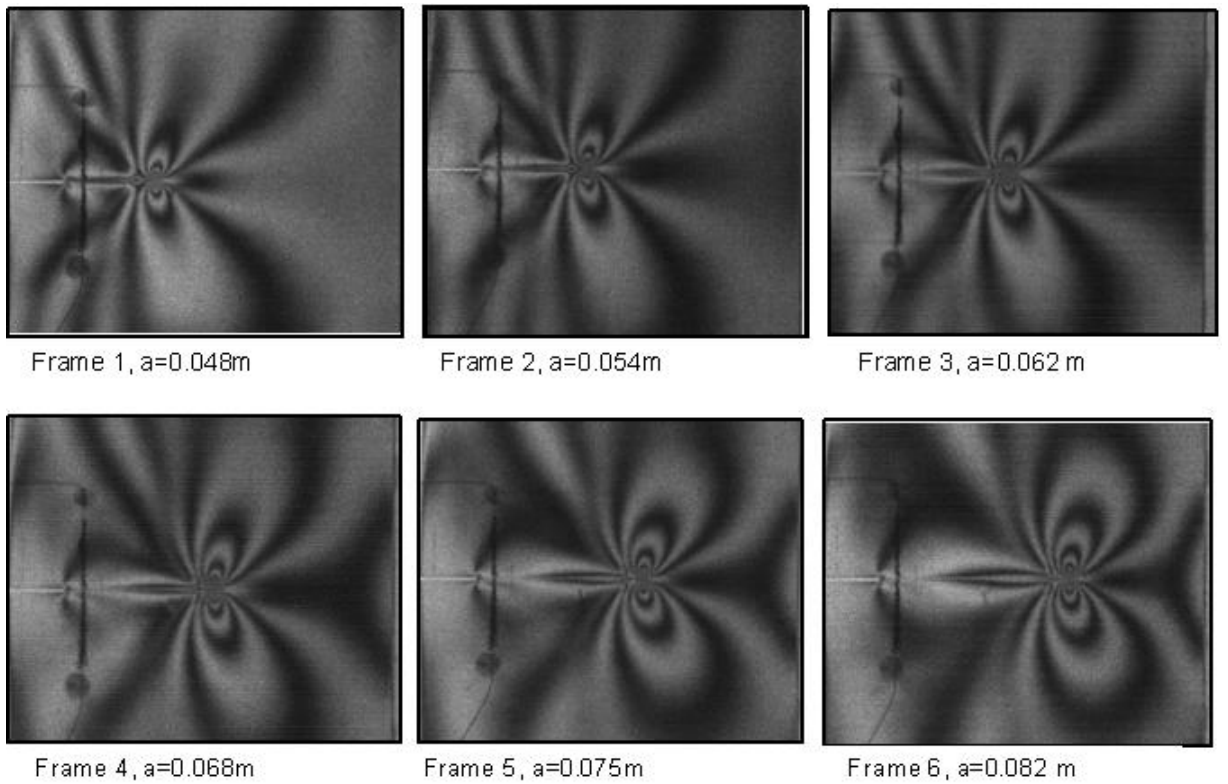


Figure 6.4. The dynamic isochromatic fringes at the crack tip for FGM with decreasing Young's modulus along the crack propagating direction. Time interval between each frame is 20 s

Typical isochromatic images obtained from the dynamic fracture of transient crack propagation loading experiments are shown in Fig. 6.7. Using these images, the crack length and velocity as a function of time is calculated and plotted as

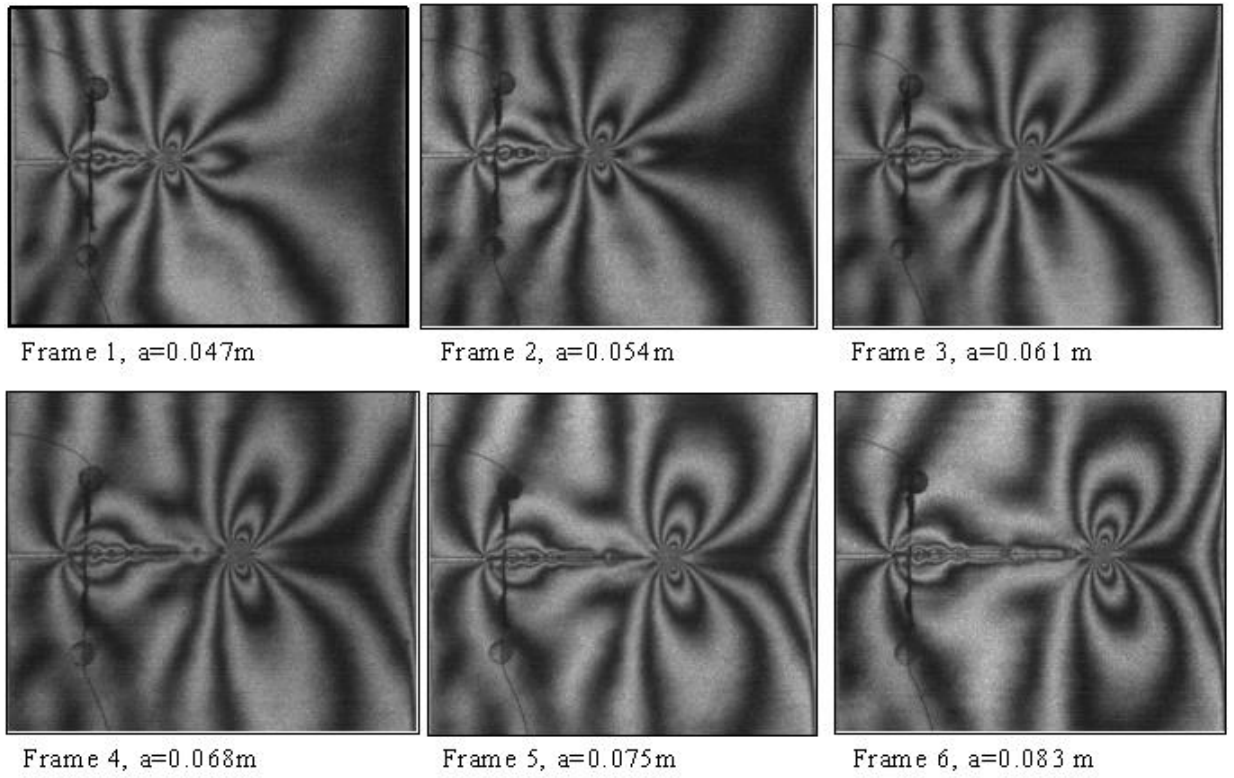


Figure 6.5. The dynamic isochromatic fringes at the crack tip for FGM with increasing Young's modulus along the crack propagating direction. Time interval between each frame is 20 s

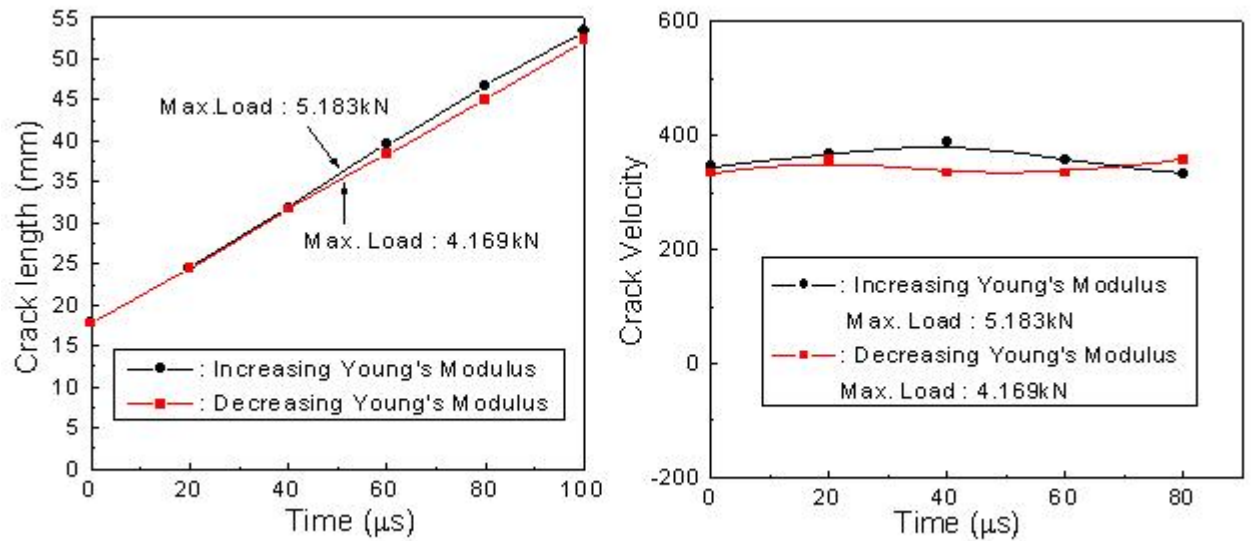


Figure 6.6. Crack length and velocity as a function of time for linearly varying FGM under dynamic loading

shown in Fig. 6.8. It is observed that the crack tip velocity increases at high acceleration until it reaches a maximum of 550 m/s and 470 m/s for increasing and decreasing stiffness respectively. Then the velocity oscillates with an average value of 300 m/s for the rest of crack propagation event.

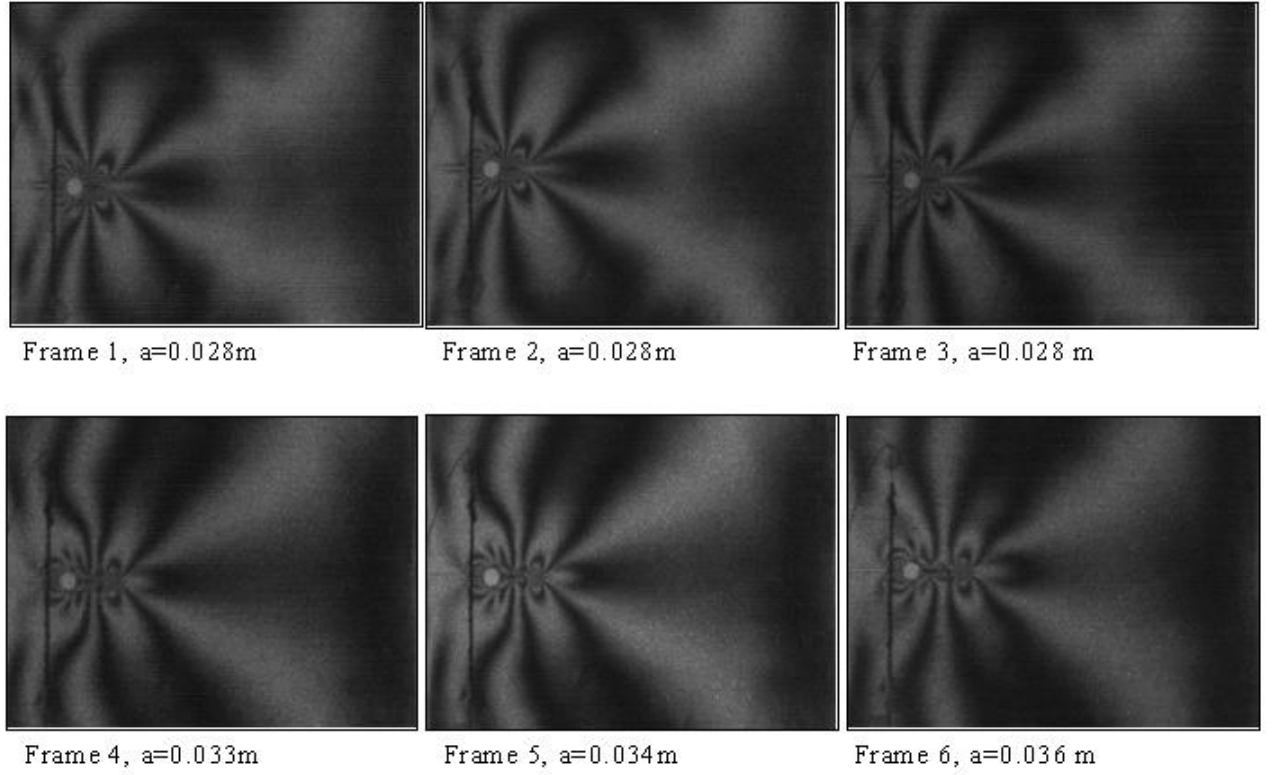


Figure 6.7. The dynamic isochromatic fringes for transient crack propagation on FGM with increasing Young's modulus along the crack propagating direction. Time interval between each frame is 7 s

6.5.2 Dynamic Stress Intensity Factor

The isochromatic fringes obtained during the dynamic experiment were used to extract the dynamic stress intensity factors. It can be seen that the isochromatics are symmetric about the crack plane, which indicates the opening mode (mode I) dominant loading at the crack-tip. In the present analysis, the dynamic stress fields for FGM with linearly varying properties developed by Lee [4] is used.

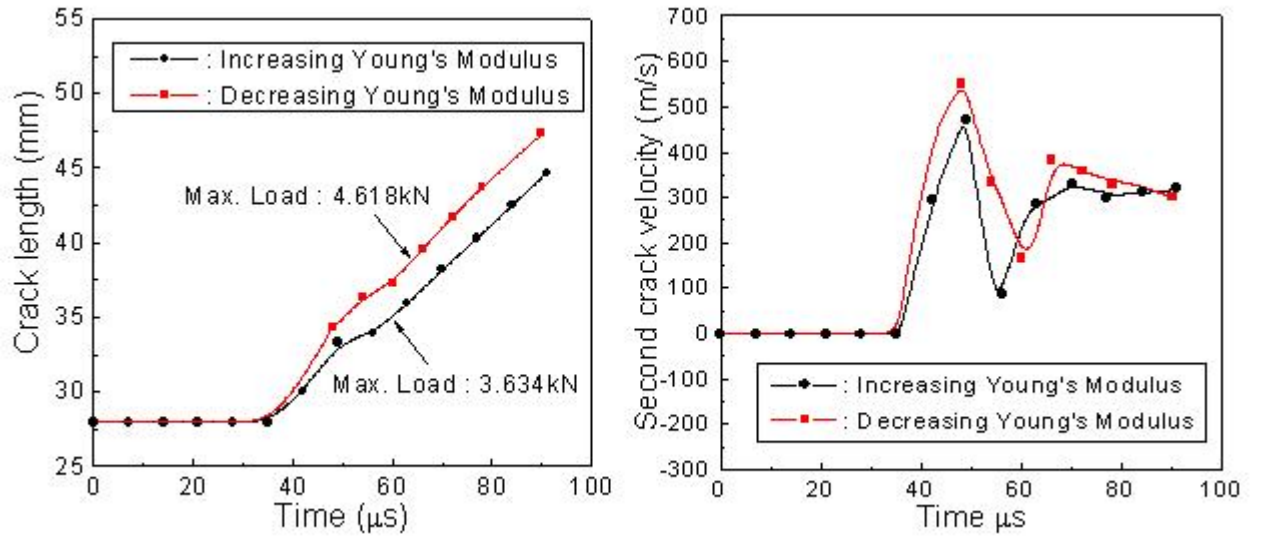


Figure 6.8. Crack length and velocity as a function of time for linearly varying FGM under transient dynamic loading

Isochromatics from each of the frames were analyzed using the aforementioned photoelastic procedure to obtain the stress intensity factor history. A detailed analysis of the isochromatic fringes associated with the dynamic fracture behavior of the crack, which contains crack initiation and propagation can be found [3, 4, 6].

However the available stress field does not support the gradation across the thickness direction. In the present experiment, it is observed that the gradation through the thickness direction has effect on the fracture behavior especially for the case of decreasing Young's modulus in the crack propagation direction. Hence, further investigation is required to accurately determine the dynamic stress intensity factor .

6.6 Summary

Simple procedure for preparing a transparent model FGMs with continuous gradation of properties was developed using two different polymer resins. The physical, elastic and fracture properties of the prepared FGMs were characterized.

Dynamic photoelasticity along with high speed photography was used to investigate the behavior of moving crack in FGMs. The propagation crack tip velocity and displacement are obtained.

List of References

- [1] R. Gibson, "Some results concerning displacements and stresses in a nonhomogeneous elastic half space," *Geotechnique*, vol. 17, p. 5867, 1967.
- [2] V. Parameswaran and A. Shukla, "Crack-tip stress fields for dynamic fracture in functionally gradient materials," *Mechanics of Materials*, vol. 31, pp. 579–596, 1999.
- [3] A. Chalivendra, V. B. Shukla and V. Parameswaran, "Dynamic out of plane displacement fields for an inclined crack in graded materials," *Journal of Elasticity*, vol. 69, pp. 99–119, 2002.
- [4] K. H. Lee, "Characteristics of a crack propagating along the gradient in functionally gradient materials," *Int. J. of Solids and Structures*, vol. 41, pp. 2879–2898, 2004.
- [5] N. Shukla, A. Jain and R. Chona, "A review of dynamic fracture studies in functionally graded materials," *Strain*, vol. 43, pp. 76–95, 2007.
- [6] V. Parameswaran and A. Shukla, "Dynamic fracture of a functionally gradient material having discrete property variation," *Journal of Material Science*, vol. 33, pp. 3303–3311, 1998.
- [7] L. J. C. B. Li, H. and S. M. H., "Experimental investigation of quasi-static fracture of functionally graded material," *International Journal Solids and Structures*, vol. 37, p. 37153732, 1999.
- [8] C. E. Rousseau and H. V. Tippur, "Influence of elastic variations on crack initiation in functionally graded glass-filled epoxy," *Engineering Fracture Mechanics*, vol. 69, p. 16791693, 2002.
- [9] N. Jain and A. Shukla, "Asymptotic analysis and reflection photoelasticity for the study of transient crack propagation in graded materials," *Journal of mechanics of materials and structures*, vol. 2(4), pp. 595–612, 2007.

CHAPTER 7

Conclusions and Recommendations

7.1 Conclusions

During this project a fundamental study was conducted to evaluate dynamic fracture and failure in functionally graded materials (FGMs) at room and at high temperatures. Room temperature studies included experimental and analytical evaluation of dynamic fracture in model materials. Analytical studies are conducted to develop thermo-mechanical stress, strain and displacement fields around stationary cracks and around cracks propagating under steady state conditions. An experimental study is also investigated on the dynamic constitutive and fracture initiation toughness of the commercially available functionally graded material (Ti/TiB). The findings from the presented study are summarized bellow.

- The stress-fields near the crack tip for mixed mode thermo-mechanical loading in homogeneous and graded material are developed using displacement potentials in conjugation with an asymptotic approach. Using the developed equations, angular variation of maximum shear stress, circumferential stress and the largest principal stress are plotted as a function of temperature around the crack-tip. Using both minimum strain energy density criterion and maximum circumferential stress criterion, the crack instability direction for various crack-tip speeds and non-homogeneous coefficients is also determined. It observed that the crack extension angle for mixed mode thermo-mechanical loading depends on the crack tip velocity, temperature and non-homogeny parameter.
- The dynamic constitutive behavior of Ti/TiB FGM under thermo-mechanical loading is investigated. The FGM showed thermal softening at higher tem-

perature with a decrease in failure stress and an increase in failure strain. Finally it is observed that, the failure mechanism changes to ductile at higher temperatures.

- The quasi-static and dynamic fracture initiation toughness of Ti/TiB FGM is investigated under thermo-mechanical loading. A simple and accurate technique has been developed to identify the time corresponding to the load at which the crack initiates. Further it is observed that the fracture initiation toughness is temperature and rate dependent.
- A model transparent graded material is used to investigate the steady state and transient crack propagation in a functionally graded material. It observed that that for both the cases, for increasing and decreasing stiffness in the crack propagation direction, the crack velocity is constant. On the other hand; for transient crack propagation experiment, it is observed that the crack tip velocity increases at high acceleration until it reaches a maximum value and then remain constant for the rest of crack propagation event.

7.2 Recommendations

The current research represents a fundamental and first step in understanding the dynamic fracture and failure of functionally graded materials under thermo-mechanical loading. In the future work, investigation should be conducted to exploit the properties of graded multi-functional materials under different loading conditions and to predict their performance and structural integrity under extreme mechanical and thermal environments. The high temperature facilities and the dynamic stress fields that has been developed as a part of the present work can be utilized. The specific deliverables of the proposed project are summarized as follows:

- Analytical development of transient stress, strain and displacement fields for propagating cracks in FGM subjected to combined and rapidly changing thermo-mechanical loading under a variety of boundary conditions.
- Dynamic response of FGM when subjected to controlled shock loading at various temperatures utilizing 3D digital image correlation techniques and high speed imaging under different boundary conditions.
- Development of constitutive models for various spatially tailored materials at high temperatures and high strain rates of loading with and without confining stresses.
- Low and high speed impact response of FGM at various temperatures and boundary conditions.
- Finally, development of physics-based failure models for the combined environment response of spatially tailored materials and structures that show good correlation between simple laboratory experiments and structural applications.

APPENDIX A

Validation Plots

Various stress fields obtained from the analytical study presented in chapter 2, if mode-I and mode-II fields are separated and plotted, are shown below. These plots perfectly matches with the isothermal solution given by Freund.

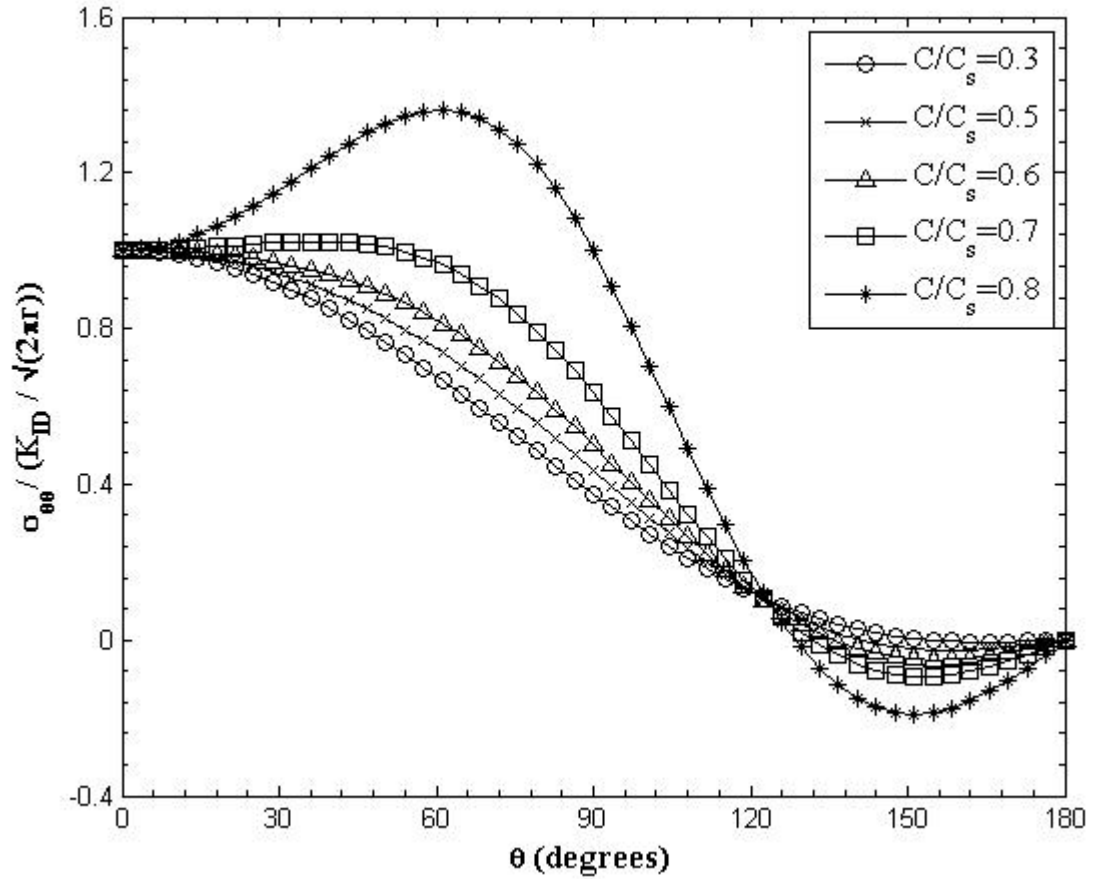


Figure A.1. Variation of the circumferential tensile stress with angle θ around the crack edge for several value of normalized crack speed. Crack growth is in mode I. ($r = 0.002\text{m}$, $K_{ID} = 1\text{MPa } m^{1/2}$)

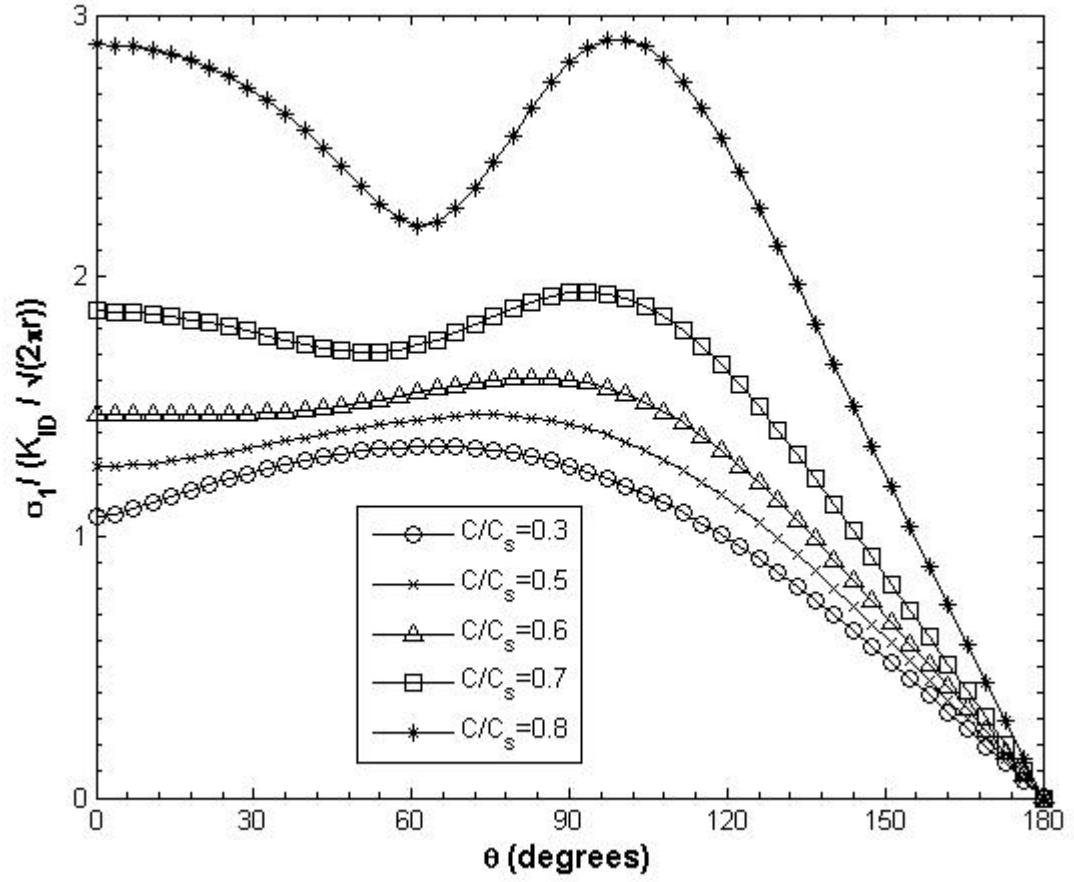


Figure A.2. Variation of maximum principal stress with angle θ around the crack edge for several value of normalized crack speed. Crack growth is in mode I. ($r = 0.002\text{m}$, $K_{ID} = 1\text{MPa } m^{1/2}$)

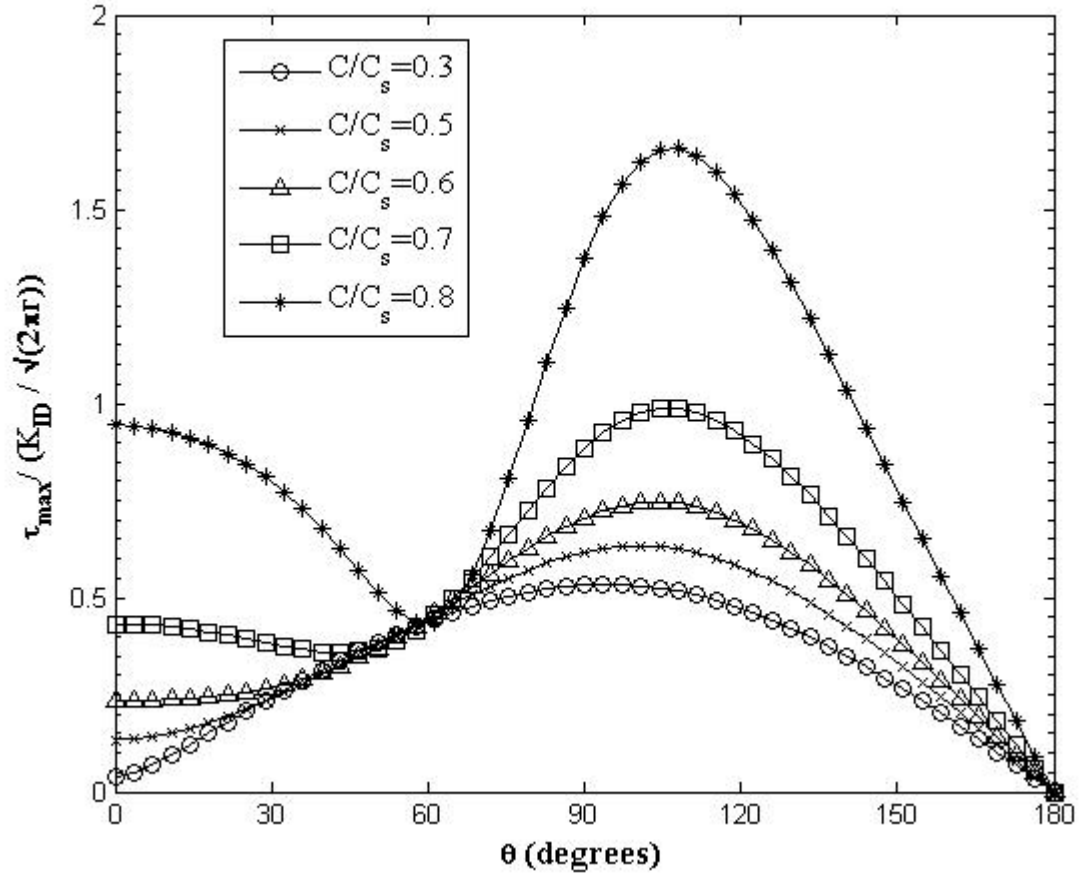


Figure A.3. Variation of the maximum shear stress with angle θ around the crack edge for several value of normalized crack speed. Crack growth is in mode II. ($r = 0.002\text{m}$, $K_{IID} = 1\text{MPa } m^{1/2}$)

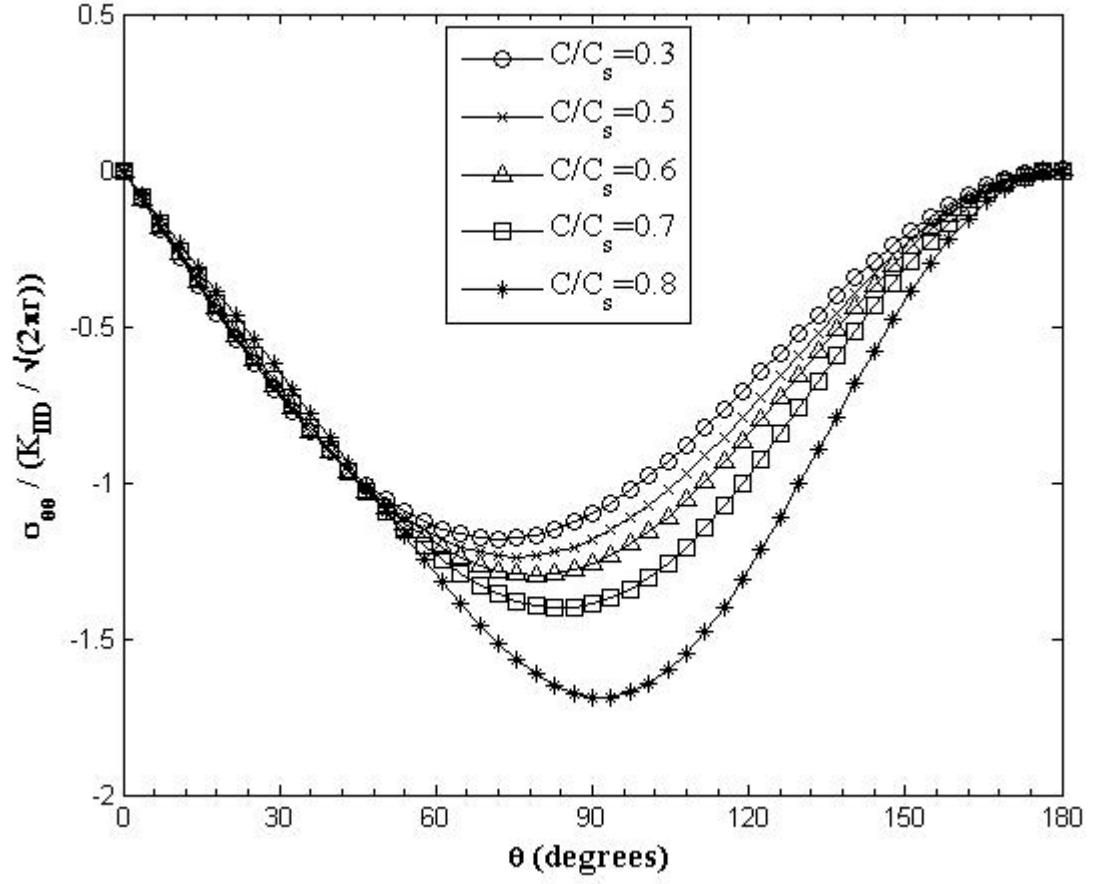


Figure A.4. Variation of the circumferential tensile stress with angle θ around the crack edge for several value of normalized crack speed. Crack growth is in mode II. ($r = 0.002\text{m}$, $K_{IID} = 1\text{MPa } m^{1/2}$)

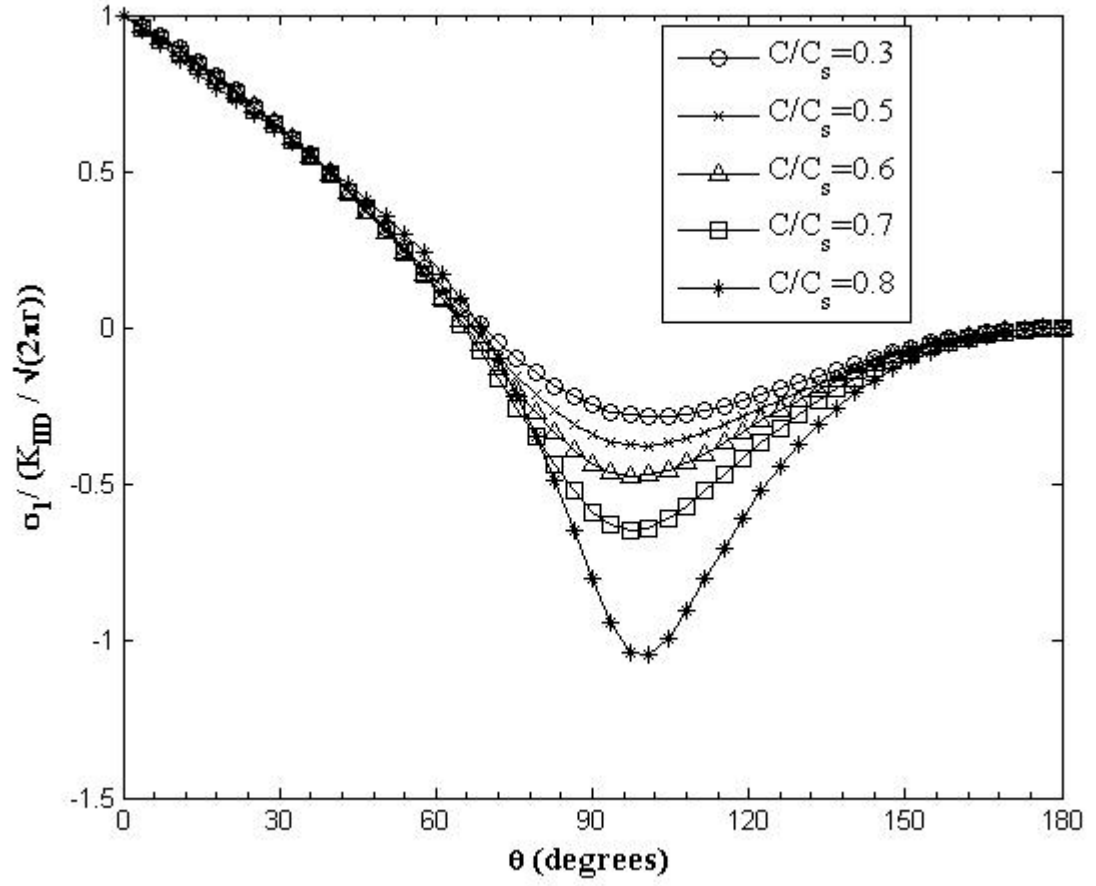


Figure A.5. Variation of maximum principal stress with angle θ around the crack edge for several value of normalized crack speed. Crack growth is in mode II. ($r = 0.002\text{m}$, $K_{IID} = 1\text{MPa } m^{1/2}$)

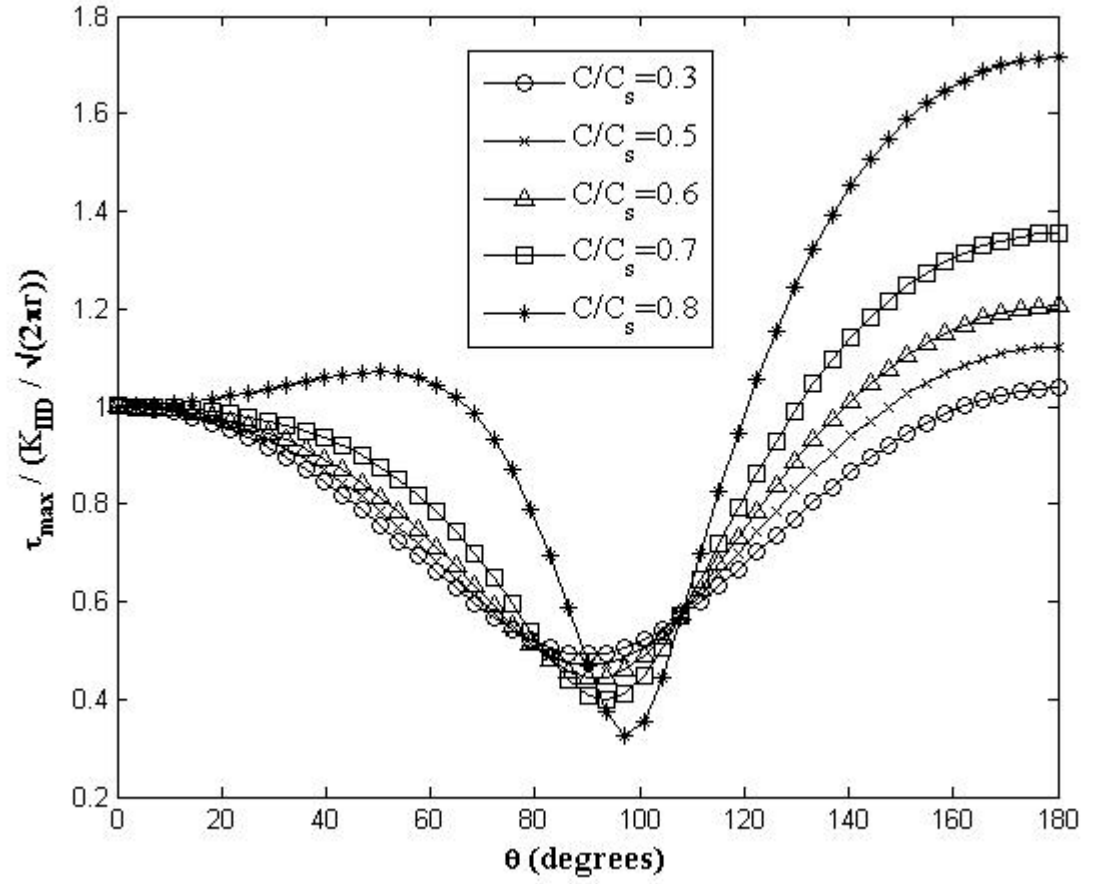


Figure A.6. Variation of the maximum shear stress with angle θ around the crack edge for several value of normalized crack speed. Crack growth is in mode I. ($r = 0.002\text{m}$, $K_{ID} = 1\text{MPa } m^{1/2}$)

APPENDIX B

Matlab Code

```
%%%%%%%%%%%%%%%%%%%%%%%%%%%%%%%%%%%%%%%%%%%%%%%%%%%%%%%%%%%%%%%%%%%%%%%%%%%%%%
%% Program to calculate and plot Thermo-Mechanical Stress and
%% Displacement Fields for Propagating Crack Tip in
%% Functionally Graded Materials
%% Program used to plot figures given in Chapter 2 and 3
%% %%%%%%%%%%%%%%%%%%%%%%%%%%%%%%%%%%%%%%%%%%%%%%%%%%%%%%%%%%%%%%%%%%%%%%%%%%%
%%%%%%%%%%%%%%%%%%%%%%%%%%%%%%%%%%%%%%%%%%%%%%%%%%%%%%%%%%%%%%%%%%%%%%%%%%%%%%

clear all;
close all;
clc;

%general constants
mue=1e09;
rho=1200;
nue=0.3;
k=2*nue/(1-2*nue);
ac=8.5e-6;
q0=250;
q1=0;
q2=0;

%The constants in the stress functions
K1D=1e6;%input('Enter the value of K1:');
K2D=0.2*K1D;
Kef=sqrt(K1D^2+K2D^2);

%Nonhomogeneous constants
beta=0;
zeta=0;%input('Enter the value of nonhomogeneity factor:');

TD=0.003;% input('the domain for fringe generation= ');
NOP=51; %input('Number of points =');
ds=2*TD/(NOP-1);
xc=[-TD:ds:TD];
yc=[-TD:ds:TD];
count_i=0;
idata=1;
```

```

mue_c=exp(TD*zeta)*mue;
rho_c=exp(TD*zeta)*rho;

cs=sqrt(mue_c/rho_c);
cl=cs*sqrt(2+k);
sr=0.5; %ratio of crack speed to shear wave speed at crack tip
c=sr*cs;

al=sqrt(1-(c/cl)^2);
as=sqrt(1-(c/cs)^2);

count_i=0;

A0=((4*(1+(as^2)))/((4*al*as)-((1+(as^2))^2)))*(K1D/(3*mue*sqrt(2*pi)));
B0=(-2*al)/(1+(as^2))*A0;

C0=(8*as)/(3*(4*as*al-(1+as^2)^2))*(K2D/(mue*sqrt(2*pi)));
D0=((1+as^2)/(2*as))*C0;

H=k*(1-al^2)+2;
G=k*(1-as^2)+2;
L=k*(1+al^2)+2;
M=k*(1+as^2)+2;
N=k-(al^2)*(k+2);
O=k-(as^2)*(k+2);
P=k+(al^2)*(k+2);
Q=k+(as^2)*(k+2);

P1=(zeta*k*(al^2))/(al^2-as^2);
P2=(zeta*as/((k+2)*(al^2-as^2)));
Q1=((3*k+2)/(k+2))*(ac/((al^2)-1));

L1=(zeta/(al^2));
L2=zeta/as;

%Expresseion for Stress

for j=1:1:NOP
    r=0.002;
    t(j)=-pi+(j-1)*2*pi/(NOP-1);
    % t(j)=(j-1)*2*pi/((NOP-1));
    x(j)=r*cos(t(j));

```

```

y(j)=r*sin(t(j));

%q1=-(1+as^2)/(1-as^2)*r^(-1/2)*q0;

r1(j)=sqrt((x(j)^2)+((al^2)*(y(j)^2)));
rs(j)=sqrt((x(j)^2)+((as^2)*(y(j)^2)));

tl(j)=atan2((al*y(j)),x(j));
ts(j)=atan2((as*y(j)),x(j));
%t(j)=atan2(y(j), x(i));
x_bar(j)=(x(j));%cos(zeta)-(y(j)*sin(zeta));

s11_1(j)=(3*H/4)*A0*(r1(j)^(-1/2))*cos(tl(j)/2)+(-3*L1*H/16)
          *A0*(r1(j)^(1/2))*cos(3*tl(j)/2)+(-3*L1/4)
          *A0*L*(r1(j)^(1/2))*cos(tl(j)/2);
s11_2(j)=- (3*H/4)*C0*(r1(j)^(-1/2))*sin(tl(j)/2)+(3*L1*H/16)*
          C0*(r1(j)^(1/2))*sin(3*tl(j)/2)+(-3*L1/4)
          *C0*L*(r1(j)^(1/2))*sin(tl(j)/2);
s11_3(j)=(3*as/2)*B0*(rs(j)^(-1/2))*cos(ts(j)/2)-(3*L2/8)
          *B0*(rs(j)^(1/2))*cos(3*ts(j)/2);
s11_4(j)=(3*as/2)*D0*(rs(j)^(-1/2))*sin(ts(j)/2)-(3*L2/8)
          *D0*(rs(j)^(1/2))*sin(3*ts(j)/2);
s11_5(j)=-3*P1*A0*(r1(j)^(1/2))*cos(tl(j)/2)-(3*P2/2)*G
          *B0*(rs(j)^(1/2))*cos(ts(j)/2);
s11_6(j)=3*P1*C0*(r1(j)^(1/2))*sin(tl(j)/2)-(3*P2/2)*G
          *D0*(rs(j)^(1/2))*sin(ts(j)/2);
s11_7(j)=2*Q1*q0*(r^(1/2))*sin(t(j)/2);
s11_8(j)=- (3*k+2)*ac*(q0*r^(1/2))*sin(t(j)/2)+q1*
          r*cos(t(j))+q2*r^(3/2)*sin(3*t(j)/2));
s11(j)=(mue*exp(zeta*(TD+x_bar(j))))*(s11_1(j)+s11_2(j)
          +s11_3(j)+s11_4(j)+s11_5(j)+s11_6(j)+s11_7(j)+s11_8(j));

s22_1(j)=(3*N/4)*A0*(r1(j)^(-1/2))*cos(tl(j)/2)-(3*L1*N/16)
          *A0*(r1(j)^(1/2))*cos(3*tl(j)/2)-(3*L1*P/4)
          *A0*(r1(j)^(1/2))*cos(tl(j)/2);
s22_2(j)=- (3*N/4)*C0*(r1(j)^(-1/2))*sin(tl(j)/2)+(3*L1*N/16)
          *C0*(r1(j)^(1/2))*sin(3*tl(j)/2)-(3*L1*P/4)
          *C0*(r1(j)^(1/2))*sin(tl(j)/2);
s22_3(j)=- (3*as/2)*B0*(rs(j)^(-1/2))*cos(ts(j)/2)+(3*L2/8)
          *B0*(rs(j)^(1/2))*cos(3*ts(j)/2);
s22_4(j)=- (3*as/2)*D0*(rs(j)^(-1/2))*sin(ts(j)/2)+(3*L2/8)
          *D0*(rs(j)^(1/2))*sin(3*ts(j)/2);
s22_5(j)=3*P1*A0*(r1(j)^(1/2))*cos(tl(j)/2)-(3*P2*0/2)
          *B0*(rs(j)^(1/2))*cos(ts(j)/2);

```



```

s22_6(j)=-3*P1*C0*(r1(j)^(1/2))*sin(t1(j)/2)-(3*P2*0/2)
        *D0*(rs(j)^(1/2))*sin(ts(j)/2);
s22_7(j)=-2*Q1*q0*(r^(1/2))*sin(t(j)/2);
s22_8(j)=-(3*k+2)*ac*(q0*r^(1/2)*sin(t(j)/2))+q1*r*cos(t(j))
        +q2*r^(3/2)*sin(3*t(j)/2));

if j==NOP %| j==1
    s22_9(j)=-ac*(3*k+2)*((1+as^2)/(1-as^2))*q0*sqrt(r);
elseif j==1
    s22_9(j)=ac*(3*k+2)*((1+as^2)/(1-as^2))*q0*sqrt(r);
else
    s22_9(j)=0;
end

s22(j)=(mue*exp(zeta*(TD+x_bar(j))))*(s22_1(j)+s22_2(j)+s22_3(j)
        +s22_4(j)+s22_5(j)+s22_6(j)+s22_7(j)+s22_8(j)+s22_9(j));

s12_1(j)=(3/2)*A0*al*(r1(j)^(-1/2))*sin(t1(j)/2)
        -(3*L1*al/8)*A0*(r1(j)^(1/2))*sin(3*t1(j)/2);
s12_2(j)=(3/2)*C0*al*(r1(j)^(-1/2))*cos(t1(j)/2)
        -(3*L1*al/8)*C0*(r1(j)^(1/2))*cos(3*t1(j)/2);
s12_3(j)=(3/4)*(1+(as^2))*B0*(rs(j)^(-1/2))*sin(ts(j)/2)-(3*L2/(as*16))
        *B0*(rs(j)^(1/2))*sin(3*ts(j)/2)+(3*L2/(as*4))*(1-(as^2))
        *B0*(rs(j)^(1/2))*sin(ts(j)/2);
s12_4(j)=-(3/4)*(1+(as^2))*D0*(rs(j)^(-1/2))*cos(ts(j)/2)-(3*L2/(as*16))
        *D0*(rs(j)^(1/2))*cos(3*ts(j)/2)-(3*L2/(as*4))*(1-(as^2))
        *D0*(rs(j)^(1/2))*cos(ts(j)/2);
s12_5(j)=2*Q1*q0*(r^(1/2))*cos(t(j)/2);
s12(j)=(mue*exp(zeta*(TD+x_bar(j))))*(s12_1(j)+s12_2(j)
        +s12_3(j)+s12_4(j)+s12_5(j));

sed(j)=(1/(4*(mue*exp(zeta*x_bar(j)))))*((1-nue)*(( s11(j))^2
        +(s22(j))^2)-2*nue* s11(j)* s22(j)+2*( s12(j))^2);
sigv(j)=s11(j)+s22(j);
sigr(j)=s11(j)*(cos(t(j)))^2+s22(j)*(sin(t(j)))^2
        +2*s12(j)*(cos(t(j))*sin(t(j)));
sigt(j)=s11(j)*(sin(t(j)))^2+s22(j)*(cos(t(j)))^2
        -2*s12(j)*(cos(t(j))*sin(t(j)));
sigrt(j)=-s11(j)*(cos(t(j))*sin(t(j)))+s22(j)*(sin(t(j))*cos(t(j)))
        +s12(j)*((cos(t(j)))^2-(sin(t(j)))^2);
sigm1(j)=((s11(j)+s22(j))/2)+sqrt((((s11(j)-s22(j))/2)^2+s12(j)^2);
tmax(j)=sqrt(((s22(j)-s11(j))/2)^2+s12(j)^2);
sedr(j)=(1/((1+nue)*4*(mue*exp(x_bar(j)))))*((sigr(j))^2
        +(sigt(j))^2-2*nue*sigt(j)*sigr(j)-nue^2*(sigr(j)

```

```

+sigrt(j))+2*(1+nue)*(sigrt(j))^2);

% To calculate the stress filed due to opposit traction at the crack face

for i=1:1:NOP
    % x(i)=xc(i);
    c(i)=i*0.00006; %0.00006; %points where the load is taken
    % p(i)=(5.5e18*c(i)^6-5.6e16*c(i)^5+2.3e14*c(i)^4-5e11*c(i)^3+
        %7e8*c(i)^2+ 6.8e4*c(i))/22;%c=100, 5 order poly
    p(i)=0; %c=0
    % p(i)=(1.2e13*c(i)^4-1e11*c(i)^3+4.25e8*c(i)^2+1.3e5*c(i))/10;
        %force distribution c=100 , 3 ord poly
    if t(j) <= 0
    % p(i)=-(5.5e18*c(i)^6-5.6e16*c(i)^5+2.3e14*c(i)^4-5e11*c(i)^3
        +7e8*c(i)^2+6.8e4*c(i))/12;%c=100, 5 order poly
    p(i)=-(3e13*c(i)^4-2.53e11*c(i)^3+1.05e9*c(i)^2+3.3e5*c(i))/12;
        %force distribution c=250
    else
    % p(i)=(5.5e18*c(i)^6-5.6e16*c(i)^5+2.3e14*c(i)^4-5e11*c(i)^3
        +7e8*c(i)^2+6.8e4*c(i))/12; %c=100, 5 order poly
    p(i)=(3e13*c(i)^4-2.53e11*c(i)^3+1.05e9*c(i)^2+3.3e5*c(i))/12;
        %force distribution c=250
    end;
    %p(i)=-(1e25*c(i)^8-1.3143e23*c(i)^7+7.162e20*c(i)^6-2e18*c(i)^5
        -3.5e15*c(i)^4-3.667e12*c(i)^3+2.6e9*c(i)^2+8.6e4*c(i))/740;
        %c=250, 7th poly
    %p(i)=2*(3e13*c(i)^4-2.53e11*c(i)^3+1.05e9*c(i)^2+3.3e5*c(i))/10;
        %force distribution c=500
    %y(j)=yc(j);
    %c(j)=j*0.00006;
    r2(j,i)=sqrt((x(j)+c(i))^2+y(j)^2);
    t2(j,i)=atan2(y(j),(x(j)+c(i)));
    pc=(p(i)*sqrt(c(i)));
    % pc=p*sqrt(b);
    % sigy(j)=(pc/(pi*r1(j).*sqrt(r)))*(cos(t1(j)+t(j)/2)
        +(1/2)*sin(t(j))*sin(t1(j)+3*t(j)/2)
        +(r/r1(j))*sin(t(j))*sin(2*t1(j)+t(j)/2));
    sigx(j,i)=(pc/(pi*r2(j,i).*sqrt(r)))*(cos(t2(j,i)+t(j)/2)
        -(1/2)*sin(t(j))*sin(t2(j,i)+3*t(j)/2)
        -(r/r2(j,i))*sin(t(j))*sin(2*t2(j,i)+t(j)/2));
    sigy(j,i)=(pc/(pi*r2(j,i).*sqrt(r)))*(cos(t2(j,i)+t(j)/2)
        +(1/2)*sin(t(j))*sin(t2(j,i)+3*t(j)/2)
        +(r/r2(j,i))*sin(t(j))*sin(2*t2(j,i)+t(j)/2));

```

```

sigxy(j,i)=(pc/(pi*r2(j,i).*sqrt(r)))*((1/2)*sin(t2(j,i))*cos(t2(j,i)
+3*t(j)/2)+(r/r2(j,i))*sin(t(j))*cos(2*t2(j,i)+t(j)/2));
end
end
for j=1:1:NOP
    sumx=0;
    sumy=0;
    sumxy=0;
    for i=1:1:NOP
        sumx=sigx(j,i)+sumx;
        sumy=sigy(j,i)+sumy;
        sumxy=sigxy(j,i)+sumxy;
    end
    sig11(j)=sumx;
    sig22(j)=sumy;
    sig12(j)=sumxy;

    sedb(j)=(1/(4*(mue*exp(x_bar(j)))))*((1-nue)*(( sig11(j))^2
+(sig22(j))^2)-2*nue* sig11(j)* sig22(j)+2*(sig12(j))^2);
    sigvb(j)=sig11(j)+sig22(j);
    sigrb(j)=sig11(j)*(cos(t(j)))^2+sig22(j)*(sin(t(j)))^2
+2*sig12(j)*(cos(t(j))*sin(t(j)));
    sigtb(j)=sig11(j)*(sin(t(j)))^2+sig22(j)*(cos(t(j)))^2
-2*sig12(j)*(cos(t(j))*sin(t(j)));
    sigrtb(j)=-sig11(j)*(cos(t(j))*sin(t(j)))
+sig22(j)*(sin(t(j))*cos(t(j)))+sig12(j)*
((cos(t(j)))^2-(sin(t(j)))^2);
    sigm1b(j)=((sig11(j)+sig22(j))/2)+sqrt((((sig11(j)
-sig22(j))/2)^2+sig12(j)^2);
    tmaxb(j)=sqrt(((sig22(j)-sig11(j))/2)^2+sig12(j)^2);
    sedrb(j)=(1/((1+nue)*4*(mue*exp(x_bar(j)))))*((sigrb(j))^2
+(sigtb(j))^2-2*nue*sigtb(j)*sigrb(j)
-nue^2*(sigrb(j)+sigtb(j))+2*(1+nue)*(sigrtb(j))^2);
end
for j=1:1:NOP
    sigma1(j)=(((s11(j)+sig11(j))+(s22(j)+sig22(j)))/2)+sqrt((((s11(j)
+sig11(j))-(s22(j)+sig22(j)))/2)^2+(s12(j)+sig12(j))^2);
    taumax(j)=sqrt((((s22(j)+sig22(j))-(s11(j)+sig11(j)))/2)^2
+(s12(j)+sig12(j))^2);
    sigmat(j)=(s11(j)+sig11(j))*(sin(t(j)))^2+(s22(j)+sig22(j))*
(cos(t(j)))^2-2*(s12(j)+sig12(j))*(cos(t(j))*sin(t(j)));
    sigmart(j)=-s11(j)+sig11(j)*(cos(t(j))*sin(t(j)))+(s22(j)
+sig22(j))*(sin(t(j))*cos(t(j)))+(s12(j)+sig12(j))*
((cos(t(j)))^2-(sin(t(j)))^2);

```

```

sigmar(j)=(s11(j)+sig11(j))*(cos(t(j)))^2+(s22(j)+sig22(j))*
        (sin(t(j)))^2+2*(s12(j)+sig12(j))*(cos(t(j))*sin(t(j)));
end

plot(t*(180/pi),(s22/(Kef/sqrt(2*pi*r))), 'mo'); % combined
xlabel('\theta (degrees)');
ylabel('u (N. mm /mm^3)');
hold on;

plot(t*(180/pi),((taumax)/(Kef/sqrt(2*pi*r))), 'b'); % raction
xlabel('\theta (degree)');
ylabel('\sigma_y_y/ (K_e_f_f / \surd(2\pir))');
hold on;

plot(t*(180/pi),(sig22)/(Kef/sqrt(2*pi*r)), 'r') % before raction
hold on;
xlabel('\theta (degrees)');
ylabel('\tau_m_a_x / (K_I / \surd(2\pir))');
title(' \sigma_y');
legend('q_o = 0', 'q_o = 1000', 'q_o= 2000');

```

APPENDIX C

Theoretical Formulation

Thermo-mechanical Displacement, Strain and Stress Field for Mixed Mode Loading in FGM

The equations of motion for a plane problem are given by Eq. C.1

$$\frac{\partial \sigma_{XX}}{\partial X} + \frac{\partial \tau_{XY}}{\partial Y} = \rho \frac{\partial^2 u}{\partial t^2}, \quad \frac{\partial \sigma_{YY}}{\partial Y} + \frac{\partial \tau_{XY}}{\partial X} = \rho \frac{\partial^2 v}{\partial t^2} \quad (C.1)$$

The relationship between stresses and strains for a plane strain thermo-mechanical problem can be written as

$$\sigma_{XX} = (\lambda + 2\mu)\epsilon_{XX} + \lambda\epsilon_{YY} - \alpha(3\lambda + 2\mu)T \quad (C.2)$$

$$\sigma_{YY} = (\lambda + 2\mu)\epsilon_{YY} + \lambda\epsilon_{XX} - \alpha(3\lambda + 2\mu)T \quad (C.3)$$

$$\tau_{XY} = \mu\epsilon_{XY} \quad (C.4)$$

where X and Y are reference coordinates, σ_{ij} and ϵ_{ij} where $i = X, Y$ and $j = X, Y$ are in-plane stress and strain components, λ and μ denote Lamé's constant and shear modulus respectively. α is coefficient of thermal expansion and T represents the change in temperature in the infinite medium. For non homogenous materials Shear modulus (μ), Lamé's constant (λ), density (ρ), thermal expansion (α) and heat conductivity (k) of the FGM are assumed to vary in an exponential manner as given by Eq. C.5, whereas, Poisson's ratio (ν) is assumed to be a constant.

$$\mu = \mu_0 e^{(\zeta X)}, \lambda = \lambda_0 e^{(\zeta X)}, \rho = \rho_0 e^{(\zeta X)}, \alpha = \alpha_0 e^{(\beta X)}, k = k_0 e^{(\beta X)} \quad (C.5)$$

subscript "o" means at $X = 0$ as shown in Fig. C.1. and ζ and β are nonhomogeneity constants that have the dimension $(length)^{-1}$. For plane strain deformation,

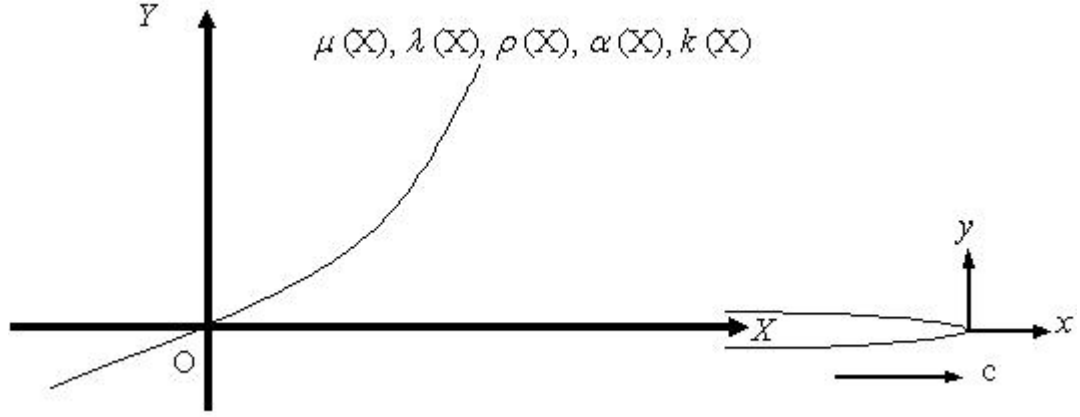


Figure C.1. Propagating crack tip orientation with respect to reference coordinate configuration.

the displacements u and v are derived from dilatational and shear wave potentials ϕ and ψ . These potentials can be expressed as

$$u = \frac{\partial \phi}{\partial X} + \frac{\partial \psi}{\partial Y}, \quad v = \frac{\partial \phi}{\partial Y} - \frac{\partial \psi}{\partial X} \quad (\text{C.6})$$

The strain can be derived from the displacement relation given by Eq. C.6

$$\begin{aligned} \epsilon_X &= \frac{\partial u}{\partial X} = \frac{\partial^2 \phi}{\partial X^2} + \frac{\partial^2 \psi}{\partial X \partial Y} \\ \epsilon_Y &= \frac{\partial v}{\partial Y} = \frac{\partial^2 \phi}{\partial Y^2} - \frac{\partial^2 \psi}{\partial X \partial Y} \\ \epsilon_{XY} &= \frac{\partial u}{\partial Y} + \frac{\partial v}{\partial X} = 2 \frac{\partial^2 \phi}{\partial X \partial Y} - \frac{\partial^2 \psi}{\partial X^2} + \frac{\partial^2 \psi}{\partial Y^2} \end{aligned} \quad (\text{C.7})$$

Substituting the relation for μ , λ , ρ , α and k from Eq. C.5 the Hookes's law for non-homogenous material can be written as

$$\sigma_{XX} = e^{(\zeta X)} ((\lambda_0 + 2\mu_0)\epsilon_{XX} + \lambda_0\epsilon_{YY} - (3\lambda_0 + 2\mu_0)\alpha_0 e^{(\beta X)} T) \quad (\text{C.8})$$

$$\sigma_{YY} = e^{(\zeta X)} ((\lambda_0 + 2\mu_0)\epsilon_{YY} + \lambda_0\epsilon_{XX} - (3\lambda_0 + 2\mu_0)\alpha_0 e^{(\beta X)} T) \quad (\text{C.9})$$

$$\tau_{XY} = e^{(\zeta X)} \mu_0 \epsilon_{XY} \quad (\text{C.10})$$

By substituting the strain relation given by Eq. C.7 into Eqs. C.8 - C.10, the Hookes's law for non-homogenous material in terms of displacement potentials can be written as

$$\begin{aligned}\sigma_{XX} = & e^{(\zeta X)}((\lambda_0 + 2\mu_0)(\frac{\partial^2 \phi}{\partial X^2} + \frac{\partial^2 \psi}{\partial X \partial Y}) + \lambda_0(\frac{\partial^2 \phi}{\partial Y^2} - \frac{\partial^2 \psi}{\partial X \partial Y}) \\ & - (3\lambda_0 + 2\mu_0)\alpha_0 e^{(\beta X)} T)\end{aligned}\quad (C.11)$$

$$\begin{aligned}\sigma_{YY} = & e^{(\zeta X)}((\lambda_0 + 2\mu_0)\frac{\partial^2 \phi}{\partial Y^2} - \frac{\partial^2 \psi}{\partial X \partial Y} + \lambda_0\frac{\partial^2 \phi}{\partial X^2} + \frac{\partial^2 \psi}{\partial X \partial Y} \\ & - (3\lambda_0 + 2\mu_0)\alpha_0 e^{(\beta X)} T)\end{aligned}\quad (C.12)$$

$$\tau_{XY} = e^{(\zeta X)}\mu_0 \left(2\frac{\partial^2 \phi}{\partial X \partial Y} - \frac{\partial^2 \psi}{\partial X^2} + \frac{\partial^2 \psi}{\partial Y^2} \right) \quad (C.13)$$

Substituting the stresses from Eqs. C.11 - C.13 into Eq. C.1 and after simplification, the equations of motion become

$$\begin{aligned}& (2\mu_0 + \lambda_0)\frac{\partial}{\partial X} \nabla^2 \phi + \mu_0\frac{\partial}{\partial Y} \nabla^2 \psi - \alpha_0 e^{\beta X}(3\lambda_0 + 2\mu_0) \left(\beta T + \frac{\partial T}{\partial X} \right) \\ & + \zeta \left(\lambda_0 \nabla^2 \phi + \mu_0(2\frac{\partial^2 \phi}{\partial X^2} + 2\frac{\partial^2 \psi}{\partial x \partial Y}) - \alpha_0 e^{\beta X}(3\lambda_0 + 2\mu_0)T \right) \\ & = \rho_0 \frac{\partial^2}{\partial t^2} \left(\frac{\partial \phi}{\partial X} + \frac{\partial \psi}{\partial Y} \right)\end{aligned}\quad (C.14)$$

$$\begin{aligned}& (2\mu_0 + \lambda_0)\frac{\partial}{\partial Y} \nabla^2 \phi - \mu_0\frac{\partial}{\partial X} \nabla^2 \psi - \alpha_0 e^{\beta X}(3\lambda_0 + 2\mu_0)\frac{\partial T}{\partial Y} \\ & + \zeta\mu_0 \left(2\frac{\partial^2 \phi}{\partial X \partial Y} - \frac{\partial^2 \psi}{\partial X^2} + \frac{\partial^2 \psi}{\partial Y^2} \right) = \rho_0 \frac{\partial^2}{\partial t^2} \left(\frac{\partial \phi}{\partial Y} - \frac{\partial \psi}{\partial X} \right)\end{aligned}\quad (C.15)$$

The above equation can be further simplified by rearranging Eqs. C.14 and C.15 in the following way

$\frac{\partial}{\partial X} (Eq. C.14) + \frac{\partial}{\partial Y} (Eq. C.15)$ after simplification gives

$$\begin{aligned}& (2\mu_0 + \lambda_0) \nabla^2 \nabla^2 \phi - \zeta \left((2\mu_0 + \lambda_0)\frac{\partial}{\partial X} \nabla^2 \phi + \mu_0\frac{\partial}{\partial Y} \nabla^2 \psi \right) \\ & - \alpha_0 e^{\beta X}(3\lambda_0 + 2\mu_0) \left(\left((\beta + \zeta)\beta T + (2\beta + \zeta)\frac{\partial T}{\partial X} \right) + \nabla^2 T \right) = \rho_0 \frac{\partial^2}{\partial t^2} \nabla^2 \phi\end{aligned}\quad (C.16)$$

Similarly $\frac{\partial}{\partial Y} (Eq.C.14) + \frac{\partial}{\partial X} (Eq.C.15)$ after simplification gives

$$\mu_0 \nabla^2 \nabla^2 \psi - \zeta \left((\mu_0 \frac{\partial}{\partial X} \nabla^2 \psi + \lambda_0 \frac{\partial}{\partial Y} \nabla^2 \phi) - \alpha_0 \epsilon^{\beta X} (3\lambda_0 + 2\mu_0) \zeta \frac{\partial T}{\partial Y} \right) = \rho_0 \frac{\partial^2}{\partial t^2} \nabla^2 \psi \quad (C.17)$$

The above equation can be further simplified to

$$\begin{aligned} & (\delta + 2) \nabla^2 \phi - \zeta \left((\delta + 2) \frac{\partial}{\partial X} \phi + \frac{\partial}{\partial Y} \psi \right) \\ & - \alpha_c (3\lambda_0 + 2\mu_0) \left(\left((\beta + \zeta) \beta \Delta^{-1} T + (2\beta + \zeta) \Delta^{-1} \frac{\partial T}{\partial X} \right) + T \right) = \frac{\rho_0}{\mu_0} \frac{\partial^2 \phi}{\partial t^2} \end{aligned} \quad (C.18)$$

$$\nabla^2 \psi - \zeta \frac{\partial \psi}{\partial X} + \zeta \delta \frac{\partial \phi}{\partial Y} - \alpha_c (3\lambda_0 + 2\mu_0) \zeta \Delta^{-1} \frac{\partial T}{\partial Y} = \frac{\rho_0}{\mu_0} \frac{\partial^2 \psi}{\partial t^2} \quad (C.19)$$

where

$$\Delta^{-1} = \frac{1}{\nabla^2}, \quad \delta = \frac{\lambda_0}{\mu_0}$$

$\alpha_c = \alpha_0 \epsilon^{\beta X}$ is the coefficient of thermal expansion in the vicinity of the instantaneous crack tip and is assumed to be constant.

Transforming to the Crack Tip Coordinates

For a propagating crack shown in Fig. C.1, the transformed crack tip coordinates can be written as $x = X - ct$ where c is constant crack tip speed. In the moving coordinate systems the above Eqs. C.18 and C.19 can be written as

$$\begin{aligned} & \alpha_l^2 \frac{\partial^2 \phi}{\partial x^2} + \frac{\partial^2 \phi}{\partial y^2} \zeta \frac{\partial \phi}{\partial x} + \frac{\zeta}{\delta + 2} \frac{\partial \psi}{\partial y} \\ & - \alpha_c \frac{(3\delta + 2)}{(\delta + 2)} \left(\left((\beta + \zeta) \beta \Delta^{-1} T + (2\beta + \zeta) \Delta^{-1} \frac{\partial T}{\partial X} \right) + T \right) = 0 \end{aligned} \quad (C.20)$$

$$\alpha_s^2 \frac{\partial^2 \psi}{\partial x^2} + \frac{\partial^2 \psi}{\partial y^2} + \zeta \frac{\partial \psi}{\partial x} + \zeta \delta \frac{\partial \phi}{\partial y} - \alpha_c (3\delta + 2) \zeta \Delta^{-1} \frac{\partial T}{\partial y} = 0 \quad (C.21)$$

where

$$\alpha_l = \sqrt{1 - \left(\frac{c}{c_l}\right)^2}, \quad \alpha_s = \sqrt{1 - \left(\frac{c}{c_s}\right)^2}, \quad c_s = \sqrt{\frac{\mu_c}{\rho_c}}, \quad \nabla^2 = \frac{\partial^2}{\partial x^2} + \frac{\partial^2}{\partial y^2}$$

$c_l = c_s \sqrt{2(1 - \nu)/(1 - 2\nu)}$ for plane strain and $c_l = c_s \sqrt{2/(1 - \nu)}$ for plane stress. c_l and c_s are the elastic dilatational wave speed and the elastic shear wave speed of the material at the crack tip.

Asymptotic Expansion of Crack Tip Stress Fields

Asymptotic approach is used in deriving solutions for displacement potentials of equations of motion Eqs. C.20 and C.21. A new set of coordinates is introduced as

$$\eta_1 = \frac{x}{\epsilon}, \quad \eta_2 = \frac{y}{\epsilon} \quad (\text{C.22})$$

$$\frac{\partial}{\partial x} = \frac{1}{\epsilon} \frac{\partial}{\partial \eta_1}, \quad \frac{\partial}{\partial y} = \frac{1}{\epsilon} \frac{\partial}{\partial \eta_2}, \quad \frac{\partial^2}{\partial x^2} = \frac{1}{\epsilon^2} \frac{\partial^2}{\partial \eta_1^2} \quad \text{and} \quad \frac{\partial^2}{\partial y^2} = \frac{1}{\epsilon^2} \frac{\partial^2}{\partial \eta_2^2} \quad (\text{C.23})$$

where ϵ is an arbitrary parameter and is assumed to be $0 < \epsilon < 1$

Equation C.20 and C.21 can be written in a new scaled coordinates (η_1, η_2) as

$$\begin{aligned} & \alpha_l^2 \frac{\partial^2 \phi}{\partial \eta_1^2} + \frac{\partial^2 \phi}{\partial \eta_2^2} - \epsilon \left(\zeta \frac{\partial \phi}{\partial \eta_1} + \frac{\zeta}{\delta + 2} \frac{\partial \psi}{\partial \eta_2} \right) - \\ & \alpha_c \frac{(3\delta + 2)}{(\delta + 2)} \left(\epsilon^2 T + \epsilon^3 (2\beta + \zeta) \Delta^{-1} \frac{\partial T}{\partial \eta_1} + \epsilon^4 (\beta + \zeta) \beta \Delta^{-1} T \right) = 0 \end{aligned} \quad (\text{C.24})$$

$$\alpha_s^2 \frac{\partial^2 \psi}{\partial \eta_1^2} + \frac{\partial^2 \psi}{\partial \eta_2^2} - \epsilon \left(\zeta \frac{\partial \psi}{\partial \eta_1} + \zeta \delta \frac{\partial \phi}{\partial \eta_2} \right) - \alpha_c (3\delta + 2) \epsilon^3 \zeta \Delta^{-1} \frac{\partial T}{\partial \eta_2} = 0 \quad (\text{C.25})$$

At this stage it is assumed that ϕ , ψ , and T can be represented as a power series

expansion in ϵ .

$$\begin{aligned}
\phi(x, y) &= \phi(\epsilon\eta_1, \epsilon\eta_2) = \sum_{m=0}^{\infty} \epsilon^{\frac{(m+3)}{2}} \phi_m(\eta_1, \eta_2) \\
\psi(x, y) &= \psi(\epsilon\eta_1, \epsilon\eta_2) = \sum_{m=0}^{\infty} \epsilon^{\frac{(m+3)}{2}} \psi_m(\eta_1, \eta_2) \\
T(x, y) &= T(\epsilon\eta_1, \epsilon\eta_2) = \sum_{m=0}^{\infty} \epsilon^{\frac{(m+1)}{2}} T_m(\eta_1, \eta_2)
\end{aligned} \tag{C.26}$$

Substituting Eq. C.26 into Eqs. C.24 and C.25 gives the following equations

$$\begin{aligned}
&\sum_{m=0}^{\infty} \left(\epsilon^{\frac{m+3}{2}} \left(\alpha_l^2 \frac{\partial^2 \phi_m}{\partial \eta_1^2} + \frac{\partial^2 \phi_m}{\partial \eta_2^2} \right) + \epsilon^{\frac{m+5}{2}} \left(\zeta \frac{\partial \phi_m}{\partial \eta_1} + \frac{\zeta}{\delta+2} \frac{\partial \psi_m}{\partial \eta_2} \right) - \right. \\
&\quad \left. \alpha_c \frac{(3\delta+2)}{(\delta+2)} \left(\epsilon^{\frac{m+5}{2}} T_m + \epsilon^{\frac{m+7}{2}} (2\beta+\zeta) \Delta^{-1} \frac{\partial T_m}{\partial \eta_1} + \epsilon^{\frac{m+9}{2}} (\beta+\zeta) \beta \Delta^{-1} T_m \right) \right) = 0
\end{aligned} \tag{C.27}$$

$$\begin{aligned}
&\sum_{m=0}^{\infty} \left(\epsilon^{\frac{m+3}{2}} \left(\alpha_s^2 \frac{\partial^2 \psi_m}{\partial \eta_1^2} + \frac{\partial^2 \psi_m}{\partial \eta_2^2} \right) + \epsilon^{\frac{m+5}{2}} \left(\zeta \frac{\partial \psi_m}{\partial \eta_1} + \zeta \delta \frac{\partial \phi_m}{\partial \eta_2} \right) - \right. \\
&\quad \left. \alpha_c (3\delta+2) \epsilon^{\frac{m+7}{2}} \zeta \Delta^{-1} \frac{\partial T_m}{\partial \eta_2} \right) = 0
\end{aligned} \tag{C.28}$$

For Eqs. C.27 and C.28 to be valid, the partial differential equations corresponding to each power of ϵ ($\epsilon^{3/2}, \epsilon^2, \epsilon^{5/2}, \dots$) should vanish independently. The solution for the first few terms of the series are considered.

For $m = 0$, the above equation Eqs. C.27 and C.28 gives

$$\begin{aligned}
&\epsilon^{\frac{3}{2}} \left(\alpha_l^2 \frac{\partial^2 \phi_0}{\partial \eta_1^2} + \frac{\partial^2 \phi_0}{\partial \eta_2^2} \right) + \epsilon^{\frac{5}{2}} \left(\zeta \frac{\partial \phi_0}{\partial \eta_1} + \frac{\zeta}{\delta+2} \frac{\partial \psi_0}{\partial \eta_2} \right) - \\
&\quad \alpha_c \frac{(3\delta+2)}{(\delta+2)} \left(\epsilon^{\frac{5}{2}} T_0 + \epsilon^{\frac{7}{2}} (2\beta+\zeta) \Delta^{-1} \frac{\partial T_0}{\partial \eta_1} + \epsilon^{\frac{9}{2}} (\beta+\zeta) \beta \Delta^{-1} T_0 \right) = 0
\end{aligned} \tag{C.29}$$

$$\begin{aligned}
&\epsilon^{\frac{3}{2}} \left(\alpha_s^2 \frac{\partial^2 \psi_0}{\partial \eta_1^2} + \frac{\partial^2 \psi_0}{\partial \eta_2^2} \right) + \epsilon^{\frac{5}{2}} \left(\zeta \frac{\partial \psi_0}{\partial \eta_1} + \zeta \delta \frac{\partial \phi_0}{\partial \eta_2} \right) - \alpha_c (3\delta+2) \epsilon^{\frac{7}{2}} \zeta \Delta^{-1} \frac{\partial T_0}{\partial \eta_2} = 0
\end{aligned} \tag{C.30}$$

For $m = 1$, the above equation Eqs. C.27 and C.28 gives

$$\begin{aligned} & \epsilon^2 \left(\alpha_l^2 \frac{\partial^2 \phi_1}{\partial \eta_1^2} + \frac{\partial^2 \phi_1}{\partial \eta_2^2} \right) + \epsilon^3 \left(\zeta \frac{\partial \phi_1}{\partial \eta_1} + \frac{\zeta}{\delta + 2} \frac{\partial \psi_1}{\partial \eta_2} \right) - \\ & \alpha_c \frac{(3\delta + 2)}{(\delta + 2)} \left(\epsilon^3 T_1 + \epsilon^4 (2\beta + \zeta) \Delta^{-1} \frac{\partial T_1}{\partial \eta_1} + \epsilon^5 (\beta + \zeta) \beta \Delta^{-1} T_1 \right) = 0 \end{aligned} \quad (\text{C.31})$$

$$\epsilon^2 \left(\alpha_s^2 \frac{\partial^2 \psi_1}{\partial \eta_1^2} + \frac{\partial^2 \psi_1}{\partial \eta_2^2} \right) + \epsilon^3 \left(\zeta \frac{\partial \psi_1}{\partial \eta_1} + \zeta \delta \frac{\partial \phi_1}{\partial \eta_2} \right) - \alpha_c (3\delta + 2) \epsilon^4 \zeta \Delta^{-1} \frac{\partial T_1}{\partial \eta_2} = 0 \quad (\text{C.32})$$

For $m = 2$, the above equation Eqs. C.27 and C.28 gives

$$\begin{aligned} & \epsilon^{\frac{5}{2}} \left(\alpha_l^2 \frac{\partial^2 \phi_2}{\partial \eta_1^2} + \frac{\partial^2 \phi_2}{\partial \eta_2^2} \right) + \epsilon^{\frac{7}{2}} \left(\zeta \frac{\partial \phi_2}{\partial \eta_1} + \frac{\zeta}{\delta + 2} \frac{\partial \psi_2}{\partial \eta_2} \right) - \\ & \alpha_c \frac{(3\delta + 2)}{(\delta + 2)} \left(\epsilon^{\frac{7}{2}} T_2 + \epsilon^{\frac{9}{2}} (2\beta + \zeta) \Delta^{-1} \frac{\partial T_2}{\partial \eta_1} + \epsilon^{\frac{11}{2}} (\beta + \zeta) \beta \Delta^{-1} T_2 \right) = 0 \end{aligned} \quad (\text{C.33})$$

$$\begin{aligned} & \epsilon^{\frac{5}{2}} \left(\alpha_s^2 \frac{\partial^2 \psi_2}{\partial \eta_1^2} + \frac{\partial^2 \psi_2}{\partial \eta_2^2} \right) + \epsilon^{\frac{7}{2}} \left(\zeta \frac{\partial \psi_2}{\partial \eta_1} + \zeta \delta \frac{\partial \phi_2}{\partial \eta_2} \right) - \alpha_c (3\delta + 2) \epsilon^{\frac{9}{2}} \zeta \Delta^{-1} \frac{\partial T_2}{\partial \eta_2} = 0 \end{aligned} \quad (\text{C.34})$$

By collecting the partial differential equations corresponding to each power of ϵ ($\epsilon^{3/2}, \epsilon^2, \epsilon^{5/2}, \dots$) leads to the following set of partial differential equations.

$\epsilon^{\frac{3}{2}}$ terms ($m = 0$)

$$\alpha_l^2 \frac{\partial^2 \phi_0}{\partial \eta_1^2} + \frac{\partial^2 \phi_0}{\partial \eta_2^2} = 0 \quad (\text{C.35})$$

$$\alpha_s^2 \frac{\partial^2 \psi_0}{\partial \eta_1^2} + \frac{\partial^2 \psi_0}{\partial \eta_2^2} = 0 \quad (\text{C.36})$$

ϵ^s terms ($m = 1$)

$$\alpha_l^2 \frac{\partial^2 \phi_1}{\partial \eta_1^2} + \frac{\partial^2 \phi_1}{\partial \eta_2^2} = 0 \quad (\text{C.37})$$

$$\alpha_s^2 \frac{\partial^2 \psi_1}{\partial \eta_1^2} + \frac{\partial^2 \psi_1}{\partial \eta_2^2} = 0 \quad (\text{C.38})$$

$\epsilon^{\frac{5}{2}}$ terms ($m = 2$)

$$\alpha_l^2 \frac{\partial^2 \phi_2}{\partial \eta_1^2} + \frac{\partial^2 \phi_2}{\partial \eta_2^2} = -\zeta \left(\frac{\partial \phi_0}{\partial \eta_1} + \frac{1}{\delta + 2} \frac{\partial \psi_0}{\partial \eta_2} \right) + \frac{3\delta + 2}{\delta + 2} \alpha_c T_0 \quad (\text{C.39})$$

$$\alpha_l^2 \frac{\partial^2 \psi_2}{\partial \eta_1^2} + \frac{\partial^2 \psi_2}{\partial \eta_2^2} = -\zeta \left(\frac{\partial \psi_0}{\partial \eta_1} + \frac{1}{\delta + 2} \frac{\partial \phi_0}{\partial \eta_2} \right) \quad (\text{C.40})$$

Eqs. C.35 - C.38 are similar to that for homogeneous material where as the partial differential equations Eqs. C.39 and C.40, associated with higher powers of ϵ are coupled to the differentials of the lower order functions through the nonhomogeneity parameters and temperature term. Eqs. C.35 - C.38 (i.e. for $m = 0$ and $m = 1$) can be easily reduced to Laplace's equation in the respective complex domains $\zeta_l = \eta_1 + i\alpha_l\eta_2$, $\zeta_s = \eta_1 + i\alpha_s\eta_2$, $i = \sqrt{-1}$ and the solutions are same as that for homogenous material and can be written as

$$\phi_m(\rho_l, \theta_l, t) = A_m \rho_l^{(m+3)/2} \cos\left(\frac{(m+3)}{2}\theta_l\right) + C_m \rho_l^{(m+3)/2} \sin\left(\frac{(m+3)}{2}\theta_l\right) \quad (\text{C.41})$$

$$\psi_m(\rho_s, \theta_s, t) = B_m \rho_s^{(m+3)/2} \sin\left(\frac{(m+3)}{2}\theta_s\right) + D_m \rho_s^{(m+3)/2} \cos\left(\frac{(m+3)}{2}\theta_s\right) \quad (\text{C.42})$$

where

$$\rho_l = (\eta_1^2 + \alpha_l^2 \eta_2^2)^{1/2}, \quad \tan(\theta_l) = \frac{\alpha_l \eta_2}{\eta_1}, \quad \rho_s = (\eta_1^2 + \alpha_s^2 \eta_2^2)^{1/2}, \quad \tan(\theta_s) = \frac{\alpha_s \eta_2}{\eta_1}$$

and A_m , B_m , C_m , and D_m are real constants.

The solution for the Eqs. C.39 and C.40 corresponding to higher powers of ϵ ($m = 2$) consists of two parts: solution for homogeneous equation and a particular solution due to nonhomogeneity and temperature and these can be obtained recursively. Eq. C.39 can be divided into four different problems as shown below

$$\alpha_l^2 \frac{\partial^2 \phi_2}{\partial \eta_1^2} + \frac{\partial^2 \phi_2}{\partial \eta_2^2} = 0 \quad (\text{C.43})$$

$$\alpha_l^2 \frac{\partial^2 \phi_2}{\partial \eta_1^2} + \frac{\partial^2 \phi_2}{\partial \eta_2^2} = -\zeta \frac{\partial \phi_0}{\partial \eta_1} \quad (\text{C.44})$$

$$\alpha_l^2 \frac{\partial^2 \phi_2}{\partial \eta_1^2} + \frac{\partial^2 \phi_2}{\partial \eta_2^2} = -\frac{\zeta}{\delta + 2} \frac{\partial \psi_0}{\partial \eta_2} \quad (\text{C.45})$$

$$\alpha_l^2 \frac{\partial^2 \phi_2}{\partial \eta_1^2} + \frac{\partial^2 \phi_2}{\partial \eta_2^2} = \frac{3\delta + 2}{\delta + 2} \alpha_c T_0 \quad (\text{C.46})$$

By solving the above partial differential equations separately and later by adding all together, the solution for ϕ_2 can obtained as

$$\begin{aligned} \phi_2 = & A_2 \rho_l^{5/2} \cos\left(\frac{5}{2}\theta_l\right) + C_2 \rho_l^{5/2} \sin\left(\frac{5}{2}\theta_l\right) \\ & - \frac{1}{4} \frac{\zeta}{\alpha_l^2} \rho_l^{5/2} \left(A_0 \cos\left(\frac{1}{2}\theta_l\right) + C_0 \sin\left(\frac{1}{2}\theta_l\right) \right) \\ & - \frac{2}{5} \frac{\zeta}{(\delta + 2)} \frac{\alpha_s}{(\alpha_l^2 - \alpha_s^2)} \rho_s^{5/2} \left(B_0 \cos\left(\frac{5}{2}\theta_s\right) + D_0 \sin\left(\frac{5}{2}\theta_s\right) \right) \\ & + \frac{4}{15} \frac{(3\delta + 2)}{(\delta + 2)} \frac{\alpha_c}{(\alpha_l^2 - 1)} q_0 \rho^{5/2} \sin \frac{5}{2}\theta \end{aligned} \quad (\text{C.47})$$

Similarly Eq. C.40 can be divided into three different problems as shown below

$$\alpha_l^2 \frac{\partial^2 \psi_2}{\partial \eta_1^2} + \frac{\partial^2 \psi_2}{\partial \eta_2^2} = 0 \quad (\text{C.48})$$

$$\alpha_l^2 \frac{\partial^2 \psi_2}{\partial \eta_1^2} + \frac{\partial^2 \psi_2}{\partial \eta_2^2} = -\zeta \frac{\partial \psi_0}{\partial \eta_1} \quad (\text{C.49})$$

$$\alpha_l^2 \frac{\partial^2 \psi_2}{\partial \eta_1^2} + \frac{\partial^2 \psi_2}{\partial \eta_2^2} = -\frac{\zeta}{\delta + 2} \frac{\partial \phi_0}{\partial \eta_2} \quad (\text{C.50})$$

By solving the above partial differential equations separately and later by adding all together, the solution for ψ_2 can be obtained as

$$\begin{aligned}\psi_2 = & B_2 \rho_s^{5/2} \cos\left(\frac{5}{2}\theta_s\right) + D_2 \rho_s^{5/2} \sin\left(\frac{5}{2}\theta_s\right) \\ & - \frac{1}{4} \frac{\zeta}{\alpha_s^2} \rho_s^{5/2} \left(B_0 \sin\left(\frac{1}{2}\theta_s\right) + D_0 \cos\left(\frac{1}{2}\theta_s\right) \right) \\ & - \frac{2}{5} \delta \frac{\zeta \alpha_l}{(\alpha_l^2 - \alpha_s^2)} \rho_l^{5/2} \left(A_0 \sin\left(\frac{5}{2}\theta_l\right) + C_0 \sin\left(\frac{5}{2}\theta_l\right) \right)\end{aligned}\quad (\text{C.51})$$

The solutions ϕ_0 , ψ_0 , ϕ_1 and ψ_1 automatically satisfy the compatibility equations because these the solutions are same as those for homogeneous materials. Since the non-homogeneous specific parts of ϕ_2 and ψ_2 are obtained from ϕ_0 and ψ_0 , they also automatically satisfy the compatibility equations.

By assembling together the above result for the first few terms and by transforming back to the $x - y$ plane, the combined solution can be written for ϕ and ψ as Eq. C.52 and C.53

$$\begin{aligned}\phi = & A_0 r_l^{3/2} \cos\left(\frac{3}{2}\theta_l\right) + C_0 r_l^{3/2} \sin\left(\frac{3}{2}\theta_l\right) + A_1 r_l^2 \cos(2\theta_l) + C_1 r_l^2 \sin(2\theta_l) \\ & + A_2 r_l^{5/2} \cos\left(\frac{5}{2}\theta_l\right) + C_2 r_l^{5/2} \sin\left(\frac{5}{2}\theta_l\right) \\ & - \frac{1}{4} \frac{\zeta}{\alpha_l^2} r_l^{5/2} \left(A_0 \cos\left(\frac{1}{2}\theta_l\right) + C_0 \sin\left(\frac{1}{2}\theta_l\right) \right) \\ & - \frac{2}{5} \frac{\zeta}{(\delta + 2)} \frac{\alpha_s}{(\alpha_l^2 - \alpha_s^2)} r_s^{5/2} \left(B_0 \cos\left(\frac{5}{2}\theta_s\right) + D_0 \sin\left(\frac{5}{2}\theta_s\right) \right) \\ & + \frac{4}{15} \frac{(3\delta + 2)}{(\delta + 2)} \frac{\alpha_c}{(\alpha_l^2 - 1)} q_0 r^{5/2} \sin \frac{5}{2}\theta\end{aligned}\quad (\text{C.52})$$

$$\begin{aligned}
\psi = & B_0 r_s^{3/2} \sin\left(\frac{3}{2}\theta_s\right) + D_0 r_s^{3/2} \cos\left(\frac{3}{2}\theta_s\right) + B_1 r_s^2 \sin(2\theta_s) + D_1 r_s^2 \cos(2\theta_s) \\
& + B_2 r_s^{5/2} \cos\left(\frac{5}{2}\theta_s\right) + D_2 r_s^{5/2} \sin\left(\frac{5}{2}\theta_s\right) \\
& - \frac{1}{4} \frac{\zeta}{\alpha_s^2} \rho_s^{5/2} \left(B_0 \sin\left(\frac{1}{2}\theta_s\right) + D_0 \cos\left(\frac{1}{2}\theta_s\right) \right) \\
& - \frac{2}{5} \delta \frac{\zeta \alpha_l}{(\alpha_l^2 - \alpha_s^2)} \rho_l^{5/2} \left(A_0 \sin\left(\frac{5}{2}\theta_l\right) + C_0 \sin\left(\frac{5}{2}\theta_l\right) \right)
\end{aligned} \tag{C.53}$$

where

$$r_l = (x^2 + \alpha_l^2 y^2)^{1/2}, \quad \tan(\theta_l) = \frac{\alpha_l y}{x}, \quad r_s = (x^2 + \alpha_s^2 y^2)^{1/2}, \quad \tan(\theta_s) = \frac{\alpha_s y}{x}$$

The above displacement potentials are now used with Eq.C.6 to get the displacements fields. The in-plane displacement can be given as

$$\begin{aligned}
u = & \left(\frac{3}{2} r_l^{1/2} \cos \left(\frac{1}{2} \theta_l \right) - \frac{1}{8} \frac{\zeta}{\alpha_l^2} r_l^{3/2} \left(3 \cos \left(\frac{1}{2} \theta_l \right) + 2 \cos \left(\frac{3}{2} \theta_l \right) \right) \right) A_0 \\
& + \left(\frac{3}{2} r_l^{1/2} \sin \left(\frac{1}{2} \theta_l \right) - \frac{1}{8} \frac{\zeta}{\alpha_l^2} r_l^{3/2} \left(-3 \sin \left(\frac{1}{2} \theta_l \right) + 2 \sin \left(\frac{3}{2} \theta_l \right) \right) \right) C_0 \\
& + \left(\frac{3}{2} \alpha_s r_s^{1/2} \cos \left(\frac{1}{2} \theta_s \right) - \frac{1}{8} \frac{\zeta}{\alpha_s} r_s^{3/2} \left(3 \cos \left(\frac{1}{2} \theta_s \right) - 2 \cos \left(\frac{3}{2} \theta_s \right) \right) \right) B_0 \\
& \left(-\frac{3}{2} \alpha_s r_s^{1/2} \cos \left(\frac{1}{2} \theta_s \right) - \frac{1}{8} \frac{\zeta}{\alpha_s} r_s^{3/2} \left(3 \sin \left(\frac{1}{2} \theta_s \right) + 2 \sin \left(\frac{3}{2} \theta_s \right) \right) \right) D_0 \\
& + 2A_1 r_l \cos(\theta_l) + 2C_1 r_l \sin(\theta_l) + 2B_1 r_s \alpha_s \cos(2\theta_s) + 2D_1 r_s \alpha_s \sin(2\theta_s) \\
& + \frac{5}{2} A_2 r_l^{3/2} \cos \left(\frac{3}{2} \theta_l \right) + \frac{5}{2} B_2 \alpha_s r_s^{3/2} \cos \left(\frac{3}{2} \theta_s \right) + \frac{5}{2} \\
& + C_2 r_l^{3/2} \sin \left(\frac{3}{2} \theta_l \right) - \frac{5}{2} D_2 \alpha_s r_s^{3/2} \sin \left(\frac{3}{2} \theta_s \right) \\
& - \frac{\zeta \delta \alpha_l^2}{\alpha_l^2 - \alpha_s^2} \left(A_0 r_l^{3/2} \cos \left(\frac{3}{2} \theta_l \right) + C_0 r_l^{3/2} \sin \left(\frac{3}{2} \theta_l \right) \right) \\
& - \frac{\zeta}{\delta + 2} \frac{\alpha_s}{\alpha_l^2 - \alpha_s^2} \left(B_0 r_s^{3/2} \cos \left(\frac{3}{2} \theta_s \right) + D_0 r_s^{3/2} \sin \left(\frac{3}{2} \theta_s \right) \right) \\
& - \frac{\zeta \delta \alpha_l^2}{\alpha_l^2 - \alpha_s^2} \left(A_0 r_l^{3/2} \cos \left(\frac{3}{2} \theta_l \right) - C_0 r_l^{3/2} \sin \left(\frac{3}{2} \theta_l \right) \right) \\
& - \frac{\zeta}{\delta + 2} \frac{\alpha_s}{\alpha_l^2 - \alpha_s^2} \left(B_0 r_s^{3/2} \cos \left(\frac{3}{2} \theta_s \right) - D_0 r_s^{3/2} \sin \left(\frac{3}{2} \theta_s \right) \right) \\
& + \frac{3}{2} \frac{(3\delta + 2)}{(\delta + 2)} \frac{\alpha_c}{(\alpha_l^2 - 1)} q_0 r^{3/2} \sin \frac{3}{2} \theta
\end{aligned} \tag{C.54}$$

$$\begin{aligned}
v = & \left(-\frac{3}{2}\alpha_l r_l^{1/2} \sin\left(\frac{1}{2}\theta_l\right) - \frac{1}{8}\frac{\zeta}{\alpha_l} r_l^{3/2} \left(3\sin\left(\frac{1}{2}\theta_l\right) + 2\sin\left(\frac{3}{2}\theta_l\right) \right) \right) A_0 \\
& + \left(\frac{3}{2}\alpha_l r_l^{1/2} \cos\left(\frac{1}{2}\theta_l\right) - \frac{1}{8}\frac{\zeta}{\alpha_l} r_l^{3/2} \left(3\cos\left(\frac{1}{2}\theta_l\right) - 2\cos\left(\frac{3}{2}\theta_l\right) \right) \right) C_0 \\
& + \left(-\frac{3}{2}r_s^{1/2} \sin\left(\frac{1}{2}\theta_s\right) - \frac{1}{8}\frac{\zeta}{\alpha_s^2} r_s^{3/2} \left(3\sin\left(\frac{1}{2}\theta_s\right) - 2\sin\left(\frac{3}{2}\theta_s\right) \right) \right) B_0 \\
& + \left(-\frac{3}{2}r_s^{1/2} \cos\left(\frac{1}{2}\theta_s\right) - \frac{1}{8}\frac{\zeta}{\alpha_s^2} r_s^{3/2} \left(-3\cos\left(\frac{1}{2}\theta_s\right) - 2\cos\left(\frac{3}{2}\theta_s\right) \right) \right) D_0 \\
& - 2A_1 r_l \alpha_l \sin(\theta_l) - 2B_1 r_s \sin(\theta_s) + 2C_1 \alpha_l r_l \cos(\theta_l) - 2D_1 r_s \cos(\theta_s) \\
& - \frac{5}{2}A_2 \alpha_l r_l^{3/2} \sin\left(\frac{3}{2}\theta_l\right) - \frac{5}{2}B_2 r_s^{3/2} \cos\left(\frac{3}{2}\theta_s\right) \\
& + \frac{5}{2}C_2 \alpha_l r_l^{3/2} \sin\left(\frac{3}{2}\theta_l\right) - \frac{5}{2}D_2 r_s^{3/2} \cos\left(\frac{3}{2}\theta_s\right) \\
& + \frac{\zeta \delta \alpha_l}{\alpha_l^2 - \alpha_s^2} \left(A_0 r_l^{3/2} \sin\left(\frac{3}{2}\theta_l\right) + C_0 r_l^{3/2} \cos\left(\frac{3}{2}\theta_l\right) \right) \\
& + \frac{\zeta}{\delta + 2} \frac{\alpha_s^2}{\alpha_l^2 - \alpha_s^2} \left(B_0 r_s^{3/2} \sin\left(\frac{3}{2}\theta_s\right) - D_0 r_s^{3/2} \cos\left(\frac{3}{2}\theta_s\right) \right) \\
& + \frac{3}{2} \frac{(3\delta + 2)}{(\delta + 2)} \frac{\alpha_c}{(\alpha_l^2 - 1)} q_0 r^{3/2} \cos \frac{s}{2} \tag{C.55}
\end{aligned}$$

Temperature Fields around the Crack Tip

In this analysis it is assumed that the temperature field around the crack tip changes asymptotically. Also, the transient effects are neglected. The heat conductivity is assumed to vary exponentially as given by Eq. C.5. The steady state heat conduction equation can be written as

$$\frac{\partial}{\partial X} \left(k \frac{\partial T}{\partial X} \right) + \frac{\partial}{\partial Y} \left(k \frac{\partial T}{\partial Y} \right) = 0 \tag{C.56}$$

Where k is the coefficient of thermal conductivity

Assuming that k is constant in the region considered, the above equation can be written as

$$\nabla^2 T + \beta \frac{\partial T}{\partial X} = 0 \tag{C.57}$$

where $\nabla^2 = \frac{\partial^2}{\partial X^2} + \frac{\partial^2}{\partial Y^2}$

Transforming the above equation to the crack-tip moving coordinate system ($x =$

$Xc - t, y = Y$), Eq. C.57 can be written as

$$\nabla^2 T + \beta \frac{\partial T}{\partial x} = 0 \quad (\text{C.58})$$

where $\nabla^2 = \frac{\partial^2}{\partial x^2} + \frac{\partial^2}{\partial y^2}$

As this stages asymptotic analysis is performed to solve the above Eq. C.58.

Eq. C.58 in a new scaled coordinates (η_1, η_2) given by Eq. C.22 can be written as

$$\nabla^2 T + \epsilon \beta \frac{\partial T}{\partial \eta_1} = 0 \quad (\text{C.59})$$

where $\nabla^2 = \frac{\partial^2}{\partial \eta_1^2} + \frac{\partial^2}{\partial \eta_2^2}$

For the asymptotic analysis T is represented as a power series expansion in ϵ as

$$T(x, y) = T(\eta_1 \epsilon, \eta_2 \epsilon) = \sum_{m=0}^{\infty} \epsilon^{\frac{(m+1)}{2}} T_m(\eta_1, \eta_2) \quad (\text{C.60})$$

Substituting Eq.C.60 into Eq.C.59 gives the following equation.

$$\sum_{m=0}^{\infty} \epsilon^{\frac{(m+1)}{2}} \left(\left(\frac{\partial^2 T_m}{\partial \eta_1^2} + \frac{\partial^2 T_m}{\partial \eta_2^2} \right) + \epsilon^{\frac{(m+3)}{2}} \beta \frac{\partial T_m}{\partial \eta_1} \right) = 0 \quad (\text{C.61})$$

For Eq.C.61 to be valid, the partial differential equations corresponding to each power of ϵ ($\epsilon^{1/2}, \epsilon, \epsilon^{3/2}, \dots$) should vanish independently. This leads to the set of partial differential equations.

For $m = 0$, the above equation Eq. C.61 gives

$$\epsilon^{1/2} \left(\frac{\partial^2 T_0}{\partial \eta_1^2} + \frac{\partial^2 T_0}{\partial \eta_2^2} \right) + \epsilon^{3/2} \beta \frac{\partial T_0}{\partial \eta_1} = 0 \quad (\text{C.62})$$

For $m = 1$, the above equation Eq. C.61 gives

$$\epsilon \left(\frac{\partial^2 T_1}{\partial \eta_1^2} + \frac{\partial^2 T_1}{\partial \eta_2^2} \right) + \epsilon^2 \beta \frac{\partial T_0}{\partial \eta_1} = 0 \quad (\text{C.63})$$

For $m = 2$, the above equation Eqs. C.61 gives

$$\epsilon^{3/2} \left(\frac{\partial^2 T_2}{\partial \eta_1^2} + \frac{\partial^2 T_2}{\partial \eta_2^2} \right) + \epsilon^{5/2} \beta \frac{\partial T_2}{\partial \eta_1} = 0 \quad (\text{C.64})$$

By collecting the partial differential equations corresponding to each power of ϵ ($\epsilon^{1/2}, \epsilon, \epsilon^{3/2}, \dots$) leads to the following set of partial differential equations.

$\epsilon^{\frac{1}{2}}$ terms ($m = 0$)

$$\left(\frac{\partial^2 T_0}{\partial \eta_1^2} + \frac{\partial^2 T_0}{\partial \eta_2^2} \right) = 0 \quad (\text{C.65})$$

ϵ terms ($m = 1$)

$$\left(\frac{\partial^2 T_1}{\partial \eta_1^2} + \frac{\partial^2 T_1}{\partial \eta_2^2} \right) = 0 \quad (\text{C.66})$$

$\epsilon^{\frac{5}{2}}$ terms ($m = 2$)

$$\left(\frac{\partial^2 T_2}{\partial \eta_1^2} + \frac{\partial^2 T_2}{\partial \eta_2^2} \right) + \beta \frac{\partial T_0}{\partial \eta_1} = 0 \quad (\text{C.67})$$

Eqs. C.65 and C.66 are similar to that for homogeneous material where as the partial differential equation Eq. C.67 associated with higher powers of m is coupled to the differentials of the lower order functions through the nonhomogeneity parameters and temperature term. Eqs. C.65 and C.66 (i.e. for $m = 0$ and $m = 1$) can be easily reduced to Laplace's equation in the respective complex domains $\rho = \eta_1 + i\eta_2$, and $i = \sqrt{-1}$ and the solutions are same as that for homogenous material. By using crack tip insulated boundary condition i.e $\frac{\partial T}{\partial \theta} = 0$, at $\theta = \pi$, the solution for above laplace equation can written as

For $m = 0$

$$T_0 = q_0 \rho^{1/2} \sin \left(\frac{1}{2} \theta \right) \quad (\text{C.68})$$

For $m = 1$

$$T_1 = q_1 \rho^{1/2} \cos (\theta) \quad (\text{C.69})$$

where $\rho = (\eta_1^2 + \eta_2^2)^{1/2}$

The solution T_2 , for Eq.C.67 corresponding to higher powers of ϵ ($m = 2$) has two

parts: homogeneous and particular solution and can be written independently as follows

$$\left(\frac{\partial^2 T_2}{\partial \eta_1^2} + \frac{\partial^2 T_2}{\partial \eta_2^2}\right) = 0 \quad (\text{C.70})$$

$$\left(\frac{\partial^2 T_2}{\partial \eta_1^2} + \frac{\partial^2 T_2}{\partial \eta_2^2}\right) = -\beta \frac{\partial T_0}{\partial \eta_1} \quad (\text{C.71})$$

Eq. C.70 is similar to that for homogeneous material and the particular solution can be obtained using recursive approach, and the complete solution for Eq. C.70 and Eq. C.71 is given below.

$$T_2 = q_2 \rho^{3/2} \sin\left(\frac{3}{2}\theta\right) + \left(\frac{1}{4}\right) q_0 \beta \rho^{3/2} \sin\left(\frac{1}{2}\theta\right) \quad (\text{C.72})$$

By adding the above terms, the temperature field for the first 2 terms can be given as

$$T = q_0 \rho^{1/2} \sin\left(\frac{1}{2}\theta\right) + q_1 \rho \cos(\theta) + q_2 \rho^{3/2} \sin\left(\frac{3}{2}\theta\right) + \left(\frac{1}{4}\right) q_0 \beta \rho^{3/2} \sin\left(\frac{1}{2}\theta\right) \quad (\text{C.73})$$

where $\rho = (\eta_1^2 + \eta_2^2)^{1/2}$ and $\theta = \tan^{-1}\left(\frac{\eta_2}{\eta_1}\right)$

Transforming back to crack tip coordinates (x and y), the temperature field near the crack tip is given as

$$T = q_0 r^{1/2} \sin\left(\frac{1}{2}\theta\right) + q_1 r \cos(\theta) + q_2 r^{3/2} \sin\left(\frac{3}{2}\theta\right) + \left(\frac{1}{4}\right) q_0 \beta r^{3/2} \sin\left(\frac{1}{2}\theta\right) \quad (\text{C.74})$$

where $r = (x^2 + y^2)^{1/2}$ and $\theta = \tan^{-1}\left(\frac{y}{x}\right)$

In-plane Strain Fields

By substituting the eqs. C.54 and C.55 in to Eq. C.7, and after simplification the in plane strain can written as

$$\begin{aligned}
\epsilon_{xx} = & \left(\frac{3}{4} r_l^{-1/2} \cos\left(\frac{\theta_l}{2}\right) - \frac{1}{8} \frac{\zeta}{\alpha_l^2} r_l^{1/2} \left(6 \cos\left(\frac{\theta_l}{2}\right) + \frac{3}{2} \cos\left(\frac{3\theta_l}{2}\right) \right) \right) A_0 \\
& + \left(-\frac{3}{4} r_l^{-1/2} \sin\left(\frac{\theta_l}{2}\right) - \frac{1}{8} \frac{\zeta}{\alpha_l^2} r_l^{1/2} \left(6 \sin\left(\frac{\theta_l}{2}\right) - \frac{3}{2} \sin\left(\frac{3\theta_l}{2}\right) \right) \right) C_0 \\
& + \left(\frac{3}{4} \alpha_s r_s^{-1/2} \cos\left(\frac{\theta_s}{2}\right) - \frac{3}{16} \frac{\zeta}{\alpha_s} r_s^{1/2} \cos\left(\frac{3\theta_s}{2}\right) \right) B_0 + 2A_1 \\
& + \left(\frac{3}{4} \alpha_s r_s^{-1/2} \sin\left(\frac{\theta_s}{2}\right) - \frac{3}{16} \frac{\zeta}{\alpha_s} r_s^{1/2} \sin\left(\frac{3\theta_s}{2}\right) \right) D_0 + 2B_1 \alpha_s \\
& + \frac{15}{4} r_l^{1/2} \cos\left(\frac{\theta_l}{2}\right) A_2 + \frac{15}{4} r_s^{1/2} \alpha_s \cos\left(\frac{\theta_s}{2}\right) B_2 \\
& + \frac{15}{4} r_l^{1/2} \sin\left(\frac{\theta_l}{2}\right) C_2 - \frac{15}{4} r_s^{1/2} \alpha_s \sin\left(\frac{\theta_s}{2}\right) D_2 \\
& - \frac{3}{2} \frac{\zeta \delta \alpha_l^2}{\alpha_l^2 - \alpha_s^2} r_l^{1/2} \left(A_0 \cos\left(\frac{\theta_l}{2}\right) - C_0 \sin\left(\frac{\theta_l}{2}\right) \right) \\
& + \frac{3}{2} \frac{\zeta}{\delta + 2} \frac{\alpha_s}{\alpha_l^2 - \alpha_s^2} r_s^{1/2} \left(B_0 \cos\left(\frac{\theta_l}{2}\right) + D_0 \sin\left(\frac{\theta_l}{2}\right) \right) \\
& + \frac{3\delta + 2}{\delta + 2} \frac{\alpha_c}{\alpha_l^2 - 1} r^{1/2} q_0 \sin\left(\frac{\theta}{2}\right)
\end{aligned} \tag{C.75}$$

$$\begin{aligned}
\epsilon_{yy} = & \left(-\frac{3}{4}r_l^{-1/2} \cos\left(\frac{\theta_l}{2}\right) - \frac{1}{8}\zeta r_l^{1/2} \left(6 \cos\left(\frac{\theta_l}{2}\right) - \frac{3}{2} \cos\left(\frac{3\theta_l}{2}\right) \right) \right) A_0 \\
& + \left(\frac{3}{4}r_l^{-1/2} \sin\left(\frac{\theta_l}{2}\right) - \frac{1}{8}\zeta r_l^{1/2} \left(6 \sin\left(\frac{\theta_l}{2}\right) + \frac{3}{2} \sin\left(\frac{3\theta_l}{2}\right) \right) \right) C_0 \\
& + \left(-\frac{3}{4}\alpha_s r_s^{-1/2} \cos\left(\frac{\theta_s}{2}\right) + \frac{3}{16} \frac{\zeta}{\alpha_s} r_s^{1/2} \cos\left(\frac{3\theta_s}{2}\right) \right) B_0 + 2A_1\alpha_l^2 \\
& + \left(-\frac{3}{4}\alpha_s r_s^{-1/2} \sin\left(\frac{\theta_s}{2}\right) + \frac{3}{16} \frac{\zeta}{\alpha_s} r_s^{1/2} \sin\left(\frac{3\theta_s}{2}\right) \right) D_0 + 2B_1\alpha_s \\
& - \frac{15}{4}\alpha_l^2 r_l^{1/2} \cos\left(\frac{\theta_l}{2}\right) A_2 - \frac{15}{4}r_s^{1/2}\alpha_s \cos\left(\frac{\theta_s}{2}\right) B_2 \\
& - \frac{15}{4\alpha_l^2} r_l^{1/2} \sin\left(\frac{\theta_l}{2}\right) C_2 + \frac{15}{4}r_s^{1/2}\alpha_s \sin\left(\frac{\theta_s}{2}\right) D_2 \\
& + \frac{3}{2} \frac{\zeta \delta \alpha_l^2}{\alpha_l^2 - \alpha_s^2} r_l^{1/2} \left(A_0 \cos\left(\frac{\theta_l}{2}\right) - C_0 \sin\left(\frac{\theta_l}{2}\right) \right) \\
& + \frac{3}{2} \frac{\zeta}{\delta + 2} \frac{\alpha_s^3}{\alpha_l^2 - \alpha_s^2} r_s^{1/2} \left(B_0 \cos\left(\frac{\theta_l}{2}\right) + D_0 \sin\left(\frac{\theta_l}{2}\right) \right) \\
& - \frac{3\delta + 2}{\delta + 2} \frac{\alpha_c}{\alpha_l^2 - 1} r^{1/2} q_0 \sin\left(\frac{\theta}{2}\right)
\end{aligned} \tag{C.76}$$

$$\begin{aligned}
\epsilon_{xy} = & \left(\frac{3}{4} \alpha_l r_l^{-1/2} \sin \left(\frac{\theta_l}{2} \right) - \frac{3}{16} \frac{\zeta}{\alpha_l} r_l^{1/2} \sin \left(\frac{3\theta_l}{2} \right) \right) A_0 \\
& + \left(\frac{3}{4} \alpha_l r_l^{-1/2} \cos \left(\frac{\theta_l}{2} \right) - \frac{3}{16} \frac{\zeta}{\alpha_l} r_l^{1/2} \cos \left(\frac{3\theta_l}{2} \right) \right) C_0 \\
& + \left(\frac{3}{8} r_s^{-1/2} (1 + \alpha_s^2) \sin \left(\frac{\theta_s}{2} \right) \right) B_0 \\
& - \left(\frac{3}{32} \frac{\zeta}{\alpha_s^2} r_s^{1/2} \left(\sin \left(\frac{3\theta_s}{2} \right) (1 + \alpha_s^2) + 4 \sin \left(\frac{\theta_s}{2} \right) (\alpha_s^2 - 1) \right) \right) B_0 \\
& - \left(\frac{3}{8} r_s^{-1/2} (1 + \alpha_s^2) \cos \left(\frac{\theta_s}{2} \right) \right) D_0 \\
& + \left(\frac{3}{32} \frac{\zeta}{\alpha_s^2} r_s^{1/2} \left(\cos \left(\frac{3\theta_s}{2} \right) (1 + \alpha_s^2) - 4 \cos \left(\frac{\theta_s}{2} \right) (\alpha_s^2 - 1) \right) \right) D_0 \\
& + 2C_1 \alpha_l - D_1 (1 - \alpha_s^2) - \left(\frac{15}{4} \alpha_l r_l^{1/2} \sin \left(\frac{\theta_l}{2} \right) \right) A_2 + \left(\frac{15}{4} \alpha_l r_l^{1/2} \alpha_l \cos \left(\frac{\theta_l}{2} \right) \right) C_2 \\
& - \left(\frac{15}{8} r_s^{1/2} (1 + \alpha_s^2) \sin \left(\frac{\theta_s}{2} \right) \right) B_2 - \left(\frac{15}{8} r_s^{1/2} (1 + \alpha_s^2) \cos \left(\frac{\theta_s}{2} \right) \right) D_2 \\
& + \frac{3}{4} \frac{\zeta \delta \alpha_l}{\alpha_l^2 - \alpha_s^2} r_l^{1/2} \left((1 + \alpha_l^2) \sin \left(\frac{\theta_l}{2} \right) A_0 + (1 + \alpha_s^2) \cos \left(\frac{\theta_l}{2} \right) C_0 \right) \\
& + \frac{3}{2} \frac{\zeta}{\delta + 2} \frac{\alpha_s^2}{\alpha_l^2 - \alpha_s^2} r_s^{1/2} \left(\sin \left(\frac{\theta_s}{2} \right) B_0 - \cos \left(\frac{\theta_s}{2} \right) D_0 \right) \\
& + \left(\frac{3\delta + 2}{\delta + 2} \frac{\alpha_c}{\alpha_l^2 - 1} r^{1/2} \cos \left(\frac{\theta}{2} \right) \right) q_0
\end{aligned} \tag{C.77}$$

In-plane Stress Fields

The strain fields given by Eqs. C.75 - C.77 and the temperature field given by Eq. C.74 are substituted into Eqs. C.2 - C.4 to obtain the in-plan stress fields

around the crack tip presented given by Eqs. C.78 - C.80

$$\begin{aligned}
\frac{\sigma_{xx}}{\exp(\zeta x)\mu_0} = & \left(\frac{3}{4} r_l^{-1/2} \cos\left(\frac{\theta_l}{2}\right) (\delta (1 - \alpha_l^2) + 2) \right) A_0 \\
& - \left(\frac{3}{16} \frac{\zeta}{\alpha_l^2} r_l^{1/2} \cos\left(\frac{3\theta_l}{2}\right) (\delta (1 - \alpha_l^2) + 2) \right) A_0 \\
& - \left(\frac{3}{4} \frac{\zeta}{\alpha_l^2} r_l^{1/2} \cos\left(\frac{\theta_l}{2}\right) (\delta (1 + \alpha_l^2) + 2) \right) A_0 \\
& - \left(\frac{3}{4} r_l^{-1/2} \sin\left(\frac{\theta_l}{2}\right) (\delta (1 - \alpha_l^2) + 2) \right) C_0 \\
& + \left(\frac{3}{16} \frac{\zeta}{\alpha_l^2} r_l^{1/2} \sin\left(\frac{3\theta_l}{2}\right) (\delta (1 - \alpha_l^2) - 2) \right) C_0 \\
& + \left(\frac{3}{4} \frac{\zeta}{\alpha_l^2} r_l^{1/2} \sin\left(\frac{\theta_l}{2}\right) (\delta (1 + \alpha_l^2) + 2) \right) C_0 \\
& + \left(\frac{3}{2} r_s^{-1/2} \alpha_s \cos\left(\frac{\theta_s}{2}\right) - \frac{3}{8} \frac{\zeta}{\alpha_s} r_s^{1/2} \cos\left(\frac{3\theta_s}{2}\right) \right) B_0 \\
& + \left(\frac{3}{2} r_s^{-1/2} \alpha_s \sin\left(\frac{\theta_s}{2}\right) - \frac{3}{8} \frac{\zeta}{\alpha_s} r_s^{1/2} \sin\left(\frac{3\theta_s}{2}\right) \right) D_0 \\
& + 2A_1 (\delta (1 - \alpha_l^2) + 2) + 4B_1 \alpha_s \\
& + \left(\left(\frac{15}{4} r_l^{1/2} \cos\left(\frac{\theta_l}{2}\right) (\delta (1 - \alpha_l^2) + 2) \right) A_2 + \left(\frac{15}{2} r_s^{1/2} \alpha_s \cos\left(\frac{\theta_s}{2}\right) \right) B_2 \right) \\
& + \left(\left(\frac{15}{4} r_l^{1/2} \sin\left(\frac{\theta_l}{2}\right) (\delta (1 - \alpha_l^2) + 2) \right) C_2 - \left(\frac{15}{2} r_s^{1/2} \alpha_s \sin\left(\frac{\theta_s}{2}\right) \right) D_2 \right) \\
& - \left(\left(3 \frac{\zeta \delta \alpha_l^2}{\alpha_l^2 - \alpha_s^2} r_l^{1/2} \cos\left(\frac{\theta_l}{2}\right) \right) A_0 - \left(3 \frac{\zeta \delta \alpha_l^2}{\alpha_l^2 - \alpha_s^2} r_l^{1/2} \sin\left(\frac{\theta_l}{2}\right) \right) C_0 \right) \\
& - \left(\frac{3}{2} \frac{\zeta}{\delta + 2} \frac{\alpha_s}{\alpha_l^2 - \alpha_s^2} r_s^{1/2} \cos\left(\frac{\theta_l}{2}\right) (\delta (1 - \alpha_s^2) + 2) \right) B_0 \\
& + \left(\frac{3}{2} \frac{\zeta}{\delta + 2} \frac{\alpha_s}{\alpha_l^2 - \alpha_s^2} r_s^{1/2} \sin\left(\frac{\theta_s}{2}\right) (\delta (1 - \alpha_s^2) + 2) \right) D_0 \\
& + 2 \left(\frac{3\delta + 2}{\delta + 2} \frac{\alpha_c}{\alpha_l^2 - 1} r^{1/2} \sin\left(\frac{\theta}{2}\right) \right) q_0 \\
& - \alpha_c (3\delta + 2) (q_0 r^{1/2} \sin\left(\frac{\theta}{2}\right) + q_1 r \cos(\theta) + q_2 r^{3/2} \sin\left(\frac{3\theta}{2}\right) \\
& + \frac{1}{4} q_0 \beta r^{3/2} \sin\left(\frac{\theta}{2}\right))
\end{aligned} \tag{C.78}$$

$$\begin{aligned}
\frac{\sigma_{YY}}{\exp(\zeta x)\mu_0} = & \left(\frac{3}{4} r_l^{-1/2} \cos\left(\frac{\theta_l}{2}\right) (\delta - \alpha_l^2 (\delta + 2)) \right) A_0 \\
& - \left(\frac{3}{16} \frac{\zeta}{\alpha_l^2} r_l^{1/2} \cos\left(\frac{3\theta_l}{2}\right) (\delta - \alpha_l^2 (\delta + 2)) \right) \\
& - \left(\frac{3}{4} \frac{\zeta}{\alpha_l^2} r_l^{1/2} \cos\left(\frac{\theta_l}{2}\right) (\delta + \alpha_l^2 (\delta + 2)) \right) A_0 \\
& - \left(\frac{3}{4} r_l^{-1/2} \sin\left(\frac{\theta_l}{2}\right) (\delta - \alpha_l^2 (\delta + 2)) \right) C_0 \\
& - \left(\frac{3}{16} \frac{\zeta}{\alpha_l^2} r_l^{1/2} \sin\left(\frac{3\theta_l}{2}\right) (\delta - \alpha_l^2 (\delta + 2)) \right) C_0 \\
& + \left(\frac{3}{4} \frac{\zeta}{\alpha_l^2} r_l^{1/2} \sin\left(\frac{\theta_l}{2}\right) (\delta + \alpha_l^2 (\delta + 2)) \right) C_0 \\
& - \left(\frac{3}{2} r_s^{-1/2} \alpha_s \cos\left(\frac{\theta_s}{2}\right) - \frac{3}{8} \frac{\zeta}{\alpha_s} r_s^{1/2} \cos\left(\frac{3\theta_s}{2}\right) \right) B_0 \\
& - \left(\frac{3}{2} r_s^{-1/2} \alpha_s \sin\left(\frac{\theta_s}{2}\right) - \frac{3}{8} \frac{\zeta}{\alpha_s} r_s^{1/2} \sin\left(\frac{3\theta_s}{2}\right) \right) D_0 \\
& - 4A_1 (\delta - \alpha_l^2 (\delta + 2)) - 4B_1 \alpha_s \\
& + \left(\left(\frac{15}{4} r_l^{1/2} \cos\left(\frac{\theta_l}{2}\right) (\delta - \alpha_l^2 (\delta + 2)) \right) A_2 - \left(\frac{15}{2} r_s^{1/2} \alpha_s \cos\left(\frac{\theta_s}{2}\right) \right) B_2 \right) \\
& + \left(\left(\frac{15}{4} r_l^{1/2} \sin\left(\frac{\theta_l}{2}\right) (\delta - \alpha_l^2 (\delta + 2)) \right) C_2 + \left(\frac{15}{2} r_s^{1/2} \alpha_s \sin\left(\frac{\theta_s}{2}\right) \right) D_2 \right) \\
& + \left(\left(3 \frac{\zeta \delta \alpha_l^2}{\alpha_l^2 - \alpha_s^2} r_l^{1/2} \cos\left(\frac{\theta_l}{2}\right) \right) A_0 - \left(3 \frac{\zeta \delta \alpha_l^2}{\alpha_l^2 - \alpha_s^2} r_l^{1/2} \sin\left(\frac{\theta_l}{2}\right) \right) C_0 \right) \\
& - \left(\frac{3}{2} \frac{\zeta}{\delta + 2} \frac{\alpha_s}{\alpha_l^2 - \alpha_s^2} r_s^{1/2} \cos\left(\frac{\theta_l}{2}\right) (\delta - \alpha_s^2 (\delta + 2)) \right) B_0 \\
& - \left(\frac{3}{2} \frac{\zeta}{\delta + 2} \frac{\alpha_s}{\alpha_l^2 - \alpha_s^2} r_s^{1/2} \sin\left(\frac{\theta_s}{2}\right) (\delta - \alpha_s^2 (\delta + 2)) \right) D_0 \\
& - 2 \left(\frac{3\delta + 2}{\delta + 2} \frac{\alpha_c}{\alpha_l^2 - 1} r^{1/2} \sin\left(\frac{\theta}{2}\right) \right) q_0 \\
& + \alpha_c (3\delta + 2) (q_0 r^{1/2} \sin\left(\frac{\theta}{2}\right) + q_1 r \cos(\theta) + q_2 r^{3/2} \sin\left(\frac{3\theta}{2}\right) \\
& + \frac{1}{4} q_0 \beta r^{3/2} \sin\left(\frac{\theta}{2}\right)) \tag{C.79}
\end{aligned}$$

$$\begin{aligned}
\frac{\sigma_{xy}}{\exp(\zeta x)\mu_0} = & \left(\frac{3}{2}\alpha_l r_l^{-1/2} \sin\left(\frac{\theta_l}{2}\right) - \frac{3}{8}\frac{\zeta}{\alpha_l} r_l^{1/2} \sin\left(\frac{3\theta_l}{2}\right) \right) A_0 \\
& + \left(\frac{3}{2}\alpha_l r_l^{-1/2} \cos\left(\frac{\theta_l}{2}\right) - \frac{3}{8}\frac{\zeta}{\alpha_l} r_l^{1/2} \cos\left(\frac{3\theta_l}{2}\right) \right) C_0 \\
& + \left(\frac{3}{4}r_s^{-1/2} (1 + \alpha_s^2) \sin\left(\frac{\theta_s}{2}\right) \right) B_0 \\
& - \left(\frac{3}{16}\frac{\zeta}{\alpha_s^2} r_s^{1/2} \left(\sin\left(\frac{3\theta_s}{2}\right) (1 + \alpha_s^2) + 4 \sin\left(\frac{\theta_s}{2}\right) (\alpha_s^2 - 1) \right) \right) B_0 \\
& - \left(\frac{3}{4}r_s^{-1/2} (1 + \alpha_s^2) \cos\left(\frac{\theta_s}{2}\right) \right) D_0 \\
& + \left(\frac{3}{16}\frac{\zeta}{\alpha_s^2} r_s^{1/2} \left(\cos\left(\frac{3\theta_s}{2}\right) (1 + \alpha_s^2) - 4 \cos\left(\frac{\theta_s}{2}\right) (\alpha_s^2 - 1) \right) \right) D_0 \\
& - \left(\left(\frac{15}{2}\alpha_l r_l^{1/2} \sin\left(\frac{\theta_l}{2}\right) \right) A_2 - \left(\frac{15}{2}\alpha_l r_l^{1/2} \alpha_l \cos\left(\frac{\theta_l}{2}\right) \right) C_2 \right) \\
& - \left(\left(\frac{15}{4}r_s^{1/2} (1 + \alpha_s^2) \sin\left(\frac{\theta_s}{2}\right) \right) B_2 + \left(\frac{15}{4}r_s^{1/2} (1 + \alpha_s^2) \cos\left(\frac{\theta_s}{2}\right) \right) D_2 \right) \\
& + \left(\frac{3}{2}\frac{\zeta\delta\alpha_l}{\alpha_l^2 - \alpha_s^2} r_l^{1/2} (1 + \alpha_l^2) \sin\left(\frac{\theta_l}{2}\right) \right) A_0 \\
& + \left(\frac{3}{2}\frac{\zeta\delta\alpha_l}{\alpha_l^2 - \alpha_s^2} r_l^{1/2} (1 + \alpha_s^2) \cos\left(\frac{\theta_l}{2}\right) \right) C_0 \\
& + \left(3\frac{\zeta}{\delta + 2}\frac{\alpha_s^2}{\alpha_l^2 - \alpha_s^2} r_s^{1/2} \sin\left(\frac{\theta_s}{2}\right) \right) B_0 \\
& - \left(3\frac{\zeta}{\delta + 2}\frac{\alpha_s^2}{\alpha_l^2 - \alpha_s^2} r_s^{1/2} \cos\left(\frac{\theta_s}{2}\right) \right) D_0 \\
& + 2 \left(\frac{3\delta + 2}{\delta + 2}\frac{\alpha_c}{\alpha_l^2 - 1} r^{1/2} \cos\left(\frac{\theta}{2}\right) \right) q_0
\end{aligned} \tag{C.80}$$

APPENDIX D

Split Hopkinson Bar Theory

Longitudinal wave in a homogeneous bar with density ρ and Young's modulus E_b can be given as

$$\frac{\partial^2 u}{\partial t^2} = c^2 \frac{\partial^2 u}{\partial x^2} \quad (\text{D-1})$$

where c is longitudinal wave velocity in the bar given by $c = \sqrt{\frac{E_b}{\rho}}$, u is the displacement and t is time.

The general solution for the above 1D partial differential equation can be written as

$$u = f(x - ct) + g(x + ct) \quad (\text{D-2})$$

where f and g are arbitrary functions determined by initial conditions.

From Eq. D-2, the strain (ϵ), stress (σ) and particle velocity (\dot{u}) in the bar can be derived as

$$\epsilon = \frac{\partial u}{\partial x} = \frac{\partial f}{\partial x} + \frac{\partial g}{\partial x} \quad (\text{D-3})$$

$$\sigma = E\epsilon = E(f' + g') \quad (\text{D-4})$$

$$\dot{u} = \frac{\partial u}{\partial t} = \frac{\partial f}{\partial t} + \frac{\partial g}{\partial t} = -cf' + cg' = c(-f' + g') \quad (\text{D-5})$$

Split Hopkinson bar apparatus consists of two elastic bars with small specimen attached in between the bars as shown in Fig. D.1. In the figure; the incident, reflected and transmitted waves are indicated with the corresponding directions. Using Eq. D-2 the displacements of the bar (u_1 and u_2) at the interfaces can be given as,

$$u_1 = f_1(x - ct) + g_1(x + ct) = u_i + u_r \quad (\text{D-6})$$

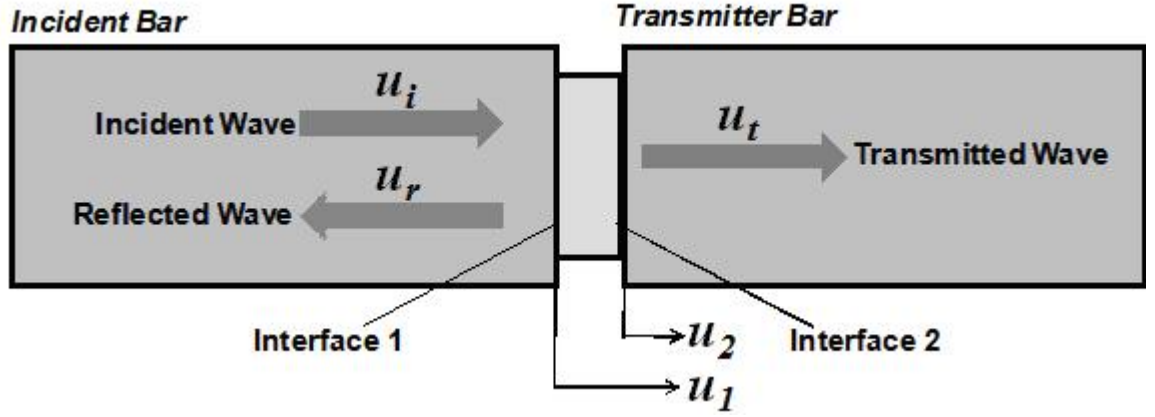


Figure D.1. Schematic representation of SHPB

$$u_2 = f_2(x - ct) = u_t \quad (\text{D-7})$$

where u_i , u_r and u_t are incident reflected and transmitted waves

Following similar procedure and using the above equations, the particle velocity, strain and stress at the interface of the bar are derived as follows

Particle velocity

$$\dot{u}_1 = c(-f'_1 + g'_1) = c(-\epsilon_i + \epsilon_r) \quad (\text{D-8})$$

$$\dot{u}_2 = c(-f'_2) = -c\epsilon_t \quad (\text{D-9})$$

Strain

$$\epsilon_1 = f'_1 + g'_1 = \dot{u}_i + \dot{u}_r = -\epsilon_i + \epsilon_r \quad (\text{D-10})$$

$$\epsilon_2 = f'_2 = \dot{u}_t = \epsilon_t \quad (\text{D-11})$$

Stress

$$\sigma_1 = E\epsilon_1 = E(\epsilon_i + \epsilon_r) \quad (\text{D-12})$$

$$\sigma_2 = E\epsilon_2 = E\epsilon_t \quad (\text{D-13})$$

So long as the stress in the bars remains under elastic limits, specimen stress, strain, and strain rate can be calculated from the recorded strain histories.

Strain rate in the specimen can be given as

$$\begin{aligned}\dot{\epsilon}_s &= \frac{\dot{u}_2 - \dot{u}_1}{l_s} \\ &= \frac{c}{l_s}(\epsilon_i - \epsilon_t - \epsilon_r)\end{aligned}\tag{D-14}$$

Strain in the specimen:

$$\begin{aligned}\epsilon_s &= \int_0^t \dot{\epsilon}_s dt \\ &= \frac{c}{l_s} \int_0^t (\epsilon_i - \epsilon_t - \epsilon_r) dt\end{aligned}\tag{D-15}$$

Stress in the specimen

$$\sigma_s = \frac{F_a}{A_s}\tag{D-16}$$

where F_a average force of two interfaces, and A and A_s are bar and specimen cross sectional areas respectively.

The average force F_a can be given as

$$\begin{aligned}F_a &= \frac{F_1 + F_2}{2} \\ &= \frac{\sigma_1 A + \sigma_2 A}{2}\end{aligned}\tag{D-17}$$

Substituting Eq. D-17 in to Eq. D-16 results in

$$\begin{aligned}\sigma_s &= \frac{\sigma_1 A + \sigma_2 A}{2A_s} \\ &= \frac{EA}{2A_s}(\epsilon_i + \epsilon_t + \epsilon_r)\end{aligned}\tag{D-18}$$

The stress and strain of the specimen must be equilibrium during the loading process, i.e

$$\epsilon_i = \epsilon_t + \epsilon_r\tag{D-19}$$

By using the above equilibrium relation, the equation for strain rate, strain and stress in the specimen can be reduce to

$$\dot{\epsilon}_s = \frac{2c}{l_s} \epsilon_r \quad (\text{D-20})$$

$$\epsilon_s = -\frac{2c}{l_s} \int_0^t \epsilon_r dt \quad (\text{D-21})$$

$$\sigma_s = \frac{EA}{A_s} \epsilon_t \quad (\text{D-22})$$

Conditions to Satisfy the Equilibrium of the Specimen

- The elastic waves in the bars must be one-dimension longitudinal wave i.e the wave length \gg radii of the bar. This can be maintained generally by making the length of the striker bar 5 times larger than the radii of the bar.
- The specimen must deform uniformly. This can be achieved by
 - a. Making the wave pulse long enough
 - b. Choosing the specimen dimension using Eq. D-24

$$\frac{l_s}{d_s} = \sqrt{\frac{3\nu_s}{4}} \quad (\text{D-23})$$

where l_s , d_s and ν_s are length, diameter and poison's ration of the specimen.

- c. Lubricating the interfaces of the bars and the specimen

Dimension of the Tungsten Carbide Inserts

During the elevated temperature testing two-carbide inserts are placed between the two bars and the specimen is sandwiched between the inserts as shown in Fig. D.2. The inserts are used to eliminate the temperature gradient in the bars. The inserts are impedance matched to the bars and hence do not disturb the incident, transmitted and reflected wave profiles.

The dimension of the tungsten carbide insert is chosen by using the impedance

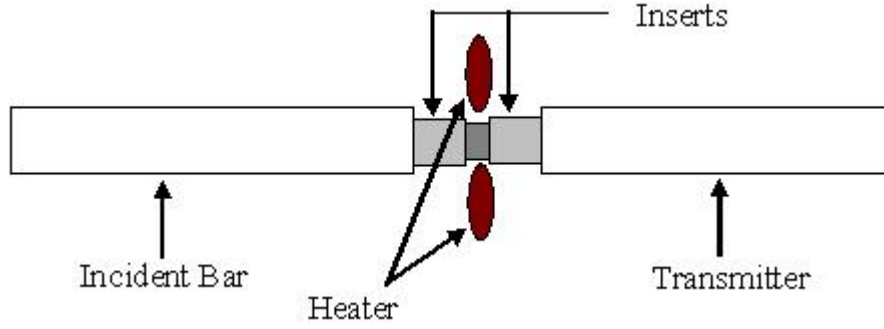


Figure D.2. Schematic description of SHPB with heaters

Table D.1. Material properties of marringing steel and tungsten carbide

Material type	Young's modulus (GPa)	Density (ρ)
Marringing steel	200	8080
Tungsten carbide	566	143800

relation given by Eq. D-25

$$\rho_s A_s c_s = \rho_c A_c c_c \quad (\text{D-24})$$

where ρ_s , A_s and c_s are density, cross sectional area and wave speed of the bar respectively and ρ_c , A_c and c_c are density, cross sectional area and wave speed of the inserts.

The mechanical and physical properties of the marringing steel and the tungsten carbide is given in the following Table. D.1

All variables in Eq. D-24, except the the cross-sectional are of the tungsten carbide inserts is known. The cross-sectional area of the tungsten carbide insert is determined from Eq. D-24 as

$$\begin{aligned} A_c &= \frac{\rho_s A_s c_s}{\rho_c c_c} \\ &= 56.6 \text{ mm}^2 \end{aligned} \quad (\text{D-25})$$

i.e

$$D_c = 8.38 \text{ mm} \quad (\text{D-26})$$

Therefore a tungsten bar with diameter of $D_c = 8.38$ mm is chosen. To make sure that the impedance is properly matched, a calibration experiment is conducted. The calibration is made by attaching the two tungsten carbide inserts and sandwiched them between the bars as shown in Fig. D.3. During loading the projectile hits the incident bar, and the stress wave propagates from incident bar to the transmitter bar through the tungsten carbide inserts. The strain on the incident and transmitter bars is measured using the strain gages (sg) attached on the bars. Fig. D.4 shows typical incident and transmitted signals from the calibration ex-



Figure D.3. Schematic description of calibration experimental setup

periment. As shown in the figure the incident and transmitted signals are identical and there is no reflected signal observed. This can be seen clearly in the Fig. D.5, where the incident signal is plotted on the top of the reflected signal.

Specimen Dimension

The length of the specimen is determined from the available plate thickness
Length of the specimen is 3.175 mm

To determine the diameter of the specimen the criteria relation given by Eq. D-23 is considered and a 10% axial strain is assumed

The axial strain in the specimen can be given as

$$\epsilon_a = \frac{\Delta L}{L} = 0.1 \quad (\text{D-27})$$

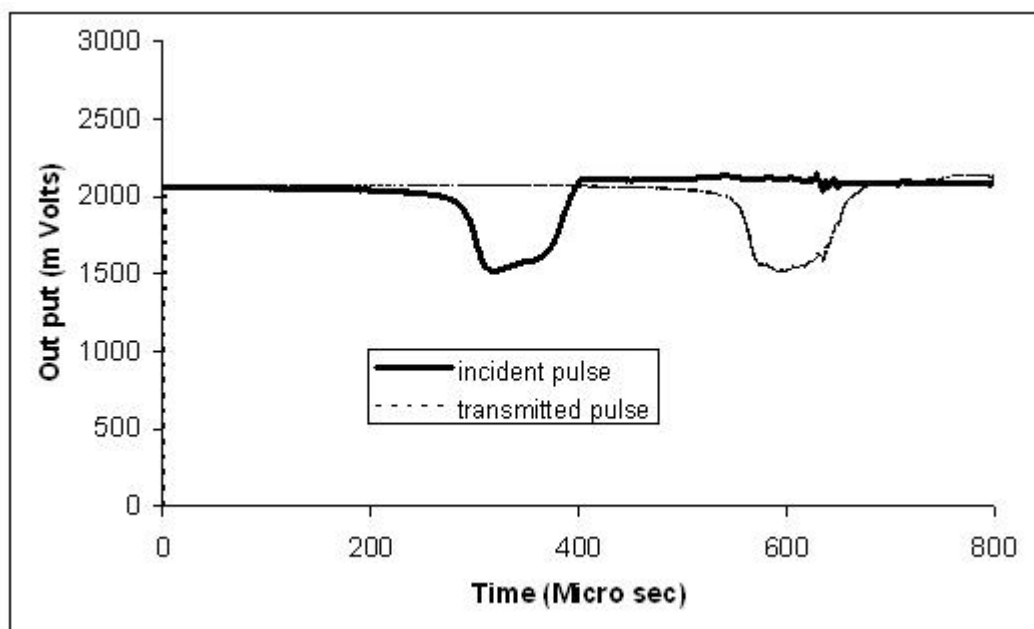


Figure D.4. Typical incident and transmitted signal from calibration experiment

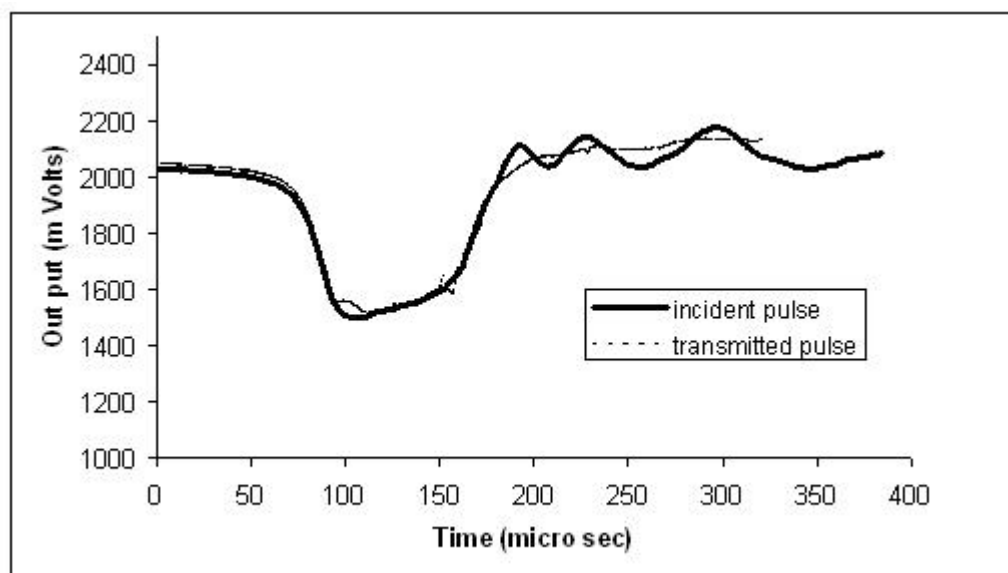


Figure D.5. Incident and transmitted signals plotted at the same position

The poisson's ration for the material considered is ν is 0.3

Therefore the lateral strain on the specimen cab be written as

$$\epsilon_a = \frac{\Delta D}{D} = \frac{D_f - D_0}{D_0} = 0.03 \quad (\text{D-28})$$

where D_f = Diameter of the specimen after deformation

D_0 = Diameter of the specimen before deformation

Rearranging Eq. D-28 will results in

$$\frac{D_f}{D_0} = 1.03 \Rightarrow D_0 = \frac{D_f}{1.03} \quad (\text{D-29})$$

At this point it should be notice that, the diameter of the deformed specimen should be less than the diameter of the inserts. i.e $D_f \leq 8.38$ mm

Using the relation given by Eq. D-29 and considering the maximum limit of the deformation, a specimen with initial diameter $D_0 = 7.62$ mm is obtained.

BIBLIOGRAPHY

- “Metals handbook, fractography and atlas of fractographs, asm vol. 9, eighth edition, 1974.”
- Broek, D., *Elementary engineering fracture mechanics*. Martinus Nishoff Publishers, 1978.
- Chalivendra, V. B. Shukla, A. and Parameswaran, V., “Dynamic out of plane displacement fields for an inclined crack in graded materials,” *Journal of Elasticity*, vol. 69, pp. 99–119, 2002.
- Chalivendra, V. B., “Asymptotic analysis of transient curved crack in functionally graded materials,” *International Journal of Solids and Structures*, vol. 44, p. 465479, 2007.
- Chalivendra, V. B., “Mode-i crack-tip stress fields for inhomogeneous orthotropic medium,” *Mechanics of Materials*, vol. 40, pp. 293–301, 2008.
- Chalivendra, V. B. and Shukla, A., “Transient elastodynamic crack growth in functionally graded materials,” *Journal of Applied Mechanics*, vol. 72, p. 23727, 2005.
- Chen, T. C. and Weng, C. I., “Coupled transient thermoelastic response in an edge-cracked plate,” *Eng. Fract. Mech.*, vol. 39, pp. 915–925, 1991.
- Chi, S. H. and Chung, Y. L., “Mechanical behavior of functionally graded material plates under transverse load part i: Analysis,” *Int. J. Solids. Struct.*, vol. 43, pp. 3657–3674, 2006.
- Clements, D.L. Atkinson, C. and Rogers, C., “Antiplane crack problems for an inhomogeneous elastic material,” *Acta Mechanica*, vol. 29, pp. 199–211, 1978.
- Dai, K.Y. Liu, G. H. X. and Lim, K., “Thermomechanical analysis of functionally graded material (fgm) plates using element-free galerkin method,” *Computers and Structures*, vol. 83, p. 14871502, 2005.
- Dally, J. and Barker, D., “Dynamic measurements of initiation toughness at high loading rates,” *Experimental Mechanics*, vol. 28, pp. 298–303, 1988.
- Delale, F. and Erdogan, F., “The crack problem for a nonhomogeneous plane,” *J. Appl. Mech.*, vol. 50, p. 6780, 1983.
- Dhaliwal, R. and Singh, B., “On the theory of elasticity of a nonhomogeneous medium,” *J. Elasticity*, vol. 8:2, pp. 211–219, 1978.

- Drake, J. T. Williamson, R. L. and Rabin, B. H., "Finite element analysis of thermal residual stresses at graded ceramic-metal interfaces, part ii: interface optimization for residual stress reduction," *Journal of Applied Physics*, vol. 74, pp. 1321–1326, 1993.
- Eischen, J., "Fracture of nonhomogeneous materials," *International Journal of Fracture*, vol. 34 (3), p. 322, 1987.
- Erdogan, F. Kaya, C. and Joseph, P., "The crack problem in bonded nonhomogeneous materials," *J. Appl. Mech.*, vol. 58, pp. 410–418, 1991.
- Erdogan, F., "Fracture mechanics of functionally graded materials," *Comp. Engng.*, vol. 5:7, pp. 753–770, 1995.
- Erdogan, F. and Sih, G. C., "On the crack extension in plates under plane loading and transverse shear," *Journal of Basic Engineering*, vol. 85, pp. 519–527, 1963.
- F, E. and Wu, B. H., "Crack problems in fgm layers under thermal stresses," *Journal of Thermal Stresses*, vol. 12, pp. 237–265, 1996.
- Freund, L. B., *Dynamic Fracture Mechanics*, first ed. Cambridge Press, 1990.
- Gerasoulis, A. and Srivastav, R., "A griffith crack problem for a nonhomogeneous medium," *Int. J. Engng. Sci.*, vol. 18, pp. 239–247, 1980.
- Giannakopoulos, A. E. Suresh, S. F. M. and Olsson, M., "Elastoplastic analysis of thermal cycling: layered materials with compositional gradient," *Acta metallurgica et materialia*, vol. 43, pp. 1335–1354, 1995.
- Gibson, R., "Some results concerning displacements and stresses in a nonhomogeneous elastic half space," *Geotechnique*, vol. 17, p. 5867, 1967.
- Hasselman, D. P. H. and Youngblood, G. E., "Enhanced thermal stress resistance of structural ceramics with thermal conductivity gradient," *Journal of the American Ceramic Society*, vol. 61, pp. 49–52, 1978.
- Hill, M. Carprnter, R. P. G. M. Z. and Gibeling, J., "Fracture resistance testing of monolithic and composite brittle materials," in *ASTM STP 1409*, 2002.
- Horgan, C. O. and Chan, A. M., "The pressurized hollow cylinder or disk problem for functionally graded isotropic linearly elastic materials," *J. Elasticity*, vol. 55, pp. 43–59, 1999.
- Hosseini-Tehrani, P. Eslami, M. R. D. H. R., "Dynamic crack analysis under coupled thermoelastic assumption," *Trans. ASME*, vol. 68, pp. 584–588, 2001.
- Irwin, G. R., "Series representation of the stress field around constant speed cracks," university of Maryland Lecture Notes.

- Jain, N. and Shukla, A., "Asymptotic analysis and reflection photoelasticity for the study of transient crack propagation in graded materials," *Journal of mechanics of materials and structures*, vol. 2(4), pp. 595–612, 2007.
- Jain, N. Chona, R. and Shukla, A., "Asymptotic stress fields for thermomechanically loaded cracks in fgmsn," *Journal of ASTM International*, vol. 3(7), 2006.
- Jiang, F. Liu, R. Z. X. K. S. V. A. R., "Evaluation of dynamic fracture toughness kid by hopkinson pressure bar loaded instrumented charpy impact test," *Engineering Fracture Mechanics*, vol. 71, pp. 279–287, 2004.
- Jiang, C.P. Zou, Z. Z. W. D. and Liu, Y. W., "A discussion about a class of stress intensity factors and its verification," *International Journal of Fracture*, vol. 49, pp. 141–157, 1991.
- Jin, Z. H. and Batra, R. C., "Stress intensity relaxation at the tip of an edge crack in a functionally graded materials subjected to a thermal shock,," *Journal of Thermal Stresses*, vol. 19, pp. 317–339,, vol. 19, pp. 317–339, 1996.
- Jin, Z. H. and Paulino, G. H., "Transient thermal stress analysis of an edge crack in a functionally graded materials,," *International Journal of Fracture*, vol. 107, pp. 73–98, 2001.
- Jin, Z. and Batra, R., "Some fracture mechanics concepts in functionally graded materials," *J. Mech. Phys. Solids*, vol. 44:8, pp. 1221–235, 1996.
- Jin, Z. and Batra, R., "R-curve and strength behavior of functionally graded material," *Mat. Sci. Engng., A*, vol. 242, pp. 70–76, 1998.
- Jin, Z. and Dodds, R., "Crack growth resistance behavior of a functionally graded material: Computational studies," *Engineering Fracture Mechanics*, vol. 71, p. 16511672, 2004.
- Jin, Z. and Noda, N., "Crack-tip singular fields in nonhomogeneous materials," *J. Appl. Mech.*, vol. 61, pp. 738–739, 1994.
- Kassir, M. K. Bergman, A. M., "Thermal stress in a solid containing parallel circular crack," *Appl. Res. Sci.*, vol. 25, pp. 262–280, 1971.
- Kassir, M., "Boussinesq problems for a nonhomogeneous solid," *Proc. ASCE, J. Engng. Mech. Div.*, vol. 98, pp. 457–570, 1972.
- Kassir, M., "A note on the twisting deformation of a nonhomogeneous shaft containing a circular crack," *Int. J. Frac. Mech.*, vol. 8:3, pp. 325–334, 1972.
- Katsareas, D. E. and Anifantis, N. K., "On the computation of mode-i and ii thermal shock stress intensity factors using a boundary-only element method," *Int. J. Numer. Methods. Eng.*, vol. 38, pp. 4157–4169, 1995.

- Kawasaki, A. and R., W., "Finite element analysis of thermal stress of the metal/ceramics multi-layer composites with controlled compositional gradients," *Journal of the Japan institute of metal*, vol. 51, pp. 525–529, 1987.
- Kawasaki, A. and Watanabe, R., "Evaluation of thermomechanical performance for thermal barrier type of sintered functionally graded materials," *Composites Part B*, vol. 28B, pp. 29–35., 1997.
- Kawasaki, A. and Watanabe, R., "Thermal fracture behavior of metal/ceramic functionally graded materials," *Engineering Fracture Mechanics*, vol. 69, p. 17131728, 2000.
- Kidane, A. and Shukla, A., "Dynamic constitutive behavior of ti/tib fgm under thermo-mechanical loading," *Journal of Material Science*, vol. 43, p. 27712777, 2008.
- Kim, J. H. and Paulino, G. H., "T-stress, mixed-mode stress intensity factors, and crack initiation angles in functionally graded materials: A unified approach using the interaction integral method," *Comput. Methods Appl. Mech. Engr.*, vol. 192, p. 14631494, 2003.
- Kokini, K. and Case, M., "Initiation of surface and interface edge cracks in functionally graded ceramic thermal barrier coatings," *ASME Journal of Engineering Materials and Technology*, vol. 119, pp. 148–152, 1997.
- Kokini, K. and Choules, B. D., "Surface thermal fracture of functionally graded ceramic coatings: effect of architecture and materials,," *Composite Engineering*, vol. 5, pp. 865–877, 1995.
- Konda, N. and Erdogan, F., "The mixed mode crack problem in a nonhomogeneous elastic medium," *Engng. Frac. Mech.*, vol. 47, pp. 533–545, 1994.
- Kuroda, Y. Kusaka, K. M. A. and Togawa, M., "Evaluation tests of zro2/ni functionally gradient materials for regeneratively cooled thrust engine applications," in *Ceramic Transactions, Functionally Gradient Materials*, J.B. Holt, M. Koisumi, T. H. and Munir, Z., Eds., vol. 34, no. 289-296. American Ceramic Society, Westerville, Ohio, vol., 1993.
- Lee, K. H., "Characteristics of a crack propagating along the gradient in functionally gradient materials," *Int. J. of Solids and Structures*, vol. 41, pp. 2879–2898, 2004.
- Lee, K. Y. and Sim, K., "Thermal shock stress intensity factor by bueckners weight function method," *Eng. Fract. Mech.*, vol. 37, pp. 799–804, 1990.
- Lennon, A. M. and Ramesh, K. T., "A technique for measuring the dynamic behavior of materials at high temperatures," *International Journal of Plasticity*, vol. 14, p. 12791292., 1998.

- Li, Y. Ramesh, K. T. and Chin, E., "Dynamic characterization of layered and graded structures under impulsive loading," *International Journal of Solids and Structures*, vol. 38(34-35), pp. 6045–6061, 2001.
- Li, H., L. J. C. B. and H., S. M., "Experimental investigation of quasi-static fracture of functionally graded material," *International Journal Solids and Structures*, vol. 37, p. 37153732, 1999.
- Nakagaki, M. Sasaki, H. and Hagihara, S., "A study of crack in functionally graded material under dynamic loading," *PVP, Dynamic Fracture, Failure and Deformation, ASME*, vol. 300, pp. 1–6, 1995.
- Niino, M. Hirai, T. and Watanabe, R., "The functionally gradient materials," *Journal of the Japan Society of Composite Materials*, vol. 13 (1), p. 257, 1987.
- Noda, N., "Thermal stress intensity for functionally graded plate with an edge crack," *Journal of Thermal Stresses*, vol. 20, pp. 373–387, 1997.
- Noda, N., "Thermal stresses in functionally graded materials, general lecture third international congress on thermal stresses," in *Thermal Stresses 99*, Cracow, Poland, June 13-17 1999.
- Parameswaran, V. and Shukla, A., "Dynamic fracture of a functionally gradient material having discrete property variation," *Journal of Material Science*, vol. 33, pp. 3303–3311, 1998.
- Parameswaran, V. and Shukla, A., "Crack-tip stress fields for dynamic fracture in functionally gradient materials," *Mechanics of Materials*, vol. 31, pp. 579–596, 1999.
- Plevako, V., "On the theory of elasticity of inhomogeneous media," *PMM*, vol. 35:, pp. 5,853, 1971.
- Popov, G. I., "Axisymmetric contact problem for an elastic inhomogeneous half-space in the presence of cohesion," *J. Appl. Math. Mech.*, vol. 37, pp. 1052–1059, 1973.
- Praveen, G. N. and Reddy, J. N., "Nonlinear transient thermoelastic analysis of functionally graded ceramic-metal plates," *Int. J. Solids Structure.*, vol. 35, pp. 4457–4476, 1998.
- Rousseau, C. E. and Tippur, H. V., "Dynamic fracture of compositionally graded materials with cracks along the elastic gradient: Experiments and analysis," *Mechanics of Materials*, vol. 33, pp. 403–421, 2001.
- Rousseau, C. E. and Tippur, H. V., "Influence of elastic variations on crack initiation in functionally graded glass-filled epoxy," *Engineering Fracture Mechanics*, vol. 69, p. 16791693, 2002.

- Rubio, L Fernandez-Saez, J. and Navarro, C., "Determination of dynamic fracture-initiation toughness using three-point bending tests in a modified hopkinson pressure bar." *Experimental Mechanics*, vol. 43 (4), pp. 379–386, 2003.
- Shazly, M. Prakash, V. and Draper, S., "Mechanical behavior of gamma-met px under uniaxial loading at elevated temperatures and high strain rates," *International Journal of Solids and Structures*, vol. 41, pp. 6485–6503, 2004.
- Shukla, A. and Jain, N., "Dynamic damage growth in particle reinforced graded materials," *International Journal of Impact Engineering*, vol. 30, p. 777803, 2004.
- Shukla, A. Jain, N. and Chona, R., "A review of dynmaic fracture studies in functionally graded materials," *Strain*, vol. 43, pp. 76–95, 2007.
- Sih, G. C., "On the singular character of thermal stress near a crack tip," *ASME J. Appl. Mech.*, vol. 29, pp. 587–589, 1962.
- Sih, G. C., "Strain-energy-density factor applied to mixed mode crack problems," *International of Journal of fracture*, vol. 10 (3), pp. 305–321, 1974.
- Singh, B., "The reissner-sagoci problem for a nonhomogeneous solid," *Def. Sci. J.*, vol. 22, pp. 81–86, 1972.
- Singh, B., "A note on the reissner-sagoci problem for a nonhomogeneous solid," *ZAAM*, vol. 53, pp. 419–420, 1973.
- Suresh, S. and Mortensen, A., *Fundamentals of functionally graded materials, processing and thermo-mechanical behavior of graded metals and metal-ceramic composites*. IOM Communications Ltd., London, 1998.
- Takahashi, H. T. Ishikawa, T. O. D. and Hashida, T., "Laser and plasma-arc thermal shock/fatigue fracture evaluation procedure for functionally gradient materials." in *Thermal Shock and Thermal Fatigue Behavior of Advanced Ceramics*, Scheneider, G. and Petzow, G., Eds. Dordrecht.: Kluwer Academic Publishers, 1993, pp. 543–554.
- Wadgaonkar, S. C. and Parameswaran, V., "Structure of near-tip stress fields and variation of stress intensity factor for a crack in a transversely graded material," *Journal of Applied Mechanics, Transactions of the ASME*, vol. 76, 2009.
- Walters, M. C. Paulino, G. H. and Dodds, J. R. H., "Stress-intensity factors for surface cracks in functionally graded materials under mode-i thermomechanical loading," *International Journal of Solids and Structures*, vol. 41, pp. 1081–1118, 2004.

- Wang, C. D. Tzeng, C. S. P. E. and Lio, J. J., “Displacements and stresses due to a vertical point load in an inhomogeneous transversely isotropic half-space,” *International Journal of Rock Mechanics and Mining Science*, vol. 40(5), pp. 667–685, 2003.
- Wilson, W. K. and Yu, I. W., “The use of the j-integral in the thermal stress crack problems,” *Int. J. Fract.*, vol. 15, pp. 377–387, 1979.
- Yoffe, E. H., “The moving griffith crack,,” *Philosophical Magazine*, vol. 42, pp. 739–750, 1952.
- Yokoyama, T., “Determination of dynamic fracture-initiation toughness using a novel impact bend test procedure,” *ASME J Pressure Vessel Technology*, vol. 115, pp. 389–396., 1993.